

Structure and Dynamics of Dust Clusters: Rotation and Magnetic Fields

Dissertation
zur Erlangung des Doktorgrades
der Mathematisch-Naturwissenschaftlichen Fakultät
der Christian-Albrechts-Universität zu Kiel

vorgelegt von
Jan Carstensen

Kiel
Mai 2013

Erster Gutachter: Prof. Dr. A. Piel
Zweiter Gutachter: Prof. Dr. S. Wolf
Tag der mündlichen Prüfung: ... 21. Juni 2013
Zum Druck genehmigt: Kiel, den 21. Juni 2013

Der Dekan

Abstract

Ensembles of charged, micrometer-sized dust particles confined in the sheath of a rf-discharge are typically in a strongly-coupled state and form crystal-like structures (dust clusters). This thesis focuses on the effects of magnetic fields and rotation on the structure and dynamics of dust clusters. Both topics, magnetization and rotation, are linked, since dust structures in the presence of magnetic fields are usually in a rotating state. Furthermore, the Larmor theorem states that the Lorentz force and the Coriolis force are mathematically equivalent and affect the dynamics of dust clusters in a similar way.

In order to systematically study the effects of cluster rotation, a dust centrifuge is introduced as a new technique to set dust clusters into rotation. This allows to clearly separate the effects of rotational motion from the influence of magnetic fields. In a frame of a rotating cluster two pseudo-forces appear: the centrifugal force, which effectively weakens the radial confinement of the dust clusters and offers the possibility to probe the dust-dust interaction. Moreover, the Coriolis force, which modifies the dynamics of a dust cluster in a similar way as it is expected from a giant magnetic field. Here, a proof-of-principle is given that the Coriolis force can be used to effectively magnetize a small dust cluster and to study the simultaneous effects of (pseudo) magnetization and strong coupling in a dusty plasma device.

The second focus of this thesis lies on the effects of magnetic fields on the dynamics of dust clusters. The mechanism of cluster rotation in the presence of an axial magnetic field is discussed. It is found that the cluster rotation is accompanied by a co-rotation of the neutral gas column, which can result in an unexpected sense of rotation and magnitude of the rotation frequencies in comparison to an established model of cluster rotation, which is based on a balance of ion and neutral drag force. Furthermore, the dust-dust interaction force is of special interest, which is substantially modified by the flow of ions in the plasma sheath and the formation of ion wakes. Here, the phase-resolved resonance method is introduced to measure the nonreciprocity of the interaction force and the partial decharging of particles in the wake of another with high precision. It turns out that both effects are not independent of each other and that the decharging effect enhances the nonreciprocity of the particle interaction due to a coupling with the external confinement. In a further step, the influence of a strong magnetic field on the ion-wake-mediated particle interaction force is studied. It is shown for the first time that a magnetic field parallel to the ion flow severely reduces the interaction forces, which is in qualitative agreement with linear response calculations predicting a reduction of the wake charge.

At last, an alternative approach to reach the realms of fully magnetized dusty plasmas is discussed. Going down in particle size from micrometer-sized dust particles to nanoparticles might allow to produce a dusty plasma, where even the motion of the dust is directly affected by a strong magnetic field. Here, two important steps towards this aim are made. First, a modified discharge geometry is proposed, which allows to confine dust clouds in a plasma column in the presence of strong magnetic fields. Second, an "Imaging Mie Ellipsometer" is introduced, which provides important parameters, such as the dust size and the dust density, with high spatiotemporal resolution.

Zusammenfassung

Geladene, mikrometer-große Staubpartikel eingefangen in der Randschicht einer HF-Entladung befinden sich typischerweise in einem Zustand starker Kopplung und formen kristallartige Strukturen (Staubcluster). Diese Arbeit beschäftigt sich mit den Effekten von Magnetisierung und Rotation auf die Struktur und Dynamik von Staubclustern. Beide Themen, Magnetisierung und Rotation, sind miteinander verbunden, da sich Staubcluster in magnetisierten Plasmen üblicherweise in Rotation befinden. Weiterhin besagt das Larmor Theorem, dass Lorentz- und Corioliskraft mathematisch äquivalent sind und die Dynamik von Staubclustern in ähnlicher Weise beeinflussen.

Um den Einfluss der Clusterrotation systematisch zu studieren, wurde eine Staubzentrifuge entwickelt, welche es erlaubt, den Einfluss von Rotation klar von den Einflüssen eines Magnetfeldes zu trennen. Im Bezugssystem eines rotierenden Clusters treten zwei Scheinkräfte auf: Die Zentrifugalkraft, welche zu einer effektiven Abschwächung des radialen Einschlusses führt und es erlaubt die Staub-Staub Wechselwirkung näher zu untersuchen. Des Weiteren die Corioliskraft, welche die Dynamik von Staubclustern in einer ähnlichen Weise beeinflusst, wie es von einem starken Magnetfeld erwartet wird. Es wird gezeigt, dass die Corioliskraft zu einer effektiven Magnetisierung von Staubclustern benutzt werden kann und es somit erlaubt, die simultanen Effekte von (Schein-) Magnetisierung und starker Kopplung in einem staubigen Plasma zu studieren.

Der zweite Schwerpunkt dieser Arbeit liegt auf der Wirkung von Magnetfeldern auf die Dynamik von Staubclustern. Es wird der Mechanismus, der Staubcluster in Gegenwart eines axialen Magnetfelds in Rotation versetzt, diskutiert. Hierbei stellt sich heraus, dass die Clusterrotation von einer Korotation der Neutralgassäule begleitet wird, welches, im Vergleich zu einem etablierten Modell der Clusterrotation, zu einer unerwarteten Richtung und Geschwindigkeit der Rotation führen kann. Weiterhin ist die Wechselwirkungskraft zwischen den Teilchen von besonderem Interesse, welche stark durch den Ionenfluss in der Plasmarandschicht und dem Auftreten von Ion-Wakes beeinflusst wird. Es wird eine phasenaufgelöste Resonanzmethode vorgestellt, die es ermöglicht, die Nichtreziprozität der Wechselwirkung und die teilweise Entladung eines Partikel im Wake eines anderen mit hoher Präzision zu bestimmen. Es stellt sich heraus, dass beide Effekte nicht unabhängig voneinander sind und der Entladungseffekt in Verbindung mit dem äußeren Einschluss die Nichtreziprozität der Wechselwirkung verstärkt. In einem weiteren Schritt wird der Einfluss eines starken Magnetfeldes auf die von Ion-Wakes modifizierten Interpartikelkräfte studiert. Es kann hier zum ersten Mal gezeigt werden, dass ein Magnetfeld parallel zum Ionenfluss zu einer Abschwächung der Kopplungskräfte führt, welches in qualitativer Übereinstimmung mit Rechnungen in Linear-Response Näherung ist, die eine Reduktion der Wake-Ladung vorhersagen.

Als letztes wird ein alternativer Weg diskutiert, ein vollständig magnetisiertes, staubiges Plasma zu erzeugen. Der Übergang von Mikrometer- zu Nanostaub erlaubt es möglicherweise ein staubiges Plasma zu realisieren, in dem die Bewegung des Staubes direkt durch das Magnetfeld beeinflusst wird. Zwei wichtige Schritte in diese Richtung werden in dieser Arbeit unternommen. Als erstes wird eine alternative Elektrodengeometrie vorgeschlagen, in der Staubwolken in einer magnetisierten Plasmasäule eingeschlossen werden können. Zweitens wird ein "Bildgebendes Mie Ellipsometer" vorgestellt, das die Bestimmung wichtiger Parameter, wie der Staubgröße und Dichte, mit hoher raumzeitlicher Auflösung zulässt.

Contents

1	Introduction	1
2	Forces and dust confinement	5
2.1	Dust charging	5
2.2	Forces on dust particles	6
2.2.1	Force of gravity	6
2.2.2	Electric field force	6
2.2.3	Neutral drag	7
2.2.4	Pair interaction	7
2.2.5	Ion drag	9
2.3	Confinement of dust clusters	10
2.4	Plasma magnetization	11
3	Precision resonance measurements	13
3.1	Phase-resolved resonance method (PRRM)	15
3.2	Stability of MF-particles in a plasma environment	16
3.3	Measurement of the friction force and comparison to the Epstein theory	18
3.4	Probing the plasma sheath by the continuous mass loss of a PMMA-particle	20
4	Dust clusters in rotation	25
4.1	The dust centrifuge and the proof of laminar gas flows	26
4.2	Centrifugal forces and probing the dust-dust interaction	28
4.3	Coriolis force and pseudo-magnetization	32
5	Dust clusters in magnetized plasmas	37
5.1	Cluster rotation in the presence of axial magnetic fields	38
5.2	Ion Wakes	44
5.3	Charging and coupling of dust particles in unmagnetized plasma flows	47
5.4	Ion-wake-mediated particle interaction in magnetized plasma flows	52
6	Outlook: magnetized nanodust	57
6.1	Imaging Mie-Ellipsometry	59
6.2	Nanodust in magnetized plasmas	62

7 Summary and Conclusions	67
References	71
A Reprints of peer-reviewed articles	85
A.1 Effect of neutral gas motion on the rotation of dust clusters in an axial magnetic field	87
A.2 Effect of centrifugal forces on the interparticle distance of two dust particles confined in a plasma	97
A.3 Determination of dust grain charge and screening lengths in the plasma sheath by means of a controlled cluster rotation	103
A.4 Mass changes of microparticles in a plasma observed by a phase-resolved resonance method	111
A.5 Charging and coupling of a vertically aligned particle pair in the plasma sheath	119
A.6 Ion-wake-mediated particle interaction in a magnetized plasma flow	125
A.7 Probing the plasma sheath by the continuous mass-loss of micro-particles . .	131
A.8 Imaging Mie ellipsometry: dynamics of nanodust clouds in an argon-acetylene plasma	137
A.9 Wake formation and wake field effects in complex plasmas	145
A.10 Magnetizing a Complex Plasma without a Magnetic Field	155

Introduction

A plasma consists of a gaseous mixture of electrons, ions and neutrals being almost electric neutral overall. Furthermore, the plasma state requires a sufficiently high number density of free charge carriers, so that the ion and electron dynamics is governed by long-range electrostatic interaction forces and collective behavior can emerge. This distinguishes the plasma state from an ordinary gas, which is why a plasma is sometimes called the “Fourth State of Matter”. When nano- or micrometer-sized solid particles (dust grains) are immersed in such a plasma environment, the dust grains become electrically charged and can act as an additional super-heavy plasma species. Such a system of electrons, ions, neutrals, and charged dust grains is termed a dusty (or complex) plasma, whereby the word complex, in analogy to complex fluids, reflects the unusual behavior such plasmas can exhibit, e.g., the occurrence of crystalline phases and self-organization processes [1, 2, 3, 4].

Dusty plasmas can be found in numerous natural and technological environments and exist in a broad parameter range over more than ten orders of magnitude in plasma density and temperature. In space, planetary rings [5], cometary tails and cosmic nebulae are prominent examples of physical systems consisting of large amounts of dust grains embedded in a background plasma. Dusty plasmas occur in protoplanetary and accretion disks [6] and are involved in the processes leading to the formation of new planets and stars. In industry, plasmas are an effective tool to etch, coat and modify the surfaces of different materials. Here, dust grains are often a disturbing by-product, which can substantially lower the production yield. Moreover, dust particles occur in fusion devices [7] or can be used for diagnostic purposes [8, 9]. Another application of dusty plasmas are nanoparticles produced by plasma-chemical processes, which allow the production of low-cost solar cells [10, 11]. With the experimental discovery of the plasma crystal [12, 13, 14, 15] in 1994, dusty plasmas came into the focus of fundamental research and could establish themselves as an independent sub-field of plasma physics. Highly-charged dust particles confined in the plasma sheath were found to form crystal-like structures. These crystals are a model system for strongly-coupled Coulomb systems, as they appear in colloidal suspensions [16], electrons in helium droplets [17], ions in traps [18, 19, 20], and may occur in quantum dots [21] or neutron stars [22]. One advantage of dusty plasmas is that dynamic phenomena, such as oscillations, waves or melting processes,

can be studied on a kinetic level with the aid of video microscopy that allows to resolve single particle motion in space and time. In contrast to pure Coulomb systems, e.g., ions in traps, where the interaction forces between the particles are given by the Coulomb force, the interaction force between dust grains in a plasma is shielded due to the ambient electron and ion populations. The resulting potential around a charged dust grain is often approximated by a Yukawa (Debye-Hückel) potential [2, 4], which is an exponentially screened Coulomb potential. For dust grains confined in the plasma sheath the situation becomes more complicated. Here, the sheath electric field sustains a strong ion flow and extended wake structures can be observed downstream to the dust grains. Characteristic for these ion wakes is a positive space charge region that modifies the particle interaction in an unusual manner. The polarization of the streaming plasma can lead to attractive forces between the like-charged dust grains, which can result in the spontaneous formation of particle strings [23, 24, 25]. Here, Nambu *et al.* [26] pointed out the similarity to the formation of Cooper pairs in superconductors. Moreover, the particle interaction parallel to the flow becomes nonreciprocal, i.e., there is a strong interaction force from one particle to a particle in its wake, but only a weak force in the other direction. This asymmetry provides an effective mechanism to convert energy from the flowing ions to the kinetic energy of the dust grains [27] resulting in different types of instabilities [28, 29], e.g., the melting of dust crystals [23]. The nonreciprocal and attractive character of the ion-wake-mediated particle interaction and their consequences for the stability of dust clusters have been studied extensively over the last two decades. Nonetheless, basic questions regarding ion wakes remain unanswered, e.g., is the alignment of particles caused by drag [30, 31] or electrostatic forces [23, 26, 32, 33, 34, 35]? How does the wake influence the charging of particles in the wake of another [36, 37, 38]?

Most experimental studies of dusty plasmas in the presence of magnetic fields were performed at low magnetic fields ($B < 100$ mT). A major task of my PhD work was the initial start up of the magnet system SULEIMAN (SUpraLEItender MAgNet) and the construction and testing of a plasma chamber to study dusty plasmas in the presence of strong magnetic fields up to magnetic inductions of 4 T. From the scientific point of view, this is a new parameter regime, as stated by Thomas *et al.* in Ref. [39] “Magnetized Dusty Plasmas: the next frontier for complex plasma research” and fundamental questions regarding the influence of magnetic fields on, e.g., the charging of dust particles [40], the modification of ion-wake fields [41, 42, 43], the appearance of ion-cyclotron wakes [44], diffusion properties [45] or dust-cyclotron wakes [46, 47] have only been studied theoretically or by means of computer simulations. So far, only a few experimental results exist. Sato *et al.* [48] reported on the rotation of dust clusters in magnetized rf-discharges up to magnetic inductions of $B = 1$ T, Vasilev *et al.* [49] studied rotating dust structures in a magnetized dc-glow discharge up to $B = 0.25$ T and Schwabe *et al.* [50] found a filamentation of the rf-discharge modifying the structure of a large dust cluster confined in the plasma sheath ($B < 2.5$ T). In particular, one outstanding experimental challenge, as it is pointed out in Ref. [39], is the preparation of a fully magnetized dusty plasma, where even the dust is magnetized and the simultaneous effects of collective motion or strong coupling and magnetization can be studied.

In this thesis, the influence of magnetic fields and rotational motion on the structure and dynamics of dust clusters confined in the plasma sheath is put into focus. Magnetized (dusty) plasmas are found to be naturally in a rotating state and it is one aim of this work to show that the rotational motion of the dust clusters itself modifies the dynamics of the clusters. Here, even for moderate rotation frequencies, the centrifugal force effectively weakens the (radial) confinement of the dust clusters and increases the particle distance, which can be used for diagnostic purposes. Furthermore, the Coriolis force on the dust particles is found to modify the oscillation spectra of rotating dust clusters in a way as it is expected from magnetized dust clusters because of the mathematical equivalence of Lorentz and Coriolis force (Larmor theorem [51]). Here, a proof-of-principle is given that cluster rotation offers the possibility to study the simultaneous effects of strong coupling and (pseudo) magnetization in a dusty plasma device. The second focus of this thesis are dust clusters in the presence of magnetic fields. The probably most obvious effect is the rotational motion of dust structures, which can even be observed for magnetic fields as weak as the magnetic field of the earth. It is shown that the rotation of the dust clusters is accompanied by a co-rotation of the neutral gas column, which can result in an unexpected sense of rotation and magnitude of the rotation frequencies in comparison to a common model of cluster rotation [52], which assumes a balance of the ion and neutral drag force for a neutral gas at rest. Furthermore, the dust-dust interaction forces in the plasma sheath are substantially modified by the flow of ions and the formation of ion wakes. Here, the nonreciprocity of the interaction forces and a partial decharging of particles in the wake of another are measured with high precision by means of a phase-resolved resonance method (PRRM). PRRM is a new experimental diagnostic developed during this work with the aim to improve the accuracy of resonance measurements, a widely used technique for the diagnostics of dusty plasmas. It turns out that the decharging effect of ion wakes and the nonreciprocal nature of the particle interaction cannot be seen independently of each other and are coupled due to the external confinement of the dust particles. In particular, the interest of this work lies on the influence of a strong magnetic field on the ion-wake-mediated particle interaction. It is shown here for the first time that a magnetic field parallel to the ion flow substantially lowers the coupling forces, which might be attributed to a reduced wake charge.

This is a cumulative thesis based on ten articles in peer-reviewed journals [A.1-A.10] and it is structured as follows:

- Chapter 2 briefly summarizes fundamental processes in dusty plasmas, which are relevant for this work, e.g., the charging of dust particles in a plasma environment, the confinement of dust particles in the plasma sheath, and the forces acting on dust particles, such as friction and interparticle forces.
- Chapter 3 focuses on precision resonance measurements by means of the phase-resolved resonance method (PRRM), which is especially sensitive for the confinement frequency

of dust grains confined in the plasma sheath. PRRM is the basis for the measurements of the ion-wake-mediated interparticle forces presented in chapter 5. In order to demonstrate the reliability and high accuracy of PRRM, it is applied on single dust particles in three specific situations. Here, the longtime stability of MF-particles in a plasma environment is studied. Moreover, the neutral gas friction force experienced by the dust particles is critically compared with the Epstein theory. In addition, it is shown that PRRM allows to precisely monitor the continuous mass loss of a PMMA-particle, which allows to probe the plasma sheath with high spatial resolution.

- In chapter 4 the pure effects of cluster rotation on the structure and dynamics of dust clusters are put into focus. Here, the dust centrifuge is introduced, which allows to set dust structures into rotation without disturbing the plasma. The effects of centrifugal and Coriolis force are discussed in detail and the similarity between rotating and magnetized dust clusters is pointed out.
- Chapter 5 focuses on the dynamics of dust clusters in the presence of magnetic fields. First, the mechanism of cluster rotation in the presence of (weak) magnetic fields is discussed. Then, the ion-wake-mediated particle interaction originating from the flow of ions in the plasma sheath is put into focus. Here, PRRM allows to precisely measure the nonreciprocal particle interaction and the partial decharging of a particle in the wake of another. It is found that a strong magnetic field parallel to the flow of ions severely modifies the particle interaction.
- Chapter 6 is intended as an outlook. Here, one promising approach to reach the realms of strongly magnetized dusty plasmas is presented. Going from micrometer-sized particles to nanometer-sized particles and lowering the neutral gas pressure might allow to produce a dusty plasma where even the dust is at least partially magnetized. Following this approach, one has to give up the possibility to resolve single particle motion and new experimental diagnostics are required. In this chapter, a new electrode geometry is proposed for the confinement of nanodust clouds in magnetized rf-discharges and the “Imaging Mie Ellipsometry” (I-Mie) is introduced, which allows to measure the density and size of a nanodust with high spatial and temporal resolution.

Forces and dust confinement

Dust particles in a plasma acquire an electric charge and are subject to different forces. This chapter starts with a brief description of the charging processes in laboratory plasmas and the basic forces acting on dust particles, e.g., electric field, drag, and pair-interaction forces, which are relevant for this work. Afterwards, the confinement of particles in the plasma sheath of a radio-frequency (rf) discharge is explained. For a more detailed overview on (dusty) plasma physics the reader is referred to standard textbooks [3, 4, 53, 54] and recent review articles [1, 2].

2.1 Dust charging

The probably most important property of dust in a plasma is its electric charge. In laboratory plasmas the dominant charging mechanism is the collection of electrons and ions. Due to the higher thermal velocity of the electrons, dust grains attain a net negative charge. In the orbital motion limit (OML)[55] the floating potential of the dust grains ϕ_d is given by the balance of electron and ion currents and depends only on the electron and ion temperature T_e, T_i and the ratio of the electron and ion masses m_e/m_i . The OML-theory holds at parameters where collisions are negligible and the dust size is much smaller than the Debye length [44, 56]. For a typical argon rf-plasma with $T_e = 3$ eV and $T_i = 0.03$ eV, it is $\phi_d = -7.5$ V. The dust charge is then given by the capacitor model [57] $Q_d = 4\pi\epsilon_0 r_d \phi_d$, which predicts a linear relation between the dust charge Q_d and the particle radius r_d , provided that the particles are small compared to the screening length of the plasma ($r_d \ll \lambda_D$), e.g., the dust charge for dust particles with $r_d = 5$ μm is $Q_d \approx -25.000e$.

In the plasma sheath, the floating potential of the dust grains depends on the position within the sheath and the flow of ions, collisions, and the nonneutrality of the plasma sheath must be taken into account. Therefore, the particle charge Q_d often shows an apparently nonlinear dependency on the particle radius r_d [8, 58], since particles of different sizes are confined at different heights above the electrode. However, the charging of dust particles in the plasma sheath is a current topic. In a recent article, Douglass *et al.* [59] argued that there are two competing effects, which determine the particle charge: a depletion of the

electrons, which reduces the negative charge of particles that are confined deeper within the plasma sheath, and the acceleration of the ions, which lowers the collection cross-section and consequently reduces the ion current to the dust grains and therefore increases the negative particle charge. Based on a self-consistent fluid model [60], this results in a floating potential, which reaches its maximum value at intermediate levitation heights of the particles and can even exceed the floating potential predicted by OML theory.

Furthermore, the dust charge might depend on the material the particles are made of. This is known for very negative floating potentials ($\phi_d < -1$ kV) as it can be relevant for space plasmas. Pavlu *et al.* [61] have shown that the charge is limited by the field emission of electrons, which strongly depends on the surface material. Moreover, Bronold *et al.* [62] argued that in a quantum mechanical treatment surface states of the material affect the physisorption of electrons at the dust grain surface, which can lower the sticking probability of the electrons, and therefore the particle charge compared to the classical OML model. However, for the experiments presented in this work, it is $\phi_d \approx -10$ V and a decharging of the dust particles due to the field emission of electrons can safely be neglected. To my best knowledge, there are currently no experimental measurements that show a material dependence of the particle charge in the parameter regime that is of interest for this work. Therefore, the material dependence of the particle charge will be neglected in the following.

2.2 Forces on dust particles

In a plasma, different forces can act on the dust particles, which can be ordered by their scaling with the dust radius r_d . For this work, the relevant forces are the force of gravity ($\propto r_d^3$), ion and neutral drag force ($\propto r_d^2$), electric field force ($\propto r_d$), and the pair interaction. Other forces, which are unimportant in the present context are described in Ref. [4], e.g., thermophoretic and photophoretic forces.

2.2.1 Force of gravity

The dust particles used in this work can be considered as nearly perfect spheres with radius r_d and mass density ρ_d . Hence, the force of gravity experienced by this particles reads

$$\mathbf{F}_g = m_d \mathbf{g} = \frac{4}{3} \pi r_d^3 \rho_d \mathbf{g} . \quad (2.1)$$

It is m_d the dust mass and \mathbf{g} the acceleration of gravity. Since \mathbf{F}_g is proportional to r_d^3 , the force of gravity is typically the dominating force for particles larger than a few μm and can be neglected for nanometer-sized dust particles.

2.2.2 Electric field force

The electric field force is given by

$$\mathbf{F}_E = Q_d \mathbf{E} . \quad (2.2)$$

It is Q_d the dust charge and \mathbf{E} the electric field. For a constant floating potential ϕ_d and dust particles smaller than the Debye length, the particle charge can be deduced from the capacitor model [57] and is given by $Q_d = 4\pi\epsilon_0 r_d \phi_d$ and is proportional to r_d . Thus, the electric field force is especially important for small particles, whereas for micrometer-sized dust grains only the strong electric fields within the plasma sheath are relevant. There, the electric field force can compensate the force of gravity and is therefore equal in magnitude.

2.2.3 Neutral drag

A particle moving at a velocity \mathbf{v} relative to a gas experiences a friction force, which is proportional to $-\mathbf{v}$. For spherical particles much smaller than the mean free path of the gas atoms/molecules, Epstein [63] obtained the following expression for the neutral drag force:

$$\mathbf{F}_n = -\frac{4}{3}\delta\pi r_d^2 n_n m_n v_{th,n} \mathbf{v} \quad (2.3)$$

It is n_n the number density, m_n the mass, T_n the temperature and $v_{th,n} = \sqrt{8k_B T_n / \pi m_n}$ the thermal velocity of the gas atoms. The reflection coefficient δ depends on how the gas atoms are reflected at the particle surface and can have values between $\delta = 1$ for specular reflection and $\delta = 1.44$ for diffuse reflection. The neutral drag force is often written in the form $\mathbf{F}_n = -2m_d \gamma \mathbf{v}$, whereas m_d is the particle mass and γ the gas friction coefficient, which is given by

$$\gamma = \delta \frac{4}{\pi} \frac{p}{r_d \rho_d v_{th,n}}, \quad (2.4)$$

whereas p is the neutral gas pressure.

For typical dusty plasma parameters, the dust particles are usually much smaller than the mean free path of the gas atoms λ_{mfp} , e.g., $r_d = 10 \mu\text{m}$ and $\lambda_{mfp} \approx 1 \text{ mm}$ for argon at room temperature and $p = 10 \text{ Pa}$. Thus, the prerequisite for applying the Epstein formula is typically well satisfied and, although the exact value of δ is unknown, it is in general accepted in the dusty plasma community. The most precise measurements of the friction coefficient for micrometer-sized particles so far suggest to choose δ close to the upper limit of $\delta = 1.44$ [64, 65, 66]. Nonetheless, there are speculations that the Epstein formula (drastically) overestimates the friction force [67, 68].

2.2.4 Pair interaction

A dusty plasma consists of electrons, ions and charged dust particles, whereas one fundamental property is its quasi-neutrality

$$n_e + Z_d n_d - n_i \approx 0. \quad (2.5)$$

Here, n_e , n_i , and n_d are the respective number densities of the electrons, ions, and dust particles and Z_d is the charge number of the dust. The Coulomb potential around a single charged dust grain is shielded by the ambient electron and ion populations. Assuming a

Maxwell distribution of speeds for the electrons and ions, which is determined by the electron and ion temperature T_e and T_i , and linearizing the Boltzmann factor one obtains the Yukawa or Debye-Hückel potential

$$\phi(r) = \frac{Q_d}{4\pi\epsilon_0 r} \exp\left(-\frac{r}{\lambda_D}\right). \quad (2.6)$$

It is $Q_d = -Z_d e$ the dust charge and λ_D the linearized screening (or Debye) length, which is given by

$$\frac{1}{\lambda_D^2} = \frac{1}{\lambda_{De}^2} + \frac{1}{\lambda_{Di}^2}, \quad (2.7)$$

whereas λ_{De} and λ_{Di} are the screening length of the electrons and ions

$$\lambda_{De}^2 = \frac{\epsilon_0 k_B T_e}{e^2 n_e} \quad \text{and} \quad \lambda_{Di}^2 = \frac{\epsilon_0 k_B T_i}{e^2 n_i}. \quad (2.8)$$

As argued by Lampe *et al.* [69], the Yukawa potential can describe the interaction force between particles at intermediate distances (a few Debye lengths), but it cannot be applied close to or far from the dust grain. Especially in the vicinity of the dust particle, the Boltzmann factor of the ions cannot be linearized and the Yukawa potential overestimates the ion density and therefore the screening effect of the ions. For this reason, the charge entering in the Yukawa potential must be considered as an effective charge Q_{eff} , somewhat larger than the real particle charge Q_d . According to Ref. [69], Q_{eff} and Q_d can differ by 30% for typical dusty plasma parameters.

The experiments presented in this thesis are performed in the plasma sheath. Here, the quasi-neutrality of the plasma is broken and the ions are drifting with a velocity u_i towards the electrode. The kinetic energy of the ions $E_i = 1/2 m_i u_i^2$ can exceed their thermal energy $k_B T_i$ by far, which has a drastic effect on the screening capability of the ions. However, Konopka *et al.* [70] have shown that under these conditions the interaction force in the horizontal direction can still be well described by a Yukawa potential, with an effective screening length λ_s . The question, whether this effective screening length is determined by the ions or the electrons is still a matter of debate. Because the effective screening length λ_s measured in experiments is often close to the bulk electron Debye length λ_{De} , screening is sometimes attributed to the electrons [1, 71, 72]. On the other hand, Daugherty *et al.* [73] gave an ion screening length of

$$\lambda_{Di}^2 = \frac{2\epsilon_0 E_i}{e^2 n_i} \quad (2.9)$$

for a mono-energetic ion energy distribution, as it is a reasonable approximation for the plasma sheath, when it is $k_B T_i \ll E_i$. Close to the sheath edge, the ion flow velocity is typically of the order of the Bohm speed

$$u_B = \sqrt{\frac{k_B T_e}{m_i}} \quad (2.10)$$

and the effective screening length of the ions λ_{Di} becomes comparable to the bulk electron Debye length λ_{De} . Thus, the ions still contribute to the screening effect of the plasma

[74, 75, 76].

In order to describe the screening in the entire range from sub-thermal to super-thermal drift velocities in quasi-neutral plasmas, Hutchinson [77] interpolated the modified screening length as

$$\lambda_s^2 = \frac{\lambda_{De}^2}{1 + k_b T_e / (k_B T_i + m_i u_i^2)} \quad (2.11)$$

and for cold plasmas with $T_e/T_i = 100$ and $u_i = u_B$ it is $\lambda_s \approx 0.7\lambda_{De}$.

In this work, the Yukawa potential will be used to describe the horizontal interaction forces between dust particles confined in the plasma sheath. In order to account for the limitations of this model, the charge and screening length entering in Eq. (2.6) will be considered as effective values. Thus, the potential distribution around a charged dust grain is given by

$$\phi(r) = \frac{Q_{\text{eff}}}{4\pi\epsilon_0 r} \exp\left(-\frac{r}{\lambda_s}\right). \quad (2.12)$$

2.2.5 Ion drag

Negatively charged dust particles subjected to an ion flow experience a drag force due to the momentum transfer from the ions to the dust. The problem of determining the ion drag force was tackled by different analytic models [56, 78, 79], simulations [77, 80] and experiments [81, 82, 83]. For an analytical description, the total ion drag force can be written as a sum of collection and orbit force [56]

$$\mathbf{F}_i = \mathbf{F}_c + \mathbf{F}_o, \quad (2.13)$$

whereas the collection force \mathbf{F}_c accounts for ions that approach the dust particle with impact parameters $b < b_c = r_d[1 - 2e\phi_d/(m_i v_s^2)]^{1/2}$ and are collected by the dust grain. Ions approaching the dust particle at larger impact parameters up to a maximum allowed impact parameter λ_s are deflected due to the electrostatic interaction with the dust grain and contribute to the orbit force \mathbf{F}_o . Assuming a Coulomb interaction between the dust grain and the ions and integrating over a shifted Maxwellian velocity distribution for the flowing ions, Barnes *et al.* [56] obtained

$$\mathbf{F}_c + \mathbf{F}_o = n_i m_i \mathbf{u}_i v_s (\pi b_c^2 + 4\pi b_{\pi/2}^2 \ln \Lambda). \quad (2.14)$$

It is \mathbf{u}_i the mean flow velocity of the ions with respect to the dust particle and $v_s = [u_i^2 + 8k_B T_i / (\pi m_i)]^{1/2}$ a combination of the flow velocity and the thermal velocity of the ions, n_i the ion density, $b_{\pi/2} = Ze^2 / (4\pi\epsilon_0 m_i v_s^2)$ the impact parameter for 90° deflection and $\ln \Lambda$ the Coulomb logarithm

$$\ln \Lambda = \frac{1}{2} \ln \left(\frac{\lambda_s^2 + b_{\pi/2}^2}{b_c^2 + b_{\pi/2}^2} \right). \quad (2.15)$$

The maximum allowed impact parameter λ_s is usually chosen to the effective screening length of the plasma. For small flow velocities, λ_s corresponds to the linearized Debye length

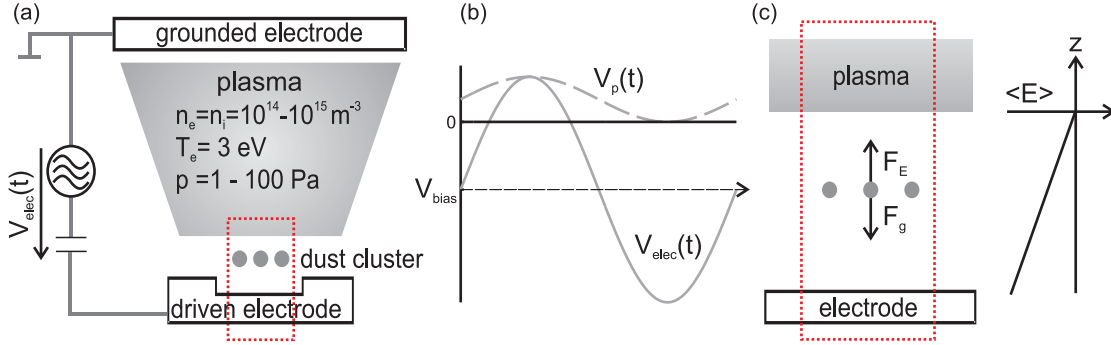


Figure 2.1: (a) Sketch of the experimental setup: An asymmetric rf-discharge burns between the lower, driven electrode, the grounded top electrode, and the vacuum vessel. Clusters of microparticles are confined in the plasma sheath above the driven electrode. A cylindrical recession in the driven electrode ensures the radial confinement of the dust particles. (b) Plasma potential V_p and voltage of the driven electrode V_{elec} for one rf-cycle. (c) Vertical confinement of dust particles in the plasma sheath. The time-averaged electric field $\langle E \rangle$ increases almost linearly from the sheath edge to the electrode.

[Eq. (2.7)] and for flow velocities of the order of the Bohm speed ($u_i = u_B$) Eq. (2.11) applies.

Khrapak *et al.* [79] argued that due to the large dust charge, the range of the ion-grain interaction can exceed the Debye sphere. Therefore, a modified Coulomb logarithm is proposed taking all ion trajectories into account, whose closest approach to the dust grain is smaller than λ_s resulting in higher values of the ion drag force compared to the standard theory. In particular, this enhancement is found for sub-thermal flow velocities, which could not be confirmed by the measurements performed by Zafiu *et al.* [82].

For the experiments presented in this thesis, the ion flow velocities are typically close to the Bohm speed ($u_i \approx u_B$) and the dust particles are much smaller than the effective screening length ($r_d \ll \lambda_s$). In this parameter regime, both models by Barnes [56] and Khrapak [79] do not differ much and are in fair agreement with the simulations by Hutchinson [77, 80]. Therefore, the simple treatment of the ion drag force presented here is sufficient for the interpretation within this thesis.

2.3 Confinement of dust clusters

In this work, clusters of micrometer-sized dust particles are confined in the sheath of a capacitively-coupled radio-frequency (rf) discharge. A sketch of the experimental setup is shown in Fig. 2.1(a). A rf-plasma burns between the lower electrode, which is driven by a rf-voltage, and the grounded top electrode. Since the electrodes are mounted into a vacuum vessel, which is grounded as well, the chamber acts as an additional electrode and the effective surface of the grounded electrode becomes larger than the surface of the driven electrode. The plasma potential V_p and the voltage at the driven electrode V_{elec} for one rf-cycle are

shown in Fig. 2.1(b) as it is described in Ref. [84]. Characteristic for such an asymmetric, capacitively-coupled rf-discharge is a negative dc-bias at the driven lower electrode, which is roughly half the amplitude of the rf-voltage. The potential difference between the plasma and the electrode is primary across the plasma sheath, where the quasi-neutrality of the plasma is broken and a net positive space charge ρ is found. Thus, there is a relatively strong dc-electric field within the plasma sheath from the positive plasma to the negatively biased electrode.

The sheath electric field exerts an electric field force \mathbf{F}_E on the negatively charged dust grains immersed into the plasma and can compensate the force of gravity \mathbf{F}_g . One important feature of the rf-sheath is that the sheath is periodically flooded with electrons during a short fraction of the rf-cycle and collapses when the potential of the electrode becomes equal to the plasma potential. Thus, the dust particles are still subject to a negative charging current and they can keep their high negative charge. Furthermore, the dust particles and the ions are too heavy to react to the rapid oscillations of the sheath electric field and the forces on the particles are only determined by the time-averaged electric field $\langle E \rangle$. The time-averaged charge density in the plasma sheath is to a good approximation constant [58] and the sheath electric field $\langle E \rangle$ increases linearly from the sheath edge to the electrode. Thus, dust particles, which are not too heavy, are confined at a well defined height above the lower electrode, when the electric field force and the force of gravity are in balance ($\mathbf{F}_E = \mathbf{F}_g$). The confinement in the vertical direction is to a good approximation harmonic, since the electric field force increases linearly towards the electrode as it is sketched in Fig. 2.1(c).

The horizontal confinement of the particles is realized by a cylindrical recession within the lower electrode, which gives the sheath electric field a small component in the horizontal direction, see Fig. 2.1(a). The horizontal confinement of the dust particles is usually much weaker than the vertical confinement. Therefore, ensembles of almost identical particles, which nearly have the same mass, are confined in a mono-layer above the driven electrode and can form two-dimensional (2d) dust clusters [12, 13, 14, 15]. Characteristic for these dust crystals is a relatively large coupling parameter

$$\Gamma = \frac{Q_d^2}{4\pi\epsilon_0 a_{\text{ws}} k_B T_d}. \quad (2.16)$$

It is $a_{\text{ws}} = (4\pi n_d/3)^{-1/3}$ the Wigner-Seitz radius and T_d the kinetic temperature of the dust. For $\Gamma > 1$ the electrostatic interaction energy of neighboring particles exceeds the thermal energy of the dust particles and the cluster is said to be in a strongly-coupled state. Under these conditions, the dust particles typically exhibit a fluid-like behavior and for $\Gamma > 170$ a transition into a solid-like phase can be observed [85, 86], which is the case for the dust clusters presented in this work.

2.4 Plasma magnetization

One focus of this thesis are magnetized plasmas. Here, I like to make clear what ‘‘magnetization’’ in the context of this work means and to introduce suitable quantities to measure

the degrees of plasma magnetization. Artificial and natural magnetic fields cover more than 18 orders of magnitudes of magnetic induction. From nT fields in the heliosphere, to the earth magnetic field (31 μ T at 0° latitude), to conventional electro magnets (1-100 mT), to the maximum field strength of SULEIMAN (4.34 T, superconducting magnet used for this thesis), to the strongest pulsed artificial magnetic field boosted by explosives (2800 T) [87], to the extreme magnetic fields of a magnetar (0.1-100 GT, special type of a neutron star) [88]. So, the question is, at which field strength is the dynamic of a (dusty) plasma substantially modified by the cyclotron motion of the charged plasma species?

There are different dimensionless measures of magnetization that are in use. Here, the quantities are introduced for the ions and can be defined like-wise for the electrons and the charged dust particles. Typically, the length or time scale of the ion cyclotron motion (Larmor radius r_{Li} or inverse cyclotron frequency $1/\omega_{ci}$) is related to a characteristic length or time scale. In Ref. [89] the ratio of the dust (or probe) radius r_d to the averaged Larmor radius is used. In this work, however, the dust particles are almost point-like, i.e., they are much smaller than the Larmor radius of the ions, the screening length or the ion mean free path. Therefore, the ratio r_d/r_{Li} is not a suitable quantity to measure magnetization in this work. Another parameter that occurs naturally, e.g., in linear-response theory [41, 42, 43] is the ratio of cyclotron frequency and plasma frequency, $\beta_i = \omega_{ci}/\omega_{pi}$, which is equivalent (up to a numerical factor of the order of unity) to the ratio of Debye length and Larmor radius. Thus, the plasma exhibits features of magnetization, when the time scale of (ion) plasma oscillations and waves $1/\omega_{pi}$ becomes comparable to the time scale of the cyclotron motion $1/\omega_{ci}$, i.e., the Larmor radius r_{Li} fits into the Debye sphere. Furthermore, the magnetization of the ions can be suppressed by collisions. The plasmas that are of interest for this work have an ionization degree of the order of 10^{-6} and the ions primarily collide with the neutrals. The Hall parameter $H_i = \omega_{ci}/\nu_{in}$ relates the cyclotron frequency to the ion-neutral collision frequency and $H_i \gtrsim 1$ can be seen as a necessary condition to speak of magnetization, as in the limit of $H_i \ll 1$ the ion cyclotron motion is completely suppressed by ion-neutral collisions.

In this work, the electrons, ions or dust particles are said to be magnetized, when the respective Hall parameter H_x and β_x exceed unity. (The index $x = e, i, d$ stands for the electrons, ions and dust). Thus it is

$$H_x = \frac{\omega_{cx}}{\nu_{xn}} > 1 \quad \text{and} \quad \beta_x = \frac{\omega_{cx}}{\omega_{px}} > 1 . \quad (2.17)$$

Since the charge-to-mass ratio of the electrons, ions and the dust differs by orders of magnitude, and so the respective cyclotron frequencies, this naturally defines three regimes of plasma magnetization. For clarity, we will use the following terminology to distinguish these three regimes of magnetization, as introduced by Sato *et al.* in Ref. [48]. *Weak magnetization*: Electrons are magnetized, ions and dust are not. *Strong magnetization*: Electrons and ions are magnetized and the dust is not. *Ultra-strong or full magnetization*: All plasma species are magnetized.

Precision resonance measurements

In this chapter, the phase-resolved resonance method (PRRM) is introduced, which is the basis for the measurements of the ion-wake-mediated particle interaction presented in Sec. 5.2. Here, the focus lies on single particle systems, whereat PRRM allows to determine the strength of the (vertical) confinement and the gas friction force with high precision in comparison to established techniques. Since PRRM is critical for the conclusions drawn in this thesis, the aim of this chapter is to demonstrate the accuracy and reliability of PRRM in three specific applications: In Sec. 3.2, the longtime stability of MF-particles is evaluated. A quantitative comparison of the neutral drag force in comparison to the Epstein model is made in Sec. 3.3 and the possibility of using the continuous mass loss of PMMA-particles to probe the plasma sheath is demonstrated in Sec. 3.4. This chapter is based on my publications [A.4] and [A.7].

The dust charge is the key parameter for the understanding of structural and dynamic properties of dusty plasmas. Therefore, experimental techniques allowing an accurate measurement of the dust charge are very much desirable. In a gaseous or vacuum environment the charge of micrometer-sized particles (or oil drops) can be measured with high precision, see, e.g., Millikan's famous oil drop experiment [90] or dust particles confined in a Paul trap [91]. In a plasma, however, the experimental determination of the dust charge remains to be a challenge, since external electric fields are shielded by the plasma and may influence the charging process. Furthermore, the dust charge fluctuates on a μs -timescale, because of the discreteness of the ion and electron currents [92], and in practice we are restricted to a measurement of the time-averaged dust charge. In the following, the phrase "dust charge" will always refer to the time-averaged value, if not otherwise mentioned.

One standard technique to determine the charge of single dust particles is the resonance method [14, 93, 94]. A dust particle confined in the plasma sheath can be set into vertical oscillation by applying an external periodic force, e.g., by modulating the electrode bias [14, 93] or by using a pulsed laser beam to exert photophoretic forces [94]. Tuning the driving frequency allows to measure the frequency response function of the particle from which the confinement and friction forces can be deduced. When the oscillation amplitude is not too large, e.g., less than 20% of the sheath width [58], the dust particle behaves like a

driven damped harmonic oscillator and the equation of motion reads

$$\ddot{\xi} + 2\gamma\dot{\xi} + \omega_0^2\xi = Ke^{i\omega t}. \quad (3.1)$$

Here, ξ is the excursion from the equilibrium position, ω_0 the confinement frequency, and K the amplitude of the sinusoidal driving force. The neutral drag force damps the oscillation and can be described by a friction coefficient γ , which is typically in good agreement with the Epstein formula [Eq. (2.4)]. The confinement frequency ω_0 is a measure of the strength of the (vertical) confinement and is related to the dust charge Q_d by

$$\omega_0^2 = \frac{1}{m} \frac{\partial}{\partial z} [E(z)Q_d(z)] = \frac{1}{m} \left[\frac{\partial E(z)}{\partial z} Q_d(z) + \frac{\partial Q_d(z)}{\partial z} E(z) \right] \approx \frac{Q_d}{m} \frac{e(n_i - n_e)}{\epsilon_0}. \quad (3.2)$$

It is E the vertical sheath electric field ($\mathbf{E} = E\mathbf{e}_z$), whereas Q_d and E may depend on the vertical position within the plasma sheath z . Thus, if the particle mass m_d is known, a measurement of ω_0 does only allow to determine the gradient of the product EQ_d . If one is interested in Q_d , the charge gradient and the sheath electric field must be known. Often $\partial Q_d/\partial z = 0$ is assumed [14, 93, 95] and $\partial E/\partial z = \rho/\epsilon_0$ is replaced by the charge density in the plasma sheath $\rho = e(n_i - n_e)$ by applying the Maxwell relations, which yields the right-hand side of Eq. (3.2). Even in this approximation a reliable absolute measurement of Q_d is difficult, because estimates of the charge densities n_e and n_i are usually subject to large uncertainties typically obtained from sheath models and plasma diagnostics in the plasma bulk. This limitation can be overcome by directly measuring the electric field in the plasma sheath with spatial resolution, e.g., by means of emissive probes [95], which itself is a challenging task and may have a feedback on the plasma sheath. Therefore, it is difficult to determine the absolute dust charge from resonance measurements with high precision.

Nonetheless, Tomme *et al.* [58] have shown that the charge density in the plasma sheath [$\rho = e(n_i - n_e)$] is almost constant in a wide parameter space. Thus, precise resonance measurements are ideally suited to resolve even small changes of the charge-to-mass ratio of the dust particles, which is shown in the following. For this purpose we have introduced the phase-resolved resonance method (PRRM) in [A.4], allowing a precise determination of the confinement frequency ω_0 . Because of this high accuracy in comparison to established resonance measurements [14, 93, 94], we have found that dust particles confined in the plasma sheath can be subject to small mass changes, which we have not been aware of so far. In the following it is shown that melamine formaldehyde (MF) particles suffer from a mass loss due to the outgassing of water and/or a mass gain due to the coating with material sputtered from the electrode. Especially for longtime measurements, these processes might lead to systematic errors if not taken into account. PRRM also allows a precise measurement of the gas friction force experienced by the dust particles. Here, the opportunity is taken to make a quantitative comparison to the Epstein theory [Eq. (2.4)] in a wide parameter range relevant for numerous dusty plasma experiments. Furthermore, the simultaneous measurement of the confinement frequency ω_0 and the gas friction coefficient γ allows to monitor the continuous mass loss of a polymethyl methacrylate (PMMA) particle and to probe the plasma sheath

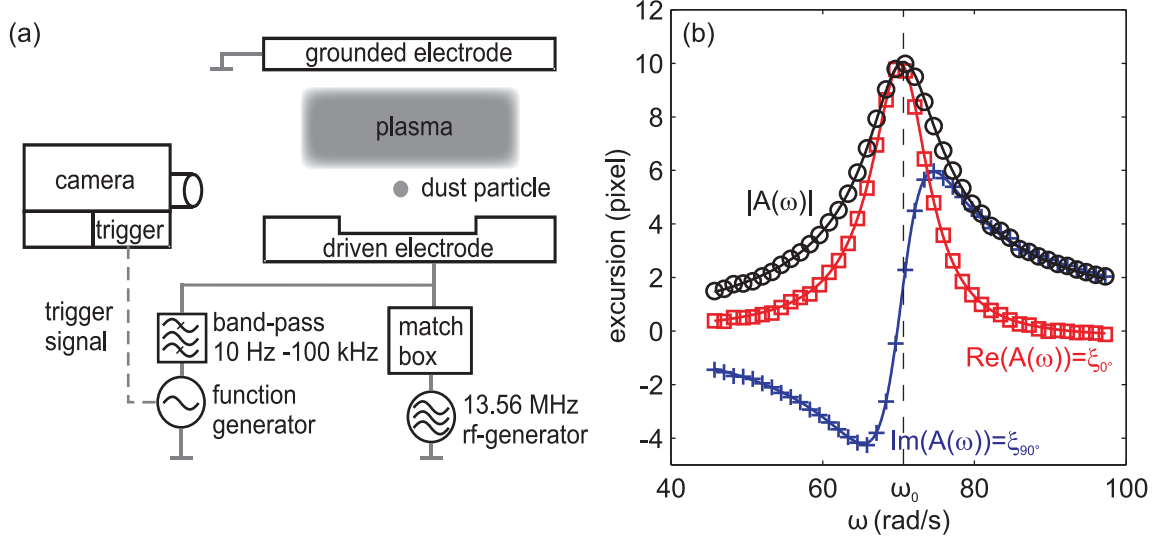


Figure 3.1: (a) Sketch of the experimental setup (not true to scale). (b) Exemplary resonance curves: Excursion of the dust particle ξ_φ at phase $\varphi = 0^\circ$ (squares) and $\varphi = 90^\circ$ (crosses) w.r.t. the excitation signal versus excitation frequency ω . The full lines are a fit of the driven damped harmonic oscillator model [Eq. (3.1)] taking into account the transfer function of the band-pass filter. For comparison, the standard amplitude resonance is shown in black (circles).

with high spatial resolution, which allows a comparison to current models of dust charging and confinement in the plasma sheath [59].

3.1 Phase-resolved resonance method (PRRM)

The phase-resolved resonance method is a modification of the classical resonance method [14, 93] and was introduced in Ref. [A.4]. The main idea is to measure phase and amplitude of a forced oscillation instead of the amplitude only [14, 93]. PRRM improves resonance measurements by one order of magnitude in precision and is especially sensitive to the confinement frequency ω_0 . This high resolution has led to new applications that will be presented in the subsequent sections.

A sketch of the setup is shown in Fig. 3.1(a). A single or a few dust particles are confined in the plasma sheath above the driven electrode. These particles are set into vertical oscillation by a sinusoidal modulation of the electrode bias at low frequencies $f_{\text{ex}} = 1 \dots 50$ Hz supplied by a function generator. A capacitively coupled band-pass filter protects the output of the function generator from the self-bias of the driven electrode and the rf-voltage. A camera, synchronized with the function generator, allows to measure the particle position z_φ at any phase angle φ with respect to the excitation signal. The excursion from the equilibrium position ξ_φ at phase φ can be determined offset-free by making use of $\xi_\varphi = \frac{1}{2}(z_\varphi - z_{\varphi+180^\circ})$. Resonance curves are obtained by measuring ξ_{0° and ξ_{90° for different excitation frequencies

$\omega = 2\pi f_{\text{ex}}$ for a constant low frequency amplitude [see Fig. 3.1(b)]. For a sinusoidal oscillation, ξ_{0° and ξ_{90° can be treated as the real and imaginary part of the complex amplitude $A(\omega) = a(\omega) + ib(\omega)$ and are sufficient to determine the (absolute) amplitude $|A(\omega)| = \sqrt{a(\omega)^2 + b(\omega)^2}$ and phase $\varphi(\omega) = \text{atan}[b(\omega)/a(\omega)]$ of the particle oscillation. The theoretical frequency response for a driven damped harmonic oscillator can then be fitted to the measurements [see Fig. 3.1(b), full lines]. In practice, the band-pass filter causes an additional phase shift and damps the oscillation and must be taken into account. In the present experiment, the transfer function of the filter in the low-frequency limit is given by that of a RC-high-pass with a cut-off frequency around $\omega_{\text{cut}} \approx 2\pi \cdot 10$ Hz. The confinement frequency ω_0 and the gas damping coefficient γ are fit parameters and can be determined with high precision. The 1σ -error of the fit parameters can be calculated from surrogate data as described in Ref. [96]. For resonance curves similar to those shown in Fig. 3.1(b), the relative error is typically $\sigma(\omega_0)/\omega_0 < 10^{-3}$ and $\sigma(\gamma)/\gamma < 10^{-2}$. Thus, PRRM allows to determine ω_0 up to three significant digits, which is an improvement in precision of one order of magnitude compared to the standard resonance method. This improvement is mainly due to the steep gradient of $\Im(A(\omega))$ at ω_0 compared to the amplitude resonance $|A(\omega)|$ used in Refs. [14, 93, 94], which attains its maximum close to ω_0 at the resonance frequency $\omega_{\text{res}} = \sqrt{\omega_0^2 - 2\gamma^2}$ [Fig 3.1(b), black curve].

3.2 Stability of MF-particles in a plasma environment

Melamine formaldehyde (MF) particles are one of the most widely used particles in dusty plasma experiments. The main advantages are the small size distribution, typically it is $\sigma(r_d)/r_d \approx 1.5\%$, the nearly perfect spherical shape, and the fact that the mass density of the particles is given by the manufacturer with four significant digits $\rho_d = 1.514$ g/cm³ [97]. Thus, in most experiments the error of the particle mass is assumed to be negligible. However, Pavlu *et al.* [91] found that there might be a problem with the longtime stability of the MF-particles. There, charged MF-particles were confined in a Paul trap under ultra-high vacuum conditions (UHV). It turned out that the particles were subject to a mass loss of a few percent over several days. This mass loss was most likely due to the outgassing of water incorporated within the MF. The high sensitivity of PRRM for the confinement frequency of single dust particles and their charge-to-mass ratio [Eq. (3.2)] offers the possibility to study the longtime stability of MF-particles in a plasma environment. It is the aim of this section to show that MF-particles in plasma are also subject to mass changes, but the time scales of this processes are of the order of hours instead of days, as it is the case under UHV conditions [91]. This section is based on my publication [A.4].

In order to study the longtime stability of MF-particles and to ensure that there is no drift of the plasma parameters over extended times, the plasma discharge was given more than one day time to reach stable conditions and the pressure and the rf-voltage were monitored for the entire measurement time. Then, single MF-particles were confined in the plasma sheath and the confinement frequency ω_0 was measured by means of PRRM for several hours. In

Fig. 3.2(a), the time evolution of ω_0 for two different measurement series is shown, one for a low rf-voltage of $U_{\text{rf}} = 240 \text{ V}_{\text{pp}}$ and one for a high rf-voltages of $U_{\text{rf}} = 340 \text{ V}_{\text{pp}}$. Both measurements were performed at moderate gas pressures of $p = 9 \text{ Pa}$ (argon). Obviously, ω_0 and with it the charge-to-mass ratio cannot be assumed constant on a time scale of a few hours. In addition, there are at least two mechanisms affecting the particle. At low rf-voltages, ω_0 increases while at high rf-voltage a monotonic decay is found.

At low rf-voltages, the increase of ω_0 saturates after approximately 10 hours. This trend and especially the saturation can be explained by a small mass loss due to the outgassing of water as reported by Pavlu *et al.* [91]. If the outgassing process affects primarily the particle mass, the drift of the confinement frequency corresponds to a mass reduction of approximately 10% within 10 h. This value is in good quantitative agreement with the findings presented in Ref. [91], but the time scales are much shorter, hours instead of days. One possible explanation for this acceleration of the outgassing process might be the heating of the particles due to the ambient plasma, e.g., due to the recombination of electrons and ions at the particle surface [98]. Moreover, these findings are in agreement with a thermogravimetric analysis performed with a small sample of MF-particles. Heating up the MF-sample to 100°C at atmospheric pressure, the sample loses 10% of weight. Thus, these consistent findings are a strong indication that MF-particles in plasma environment are subject to a mass loss due to the outgassing of water.

For higher rf-voltages, a nearly linear decrease of ω_0 is observed [Fig. 3.2(a)]. Here, the measurement series was started a few hours after the particle had been dropped into the plasma, so that the measurement was not superimposed by the outgassing process. One possible explanation for this decrease of ω_0 could be the coating of the dust grain with material sputtered from the driven electrode. To confirm that material was sputtered from the electrode, a small slice of a Silicon wafer was placed at the electrode under identical plasma conditions. Then, the surface of the Silicon wafer was analyzed by means of photo-electron spectroscopy (XPS). Among others, the XPS measurements showed iron and fluorine impurities, which is reasonable, because the electrode is made of stainless steel and the insulator consists of PTFE (polytetrafluoroethylene).

Thus, the particle mass as given by the manufacturer should be used with care for MF-particles confined in the plasma sheath, since a mass loss or gain of 10% is not negligible compared to the mass distribution given by the manufacturer ($\sigma(m_d)/m_d = 4.5\%$) and might result in a systematic error, when the particle mass is a critical parameter. Because the time scales of these processes are hours, this can safely be neglected, when the particles are in contact with the plasma only for a few minutes, but for longer measurement series one should be aware of this issue. These measurements also demonstrate that PRRM can easily resolve changes of the charge-to-mass ratio of the order of a few percent. I like to mention that PRRM even allows to resolve the narrow size (mass) distribution of MF-particles, as it is discussed in detail in Ref. [A.7].

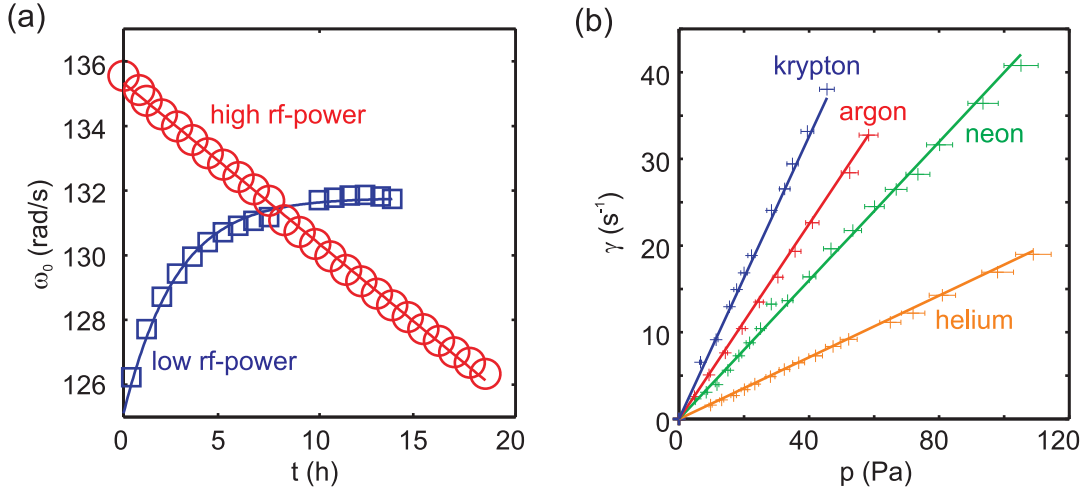


Figure 3.2: (a) Time evolution of the confinement frequency ω_0 of a single MF-particle confined in the plasma sheath at low (squares) and high (circles) rf-powers. (b) Gas friction coefficient γ versus pressure p for μm MF-particles ($r_d = 6.0 \mu\text{m}$) in different noble gases. The full line represents the Epstein formula Eq. (2.4) with $\delta = 1.44$. Taken from [A.7].

3.3 Measurement of the friction force and comparison to the Epstein theory

It is the aim of this section to show that PRRM does not only give a precise measurement of the confinement frequency ω_0 , but also of the friction coefficient γ , which determines the width of the resonance peak and is important for the measurements presented in the subsequent section 3.4. There, PRRM is used to monitor the continuous mass loss of a single PMMA-particle and to probe the plasma sheath. Here, the opportunity is taken to make a quantitative comparison to the Epstein theory [Eq. (2.4)], which applicability is sometimes questioned in the context of dusty plasma experiments.

Although the applicability of the Epstein formula is in general accepted, a precise value of the reflection coefficient δ [see Eq. (2.4)] or its dependence on parameters like the gas type, pressure, material of the particles, temperatures, etc. remains unclear. Besides, there are speculations that the Epstein formula is not applicable at all and drastically overestimates the real friction force experienced by the particles moving in a gaseous environment [67, 68]. Anyway, there are a few carefully performed experiments, dedicated to show the applicability of the Epstein law and to determine the reflection coefficient δ , but these measurements were usually performed in a very narrow parameter regime [64, 65, 66], e.g., three different particle sizes at one gas pressure [64]. There, the consistent result is that the reflection coefficient is close to the theoretical upper limit of $\delta = 1.44$, i.e., the reflection of the gas atoms at the particle surface is more diffusive than specular. The motivation for the experiments described in this section was to make an accurate measurement of the friction force in a wide parameter range representative for many dusty plasma experiments. For this reason,

we have chosen a pressure range from 1 Pa to 100 Pa and different noble gases as working gas. Since MF-particles are the workhorse of dusty plasma physics, the measurements were performed with MF-particles. Here, relatively large particles ($r_d = 6.0 \mu\text{m}$) are used, because we expect deviations from the Epstein formula, when the condition $r_d \ll \lambda_{\text{mfp}}$ is violated at the transition from Epstein to Stokes friction. It is λ_{mfp} the mean free path of the gas atoms.

In Fig. 3.2(b), the gas friction coefficient γ as measured by PRRM is plotted versus the gas pressure p for the noble gases helium, neon, argon, and krypton. There, a linear dependence of the friction coefficient on the gas pressure is found for the whole pressure range and all gases, as it is expected. For a quantitative comparison, a gas temperature of $T = 300 \text{ K}$ and a reflection coefficient of $\delta = 1.44$ is assumed, represented by the full lines in Fig. 3.2(b). Within the error margin a good quantitative agreement between the measurements and the Epstein law is found under the assumption that δ is close to the upper theoretical limit. Here, the gas temperature T_n is not a critical parameter, because the gas friction coefficient scales as $\gamma \propto \sqrt{T_n}$ and a small error of the temperature estimate results only in a minor correction of γ .

As denoted by the error bars in Fig. 3.2(b), the major uncertainty of this measurement series results from the pressure measurement, which typically has a good reproducibility of less than one percent, but a possible systematic deviation of $\pm 5\%$, which must be taken into account, when making a quantitative comparison. Here, this inhibits a more precise determination of the reflection coefficient δ , although PRRM is capable of measuring the gas friction coefficient with better than 1% precision.

Thus, we have shown that for MF-particles in a noble gas environment and pressures between 1 Pa and 100 Pa, the gas friction coefficient can be well described by the Epstein theory [Eq. (2.4)] with a reflection coefficient of $\delta = 1.44 \pm 0.15$ [99], which is in good agreement with the findings presented in Refs. [64, 65, 66]. A drastic discrepancy between the Epstein theory and the measured damping rate as reported in Refs. [67, 68] could not be confirmed. However, there is still room for improvement and the combination of PRRM with a more sophisticated pressure measurement might be a promising way to determine the reflection coefficient down to 1% precision.

3.4 Probing the plasma sheath by the continuous mass loss of a PMMA-particle

The structure of the plasma sheath is of importance for many plasma applications, because this is the region where ions are accelerated and gain energy, which strongly affects the efficiency of, e.g., sputtering and etching processes. In dusty plasmas, many experiments are performed in the sheath of collisional rf-discharges so that a detailed understanding of the sheath structure as it determines the confinement and charging of the dust particles is of high interest. The diagnostics of the plasma sheath, however, remains to be a challenge, since standard electrostatic probes are difficult to apply as they are a major disturbance to the plasma sheath. Other techniques, e.g., spectroscopic methods [100], usually require higher plasma densities and are difficult to apply at parameters relevant to dusty plasma physics. A new approach to tackle this diagnostic problem is to use dust particles as probes [98, 101, 102], as they are usually only a minor disturbance to the plasma sheath. One way is to measure the confinement frequency ω_0 of particles confined at different levitation heights z . Then, an integration of Eq. (3.2) gives a spatially resolved force profile $F(z) = E(z)Q_d(z)$, which can be set into relation with different sheath models. There are different approaches to measure ω_0 at different positions. One way is to use particles of different sizes (and masses) confined at different levitation heights [101, 103, 104, 105]. The spatial resolution of this technique is limited by the number of available particle sizes, which can be improved by measuring the nonlinearity of large-amplitude oscillations [102]. Another idea to control the levitation height is to introduce an additional thermophoretic force, which has the advantage that particles of just one size can be used [106]. One problem with this technique is that the heating of the electrodes can alter the neutral gas and plasma density, which has an unwanted feedback on the plasma sheath [107]. Beckers *et al.* [8] used a similar approach, but instead of a thermophoretic force, they mounted the entire experiment on a centrifuge. In this way, they were able to effectively increase the acceleration of gravity (hyper gravity) and to probe the plasma sheath with a single particle without altering the plasma conditions.

The aim of this section is two-fold. First, I like to present a complementary approach to the hyper gravity experiments [8] and to probe the plasma sheath by making use of a continuous mass loss of a single PMMA-particle, which results most likely from (chemical) sputtering processes at the surface of the particle. Here, the phase-resolved resonance method (Sec. 3.1) is used to monitor this sputtering process, while the PMMA-particle moves slowly through the plasma sheath. Furthermore, I will compare the measurements presented here to a recent model of particle charging in the plasma sheath developed by Douglass *et al.* [59]. This section is based on my publication [A.7].

The floating potential ϕ_d of dust particles confined in the plasma sheath depends on the position within the sheath. This typically leads to a nonlinear dependence of the particle charge Q_d on the dust radius r_d , since particles of different sizes (masses) are confined at different heights above the electrode z and it is $Q_d = 4\pi\epsilon_0\phi_dr_d$ according to the spherical capacitor model [57] for dust particles with $r_d \ll \lambda_D$. At first glance, there are contradicting experimental findings. The hyper gravity experiments performed by Beckers *et al.* [8] show

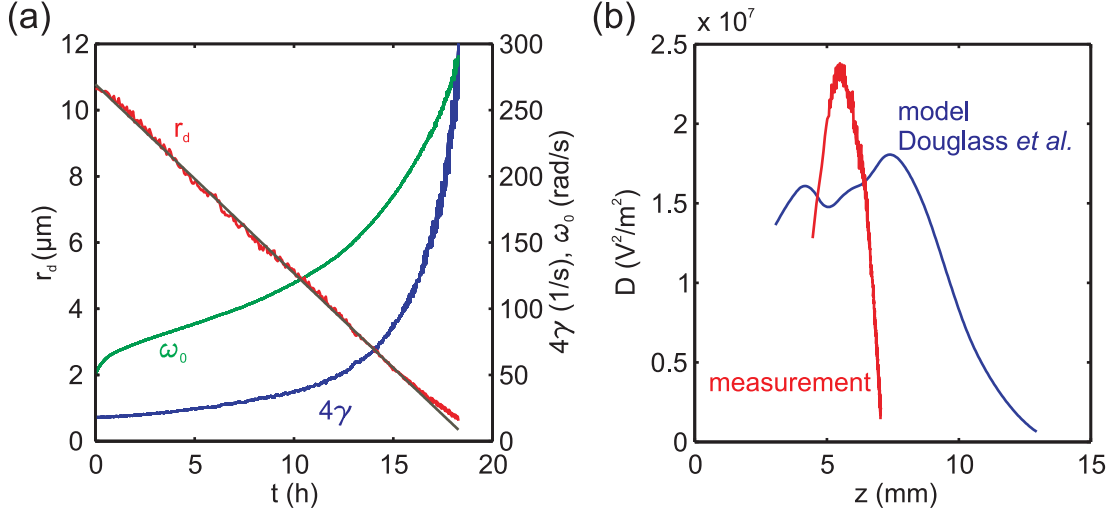


Figure 3.3: (a) Time evolution of the confinement frequency ω_0 (green line), the gas friction coefficient γ (blue line), and the particle radius r_d (red line) for a single PMMA-particle confined in the plasma sheath. The straight gray line is a linear regression yielding an initial particle radius of $r_0 = 10.8 \mu\text{m}$ and an effective sputtering rate of $\alpha = 0.57 \mu\text{m}/\text{h}$. (b) Effective spring constant D representing the strength of the vertical confinement versus levitation height above the lower electrode z as obtained from the measurement (a) and the sheath model [59]. Taken from [A.7].

that the particle charge becomes less negative, when the dust particle is pushed deeper into the plasma sheath. On the other hand, we have found that the floating potential of dust particles confined deeper within the plasma sheath becomes more negative by probing the dust-dust interaction by means of centrifugal forces, as it is presented in Sec. 4.2 of this work and published in [A.3]. There, a nearly quadratic scaling of the particle charge on the dust radius is found, which had been observed by, e.g., Tomme *et al.* [58] as well. These contradicting findings were tackled by Douglass *et al.* [59] by means of a charging model based on a self-consistent fluid model for the plasma sheath [60] taking two competing mechanisms into account, which affect the dust charge: a depletion of the electron population towards the electrode, which lowers the negative dust charge, and an acceleration of the ion flow, which lowers the ion-collection cross-section of the dust particles and makes the particles more negative. There, it is found that the particles attain their most negative floating potential (highest negative charge) at intermediate levitation heights. Therefore, one explanation for the different experimental findings is that in our experiments [A.3] and those by Tomme *et al.* [58] the particles were confined above this maximum of the floating potential and in the hyper gravity experiment [8] the dust particle were pushed below this maximum.

To show experimentally that there is indeed such a maximum of the negative floating potential of the dust grains, we confined a relatively large and heavy PMMA-particle deep within the plasma sheath. As found for the MF-particles presented in Sec. 3.2, the ambient

plasma results in a slow and continuous mass loss. Here again, we measured the gas friction coefficient γ and the confinement frequency ω_0 by means of PRRM. The time evolution of these two quantities is shown in Fig. 3.3(a). In contrast to the MF-particles, there is no saturation of $\omega_0(t)$ and this monotonic increase cannot be attributed to a release of gas incorporated within the PMMA-particle. Another possible mechanism is the reactive sputtering of PMMA due to oxygen impurities, as found by Zeuner *et al.* [108] for PMMA in an argon discharge. Furthermore, the sputtering of PMMA by the impinging argon ions might contribute to this process. For such a (reactive) sputtering process we would expect a constant sputtering rate since the discharge parameters are kept constant. And this is exactly what we see. The friction coefficient γ is inverse proportional to the particle radius and therefore allows to determine r_d [see Eq. (2.4)]. For a quantitative determination of the particle radius, we have calibrated this measurement by making use of MF-particles with a well-defined size, for details see Ref. [A.7]. In Fig. 3.3(a) the particle radius r_d is plotted versus the time t and can be well described by a linear decay. A linear regression yields an effective sputtering rate of $\alpha = 0.57 \mu\text{m/h}$ and an initial particle radius of $r_0 = 10.8 \mu\text{m}$, which agrees well with the size given by the manufacturer [97] of the PMMA-particles [$r_d = (10.9 \pm 0.18) \mu\text{m}$]. Over the entire measurement time of 18 h, the radius of the PMMA-particle is reduced from $r_0 = 10.8 \mu\text{m}$ to $r_d < 1 \mu\text{m}$. Thus, the particle has lost more than 99% of its initial mass, which affects the levitation height of the particle z above the electrode. At the beginning of the measurement the particle is confined deep within the plasma sheath and at the end it levitates close to the sheath edge. Here, I like to mention that we are not sure about the physical process affecting the PMMA-particle. Therefore, I will use the phrase *effective sputtering* for this process in the following.

In order to perform a quantitative comparison with the model of particle charging in the plasma sheath by Douglass *et al.* [59], we introduce the quantity

$$D = \left(\phi_d \frac{\partial E}{\partial z} + E \frac{\partial \phi_d}{\partial z} \right) = \frac{m_d \omega_0^2}{4\pi\epsilon_0 r_d}, \quad (3.3)$$

which can be interpreted as an effective spring constant being a measure of the strength of the (harmonic) confinement, see Eq. (3.2). This allows us to avoid the problem of separating E and ϕ_d (or E and $Q_d = 4\pi\epsilon_0 r_d \phi_d$), whereas D can be easily deduced from the measurements presented in Fig. 3.3(a) and the theoretical curves from Ref. [59]. This is shown in Fig. 3.2(b). The parameter D is plotted versus the levitation height of the particle above the lower electrode z . Obviously, both curves do not coincide, which may be explained by a difference in the gas pressures p . In the model $p = 20 \text{ Pa}$ is assumed, while the experiment was performed at $p = 11.5 \text{ Pa}$ for technical reasons. Nonetheless, both curves show a distinct maximum and a steep decrease towards the sheath edge. The absolute values of D are of the same order of magnitude, whereas the maximum of the measurement is larger compared to the model, which is reasonable, because the voltage drop about the sheath is approximately the same and the model is more extended in the z -direction. Therefore, the electric fields in the model and the parameter D are smaller compared to the measured values.

In conclusion, the model [59] and the presented measurements show a distinct maximum of the effective spring constant D at intermediate heights above the electrode. Therefore, these measurements strengthen the findings of Douglass *et al.* that the charge of dust particles becomes most negative at intermediate levitation heights. There, the maximum of D corresponds to the position where the floating potential ϕ_d becomes maximal. This gives a reasonable explanation for the almost quadratic scaling of the particle charge Q_d on the particles radius r_d as it is found by Tomme *et al.* [58] and in the measurements presented in Sec. 4.2, since for particles that are confined above this floating potential maximum, a disproportional increase of the particle charge on the particle radius is expected. Furthermore, for dust particles that are confined below this maximum and pushed deeper into the plasma sheath, e.g., by hyper gravity [8], a lowering of the particle charge is expected.

Besides the physical aspects discussed above, this shows that precision resonance measurements are ideally suited to improve the idea of using dust particles as plasma probes. The spatial resolution obtained here exceeds the resolution of the measurements described in Refs. [103, 104, 105, 109] by far. The effective sputtering of a single particle does not affect the plasma sheath, as it might be the case when applying a thermophoretic force [106, 107]. In addition, the experimental setup is not as complex as it is required for measurements under hyper gravity [8]. A disadvantage is the long time a single measurement series needs (several hours), during which constant plasma parameters are required.

Dust clusters in rotation

This chapter is devoted to the effects of rotational motion on the structure and dynamics of dust clusters. Cluster rotation occurs naturally in magnetized plasmas (see Sec. 5.1) and the physics of rotating and magnetized dust ensembles are closely related because of the mathematical equivalence of Lorentz and Coriolis force (Larmor theorem [51]). The aim is to show how even modest rotation frequencies of a few Hz can modify the behavior of dust ensembles and to clearly separate the effects of rotation from the influence of magnetic fields (chapter 5). This chapter is based on my publications [A.1,A.3,A.10], where these aspects have been addressed experimentally for the first time in the context of dusty plasma physics.

In the following Sec. 4.1, the dust centrifuge is introduced, which allows to set dust clusters into rotation without disturbing the plasma. The basic idea is that a rotating top electrode can act as a neutral gas drive, which in turn sets the cluster into rotation. Neutral gas flows driven by ion-neutral collisions may contribute to the rotation of dust clusters in the presence of magnetic fields as it is discussed in detail in Refs. [A.1], [110, 111, 112] and Sec. 5.1 of this work. There, the assumption is made that the gas flow is in a laminar flow regime and that at surfaces of, e.g., the electrodes a no-slip boundary condition applies for the gas flow, which results in a sheared rotation of the neutral gas column in front of the electrode. Here, this assumption of laminar gas flows is proven for typical dusty plasma parameters. The rotating electrode can be used as a well-defined neutral gas drive, which allows to make a quantitative comparison between experimental observations and a laminar flow model.

The maximum rotation frequencies of the dust clusters Ω realizable by the dust centrifuge can exceed the radial confinement frequency ω_r of the clusters. For such high rotation frequencies the structure and dynamics of the cluster is modified and two pseudo-forces appear in the frame of the rotating dust cluster. The first is the centrifugal force, which effectively weakens the (harmonic) confinement and allows to probe the dust-dust interaction forces as it is discussed in Sec. 4.2. The horizontal interaction force is found to be well reproduced by a Yukawa potential [Eq. (2.12)] being in agreement with the observations presented in, e.g., Ref. [70] and linear response theory for flowing plasmas [69]. Here, the effective charge Q_{eff} entering in the Yukawa potential can be determined from the experiment and is set into relation to current models of particle charging in the plasma sheath [59] that are discussed in

Sec. 3.4 of this work. Furthermore, the question whether the screening in the plasma sheath is dominated by the electrons [1, 71, 72] or ions [74, 75, 76] is addressed by comparing the measured Debye length λ_s to the screening length of the electrons and ions [Eqs. (2.8) and (2.9)].

The second pseudo-force appearing in a frame of a rotating dust cluster is the Coriolis force, which is put into focus in Sec. 4.3. The Coriolis force is found to modify the oscillation spectra of a rotating dust cluster. Here, the similarity between rotating and magnetized dust clusters is discussed, which originates from the mathematical equivalence of Coriolis and Lorentz force (Larmor theorem [51]) and allows to mimic the effects of magnetization. Similar concepts have been successfully applied in, e.g., rotating Bose-Einstein condensates [113, 114, 115, 116].

4.1 The dust centrifuge and the proof of laminar gas flows

The dust centrifuge is a new experimental approach to set dust clusters into rotation and to exert centrifugal and Coriolis forces on dust ensembles leaving the plasma and the charging of the dust practically unaffected. A sketch of the experimental setup is shown in Fig. 4.1(a). The basic idea is to make use of the frictional coupling between the electrodes, the neutral gas, and the dust particles. A disk is used as a top electrode, which rotates at a constant angular velocity, and sets the entire neutral gas column into a vertically sheared rotation, which in turn convects the dust clusters that are confined in the plasma sheath above the driven electrode. The purpose of this section is to show that the neutral gas flow is still in a hydrodynamic regime and can be described by the Navier-Stokes equation assuming a no-slip boundary condition at the surfaces, i.e., the gas sticks to the electrodes and the chamber walls, resulting in a laminar sheared gas flow in front of the driven electrode. Here, the assumption of a laminar gas flow is proven experimentally, which is a prerequisite for the ion-driven neutral wind model presented in Sec. 5.1 and Refs. [110, 111, 112].

To characterize the neutral gas flow, the Reynolds number Re , the Mach number M and the Knudsen number Kn are taken into account. For a slow rotation of the upper electrode with a frequency of $f_{elec} = 1$ Hz it is

$$Re = \frac{\rho_n u_n H}{\eta} \approx 0.07 \quad , \quad M = v_n/c \ll 1 \quad \text{and} \quad Kn = \lambda_{mfp}/H \approx 0.01 \quad , \quad (4.1)$$

whereas $\eta = 22 \times 10^{-6}$ Pa s is the dynamic viscosity of argon at low gas pressures and room temperature [117], $H = 10$ cm is a characteristic length scale for the flow problem, e.g., the distance between the electrodes, $\rho_n = 1.6 \times 10^{-4}$ kg/m³ is the density of argon at $p = 10$ Pa, $u_n = 0.1$ m/s is a characteristic flow velocity, $c \approx 320$ m/s is the sound speed in argon and $\lambda_{mfp} \approx 1$ mm the mean free path of the argon atoms. Therefore, we can treat the gas flow as incompressible, since it is $M \ll 1$. Furthermore, we will neglect inertial forces. This approximation is well satisfied for the gas flow close to the lower electrode, there it is $u_n < 0.01$ m/s and $Re \ll 1$. For the gas flow close to the rotating electrode Re , can be of the order of 0.1 and this approximation might lead to a small systemic error. In this limit, only

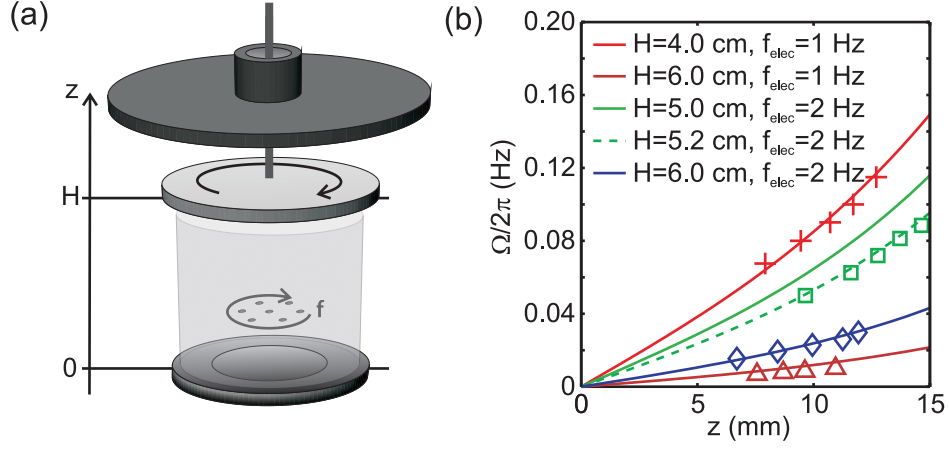


Figure 4.1: (a) Sketch of the dust centrifuge. The glass tube between the electrodes is only used for the analysis of the neutral gas flow. (b) Rotation frequency Ω of the dust cluster versus levitation height above the driven electrode z (symbols) for different distances between the electrodes (heights of the glass tube) H and rotation frequencies of the upper electrode f_{elec} . For comparison, the lines represent the laminar flow model Eq. (4.3).

the viscous forces are balancing the externally applied force and the Navier-Stokes equation reduces to the Laplace equation

$$\Delta \mathbf{u}_n = 0, \quad (4.2)$$

with \mathbf{u}_n being the flow velocity of the gas. For a Knudsen number of $Kn = 0.01$, the gas flow is at the transition from the hydrodynamic to the Knudsen regime [118], which is important for the correct treatment of the gas flow close to surfaces. In the hydrodynamic regime, the gas sticks to the walls and a no-slip boundary condition applies. The applicability of the Navier-Stokes equation can be extended into the Knudsen regime, when a slip is allowed between the gas flow and the surfaces (slip boundary condition).

To prove that the gas flow is still in the hydrodynamic regime for typical experimental parameters, we have performed the following experiment, sketched in Fig. 4.1(a). A glass tube is placed between the electrodes to ensure well-defined boundary conditions for the flow problem. A cluster of dust particles is confined at the axis of the cylindrical volume. The forces acting in radial direction on the dust particles are the (radial) confinement, inertia, and centrifugal force as discussed in the following section 4.2. Moreover, the only forces acting in azimuthal direction are the force of inertia and the neutral drag force. For MF-particles with $6 \mu\text{m}$ radius, the friction coefficient [Eq. (2.4)] is $\gamma \approx 5 \text{ s}^{-1}$ and on a characteristic time scale of $1/\gamma$, the velocity of the dust particles adjusts to the flow velocity of the neutral gas. Thus, a few seconds after changing the rotation frequency of the top electrode, the cluster can be seen as a tracer for the rotation frequency of the neutral gas column at the position of the cluster. By varying the rf-voltage and with it the levitation height of the dust cluster above the driven electrode z , we can measure the dependence of the rotation frequency on z in a certain interval, which is shown in Fig. 4.1(b) for different rotation frequencies of the

top electrode f_{elec} and for glass tube of different heights (distances between the electrodes) H . Here, we assume a no-slip boundary condition for the gas flow. Thus, the azimuthal flow velocity at the lower electrode and the cylindrical glass tube is $u_\phi = 0$. At the rotating electrode the gas performs a rigid rotation with $u_\phi = 2\pi f_{\text{elec}}r$. For a cylindrical geometry, the Laplace equation (4.2) can be solved analytically (see [119, 120]) and the expected azimuthal flow velocity is given by

$$u_\phi(r, z) = \sum_{m=0}^{\infty} \frac{2f_{\text{elec}}J_1(k_m r) \sinh(k_m z)}{r_0^2 \sinh(k_m H) [J_2(k_m r_0)]^2} \int_0^{r_0} J_1(k_m r') r'^2 dr' . \quad (4.3)$$

It is r_0 the radius of the glass tube, J_i the Bessel functions of the first kind, $k_m = \alpha_m/r_0$, α_m the roots of J_1 and H the distance between the electrodes. The expected rotation frequencies for the dust clusters as deduced from Eq. (4.3) are represented by the lines in Fig. 4.1(b). The measurements and the theoretical flow profile are in good agreement, which shows that the gas flow is still in a hydrodynamic regime. The sticking of the gas flow at the electrode results in a vertically sheared rotation, but 2d clusters levitating at a constant height above the driven electrode perform a rigid rotation. Furthermore, the authors of Refs. [121, 122] adopted this method and made explicit use of the sheared gas flow to study the shear stability and shear induced melting processes of 3d clusters.

Besides studying neutral gas flows, this setup is ideally suited to set dust cluster into a well-controllable rotation. In practice, a nearly perfect cylindrical symmetric setup is required to ensure a smooth rotation of the dust clusters. Any disturbances to the gas flow, e.g., the dust dropper or additional probes have to be removed during the measurements. If the plasma chamber itself is axisymmetric, the glass tube is, in general, not required. A disadvantage of this setup is that the top view is blocked by the rotating electrode and the dust clusters must either be observed from the side or through a transparent electrode (e.g., made of ITO coated glass). The dust centrifuge is a new tool to manipulate dust particles in a controlled manner by means of centrifugal and Coriolis forces, as shown in the following sections. One advantage of this technique is that a slow neutral gas flow does not alter the plasma conditions or the particle charging.

4.2 Exerting centrifugal forces on the dust particles and probing the dust-dust interaction

The dust centrifuge, as presented in the previous section 4.1, allows rotation frequencies Ω of dust clusters up to a few Hz, which are comparable to or even exceed the radial confinement frequency ω_r of the dust particles. Therefore, the centrifugal force makes a significant contribution to the radial force balance and increases the interparticle distance within the dust clusters, which can be seen as an effective weakening of the radial confinement. In the frame of the rotating dust cluster the effective radial confinement frequency is given by $\bar{\omega}_r = \sqrt{\omega_r^2 - \Omega^2}$ [A.10]. The purpose of this section is to show that a tuning of the rotation

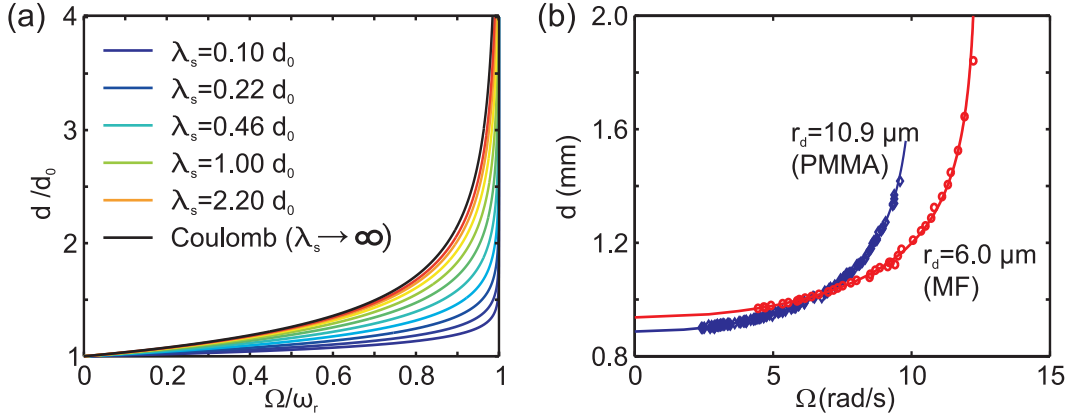


Figure 4.2: (a) Interparticle distance d normalized to the interparticle distance at rest ($\Omega = 0$) versus rotation frequency Ω for different screening length λ_s as obtained from Eq. (4.4). (b) Interparticle distance d versus rotation frequency Ω as measured for a pair of MF-particles ($r_d = 6.0 \mu\text{m}$) and PMMA-particles ($r_d = 10.9 \mu\text{m}$) at a gas pressure of $p = 4 \text{ Pa}$ and a rf-voltage of $200 \text{ V}_{\text{pp}}$. The full lines represent a fit of Eq. (4.4). Taken from [A.3].

frequencies allows to probe the dust-dust interaction forces and a measurement of the effective dust charge Q_{eff} and screening length λ_s assuming that the interaction force is Yukawa-like [Eq. (2.12)]. The experiments presented here are performed at lower gas pressures compared to the experiments described in the previous section 4.1, $p = 4 \text{ Pa}$ instead of $p = 10 \text{ Pa}$, and the rotation frequencies of the rotating electrode are higher, $f_{\text{elec}} \approx 10 \text{ Hz}$ instead of $f_{\text{elec}} \approx 1 \text{ Hz}$, so that we might have left the regime of laminar gas flows. But this is not critical for this section since here we are only interested in the influence of the centrifugal force on the dynamics of the dust cluster in its electrostatic potential well. Furthermore, we have checked that at even the highest possible rotation frequencies, the plasma glow is not affected by the neutral gas motion. Therefore, a neutral wind, which may reach maximal flow velocities of the order of 1 m/s close to the rotating electrode, is not expected to have a significant effect on the plasma and the electrostatic forces between the particles.

Let us consider a generic model system of two identical particles rotating about their center of mass at a certain rotation frequency Ω . In a stationary state, the centrifugal force and Yukawa repulsion must be balanced by the confinement force and the force balance reads

$$m_d \Omega^2 \frac{d}{2} + \frac{Q_{\text{eff}}^2}{4\pi\epsilon_0 d} \left(\frac{1}{\lambda_s} + \frac{1}{d} \right) \exp\left(-\frac{d}{\lambda_s}\right) - m_d \omega_r^2 \frac{d}{2} = 0. \quad (4.4)$$

Here, Q_{eff} and m_d are the effective charge and the mass of the dust particles, λ_s is the effective screening length of the plasma, and d the interparticle distance. The dependence of the interparticle distance d on the rotation frequency Ω as given by Eq. (4.4) is shown in Fig. 4.2(a). The interparticle distance is a monotonically increasing function of the rotation frequency. There is a pole at $\Omega = \omega_r$, when the centrifugal force equals the confinement force and the system becomes unstable. The screening affects the shape of this function and for a

decreasing screening length the function becomes steeper close to the pole.

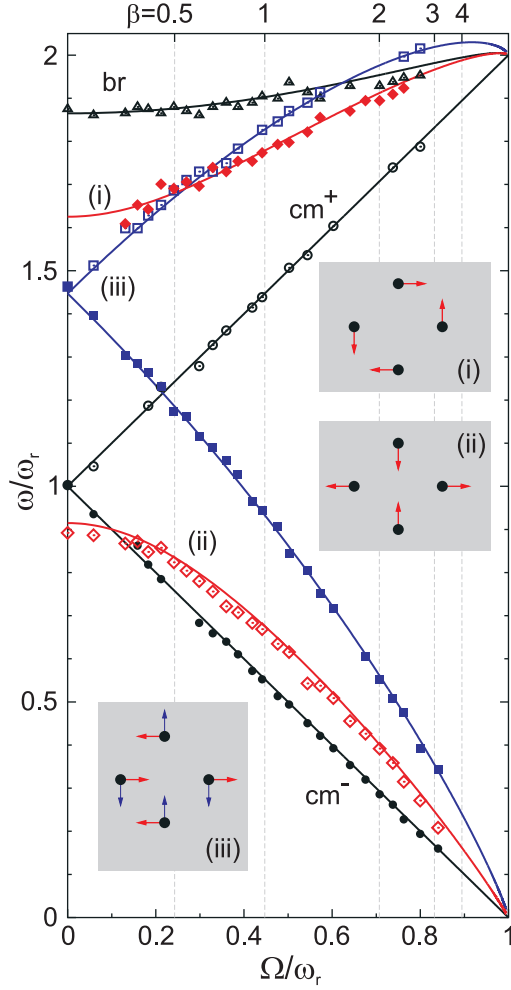
We have measured the dependence of the interparticle distance on the rotation frequency for a pair of MF-particles and PMMA-particles confined in the plasma sheath. The radii (sizes) of the particles were $r_d = 6.0 \mu\text{m}$ (MF) and $r_d = 10.9 \mu\text{m}$ (PMMA). The results are shown in Fig. 4.2(b). The interparticle distance could be increased by a factor of two and within the entire measurement interval, the experiments show the expected behavior. A fit of Eq. (4.4) (full lines) is in excellent agreement with the measurements, which proves that the interaction force can be well approximated by a Yukawa interaction and accurate estimates for the effective particle charge Q_{eff} and screening length λ_s can be deduced from the fit parameters. Here, a disproportional increase of the particle charge with the particle radius is found. It is $Q_{\text{eff}} = 20,000e$ for the MF-particles ($r_d = 6.0 \mu\text{m}$) and $Q_{\text{eff}} = 60,000e$ for the PMMA-particles ($r_d = 10.9 \mu\text{m}$), i.e., Q_{eff} scales approximately as $Q_{\text{eff}} \propto r_d^2$. A similar scaling was also observed, e.g., by Tomme *et al.* [58]. There, the dust charge was estimated from the levitation height of different MF-particles with diameters between $2 \mu\text{m}$ and $14 \mu\text{m}$ after the parabolic nature of the electric confinement potential had been determined. This clearly indicates that the floating potential ϕ_d of the dust grains depends on the position within the plasma sheath. (It is $Q_d = 4\pi\epsilon_0 r_d \phi_d$ [57].) Here, the floating potential becomes more negative for particles that are confined deeper within the plasma sheath. This result can be qualitatively explained by the findings presented in Sec. 3.4. There, the floating potential of the dust grains takes a maximum at intermediate levitation heights of the dust particles as it was found by Douglass *et al.* [59] as well. Thus, this disproportionate increase of the particle charge on the particle radius as it is found here and in the experiments performed by Tomme *et al.* [58] is reasonable, when the dust particles are all confined above the floating potential maximum.

Now, let's have a look at the screening length λ_s obtained from the fit of Eq. (4.4). For simplicity, I will focus here on the measurements performed with the pair of PMMA-particles, an analysis for the MF-particles can be done in the same way, see [A.3]. For the PMMA-particles, we obtained an effective screening length of $\lambda_s = (0.6 \pm 0.16) \text{ mm}$, which is comparable to the interparticle distance $d \approx 0.9 \text{ mm}$ at $\Omega = 0$. For an estimate of the screening length of the electrons and ions we assume the real particle charge to be $Q_d = 0.7 \times Q_{\text{eff}}$ as it is given by Lampe *et al.* [69] for an argon plasma with slightly different parameters, e.g., there it is $T_e/T_i = 25$ and here it is $T_e/T_i \approx 100$. Then, the strength of the sheath electric field E can be determined from the levitation condition $EQ_d = m_d g$. The ion flow velocity is given by $u_i = \mu_i E$, whereas μ_i is the ion mobility of argon ions in their parent gas determined by Frost [123]. Assuming a typical electron temperature of $T_e = 3 \text{ eV}$ [124], the Mach number of the ion flow is $M = u_i/u_B = 1.5$, whereas the Bohm velocity is given by $u_B = \sqrt{k_B T_e/m_i}$. Furthermore, we have measured the vertical confinement frequency $\omega_0 = 86 \text{ rad/s}$ from the thermally excited oscillations of the dust particle. Thus, Eq. (3.2) allows us to determine the charge density $\rho = e(n_i - n_e)$ in the plasma sheath, if we neglect a gradient of the particle charge with respect to the position within the plasma sheath. For an electron duty-cycle of $\alpha = n_e/n_i = 0.2 \pm 0.1$, the respective densities of the electrons and ions

are $n_e = (1.45 \pm 0.85) \times 10^{14} \text{ m}^{-3}$ and $n_i = (6.8 \pm 0.8) \times 10^{14} \text{ m}^{-3}$. For a Maxwell distribution of speeds, the electron screening length is given by Eq. (2.8) and it is $\lambda_{De} = (1.3 \pm 0.4) \text{ mm}$. For a monotonic energy distribution of the ions, the screening length is given by Eq. (2.9) according to Daugherty *et al.* [73], whereas $E_i = 0.5m_i u_i^2 \gg k_B T_i$ is the kinetic energy of the ions. This yields an ion screening length of $\lambda_{Di} = (0.74 \pm 0.05) \text{ mm}$. Therefore, the theoretical effective screening length is $\lambda_s^{\text{theo}} = (0.63 \pm 0.09) \text{ mm}$ [Eq. (2.7)]. This value is in good quantitative agreement with the measured value $\lambda_s = (0.6 \pm 0.16) \text{ mm}$, although we had to make some approximations for this estimate. Moreover, within this estimation it is $\lambda_{De} > \lambda_{Di}$, which suggests that the screening is primary due to the ions as it is argued in Refs. [74, 75, 76].

Thus, centrifugal forces can be used to probe the dust-dust interaction forces and at intermediate interparticle distances the interaction force is found to be Yukawa-like as it is found in Refs. [69, 70]. The observed disproportional increase of the particle charge on the particle radius is in agreement with the measurements by Tomme *et al.* [58] and can be qualitatively reproduced by current models of particle charging in the plasma sheath [59]. The screening length λ_s is in good quantitative agreement with the effective screening length estimated from the local plasma parameters. There, λ_s is close to the screening length of the ions as given by Daugherty *et al.* [73] for a monoenergetic flow of ions, i.e., the screening is dominated by the ions. Although this technique allows only a measurement of the effective particle charge, it does not require any plasma parameters as input, as the (phase-resolved) resonance method does [14, 93],[A.4]. There are other techniques to measure Q_{eff} and λ_s , which evaluate dynamical or structural properties of particle ensembles and are assuming a Yukawa interaction, e.g., the analysis of dust waves [125, 126, 127], normal mode oscillations [128, 129, 130], particle collisions [131], the compression of a dust cluster in a parabolic potential well [132] or above an inclined plane [133]. The advantage of introducing centrifugal forces is that the particle mass and the rotation frequency can be determined with small error margins, which allows an accurate measurement of the absolute value of the centrifugal force. Furthermore, this technique is also applicable at higher gas pressures, since in a stationary state, the particles do not move with respect to the (rotating) neutral gas background and are not affected by the neutral drag force. In contrast to methods that are based on dynamical properties, which are usually restricted to low gas pressures, since waves [125, 126, 127] and oscillations [128, 129, 130] are overdamped when the neutral drag coefficient of the dust particles γ exceeds the natural frequency scale of the particle motion, e.g., the confinement frequency ω_r .

Figure 4.3: Comparison of experiment and theory: frequencies of the seven nontrivial normal modes of $N = 4$ dust particles as a function of the scaled rotation frequency. Symbols denote experimental results ($\omega_r/2\pi = 2.52 \text{ s}^{-1}$), lines are the theoretical eigenfrequencies with $\kappa = 0.7$. The eigenvectors in the unmagnetized limit ($\Omega = 0$) are sketched for four particular modes. The two modes (iii) are degenerate in this case. The breathing mode and the two center-of-mass modes are indicated by br and cm^\pm , respectively. The effective magnetization $\beta = 2\Omega/\bar{\omega}_r$ is shown on the upper axis. Taken from [A.10].



4.3 Coriolis force and pseudo-magnetization

In the frame of a rotating dust cluster two pseudo-forces appear, the centrifugal force (see Sec. 4.2) and the Coriolis force. The latter can be used to tackle the problem of magnetizing the dust in a real experimental device. This approach was proposed by Kählerlert *et al.* [134, 135] and the idea is to make use of the Larmor theorem [51] and to mimic the magnetization of the dust by the action of the Coriolis force. Similar concepts have been recently applied in rotating Bose-Einstein condensates (see Refs. [113, 114, 115, 116] and references therein). There, most of the investigations are focused on the formation and structure of vortex lines, which carry the total vorticity of the velocity field of the rotating Bose condensate. Since the Larmor theorem does also apply in quantum physics, these systems are almost equivalent (except for the radial confinement) to electrons in type-II superconductors penetrated by a magnetic field [115]. There, each quantum of magnetic flux is carried by one vortex of a circulating supercurrent. The aim of this section is to give a proof-of-principle of this

approach at typical dusty plasma parameters by analyzing the normal mode oscillations of a rotating dust cluster. As in the last section 4.2, the cluster rotation is excited by means of the dust centrifuge presented in Sec. 4.1, which allows a fine tuning of the cluster rotation without disturbing the plasma discharge.

The Larmor theorem states that the Lorentz force on a dust particle with charge Q_d and mass m_d moving in a homogeneous magnetic field \mathbf{B} is equivalent to the Coriolis force experienced by the particle in a system rotating at a frequency $\Omega/2\pi$ about an axis parallel to \mathbf{B} . Without loss of generality, consider a magnetic field (rotation axis) in z -direction $\mathbf{B} = (0, 0, B)$. Thus, the Lorentzian force \mathbf{F}_L and the Coriolis force \mathbf{F}_C read

$$\mathbf{F}_L = Q_d(\mathbf{v} \times B\mathbf{e}_z) = m_d(\mathbf{v} \times \omega_{cd}\mathbf{e}_z) \quad \text{and} \quad \mathbf{F}_C = m_d(\mathbf{v} \times 2\Omega\mathbf{e}_z). \quad (4.5)$$

It is $\omega_{cd} = Q_d B/m_d$ the cyclotron frequency and obviously both forces are equal, when $\omega_{cd} = 2\Omega$. Thus, setting a dust cluster into rotation, e.g., by the dust centrifuge (Sec. 4.1), allows to mimic a magnetic field with an effective magnetic induction of $B_{\text{eff}} = 2\Omega m_d/Q_d$. Because of the small value of the charge-to-mass ratio of the dust grains, even modest rotation frequencies of a few Hz would lead to effective magnetic inductions of the order of $B_{\text{eff}} = 10.000$ T, which is far beyond any experimental capabilities.

To prove that the dynamics of a rotating dust cluster shows features of an *effective* magnetization, we have analyzed the normal mode frequencies of a small cluster with $N = 4$ particles in the rotating frame of reference and compared it to the normal mode oscillations predicted for a magnetized dust cluster [136]. In Sec. 2.4, we defined the magnetization of the dust species as the ratio of cyclotron and plasma frequency $\beta_d = \omega_{cd}/\omega_{pd}$ provided that the Hall parameter is $H_d > 1$. The plasma frequency, however, is a natural frequency scale for the collective motion of many interacting particles ($N \gg 1$) and is not appropriate in the context of small dust clusters with only a few particles. For this reason, the role of the plasma frequency is taken over by the (radial) confinement frequency ω_r , which corresponds to the center-of-mass oscillation of the dust cluster and provides a characteristic frequency scale for the normal mode oscillations. Furthermore, the effective weakening of the radial confinement due to centrifugal force has to be taken into account. Hence, the effective confinement frequency in the rotating frame is given by $\bar{\omega}_r = \sqrt{\omega_r^2 - \Omega^2}$ and the effective magnetization is $\beta_{\text{eff}} = \omega_c/\bar{\omega}_r = 2\Omega/\bar{\omega}_r$. Here, relatively large PMMA-particles ($r_d = 10.9 \mu\text{m}$) are used at low gas pressures of $p = 0.4$ Pa (argon) to ensure that the oscillations of the dust particles are not strongly damped by neutral gas friction. Here, it is $\gamma/\omega_r \approx 1/50$, whereas γ is the Epstein friction coefficient Eq. (2.4).

In Fig. 4.3, the measured mode frequencies for a $N = 4$ particle cluster are plotted versus the rotation frequency and effective magnetization. The mode frequencies were determined from the thermally excited normal mode oscillations of the cluster. In two dimensions, there are seven nontrivial normal modes, two center of mass modes (cm), the breathing mode (br) and four modes, whose eigenfunctions are depicted in the inlets of Fig. 4.3. The dust centrifuge [Sec. 4.1] allows rotation frequencies Ω that can even exceed the radial confinement frequency of $\omega_r/2\pi = 2.52 \text{ s}^{-1}$. Therefore any degree of magnetization should be realizable,

since it is $\beta_{\text{eff}} \rightarrow \infty$ for $\Omega \rightarrow \omega_r$. In the presented experiment, however, the weakening of the radial confinement limits the maximum achievable magnetization, because the cluster reacts more sensitive to external perturbations, e.g., vibrations caused by the rotating electrode, the transmission and the motor. Here, we were able to reach effective magnetizations of $\beta_{\text{eff}} \approx 3$, at which the normal modes are substantially affected. For comparison, the full lines in Fig. 4.3 represent the mode frequencies expected for a magnetized dust cluster [136] for $\kappa = a/\lambda_s = 0.7$, whereas a is a characteristic interparticle distance given by $a = [Q_d^2/(4\pi\epsilon_0 m_d \omega_r^2)]^{1/3}$. Obviously, there is an excellent agreement between measurement and theory and typical features of magnetization are well reproduced. Here, the modes are split into a lower and upper branch and the degeneracy of the center-of-mass and the asymmetric mode is lifted. The effective magnetic induction at $\beta_{\text{eff}} = 3$ is $B_{\text{eff}} \approx 17,000$ T assuming a particle charge of $Q_d = 60,000e$ [Sec. 4.2], which is orders of magnitude larger than any real magnetic induction realizable under laboratory conditions. In addition, this shows that even strongest (real) magnetic fields of a few Tesla, which are realizable under laboratory conditions, have only a marginal effect on the motion of micrometer-sized dust particles via the Lorentz force.

At first glance, this technique to magnetize dust clusters by rotation seems to produce a peculiar plasma state of matter, because only the heavy dust component is magnetized and the much lighter electrons and ions are not, since the respective plasma frequencies are orders of magnitude larger than the achievable rotation frequencies, e.g., the effective magnetizations for the plasma species are $\beta_{\text{eff},e} < \beta_{\text{eff},i} \ll 1 \approx \beta_{\text{eff},d}$. In reality, the effects of a magnetic field are stronger for the light plasma components and the magnetization is stronger for the electrons than for the ions and even much stronger than for the dust particles, $\beta_e > \beta_i > 1 \gg \beta_d$. Nonetheless, we have prepared a system that is governed by the simultaneous effects of strong-coupling and (pseudo) magnetization. Such systems are currently of high interest as they are believed to occur in extreme states of matter [137] or for cold ions in Penning traps [138]. In addition, there are theoretical studies on the effects of magnetic fields on diffusion properties [45] and wave spectra [139, 140, 141, 142, 143] in magnetized Yukawa systems. Thus, rotating dusty plasmas may be seen as a new approach to study the effects of (pseudo) magnetization and strong coupling in a real laboratory device benefiting from the outstanding features of dusty plasmas, which allow to resolve the single particle motion in space and time.

One the other hand, the pseudo-magnetization of dust structures may complicate the attempts to attribute features of magnetization, e.g., dust cyclotron waves [47], to a real magnetic field. It is an outstanding challenge to prepare a fully magnetized plasma [39], whereas magnetized dusty plasmas are usually in a rotating state, see chapter 5. We have seen that for dust clusters rotating at moderate rotation frequencies the Coriolis force can be orders of magnitude larger than the Lorentz force, whereas both forces act in the same way. Thus, in rotating dust structures it could be difficult to clearly separate the effects that result from the pseudo-magnetization of the dust cloud from the effects of a real magnetic

field. One solution for this may be the reduction of the particle size, which will be discussed in chapter 6 of this work.

Dust clusters in magnetized plasmas

The focus of this chapter lies on the dynamics of dust clusters and the interaction forces between micrometer-sized dust particles confined in the plasma sheath in the presence of magnetic fields. We will see that dust structures in a magnetized plasma are naturally in a rotating state, which is one motivation for studying rotational effects presented in the previous chapter 4. Furthermore, it has been shown in Sec. 4.3 that under laboratory conditions the Lorentz force on micrometer-sized dust particles is usually negligibly small and therefore does only have a marginal effect on the motion of the dust particles. But, the magnetization of the electrons and ions gives rise to a modified plasma response and can indirectly affect the structure and dynamics of dust clusters via a modification of the dust-dust interaction forces. Here, the focus lies on the ion-wake-mediated particle interaction, which originates from the flow of ions in the plasma sheath. In particular, the interest lies on the modification of the ion-wake-mediated particle interaction in the presence of strong magnetic fields, which we have studied for the first time in the context of dusty plasma physics.

Dust structures in the presence of an (axial) magnetic field are often found to perform a rotational motion about their axis, which is probably the most obvious effect of magnetic fields on dust structures. This has been observed in numerous experiments, e.g., see Refs [52, 112, 144, 145, 146, 147]. However, the mechanism responsible for dust cluster rotation is still a matter of debate. Often the sense of cluster rotation is found to coincide with the azimuthal component of the ion drag force [52, 144, 145], which results from a deflection of the ions in crossed radial electric and axial magnetic fields. Konopka *et al.* [52] supposed that the rotation frequency is determined by a balance of ion and neutral drag force for a neutral gas at rest. However, this classical ion drag model was found to significantly underestimate the rotation frequencies observed in Refs. [145, 146, 148]. In this work, an additional mechanism of cluster rotation is proposed based on a co-rotation of the neutral gas column. Here, one important prerequisite is that the gas is in a laminar-flow regime, which has been shown in Sec. 4.1.

Ion wakes in unmagnetized plasmas and their effects on the dynamics and structure of dust clusters have been studied extensively over the last two decades, a brief summary of the available literature is given in section 5.2. Furthermore, dusty plasmas in the presence of strong magnetic fields are a new parameter regime [39], where only a few experimental observations exist [48, 50]. There are only a few theoretical calculations in the limit of linear response theory (LRT) [41, 42, 43] or computer simulations [44, 149] for ion wakes in magnetized plasma flows available. In particular, the LRT calculations predict a damping of the wake oscillations by the magnetic field and a reduction of the wake charge, which should have consequences for the ion-wake-mediated interparticle forces.

This chapter is based on my publications [A.1],[A.5],[A.6] and is ordered along the degrees of plasma magnetization. Sec. 5.1 is about the mechanism of dust cluster rotation in the presence of weak magnetic fields. Sec. 5.2 gives a brief introduction to ion wake related phenomena. In Sec. 5.3, the ion-wake-mediated particle interaction is studied by means of PRRM for an unmagnetized plasma, whereas the focus of Sec. 5.4 lies on the particle interaction in the presence of strong magnetic fields.

5.1 Cluster rotation in the presence of axial magnetic fields

Dust clusters in the presence of magnetic fields are often found to be in a rotational state, even for magnetic fields as weak as the magnetic field of the earth [120]. One of the first observations of rotating dust structures in the presence of magnetic fields were reported by Nunomura *et al.* [150] and Juan *et al.* [144]. Juan speculated that the rotation is caused by the ion drag force, which results from a deflection of the ions in crossed radial electric and axial magnetic fields and may be accompanied by a slow rotation of the neutral gas column. Sato *et al.* [48] studied the rotation of dust structures in a coupled dc-rf-discharge for magnetic inductions up to 1 T. There, the rotation frequencies of the dust structures and the sense of rotation were found to strongly depend on an applied bias voltage to the lower electrode. The bias voltage affects the radial density and potential profiles outside the region of particle levitation, while the potential profiles inside the confinement region are almost independent of the applied bias voltage. Konopka *et al.* [52] observed the rigid and differential rotation of dust clusters in a rf-discharge. There, the sense of rotation corresponds to the azimuthal component of the ion drag force and it is assumed that the rotation frequency of the dust structures is determined by the balance of ion and neutral drag force for a neutral gas at rest. This *classical ion drag model* was found to give a qualitative explanation for a number of experimental observations [145, 146, 148, 151], but the absolute values of the observed rotation frequencies were found to be significantly larger than expected [145, 146, 148]. Furthermore, rotating dust structures were found in magnetized dc-glow discharges [49, 147]. There, an inversion of the cluster rotation at a critical magnetic field has been attributed to an inversion of the radial ambipolar field, when the electrons become magnetized.

However, the physical mechanism setting dust clusters into rotation in the presence of magnetic fields is still a matter of debate. It is the aim of this section to show that the

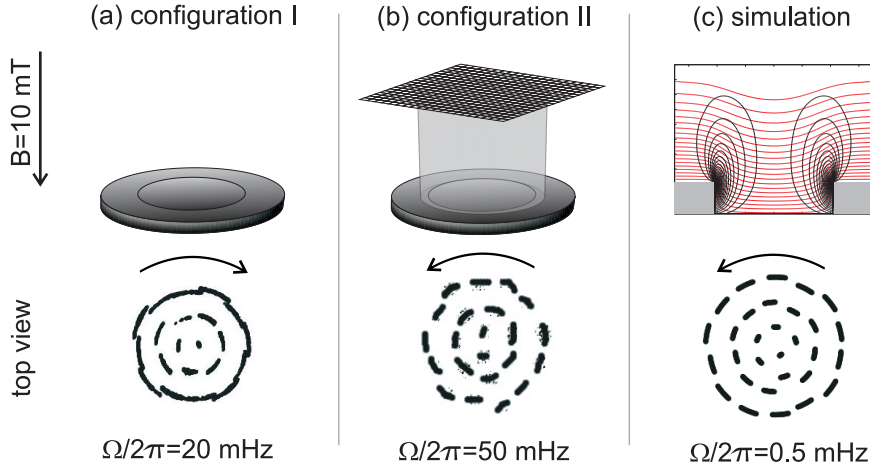


Figure 5.1: Cluster rotation observed in different experimental configurations and as predicted by the classical ion-drag model for a magnetic induction of $B = 10$ mT, whereas the magnetic field vector points downwards. The arrows denote the sense of rotation, when looking from the top. (a) Standard setup: The discharge burns between the lower (driven) electrode and the grounded chamber walls. (b) The effective plasma volume is restricted to a small cylinder by placing a glass tube on the electrode covered by a conducting grid, to allow an observation from the top. (c) Cluster rotation as predicted by the classical ion drag model based on the sheath model shown in Fig. 5.2(a).

classical ion drag model cannot be the only mechanism of cluster rotation. Here, the idea of a co-rotation of the neutral gas column [144] is taken up again to explain the magnitude of the observed rotation frequencies and the sense of rotation in certain experimental configurations. This section is primarily based on the results described in my Diploma thesis [120] and published in Ref. [A.1]. The results presented here are the starting point of my PhD-work and are one motivation to study neutral gas flows (Sec. 4.1) and magnetic field effects on dust clusters.

In Fig. 5.1(a), a long-exposure photo of a small 2d-cluster of 21 MF-particles is shown. There, a magnetic field pointing in the downward direction is applied with an induction of $B = 10$ mT. The cluster performs a rigid rotation about its center of mass in the clock-wise direction, when viewed from the top in the direction of the magnetic field. The rotation frequency is $\Omega/2\pi = 20$ mHz. The experimental setup is similar to those described in chapter 4, except that the rotating electrode is replaced by a large window, which allows an observation from the top. In the following, it will be shown that this observation cannot be explained by the classical ion drag model, since the observed rotation frequency is two orders of magnitude too large and the sense of rotation is in opposite direction to the local ion drag force.

In order to obtain an accurate estimate for the electric fields and the ion densities in the plasma sheath above the lower electrode, where the dust cluster is confined, the sheath model used in the simulation code described in Ref [152] was adopted by L. J. Hou to best match the experimental parameters. It is $n_i = 5.8 \times 10^{14} \text{ m}^{-3}$ the ion density and $T_e = 3$ eV the

electron temperature in the plasma bulk measured by Langmuir probes and $p = 15$ Pa the gas pressure. There, the rf-plasma sheath is treated by a dynamical fluid model, which explicitly takes the geometry of the electrode into account to correctly describe the radial confinement (radial electric fields) of the dust clusters. The time-averaged potential above the electrode is shown in Fig. 5.2(a). At these gas pressures, the flow of ions is mobility-limited because the mean free path of the ions $\lambda_{i,\text{mfp}} = 0.7$ mm is significantly smaller than the sheath width ($d_{\text{sh}} \approx 1$ cm) and the ion flow velocity \mathbf{u}_i is given by

$$\mathbf{u}_i = \mu_i \mathbf{E} . \quad (5.1)$$

It is $\mathbf{E} = E_r \mathbf{e}_r + E_z \mathbf{e}_z$ the local electric field having a component in radial and vertical direction, whereas at the position of the dust clusters it is $E_r \ll E_z$. The mobility of the argon ions μ_i in their parent gas was measured by Frost and can be taken from Ref. [123]. When a magnetic field is applied, μ_i becomes a tensor. For a magnetic field in axial direction, i.e., $\mathbf{B} = (0, 0, B_z)$, it is

$$\mathbf{u}_i = \mu_i \begin{pmatrix} \frac{1}{1+\mu_i^2 B_z^2} & \frac{\mu_i B_z}{1+\mu_i^2 B_z^2} & 0 \\ -\frac{\mu_i B_z}{1+\mu_i^2 B_z^2} & \frac{1}{1+\mu_i^2 B_z^2} & 0 \\ 0 & 0 & 1 \end{pmatrix} \mathbf{E} . \quad (5.2)$$

For weak magnetic fields ($\mu_i B_z \ll 1$) the argon ions experience a deflection in azimuthal direction with

$$u_{i,\phi} = \mu_i^2 E_r B_z . \quad (5.3)$$

Thus, with the potential and density profiles taken from the simulation, we can determine the azimuthal component of the ion drag force at the position of the dust clusters. In the classical ion drag model the rotation frequencies can then be deduced from the balance of ion and neutral drag force for a neutral gas at rest. The expected rotation frequencies $f_{i\text{-drag}}$ are shown in Fig. 5.1(c). For weak magnetic fields, we find a linear dependence of $f_{i\text{-drag}}$ on B_z , because it is $u_{i,\phi} \propto B_z$. For $B_z = 10$ mT, the rotation frequency is $f_{i\text{-drag}} = 0.5$ mHz, which is a factor of 40 smaller than the value observed in the experiment [Fig. 5.1(a)]. The expected sense of rotation is of course in direction of the azimuthal component of the ion drag force pointing in $E_r \mathbf{e}_r \times B_z \mathbf{e}_z$ direction. Thus, for E_r pointing radially outward and a magnetic field in downward direction a rotation in the counter-clock-wise direction is expected, which is in conflict with the observations shown in Fig. 5.1(a). Moreover, in the classical ion drag model, the azimuthal component of the ion flow velocity does only depend on the local electric and magnetic fields, and therefore the rotation frequency should only depend on the local plasma and dust parameters. If we modify the experimental setup and place a glass cylinder on the electrode, which is covered by a conducting grid [see Fig. 5.1(b)], the local electric fields at the position of the dust clusters are approximately the same in both experimental configurations, since both clusters are confined at almost the same height above the electrode and the interparticle distances are comparable. But now the observed sense of rotation is in

the counter-clock-wise direction (as predicted by the simulation), although the magnitude of the rotation frequency is still two orders of magnitude larger than the values deduced from the balance of ion and neutral drag.

This discrepancy between the classical ion drag model and our observations shows that there must be at least one more mechanism of dust cluster rotation. In Ref. [A.1], we have proposed an additional mechanism, which takes the neutral gas into account. The idea is that the deflection of the ions in the azimuthal direction due to crossed electric and magnetic fields does not only exert a torque on the dust clusters via the ion drag force, but also a torque on the neutral gas via a collisional momentum transfer from the ions to the neutrals. Thus, radial electric fields, which are found, e.g., at the edges of the electrodes or ambipolar fields within the plasma bulk in combination with the axial magnetic field can act as a neutral gas drive. Consequently, a sheared neutral gas flow establishes in the entire plasma chamber as it is found for the mechanical drive in Sec. 4.1, which in turn sets the cluster into rotation. This would explain why the change of the experimental configuration from Fig. 5.1(a) to Fig. 5.1(b) substantially affects the rotational motion of the dust cluster, since in the second configuration [Fig. 5.1(b)] the plasma volume outside the glass tube cannot contribute to the cluster rotation inside the glass tube. For a quantitative estimate of the neutral gas rotation frequency one needs the total torque transferred from the ions to the neutrals within the entire plasma chamber, which would require a complete set of the plasma potential and density profiles within the chamber. However, we do not have such profiles, but we have the simulation data shown in Fig. 5.2(a) and we can calculate the contribution of the sheath electric field of the lower electrode to the neutral gas rotation frequency. The aim is to show that the sheath electric field alone would result in a neutral gas rotation frequency, which exceeds the value deduced from the classical ion drag model [Fig. 5.1(c)]. Thus, the neutral gas cannot be assumed to be at rest.

In Ref. [A.1], an estimate of this effect is given based on an analytic model, which assumes a rigid rotation of the ion column in the plasma sheath. Here, I like to give a more accurate estimate based on the density and potential profiles taken from the simulation [Fig. 5.2(a)]. The force per volume dV exerted on the neutral gas from the collisional momentum transfer from the ions to the dust in azimuthal direction is

$$dF_{i,\phi} = n_i m_i u_{i,\phi} \nu_{i,n} dV . \quad (5.4)$$

It is n_i the ion density, m_i the mass of the ions, $\nu_{i,n}$ the ion-neutral collision frequency and $u_{i,\phi}$ the drift velocity of the ions in azimuthal direction given by Eq. (5.3). The product $n_i \nu_{i,n} dV$ is the number of collisions within the volume dV per unit time and $m_i u_{i,\phi}$ the momentum of the ions in azimuthal direction. The force exerted on the neutral gas, as deduced from the simulation data, is shown at the left-hand side of Fig. 5.2(b). As expected, close to the edge of the cylindrical depression, where strong radial electric fields are present, the force becomes maximal. In Sec. 4.1 it is shown that the flow of the neutral gas can be described by the Navier-Stokes Eq. (5.4), whereas for slow gas-flow velocities \mathbf{u}_n the dominating force

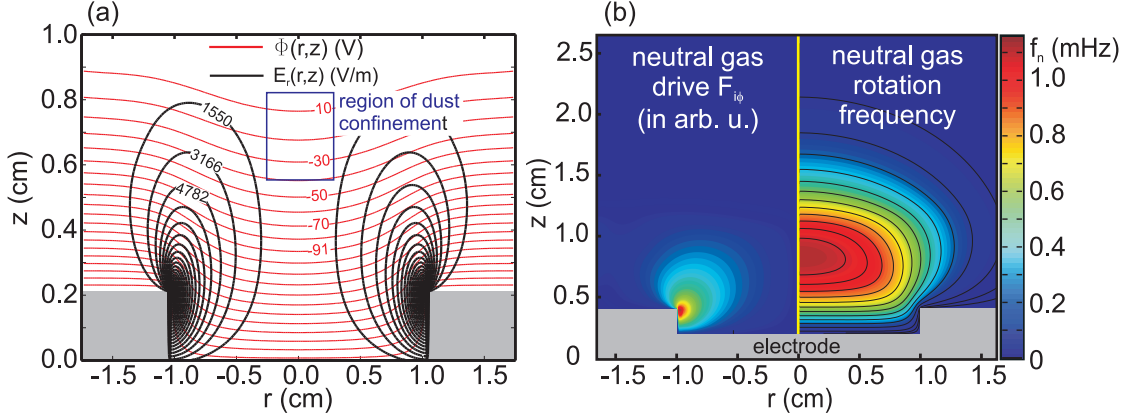


Figure 5.2: (a) Calculated potential and radial electric field above the lower electrode as shown in Ref. [A.1]. (b) Left-hand side: Contour plot of the azimuthal component of the force exerted on the neutral gas, which results from the collisional momentum transfer from the ions drifting in the crossed fields of an axial magnetic field of $B = 10$ mT and the sheath electric field [see Fig. 5.2(a)] to the neutrals. Right-hand side: Resulting neutral gas rotation frequency, assuming a laminar gas flow and a non-slip boundary condition at the surface of the electrode. This result was obtained by finite elements methods by means of the partial differential equation toolbox of MATLAB [153].

is the viscous friction force $d\mathbf{F} = -\eta\Delta\mathbf{u}_n dV$, which must be balanced by the driving force, see Eq. (5.4). Thus, the differential equation for the flow problem reads

$$\Delta\mathbf{u}_n = -\frac{dF_{i,\phi}\mathbf{e}_\phi}{\eta}. \quad (5.5)$$

For the boundary conditions, we assume a sticking of the gas flow at the surface of the electrode (no-slip boundary condition, see Sec. 4.1), while the radial and upper boundary are put far away so that they make only a negligible contribution to the neutral gas flow above the electrode. For a cylindrical symmetry, this inhomogeneous Laplace Eq. (5.5) can be solved numerically by the partial-differential equation toolbox of MATLAB [153] by means of finite elements methods. The resulting rotation frequencies of the neutral gas f_n are shown on the right-hand side of Fig. 5.2(b). There, f_n is zero close to the electrode, which is a consequence of the no-slip boundary condition, and a vertically sheared rotation of the neutral gas is established at the axis above the electrode, as it is found for the mechanical drive (Sec. 4.1) as well. The rotation frequency becomes maximal at intermediate heights above the electrode, right where the dust is confined. There, it is $f_n = 1.2$ mHz, which exceeds the rotation frequencies predicted by the classical ion drag model ($f_{i\text{-drag}} = 0.5$ mHz).

For a consistent set of parameters, which are close to the experimental conditions, the sheath model [Fig. 5.2] allows an estimate of the pure ion drag effect on the dust clusters rotation and the neutral gas rotation frequencies. There, the neutral gas rotation is the dominant source of cluster rotation, whereas most of the driving force comes from the strong electric fields at the edge of the cylindrical depression and not from the local electric field at

the position of the dust clusters, which are responsible for the dust confinement and determine the local ion drag force on the dust cluster. The neutral gas rotation frequency is still one order of magnitude smaller than the value found in the experiment and cannot explain the clock-wise rotation of the cluster in the experimental configuration shown in Fig. 5.1(a). Nonetheless, the change of the experimental configuration from Fig. 5.1(a) to Fig. 5.1(b) and the observed inversion of the sense of rotation suggests that a significant part of the neutral gas drive stems from the outer regions of the discharge, which are shielded by the glass tube in the configuration of Fig. 5.1(b). Possible sources of the observed clock-wise rotation in configuration Fig. 5.1(a) are the strong radial electric fields at the outer edge of the lower electrode pointing radially inwards. Moreover, the combination of an axial magnetic field, an asymmetric rf-discharge and a large (non-conducting) top window may give rise to a complex potential distribution in the plasma bulk as argued in Ref. [70]. The integration of the weak ambipolar fields over a large plasma volume in comparison to the strong fields in the plasma sheath restricted to a small volume could make a significant contribution to the neutral gas rotation as well.

The experiments presented here give a clear evidence that the classical ion drag model cannot be the only mechanism for cluster rotation in an axial magnetic field. In certain experimental configurations, the rotation was found to be against the local ion drag force and the magnitude of the rotation frequencies were two orders of magnitude larger than deduced from the balance of the ion and neutral drag force for a neutral gas at rest. A quantitative estimate of the neutral gas rotation frequency resulting from the cylindrical depression of the electrode, which is responsible for the radial confinement of the dust clusters, shows that the co-rotation of the neutral gas column is not negligible and can even exceed the contribution of the ion drag force to the dust cluster rotation. The assumption of a laminar gas flow and a sticking of the gas at the electrode was proven by the experiments presented in Sec. 4.1 and provides a qualitative explanation for the different sense of rotation in the two experimental configurations shown in Fig. 5.1(a,b), since an ion-driven neutral gas flow at the outer region of the plasma volume can contribute to the rotation at the center as well. Moreover, an ion-driven neutral gas rotation can also explain some features of the cluster rotation observed by Sato *et al.* [48] and Vasiliev *et al.* [49], where a modification of the radial electric field due to the magnetization of the electrons [49] or the bias voltage [48] has a drastic effect on the cluster rotation and can even invert the sense of rotation, although the local confinement of the dust structures is almost not affected.

Simultaneous with my publication [A.1], Nedospasov [110] argued that the co-rotation of the neutral gas column can explain the observed inversion of rotation at a critical magnetic field strength of dust ensembles in dc-glow discharges [154, 155]. There, the neutral gas rotation was estimated in a similar way assuming a balance of viscous friction forces and momentum transport from the ions to the neutrals. Later, this model was taken up by Vasiliev *et al.* [111], being in good quantitative agreement with their measurements, although this model provides only an upper estimate of the neutral gas rotation frequencies, since it does only take the transverse and not the longitudinal momentum transport to the walls

by viscous friction forces into account. Two years later, Pal *et al.* [112] analyzed the role of the neutral wind for the rotational motion of dust particles in a rf-magnetron discharge. There, the existence of a neutral gas flow was proven by the excursion of a torsion blade. Their measurements were in good agreement with a hydrodynamic flow model, whereas even the momentum transport from the electrons to the neutrals was found to make a significant contribution, which is neglected in the model presented above and those described by Nedospasov [110]. They concluded that at least for heavy argon ions the neutral gas rotation is the dominant source of cluster rotation, while for lighter gases (hydrogen), cluster rotation is dominated by the ion drag force.

In a laboratory plasma, sheath electric fields or ambipolar electric fields within the plasma bulk are inevitable, and an axial magnetic field deflects the electrons and ions into the azimuthal direction. The rotation of the plasma column is accompanied by a co-rotation of the neutral gas due to a collisional momentum transfer from the charged plasma species to the neutrals. In rf-magnetron discharges [112], dc-glow discharges [111] or rf-discharges [A.1], the neutral gas flow is one reason for the observed dust cluster rotation in addition to the ion drag force. Thus, dust clusters in magnetized plasmas are naturally in a rotating state, which was one motivation to study the effects of rotational motion on the structure and dynamics of dust clusters presented in the previous chapter 4 of this work.

5.2 Ion Wakes

In the plasma sheath, the flow of ions and the formation of ion wakes considerably modifies the potential distribution around a dust particle. A sketch of an ion wake is shown in Fig. 5.3(a). The negatively charged dust grain acts as an electrostatic lens focusing the flow of ions. Downstream to the dust particle an ion wake is formed with an excess of positive charges. This positive wake charge can attract nearby dust particles and is responsible, e.g., for the alignment of dust particles parallel to the ion flow [23, 24, 25]. Ion wakes have a substantial influence on the dynamics and structure of dust clusters confined in the plasma sheath, especially at low gas pressures, where the ion wake effects are more pronounced and are not suppressed by ion-neutral collisions. Ion wakes have been studied extensively for the last two decades and the purpose of this section is to briefly summarize some of the works on ion wake phenomena, which have implications for the measurements and conclusions presented in this work.

Wake fields occur in numerous plasma environments, when a plasma flows relative to a charged macroscopic object (or the object moves relative to the plasma). In space, the solar wind causes the formation of extended wake structures behind planets and moons [156] affecting the charging of space-crafts and asteroids passing through it [157]. Likewise, wake charging can be a real concern for space-craft docking operations, since large potential differences may lead to arc discharges [158]. Plasma wakes can be observed behind electrostatic probes in flowing plasmas, e.g., Mach probes, and are important for the interpretation of the

measured characteristics [159]. Furthermore, plasma wakes generated by high energy pulsed lasers [160, 161] or by bunches of electrons traveling at relativistic velocities [162, 163] are new techniques for the acceleration of electrons and ions to high energies.

In contrast to the aforementioned examples, the charge-to-mass ratio of dust particles in a plasma is comparatively high and, besides wake-charging, the electrostatic interaction of dust grains with the wake fields becomes important. The negatively charged dust particles act as an electrostatic lens focusing the flow of ions downstream to the particle. This wake region is characterized by an excess of positive space charges, which strongly modifies the electrostatic interaction between the particles. Wake effects are most pronounced, when the ion flow velocity u_i is of the order of the Bohm speed $u_B = \sqrt{k_B T_e / m_i}$, e.g., the Mach number is $M = u_i / u_B \approx 1$, as it is the case for the ion flow in the plasma sheath close to the sheath edge. Especially for dusty plasmas in a strongly-coupled state this modification of the interaction forces has strong implications for the dynamics and structure of dust clusters. One interesting feature of these ion-wake-mediated interaction forces is the occurrence of attractive forces between the dust particles, which can lead to the spontaneous formation of particle strings [23, 24, 25]. Nambu *et al.* pointed out the similarity of this attractive forces between the like-charged particles to the formation of Cooper pairs in superconductors [26]. Today, important questions regarding the formation of particle strings are whether these stabilizing attractive forces are due to electrostatic forces [23, 26, 32, 33, 34, 35] or drag forces [30, 31] and what is the minimal Mach number necessary for the formation of particle strings. Recent observations [164] of extended three dimensional dust clouds under microgravity show the formation of particle strings at subsonic ion flows with estimated Mach numbers of $M < 0.1$, while PIC simulations [165] show an abrupt disappearance of the potential peaks for $M < 0.3$ questioning the role of the ion wake for the observed alignment of the particles parallel to the ion flow.

PIC codes (see Refs. [77, 166, 167, 168] and references therein) are one tool to model the wake fields behind dust grains from first principle on, which is a challenging task, because the time scales of electrons, ions and the dust differ by orders of magnitude. Further, the finite grid size makes it difficult to account for particles much smaller than the Debye length, which is typically the case in experiments. Today's most sophisticated PIC codes calculate the ion dynamics assuming a Maxwell velocity distribution for the electrons [77, 166] or even fully resolve the motion of ions and electrons [167, 168], whereas the dust particles are stationary and the number of dust particles is limited to $N < 10$ due to computational demands. An alternative approach is Linear Response Theory (LRT), which describes the averaged electron and ion dynamics by a dielectric function and calculates the wake potential in linear approximation [34, 169, 170]. In LRT dust particles are treated as point charges, which is typically well satisfied in experimental situations, but LRT does not include charging processes. For single and small particles ($d < 0.01 \lambda_{De}$ [166]) a detailed comparison shows a good agreement between PIC simulations and LRT and only for larger particles nonlinear effects become important [170]. The largest disagreement between PIC codes and LRT is found in the vicinity of the dust grains. There, LRT does not treat the trapped ions correctly

and overestimates the asymmetry of the plasma polarization [171]. Furthermore, Miloch *et al.* [172] used a PIC code to simulate the wakes of two dust grains approaching each other. There, the formation of a common wake is observed, which is not a superposition of single-particle wakes and therefore cannot be described by LRT. Nonetheless, the idea to use particles as a probe for the wake of another particle was analyzed in PIC simulations by Hutchinson *et al.* [173]. There, (the lateral component of) the force on the probe particle with charge Q_d was to a good approximation the same as the electric field force $\mathbf{F}_E = Q_d \mathbf{E}$ deduced from the single-particle wake potential. Although there are a lot of experimental works performed within the plasma sheath, most PIC simulations and LRT calculations assume a quasi-neutral plasma flow. To my best knowledge, there is only one work from 2003 by Hou *et al.*, which explicitly accounts for an inhomogeneous plasma and the sheath electric field in linear response approximation [174]. There, the wake oscillations are damped and a long tail for the induced potential is observed compared to the homogeneous case.

Besides its influence on the arrangement and structure of dust ensembles, ion wakes also strongly affect the dynamics of dust clusters. The effective wake potential is asymmetric in ion flow direction inducing nonreciprocal interparticle forces, which is a result of the openness of the system, since there is a constant flow of ions to and from the dust particle. In fact, these nonreciprocal forces provide an efficient mechanism to transfer energy from the ions to the dust grains [27, 29, 175]. This causes the melting of multilayer dust clusters below a critical gas pressure [23, 176, 177] and can trigger self-excited oscillations in few particle systems [28, 178]. Often the kinetic temperature of the dust particles confined in the plasma sheath is large compared to the other plasma components. Especially in the ion flow direction the heating is more effective at low gas pressures [179], where the wake fields are more pronounced. Moreover, ion wakes are responsible for the coupling of wave modes in 1d chains [180] and 2d clusters [176, 181, 182, 183, 184, 185].

Particle pairs confined in the plasma sheath are often used as a generic model system to study the wake-mediated interparticle forces. In particular, the transition from an alignment perpendicular to the flow to a parallel alignment has been studied in detail in Refs. [186, 187, 188]. The transition can be induced by either altering the gas pressure [25], the self-bias [189] or the rf-voltage [190] affecting the strength of the perpendicular and vertical confinement or by an external driver [191]. Typically, a hysteresis is observed, when switching between the configurations, which is due to the interaction with a positive wake charge. Furthermore, the transition into the parallel alignment takes place abruptly, when one particles passes a critical point [191], which is, according to simulations, the point when one particle enters the wake of the other and a common wake is formed [189].

5.3 Charging and coupling of dust particles in unmagnetized plasma flows

This section is based on the results published in [A.5] and adopts the idea of using two particles as a generic model system to study ion-wake-mediated interparticle forces. Here, the phase-resolved resonance method (Sec. 3.1) is applied at a particle pair aligned parallel to the ion flow and the confinement and nonreciprocal coupling forces are determined with high precision. A quantitative comparison with the resonances of single, but identical particles, shows a partial decharging of the downstream particle in the wake of the upstream particle. In contrast to earlier works doing quantitative measurements on wake forces [192, 193, 194], it is shown here that the decharging effect and the nonreciprocal nature of the coupling force must be taken into account simultaneously to fully explain the experimentally measured frequency response. Here, the focus lies on unmagnetized plasmas, whereas magnetic fields will be taken into account in the subsequent section 5.4.

The resonance measurements presented here are restricted to small oscillation amplitudes, which allows to linearize the interparticle forces and to express them in terms of effective spring constants D_{jk} . Apart from that, the equation of motion is the same as for the single particle system described in chapter 3 and the equations of motion read

$$\begin{aligned}\ddot{\xi}_1 + 2\gamma_1\dot{\xi}_1 + \omega_1^2\xi_1 + D_{12}(\xi_1 - \xi_2) &= H(\omega)K_1 \exp(i\omega t) \\ \ddot{\xi}_2 + 2\gamma_2\dot{\xi}_2 + \omega_2^2\xi_2 + D_{21}(\xi_2 - \xi_1) &= H(\omega)K_2 \exp(i\omega t) \quad ,\end{aligned}\quad (5.6)$$

in which ξ_j is the excursion from the equilibrium position of the upstream ($j = 1$) and downstream particle ($j = 2$), ω_j the confinement frequency, γ_j the gas friction coefficient, $H(\omega)$ the transfer function of the coupling network and K_j the amplitude of the sinusoidal excitation. In particular, $D_{12} \neq D_{21}$ is allowed to account for the nonreciprocity of the interaction. A typical frequency response of a particle pair is shown in Fig. 5.3(a). The measurements were performed at low gas pressures [$p = 3.4$ Pa (argon)] and low rf-voltages ($U_{\text{rf}} = 120$ V_{pp}) at which the particles are aligned parallel to the flow [25, 190]. A fit of the nonreciprocal coupled harmonic oscillator model Eq. (5.6) (full lines) is in excellent agreement with the measurements (crosses), which justifies the linearization of the interparticle forces, although the maximal oscillation amplitudes are larger than 10% of the interparticle distance. The fitted model parameters are compiled in Tab. 5.1. The relative errors (1σ) for all fit parameters are less than 1% estimated from surrogate data as described in Ref. [96].

The confinement frequency of the downstream particle obtained from the model ($\omega_2 = 46.3$ rad/s) is smaller than that of the upstream particle ($\omega_1 = 63.1$ rad/s). Neglecting a charge gradient in the plasma sheath, this corresponds to a smaller charge-to-mass ratio of the downstream particle [Eq. (3.2)]. To proof that this is in part due to a reduced charge of the downstream particle in the wake of the upstream particle and not solely due to different particle masses, the upstream particle was removed from the discharge and we have measured the frequency response of the undisturbed, formerly downstream particle as shown

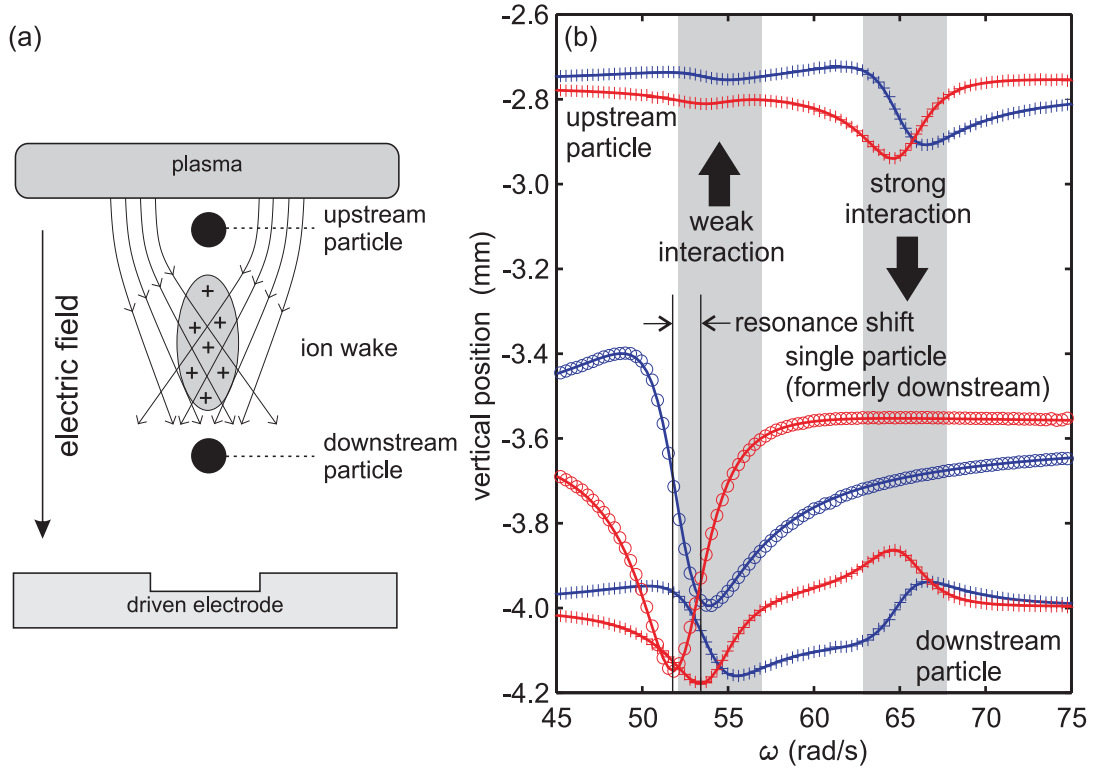


Figure 5.3: (a) Sketch of the experimental situation (not true to scale). (b) Measured frequency response function for the particle pair (crosses) and for the single, formerly downstream particle, after removing the upstream particle (circles).

in Fig. 5.3(b) (circles). There is a small shift of the resonance frequency of the downstream particle and it is $\omega_2^* = 52.3$ rad/s ($> \omega_2 = 46.3$ rad/s) the confinement frequency of the undisturbed particle. Now, this difference of the confinement frequencies can be related to a partial decharging of the downstream particle in the wake of the other of approximately 20%, because a mass effect can be ruled out, since here the confinement frequencies of the same particle in different situation are compared. This is supported by the observation that the levitation height of the downstream particle increases when the upstream particle is removed [Fig. 5.5(a)]. To avoid confusions, I like to hint at the fact that the shift of the resonance frequencies is in the opposite direction and smaller compared to the shift of the confinement frequencies. The reason for this is the strong interaction force shifting the resonance frequency of the downstream particle to larger values $\omega_{\text{res},2} \approx \sqrt{\omega_2^2 + D_{21}} = 54.8$ rad/s (the effect of the gas friction on the resonance frequency is neglected). To check if the downstream particle influences the charge of the upstream particle, the experiment was repeated, but this time the downstream particle was removed instead of the upstream particle. In this case no significant change of confinement frequency ω_1 or the levitation height was observed. Thus, the downstream particle does not noticeably affect the charging of the upstream particle.

Two-particle system				
ω_1	γ_1	K_1	D_{12}	$\omega_{\text{res},1}$
63.1 rad/s	2.25 s ⁻¹	0.133 ms ⁻²	156 s ⁻²	64 rad/s
ω_2	γ_2	K_2	D_{21}	$\omega_{\text{res},2}$
46.3 rad/s	2.34 s ⁻¹	0.045 ms ⁻²	868 s ⁻²	54 rad/s
Single-particle system				
ω_2^*	γ_2^*	K_2^*		$\omega_{\text{res},2}^*$
52.3 rad/s	2.37 s ⁻¹	0.371 ms ⁻²		52 rad/s

Table 5.1: Fit parameters of the coupled harmonic oscillator model Eq. (5.6) for the measured frequency response functions shown in Fig. 5.5(b). For comparison, the resonance frequencies $\omega_{\text{res},i} \approx \sqrt{\omega_i^2 + D_{ij}}$ are given in the last column.

The frequency response functions directly reflect the nonreciprocity of the ion-wake-mediated interaction forces. The resonance frequency of the upstream particle is at $\omega = 65$ rad/s and the downstream particle shows a strong reaction to the large amplitude oscillation of the upstream particle. On the other hand, the resonance frequency of the downstream is at $\omega = 54$ rad/s and there is only a weak response of the upstream particle. The determination of the coupling constants (see Tab. 5.1) now allows to quantify the degree of nonreciprocity and in the presented situation the force in downstream direction is roughly five times larger than in the upstream direction ($D_{21}/D_{12} = 5.5$). This strong asymmetry of the interaction force is well known for the lateral component of the coupling force stabilizing the vertical alignment as shown by Melzer *et al.* [25]. There, the degree of asymmetry was even larger and the attractive force from the wake charge exceeds the Coulomb repulsion by a factor of 20 ± 10 . Here, the interaction force parallel to the ion flow was considered, but the trend is the same. However, Kong *et al.* [194] evaluated the resonances of a parallel aligned particle pair as well for similar conditions and found the force in upstream direction to be stronger as in downstream direction ($D_{21}/D_{12} < 0.66$). There, the step response to a sudden increase of the electrode bias was evaluated. The discrepancy to our findings may come from the occurrence of transients in their work. For the measurements presented here, the oscillating particle pair was given some time to reach a steady state so that all transients are damped out.

The nonreciprocal particle interaction and the decharging effect can be reproduced by PIC simulations. W. Miloch adopted the simulation code described in Ref. [172] to best match the experimental parameters, e.g., $T_e = 3$ eV, $T_i = 0.03$ eV, $\lambda_D = 0.7$ mm and a Mach number of $M = 1$. Although the simulation does not account for the electric field and the non-neutrality of the plasma sheath and assumes larger particles than in the experiments, this allows a qualitative comparison, while exact numbers should be taken with care. The simulation yields a stronger decharging effect but a smaller degree of asymmetry of the interaction force. The simulation gives $Q_2/Q_2^* \approx 0.5$ and $D_{21}/D_{12} \approx 1.5$, when the downstream particle is located at the self consistent equilibrium position. The experimental results are $Q_2/Q_2^* \approx 0.78$ and $D_{21}/D_{12} \approx 5.5$. Thus, the decharging effect is fairly reproduced, while the simulation

underestimates the degree of asymmetry of the particle interaction. This can be resolved if the particle confinement and the dependence of the particle charge on the interparticle distance is taken into account, which gives rise to an additional effective interaction force enhancing the degree of asymmetry. Let us assume a constant charge gradient with respect to the interparticle distance, as it is found in the simulations described in Refs. [172, 195]. If now the upstream particle approaches the downstream particle, this will further reduce its charge and the sheath electric field will not fully compensate the force of gravity anymore. Consequently, the downstream particle experiences a net force in the downstream direction.

For an order of magnitude approximation of this effect, we will assume the charge of the downstream particle Q_2 to be linearly dependent on the interparticle distance d . Here, the dependence of the particle charge on the position in the sheath will be neglected for simplicity. A Taylor expansion about the equilibrium interparticle distance d_0 yields $Q_2 = Q_2^0 + Q_2'(d - d_0) = Q_2^0 + Q_2'(\xi_2 - \xi_1)$. It is Q_2^0 the equilibrium charge of the downstream particle, Q_2' the charge gradient with respect to d and ξ_1 (ξ_2) the excursion from the equilibrium position of the upstream (downstream) particle. For a harmonic confinement, the sheath electric field can be written as $E = E_0 + E'\xi_2$, where E_0 is the field strength at the equilibrium position and E' the gradient of the electric field. Thus, the electric field force on the downstream particle due to the sheath electric field is given by

$$F_E = EQ_2 = (E_0 + E'\xi_2)(Q_2^0 + Q_2'(\xi_2 - \xi_1)) \approx E_0Q_2^0 + E'Q_2^0\xi_2 + E_0Q_2'(\xi_2 - \xi_1) \quad (5.7)$$

Neglecting terms of the order of $E'Q_2'$ gives the right-hand side of Eq. (5.7). Here, the first term $E_0Q_2^0$ compensates the force of gravity, the second term $E'Q_2^0\xi_2$ represents the vertical confinement and is related to the confinement frequency $\omega_2^2 = E'Q_2^0/m$. The last term represents the effective interaction force from the charge gradient. Assuming the attractive force from the ion wake to be small compared to the force of gravity, we can eliminate E_0 by using the regular force balance of the force of gravity and the electric field force $E_0Q_2^0 = mg$. Then, the effective coupling constant can be defined in analogy to Eq. (5.6) as $D_{21}^{\text{eff}} = gQ_2'/Q_2^0$.

In the presented experiment, the interaction force has two contributions, one from the electrostatic interaction with the ion wake D_{21}^ϕ , which is modeled by the simulation, and one from the charge gradient D_{21}^{eff} , i.e., it is $D_{21} = D_{21}^\phi + D_{21}^{\text{eff}}$. To obtain a rough estimate of the charge gradient effect on the coupling constant we approximate Q_2' by $\Delta Q_2/d_0$. It is $\Delta Q_2 \approx 0.2Q_2^0$ the charge reduction found in the presented experiment. A characteristic length scale is provided by the interparticle distance $d_0 = 1.2$ mm. This yields $D_{21}^{\text{eff}} = 1600 \text{ s}^{-2}$ approximately twice the value measured in the experiment ($D_{21} = 870 \text{ s}^{-2}$). This shows that even small relative charge gradients Q_2'/Q_2^0 , which are considerably smaller than those found in the simulations [172, 195], can induce interaction forces that are at least comparable or may even exceed the interaction forces due to the electrostatic interaction with the wake potential. This effect can explain the observed strong asymmetry ($D_{21}/D_{12} \approx 5.5$) in comparison to the simulation ($D_{21}/D_{12} \approx 1.5$), because the charge gradient enhances the degree of asymmetry of the interaction force, since the upstream particle has a much stronger effect

on the charge of the downstream particle than vice versa.

In this section I have shown that the phase-resolved resonance method (Sec. 3.1) is well suited to study charging and interaction forces between two particles. The decharging due to the ion wake and the asymmetric coupling could be quantified simultaneously with high precision. Here, the focus lies on the interaction force in flow direction in contrast to the works by Melzer *et al.* [25] and Hebner *et al.* [193, 196] concentrating on the lateral component of the interaction force responsible for the stabilization of the vertical alignment. Prior *et al.* [192] analyzed the coupled modes of a particle pair and have obtained a decharging of the downstream particle by 30%, which is close to our value, but they assumed a symmetric particle interaction, which is not the case if the forces are mediated via an ion wake and might cause a systematic error. It turns out that for pairs of particles confined in the plasma sheath, the decharging of the downstream particle within the wake of the other and the asymmetric interaction forces cannot be seen to be independent of each other, both effects are coupled due to the external confinement, which enhances the degree of asymmetry of the interaction force. This results might help to improve models [186, 187, 188, 190] describing the transition from a vertical to a horizontal alignment of particles, when altering the discharge parameters. There, the assumption is made that the confinement frequencies of both particles are equal, which does not hold in the vertical configuration, where the decharging effect lowers the confinement frequency and the levitation height of the downstream particle.

5.4 Ion-wake-mediated particle interaction in magnetized plasma flows

In Sec. 4.3, we have seen that the Lorentz force on micrometer-sized dust particles in laboratory plasmas is small compared to the force of gravity, confinement or the dust-dust interaction forces and the direct effect of a magnetic field on the dynamics of dust clusters is marginal. Therefore, magnetic fields can only indirectly affect the dynamics of dust clusters via the magnetization of the electrons and ions, e.g., resulting in a rotational motion of the dust clusters (Sec. 5.1). In the previous section 5.3 we have seen that the polarization of the ion flow in the plasma sheath and the formation of ion wakes has a strong effect on the dust-dust interaction force parallel to the flow and on the charging of the dust particles in the wake of another. At these parameters, a strong magnetic field parallel to the flow of ions can modify the scattering of ions in the Coulomb field of a charged dust particle as it is shown in Fig. 5.4(a,b). In this simplified model (neglecting collisions and collective phenomena), the focusing effect and therefore an increased ion density in the focusing region is clearly visible for the unmagnetized case [Fig. 5.4(a)]. If a strong magnetic field ($B = 2$ T) parallel to the flow is applied, the flow pattern is severely modified [Fig. 5.4(b)]. The scattering process transfers energy into the lateral ion motion, which triggers a helical ion flow and an extended ion shadow is formed. It is the aim of this section to show that magnetic fields indeed have a strong influence on ion wakes and modify the ion-wake-mediated particle interaction in a magnetized plasma flow, as it is discussed in my publication [A.6].

Dusty plasmas in the presence of strong magnetic fields are a new parameter regime [39], where only a few experimental observations exist. Sato *et al.* [48] studied cluster rotation for magnetic induction up to 1 T and Schwabe *et al.* [50] reported on the filamentation of a rf-discharge accompanied by the formation of patterns of spirals and concentric circles perpendicular to the magnetic field. There is a lack of experimental works concerning wake effects in magnetized dusty plasmas and only a few theoretical predictions [41, 42, 43] and simulations [44, 149] exist. Particle-in-cell simulations performed by Patacchini *et al.* [44, 149] showed the appearance of ion cyclotron wakes in crossed electric and magnetic fields, when cyclotron damping is not too strong. Furthermore, Salimullah *et al.* [42] calculated the ion wake potential in a magnetized plasma flow in the limit of linear response theory (LRT). In Fig. 5.4(c) the wake potential ϕ_{wake} at a certain position downstream to the dust particle is plotted versus the magnetization parameter $f = 1/\beta_i^2 \propto 1/B^2$ for different Mach numbers of the ion flow. There, the magnetic field strongly damps the wake oscillations, when the ions become magnetized ($f < 1$ or $\beta_i > 1$) and the ion cyclotron frequency starts to exceed the ion plasma frequency. Thus, LRT predicts a reduction of the space charge stored within the wake for increasing magnetic inductions.

In order to allow a direct comparison to the LRT results shown in Fig 5.4(c), we will use the parameter $\beta_i = \omega_{ci}/\omega_{pi}$ as a measure of the ion magnetization as it is introduced in Sec. 2.4. In contrast to the LRT calculations, which are made for collisionless plasma flows, ion-neutral collisions will certainly affect the ion wake in the presented experiments.

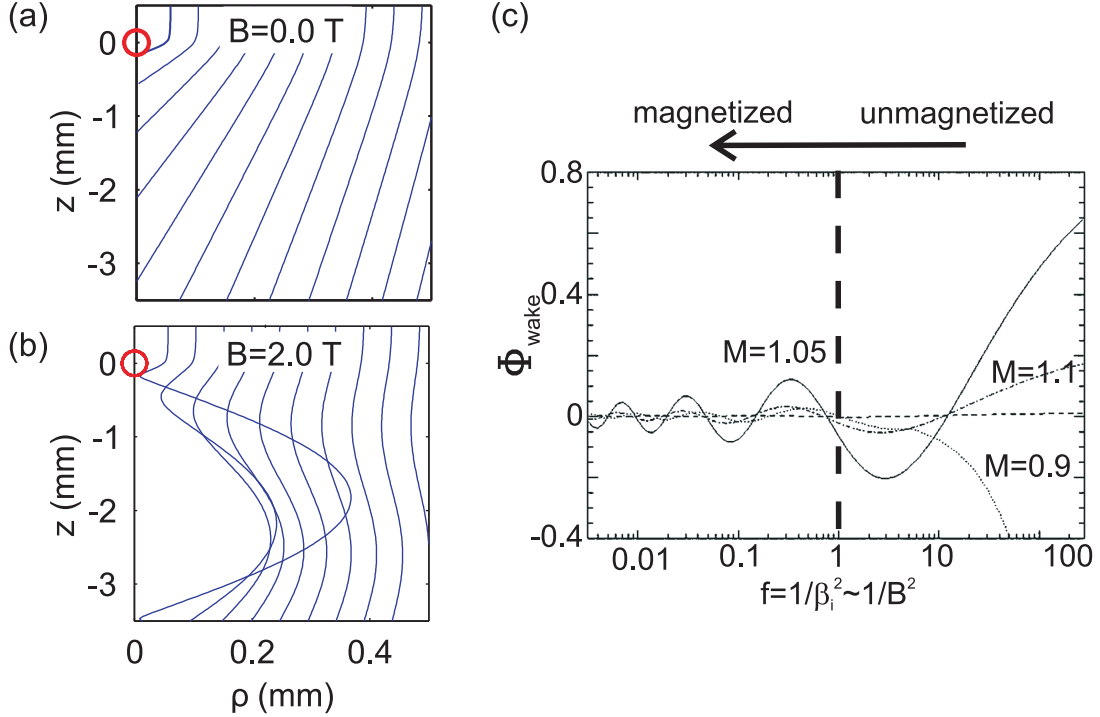


Figure 5.4: (a) Trajectories of argon ions flowing with a Mach number of $M = 1$ in downward direction and scattered in the pure Coulomb field of a dust particle (Rutherford scattering). The circle marks the position of the dust particle and $\rho = \sqrt{x^2 + y^2}$ is the lateral displacement from the axis. (b) Trajectories, when an additional magnetic field of $B = 2$ T is applied parallel to the flow. (c) Linear response calculation taken from Ref. [42]: Wake potential Φ_{wake} at a fixed position ($2\lambda_{De}$ downstream to the dust particle and $2\lambda_{De}$ in lateral direction) versus magnetization parameter $f = 1/\beta_i^2$ for different Mach numbers M .

Nonetheless, $\beta_i > 1$ is still a reasonable criterion to separate unmagnetized and magnetized wakes, since the experiments were performed at low gas pressures so that for $\beta_i > 1$ the Hall parameter of the ions becomes larger than unity ($H_i = \omega_{ci}/\nu_{in} > 1$). For this specific situation of magnetized ion wakes, this parameter β_i can be interpreted in the following way: for ions flowing at Bohm speed ($u_B = \sqrt{k_B T_e/m_i}$) the effective screening length of the ions is given by Eq. (2.9) and it is $\lambda_{Di} = \sqrt{\epsilon_0 k_B T_e / (n_i e^2)}$. As argued in Sec. 4.2, the screening in the plasma sheath is dominated by the ions and the effective screening length is $\lambda_s \approx \lambda_{Di}$. The deflection of the ions passing by a charged dust particle takes place primarily within the Debye sphere of the dust particle. Thus, the Lorentz force makes a significant contribution to the scattering process, when the transit time of the ions $\tau_t = \lambda_s/u_B$ is comparable to the time scale of the cyclotron motion $\tau_{ci} = 1/\omega_{ci}$, e.g., it is $\beta_i = \tau_t/\tau_{ci} = \omega_{ci}/\omega_{pi}$. Thus, for $\beta_i > 1$ the presence of a magnetic field significantly affects the scattering of single ions at the dust particle and therefore modifies the structure of the wake field.

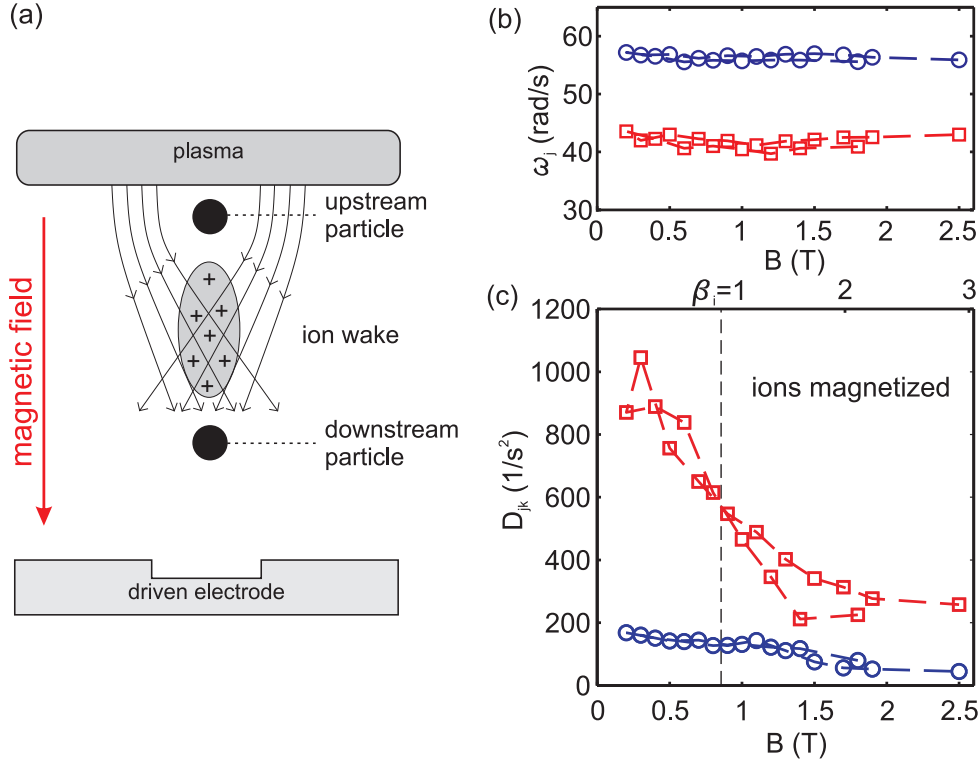


Figure 5.5: (a) Sketch of the experimental situation (b) Confinement frequencies ω_j of the upstream (circles) and downstream (squares) particle versus magnetic induction B . (c) Coupling constants D_{12} (circles) and D_{21} (squares) versus magnetic induction B and ion magnetization $\beta_i = \omega_{ci}/\omega_{pi}$.

Except for the magnetic field, the experimental situation is nearly the same as in the previous section 5.3 and sketched in Fig. 5.5(a). Two MF-particles ($r_d = 5.8 \mu\text{m}$) are confined in the plasma sheath at a gas pressure of $p = 8 \text{ Pa}$ (argon) and a moderate rf-voltage of $U_{\text{rf}} = 100 V_{\text{pp}}$. At these parameters, it is $M \approx 1$ the Mach number of the ion flow, $n_i \approx 10^{14} \text{ m}^{-3}$ the ion density and $T_e \approx 3 \text{ eV}$ the electron temperature. The plasma chamber is mounted into the superconducting magnet system SULEIMAN providing a homogenous magnetic field of up to 4 T at its center. Here, we have chosen the magnetic field to be aligned with the sheath electric field and the force of gravity and are interested in a range of magnetic inductions between $B = 0.2 \text{ T}$ and $B = 2.5 \text{ T}$ for the following reasons. At these parameters the electrons are fully magnetized ($H_e \gg 1$) and a change of the magnetic induction should have only a minor effect on the electron dynamics. Since the flow of ions within the plasma sheath and the magnetic field are aligned, the sheath structure is almost independent of the magnetic induction, which we have verified by measurements of the plasma glow (details see [A.6]). Thus, we can relate changes of the resonances of the particle pair to a modification of the dust charge or interaction forces. At $B > 2.5 \text{ T}$, the filamentation of the plasma discharge [50] becomes too strong, which destabilizes the confinement of the particle pair and inhibits further measurements. Moreover, at $B = 0.2 \text{ T}$, the magnetization of the ions

is $\beta_i \approx 0.15$ and at $B = 2.5$ T it is $\beta_i \approx 3$. Thus, in this range of magnetic inductions the ions become magnetized and this is just the parameter range where the LRT calculations [Fig 5.4(c)] predict the ion wake to react sensitively to the magnetic induction.

Here, the particle pair is aligned parallel to the flow of ions, as it was the case for the measurements of the unmagnetized ion wake presented in the previous section 5.3. The confinement frequencies of both dust particles and the nonreciprocal interaction forces were measured by means of the phase-resolved resonance method (Sec. 3.1) for the entire range of magnetic inductions. In Fig. 5.5(b), the confinement frequencies of the upstream (ω_1 , circles) and the downstream particle (ω_2 , squares) are plotted versus the magnetic induction B . The measurements were started at $B = 1.8$ T, then the magnetic induction was ramped down to $B = 0.2$ T and ramped up again to $B = 2.5$ T, which is denoted by the dashed line. There is a small drift of the confinement frequencies ω_j , which may result from a change of the plasma parameters or the properties of the dust particles over the measurement time of a few hours (see Sec. 3.2), which will be neglected in the following. Apart from that, both confinement frequencies are to a good approximation constant and can be seen as a measure of the dust charge of both particles, because it is $\omega_j^2 \propto Q_j$ according to Eq. (3.2). Thus, for the presented measurement, the dust charge does not depend on the magnetic induction, which is further supported by the observation that the levitation height of the particle pair is constant for the entire range of magnetic inductions. For the upstream particle this a reasonable result because the charging currents onto the upstream particle are similar to those of an isolated particle, since the charging of the upstream particle is not affected by the downstream particle (Sec. 5.3). For isolated particles, Patacchini *et al.* [44] argued that the ion current to the dust grain is not affected by the cyclotron motion of the ions, when the particle radius is small compared to the averaged Larmor radius of the ions and the Debye length, which is the case for the experiments presented here and the entire range of magnetic inductions. Thus, the magnetization of the ions should not affect the charging of the upstream particle. For the downstream particle, however, the situation is more complex. In the previous section 5.3, we have seen that particles in the wake of another are partially discharged, as it is found in simulations [172] as well. Here, this discharging effect is not further modified by the magnetic field. To my best knowledge, there is no theory or simulation available addressing the question of the charging of particles in the wake of another in an magnetized plasma flow. This issue might be taken up in the future and is beyond the scope of this thesis.

The interparticle forces, on the other hand, are strongly affected by the magnetic field. In Fig. 5.5(c), the interparticle forces are given in terms of the coupling constants D_{jk} and are plotted versus the magnetic induction B and the ion magnetization β_i . At $B = 0.2$ T the ions are partially magnetized ($\beta_i \approx 0.15$) and the measured values of D_{jk} show a strong nonreciprocity of the particle interaction force and are comparable to those measured for the unmagnetized wake under similar conditions (Sec. 5.3). For increasing magnetic induction there is a monotonic reduction of the interaction forces, which reaches a factor of three for a magnetic induction of $B = 1.5$ T, when the ions are magnetized ($\beta_i \approx 1.2$). Because the particle charges are to a good approximation independent of the magnetic induction,

this gradual reduction of the interparticle forces can be attributed to a modification of the wake-mediated interparticle forces. This result is in qualitative agreement with the LRT calculations [41, 42, 43], see Fig. 5.4(c). There, a magnetic field damps the wake oscillations and reduces the electrostatic charge stored within the wake. Thus, the electrostatic force exerted from the wake of the upstream particle on the downstream particle should be reduced, as it is observed in the presented experiment. Furthermore, the reduction of the interparticle forces is found in theory and experiment, when the ion cyclotron frequency ω_{ci} becomes comparable to the ion-plasma frequency ω_{pi} ($\beta_i \approx 1$).

To conclude, the measurements presented here are the first experimental proof that strong magnetic fields parallel to the flow of ions can have a substantial effect on the dust-dust interaction force in direction of the flow. Here, a strong reduction of the interparticle forces is observed, when the ion cyclotron frequency ω_{ci} exceeds the ion plasma frequency ω_{pi} , i.e., the ions are magnetized. This weakening of the interparticle forces may be attributed to a reduction of the wake charge, as it is predicted by LRT calculations [41, 42, 43]. The non-reciprocal particle interaction is an effective mechanism to transfer energy from the flowing ions to the dust particles [27] resulting in different types of instabilities [23, 28, 29]. Furthermore, the attractive force from the wake charge is responsible for the formation of particle chains [23, 24, 25]. Thus, a modification of the ion-wake-mediated particle interaction by a strong magnetic field implies that the structure and dynamics of dust structures in strongly magnetized plasmas can be substantially different from unmagnetized plasmas. Moreover, the magnetization of the ions does not influence the charging of the particles. The problem of wake charging in a magnetized plasma flow may be addressed in the future by computer simulations and may provide a deeper insight into this topic. This might also be interesting for space physics, since wake charging is also relevant for the charging of asteroids and spacecrafts in the wake of another [158] or in the wake of planets and moons [165, 197], which are subject to the solar wind.

6

Outlook: magnetized nanodust

An outstanding challenge in dusty plasma physics is the experimental realization of a fully magnetized plasma, where even the motion of the dust particles is substantially affected by the Lorentz force [39]. One approach to achieve this goal was presented in Sec. 4.3. There, the equivalence of Larmor and Coriolis force was used to mimic the effects of magnetization by setting a dust cluster into rotation. Here, I like to discuss another approach to tackle this problem. The main idea is to make use of the strong magnetic fields provided by the superconducting magnet system SULEIMAN ($B = 4\text{ T}$) and nanometer-sized dust particles, which have a much larger charge-to-mass ratio as the micrometer-sized particles considered in this work so far. This chapter is intended as an outlook and two major steps towards this aim are done: first, we have to give up the capability to resolve single particle motion and new diagnostics for the dust size and density of nanodust clouds are required. Second, a new discharge geometry is proposed, which allows the confinement and production of nanodust clouds in a magnetized plasma column.

One prerequisite for the dust particles to perform a cyclotron-like motion is that the cyclotron frequency is comparable to, or even exceeds, the neutral gas friction, i.e., the Hall parameter of the dust H_d is larger than unity. The Hall parameter H_d is inverse proportional to the dust radius r_d if we assume a linear scaling of the dust charge on the dust radius ($Q_d \propto r_d$) [39] and homogeneous spherical particles with $m_d \propto r_d^3$,

$$H_d = \frac{\omega_{cd}}{\gamma} \propto \frac{1}{r_d} . \quad (6.1)$$

It is $\omega_{cd} = Q_d B / m_d$ the dust cyclotron frequency and the dust-neutral collision frequency ν_{nd} is given by the Epstein friction coefficient Eq. (2.4) and it is $\gamma \propto 1/r_d$. For the maximum magnetic induction of SULEIMAN ($B = 4\text{ T}$), a dust charge of $Q_d = 60,000e$ for PMMA-particles with $r_d = 10\ \mu\text{m}$ (see Sec. 4.2) and a low gas pressure of $p = 1\text{ Pa}$ (argon), the Hall parameter of the dust H_d can be extrapolated to smaller dust sizes, which is shown in Fig. 6.1. There, it is $H_d > 1$ for dust radii smaller than 200 nm. Thus, for parameters that are realizable under laboratory conditions the Lorentz force on nanometer-sized dust grains may exceed the neutral gas friction force.

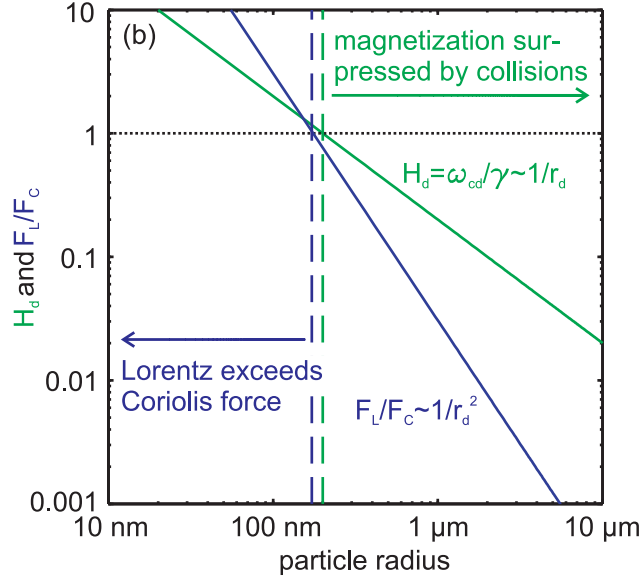


Figure 6.1: Dust Hall parameter H_d and ratio of Lorentz and Coriolis force versus the dust radius for a magnetic induction of $B = 4$ T and a neutral gas pressure of $p = 1$ Pa. Starting point of the extrapolation: $Q_d = 60,000e$ and $\Omega = 10$ rad/s.

Furthermore, in Sec. 5.1, we have seen that dust clusters in magnetized plasmas are usually in rotation and for a magnetic induction of $B = 4$ T, rotation frequencies of the order of $\Omega = 10$ rad/s are expected, e.g., Sato *et al.* [48] observed rotation frequencies of up to $\Omega \approx 3$ rad/s for $B = 0.3$ T in a slightly different discharge geometry. As shown in Sec. 4.3, the rotational motion itself results in a pseudo-magnetization of the dust clusters. To ensure that the dynamics of a rotating dust structure predominately show features of real and not pseudo-magnetization, the Lorentz force F_L on the dust particles should exceed the Coriolis force F_C . If we assume that the rotation of the dust structure is primarily due to the neutral gas motion and the rotation frequency does not depend on the particle size, it is

$$\frac{F_L}{F_C} = \frac{\omega_{cd}}{2\Omega} \propto \frac{1}{r_d^2}. \quad (6.2)$$

Here again we assume a magnetic induction of $B = 4$ T and a dust charge of $Q_d = 60,000e$ for particles with $r_d = 10$ μm . The ratio F_L/F_C versus the dust size is shown in Fig. 6.1. At these parameters, the Lorentz force exceeds the Coriolis force for particles with $r_d \lesssim 200$ nm as we have found it for the Hall parameter H_d as well. Therefore, the natural rotation of the dust structures likewise suggests to choose nanoparticles for the realization of a fully magnetized dusty plasma in order to suppress the effects of pseudo-magnetization. Thus, an extrapolation of the Hall parameter and of the ratio of Lorentz and Coriolis force indicates that it might be possible to magnetize dust particles with radii of the order of 100 nm at magnetic inductions of a few Tesla.

An established technique for the production of nanodust clouds in unmagnetized plasmas is the growth of amorphous hydrogenated carbon (a-C:H) particles in argon-acetylene (C_2H_2) rf-discharges, e.g., see Refs. [198, 199] and references therein. Plasma chemical reactions, coagulation, and accretion processes result in a continuous production and growth of nanoparticles. In particular, larger dust particles, which are in the accretion phase, have a narrow size distribution, are of nearly spherical shape, and the particle radius increases almost linearly with time [199]. In parallel-plate rf-discharges these nanodust clouds typically fill the entire discharge, except for a dust-free region in the center (void), until they become too large and fall out of the plasma volume and a new generation of nanoparticles starts to grow. This results in a periodic growth of the nanodust population, whereas the period of one growth cycle T_{growth} depends on the plasma parameters, e.g., C_2H_2 -concentration and discharge power, and is typically in the range between several 10 seconds and a few minutes.

One advantage of this technique of nanodust production is that we have to make only minor changes to the existing plasma chambers, which were originally designed for the confinement of clusters of micrometer-sized dust particles in the plasma sheath, e.g., a small fraction of acetylene has to be added to the working gas (argon). Since the particles are continuously growing in time and single particles cannot be resolved with standard video-microscopy, new diagnostics for the size and density of nanoparticles are required. For this purpose, we have developed an Imaging Mie-Ellipsometer (I-Mie), which is introduced in the following section 6.1. The I-Mie setup is described in detail in Ref. [A.8] and allows to determine the dust size with high spatiotemporal resolution. Moreover, the confinement of extended nanodust clouds in the presence of strong magnetic fields turns out to be difficult in a standard parallel-plate discharge and a modified electrode geometry is required. So far, we have succeeded in confining cylindrical-shaped dust clouds up to magnetic inductions of $B = 0.5$ T. Although the dust particles are still not magnetized, these nanodust clouds exhibit interesting dynamical behaviors as shown in Sec. 6.2. There, the benefits of the I-Mie technique will come into full effect.

6.1 Imaging Mie-Ellipsometry

One established technique for the in-situ diagnostic of nanoparticles is Mie-Ellipsometry. The idea is to measure the polarization state of light scattered at a nanodust cloud. Then, the Mie theory [200] relates the polarization and intensity of the scattered light to the size, density, and optical properties of the dust particles. In the simplest case the particles are monodisperse, are of spherical shape, and no multiple scattering occurs, which is usually well satisfied for a-C:H particles growing in argon-acetylene plasmas [199, 201]. There are numerous ellipsometric techniques to measure the polarization state of light, e.g., see Ref. [202]. In this section, the idea of using CCD cameras for ellipsometric measurements [203] is taken up in order to obtain a high temporal and spatial resolution, which is especially useful for the studying of magnetized nanodust clouds presented in Sec. 6.2. This section is based on the publication

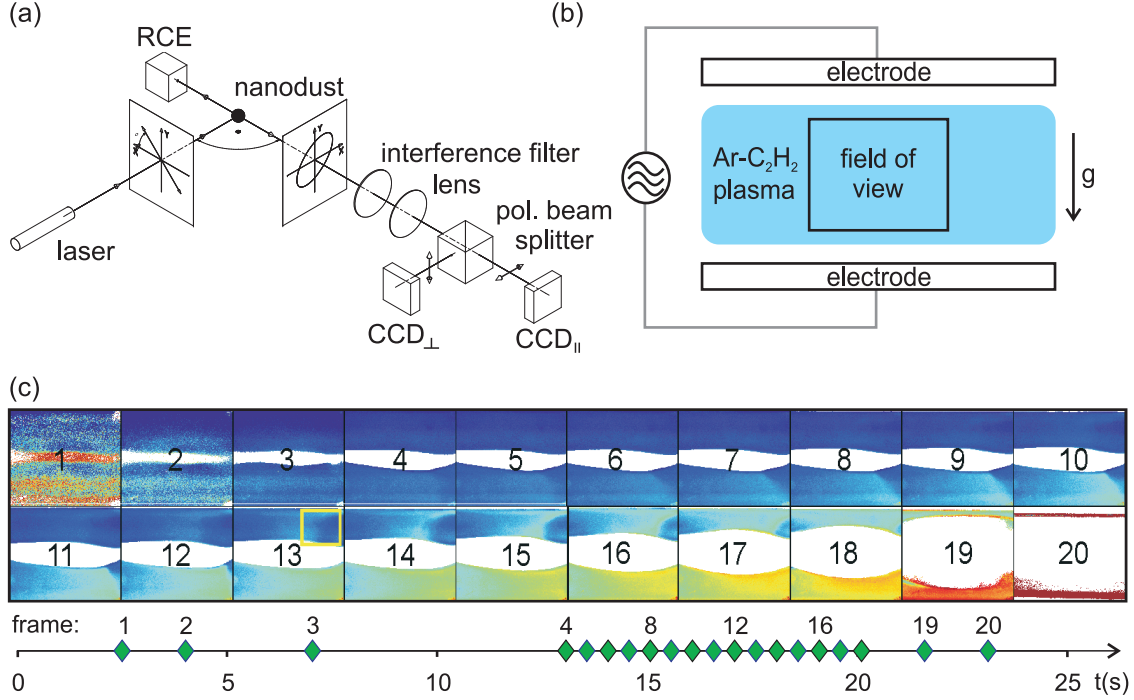


Figure 6.2: (a) Sketch of the experimental setup. A vertical laser fan polarized at 45° with respect to the scattering plane illuminates a vertical cut through a nanodust cloud. The scattered light is analyzed under $\pm 90^\circ$ by a Rotating Compensator Ellipsometer (RCE) and the Imaging Mie-Setup (I-Mie). (b) Sketch of the electrode configuration. The field of view of I-Mie is marked by the rectangular. (c) Spatial distribution of the parameter q [Eq. (6.4)] as measured by I-Mie for 20 successive frames during one growth cycle in an unmagnetized argon-acetylene discharge. The Mie theory allows to relate q to the dust size. Here, small dust particles ($r_d = 80$ nm) are blue and large dust particles ($r_d = 180$ nm) are red. The axis at the bottom denotes the time at which each frame was taken. Taken from [A.8].

[A.8], whereas a more detailed description of the applied (Imaging) Mie-Ellipsometers can be found in the diploma theses of H. Ketelsen [201] and N. Köhler [204].

The polarization state of monochromatic light can be fully described by the Stokes vector $S = (I_0, Q, U, V)$ with I_0 being the total intensity, $Q = I_{\parallel} - I_{\perp}$, $U = I_{\pi/4} - I_{-\pi/4}$, and $V = I_r - I_l$, whereas I_{\parallel} , I_{\perp} , $I_{\pi/4}$, and $I_{-\pi/4}$ are the intensities transmitted by an ideal linear polarizer at an angle of 0 , $\pi/2$, $\pi/4$, and $-\pi/4$. I_l and I_r correspond to the intensities transmitted by an ideal left- and right-handed circular polarizer [205]. The Imaging Mie setup (I-Mie) sketched in Fig. 6.2(a) allows to determine the parameter Q or the degree of linear polarization

$$P = \frac{I_{\perp} - I_{\parallel}}{I_{\perp} + I_{\parallel}} \quad (6.3)$$

as it is used in Refs. [206, 207]. A laser fan polarized at 45° with respect to the scattering plane illuminates a vertical cut through a nanodust cloud. The light scattered under an angle of 90° passes an interference filter and a lens projects an image of the illuminated cut

through the dust cloud on the sensors of two CCD cameras. A polarizing beam splitter is used to make one camera (CCD_{\parallel}) sensitive only for the light that is polarized parallel to the scattering plane and one (CCD_{\perp}) that is sensitive for the light polarized perpendicular to the scattering plane. Thus, the two cameras measure the intensities I_{\perp} and I_{\parallel} spatially resolved. Furthermore, we used a commercial Rotating Compensator Ellipsometer (RCE) to analyze the light that is scattered under an angle of -90° . The RCE, which makes use of a rotating quarter-wave plate, allows to determine the full Stokes vector of the scattered light, but it averages the scattered light about a certain ill-defined volume (poor spatial resolution) and the time resolution is limited by the mechanical rotation of the quarter-wave plate. In practice, the scattered light turns out not to be fully polarized, e.g., due to unpolarized light from the plasma glow or diffuse reflections from the laser light. The unpolarized light modifies the parameter Q as measured by I-Mie and inhibits a direct comparison to the Mie theory and a determination of the dust size. Therefore, the RCE is needed to measure the degree of polarization $DoP = I_p/I_0$, which allows to normalize the parameter Q to the intensity of the polarized light I_p

$$q = \frac{Q}{I_p} = \frac{Q}{DoP \cdot I_0}, \quad (6.4)$$

which then can be related to the Mie theory. In the following, it will be assumed that DoP is constant over the field of view of the I-Mie technique, which is justified by the measurements presented in Ref. [A.8].

In order to test the I-Mie diagnostic, we studied the growth of nanoparticles in a conventional parallel-plate rf-discharge without magnetic field [Fig. 6.2(b)]. Here, both electrodes are operated in a push-pull mode and for a discharge pressure of 30 Pa (argon) and a 15% acetylene admixture a periodic growth instability establishes with $T_{\text{growth}} \approx 30$ s. The field of view of I-Mie is 44×33 mm and is centered around the middle of the discharge. The gap between the electrodes is 40 mm. The parameter q as obtained from the I-Mie and the RCE is shown for 20 successive frames during one growth cycle in Fig. 6.2(c). There is a dust free region (void) in the middle, which is surrounded by an almost monodisperse nanodust cloud. The dust particles are continuously growing from frame 1 to frame 20. The parameter q , which is a measure of the particle size, is color-coded. Blue corresponds to a dust radius of $r_d = 80$ nm and red to $r_d = 180$ nm. The size of the void continuously increases until nearly the entire dust is removed from the discharge (frame 20), then the next growth cycle starts. The spatial resolution of I-Mie shows some features of the growth process, which remain hidden for the RCE or other ellipsometric techniques without spatial resolution [206, 208]. At the start of the growth process, the particle size is homogeneously distributed over the entire field of view (frame 1-5). Then a sedimentation of the larger particles becomes visible and the particles in the lower half of the discharge are found to be significantly larger than those in the upper half. Furthermore, growth fronts emerge in the upper right corner of frame 10-15, which might be attributed to an inhomogeneous transport of the molecules and radicals responsible for the growth of the dust particles due to an inhomogeneous inflow of the acetylene.

In comparison to an ellipsometer, which is based on a rotating compensator [209] or analyzer [208], the I-Mie setup does not measure the full Stokes vector of the scattered light and is restricted to a reduced set of parameters, e.g., Q or P . But, I-Mie has a spatial resolution that is given by the optical resolution of the used objective lens or the pixel size of the CCD cameras, and the time resolution is determined by the frame rate of the cameras and not limited by the mechanical rotation of optical components. Furthermore, the parameter q is sensitive to the particle size, i.e., it allows an estimate of the dust radius r_d , when the particles are larger than 15% of the wavelength of the scattered light. Thus, for visible laser light, I-Mie works best for particles of the order of 100 nm radius. As argued in the previous section, this is just the size where a magnetization of the nanodust might be possible.

6.2 Nanodust in magnetized plasmas

The combination of the strong magnetic fields provided by the superconducting magnet system SULEIMAN and the production of nanodust clouds by the growth of a-C:H particles in argon-acetylene plasmas might be a promising approach to produce a dusty plasma, where even the dynamics of the dust is governed by the simultaneous effects of collective motion and magnetization and can be considered as at least partially magnetized. However, the growth and confinement of nanodust in unmagnetized argon-acetylene plasmas is an established technique, but there is a lack of experimental works focusing on the production of extended nanodust clouds in the presence of strong magnetic fields. In fact, the conventional parallel plate discharge used in the previous section 6.1 turned out to be not suitable for the growth of nanodust in magnetized plasmas. Even at moderate magnetic inductions ($B = 50$ mT) the confinement of the dust is modified in a way that the dust particles are no longer confined in the plasma bulk and only small amounts of nanodust reside close the sheath edge. It is the aim of this section to show that a modification of the electrode geometry allows to confine cylindrical nanodust clouds up to magnetic inductions of at least $B = 0.5$ T, which show some interesting dynamical behaviors. The experiments presented here are a preliminary study performed in the DUSTWHEEL device, which consists of 24 water-cooled magnets and allows a maximum magnetic induction of $B = 0.5$ T in steady state. A detailed description of the experimental apparatus can be found in Ref. [210]. A transfer of these experiments to SULEIMAN and an increase of the magnetic induction by one order of magnitude is envisaged for the near future but is beyond the scope of my PhD work.

By trial and error we found an electrode configuration that allows the growth and confinement of nanodust clouds in a magnetized plasma column. A pair of hollow cylindrical electrodes operated in a push-pull mode produces a distinct plasma column as it is shown in Fig. 6.3(a). The width of the plasma column is ≈ 2 cm and the axis of the plasma column is aligned with the magnetic field and the force of gravity. Characteristic for this plasma column is a hollow density and potential profile in radial direction with steep gradients at the outer edges of the plasma column, as it is shown in the Diploma thesis of D. Gruner [211]. At low and intermediate rf-powers ($P_{\text{rf}} \approx 1 - 20$ W) and gas pressures in the range of $p = 1 - 50$ Pa

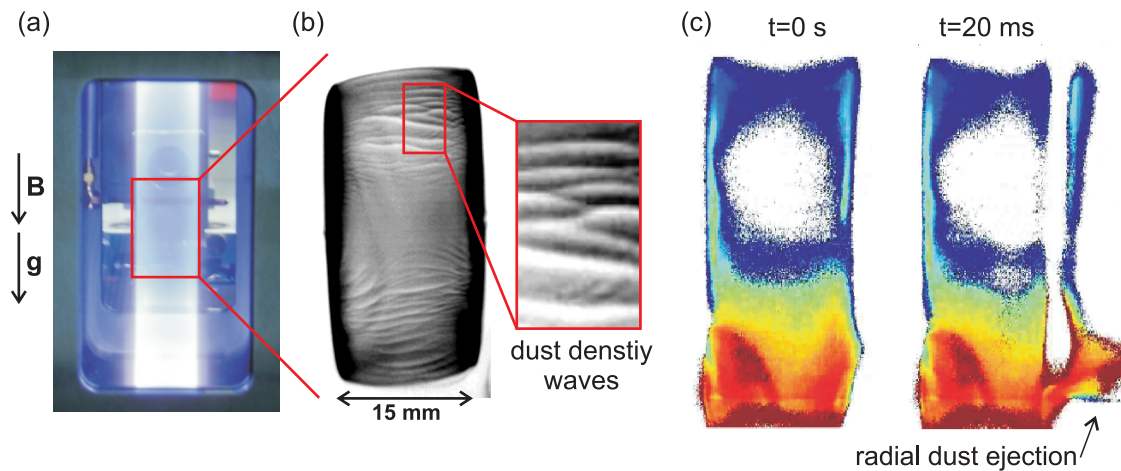


Figure 6.3: (a) Cylindrical plasma column, which is aligned parallel to the magnetic field and the force of gravity. The region, where the nanodust is confined, is marked by the red rectangular. (b) Dust density waves in a cylindrically-shaped dust cloud at $B = 0.5$ T. (c) Two successive snapshots of an unstable dust cloud, which ejects dust particles to the side, observed with I-Mie. The particle-size is color coded from blue (small) to red (large).

(argon) the admixture of acetylene results in the formation of cylindrical nanodust clouds in the center of the plasma column for magnetic inductions up to $B = 0.5$ T, which is the maximum realizable field strength provided by DUSTWHEEL. So far, the spatial distribution of the forces relevant for the confinement of the dust particles, e.g., electric field and ion drag forces, remain unclear and there are currently efforts to gain a detailed understanding of the dust confinement in this configuration [212].

Although the Hall parameter for the dust is significantly less than unity and the dust is not magnetized ($H_d \ll 1$), these dust clouds can exhibit interesting dynamical behaviors, which strongly depend on the discharge parameters and the amount of acetylene available for the growth of the dust particles. Two examples are shown in Fig. 6.3(b,c). As in the previous section 6.1, a laser fan illuminates a vertical cut through the middle of the dust cloud. In Fig. 6.3(b) a snapshot of a dust cloud with a flat density profile about the axis is shown. Dust-density waves appear in the upper and lower third of the dust cloud, which are propagating in vertical direction towards the upper and lower edge of the dust cloud, whereas the wavelength is short in comparison to the vertical expansion of the dust cloud. The merging of wave fronts, which can be clearly seen in the inset of Fig. 6.3(b), has been studied in detail for dust-density waves observed in clouds of micrometer-sized dust grains under microgravity conditions [213, 214]. This may be attributed to a spatial variation of the local plasma parameters, e.g., dust charge or dust density. Furthermore, the pure existence of the dust-density waves might be an indication for the presence of ion flows. In particular, for small ion drift velocities, the wave is expected to propagate in direction of the ion flow [215]. Moreover, dust-density waves propagating radially inwards can be seen in the left-hand side

of Fig. 6.3(b), whereas the wavelength is roughly a factor of four larger than the wavelength found for the waves propagating in the vertical direction.

In addition, we observed another type of instability, where a fraction of the dust is suddenly ejected perpendicular to the magnetic field (radial dust ejections). This instability is typically more pronounced when a positive dc bias with respect to the grounded plasma chamber is applied to the driven electrodes, e.g., $U_{\text{bias}} = 100$ V for the experiment presented here. In Fig. 6.3(c), two snapshots of such a dust cloud taken with the I-Mie technique are shown. The time interval between the two frames is 20 ms and the size of the particles is color-coded from blue (small particles) to red (large particles). Since this measurement was not calibrated with the RCE, this color-coding gives only a qualitative measure of the particle size. Obviously, there is a sedimentation of the larger particles in the lower third of the dust cloud. From frame 1 to frame 2, we see a sudden release of dust particles to the right-hand side, perpendicular to the magnetic field. This radial ejection of dust particles starts at the bottom of the dust cloud and is followed by smaller particles in the outer layer of the cloud. So far, the mechanism of this instability is unclear and an analysis of this effect is left for future works.

To conclude, a dusty plasma where even the dust component is at least partially magnetized, might be realized by the combination of nanoparticles ($r_d = 100$ nm) growing in an argon-acetylene discharge at low gas pressures ($p = 1$ Pa) and strong magnetic fields ($B = 4$ T) provided by the superconducting magnet system SULEIMAN. For the extrapolation of the dust Hall parameter H_d and the influence of pseudo-magnetization in Sec. 6, a reduction of the particle charge was omitted, when the charge density provided by the dust particles is comparable to the charge density of the electron population ($Q_d n_d \approx e n_e$) and there is a competition of the dust particles for the free electrons and ions [216, 217, 218]. This lowering of the dust charge reduces the Lorentz force exerted on the dust particles and may be a handicap for the magnetization of a nanodust cloud. However, this effect might be compensated by a further reduction of the particle size ($r_d < 100$ nm), since H_d is inverse proportional to the dust radius. Moreover, there is room to further lower the discharge pressure ($p < 1$ Pa) or to choose a lighter working gas than argon, e.g., helium, to further reduce the friction force experienced by the dust particles. In case that the natural rotation and the pseudo-magnetization of the dust cloud (Sec. 4.3) turns out to be a problem, an additional bias voltage as applied by Sato *et al.* [48] might be used to lower the rotation frequencies to a tolerable value.

Here, two important steps towards the studying of magnetized nanodust clouds have been made. First, a new electrode geometry is proposed, which has proven to confine nanodust clouds up to magnetic inductions of $B = 0.5$ T. A test of this setup at magnetic inductions of up to $B = 4$ T is envisaged for the near future. Furthermore, the I-Mie technique is a promising tool to study the dynamics of nanodust clouds in detail. As shown in this section, I-Mie allows to resolve dynamical features of these nanodust cloud, e.g., dust-density waves

and radial dust ejections in space and time and provides important parameters as the dust size and, in principle, the dust density. Moreover, the dust clouds confined in a magnetized plasma column show a complex behavior, which itself is interesting and it will be a new challenge to study phenomena like dust-density waves in the presence of strong magnetic fields.

Summary and Conclusions

The focus of this work was laid on the dynamics of dust clusters confined in the plasma sheath in the presence of ion flows, strong magnetic fields and the effects of rotational motion. Dust clusters were set into rotation either by an axial magnetic field [A.1] or mechanically by a sheared neutral gas drive excited by a rotating electrode. Especially the rotating electrode has proven to be a robust tool to study dust clusters under the influence of centrifugal [A.2], [A.3], shear [122] or Coriolis forces and to mimic giant magnetic fields [A.10]. The phase-resolved resonance method (PRRM) was introduced to detect small changes of the charge-to-mass ratio of single dust particles [A.4], [A.7] and to precisely quantify the dust-dust interaction force in two particle systems [A.5], [A.9]. In particular, strongly magnetized plasmas were studied by means of the superconducting magnet-system SULEIMAN, which is one of only a few devices world wide designed to study dusty plasmas in the presence of strong magnetic fields up to 4 T. Lastly, it was shown that Imaging Mie-Ellipsometry (I-Mie) is a promising diagnostic to study the spatiotemporal dynamics of nanodust clouds [A.8]. The key results of this work are summarized by the following statements:

Neutral gas flows at typical dusty plasma parameters are still in a laminar regime:

For typical experimental parameters, the Knudsen number of the neutral gas is of the order of 1/100, which suggests that neutral gas flows are at the transition from the hydrodynamic to the Knudsen regime [118]. Using the dust centrifuge as a well-defined neutral gas drive it could be shown that the gas flow can be still described by the Navier-Stokes-Equation assuming a no-slip boundary condition for the gas flow (hydrodynamic regime). The concept of laminar gas flows is one important prerequisite for different models describing the rotation of dust structures in the presence of magnetic fields, see Refs. [110, 111, 112] and [A.1]. Characteristic is a sheared gas flow in front of the electrodes, which provides a natural explanation, why dust clusters, which are confined closer to the electrode (heavier particles or altered plasma parameters), exhibit a slower rotation [112].

Magnetized plasmas are naturally in a rotating state:

In a laboratory plasma, sheath electric fields or ambipolar electric fields within the plasma bulk are inevitable, because of the finite size of the plasma. An additional axial magnetic field deflects the electrons and ions in the azimuthal direction due to a drift in crossed (radial) electric and (axial) magnetic fields and the plasma column rotates about the discharge axis. In addition to the azimuthal component of the ion drag force [52], the collisional momentum transfer from the rotating plasma column sets the entire neutral gas column into a globally sheared rotation, which is one source of dust cluster rotation in the presence of magnetic fields. Thus, in magnetized plasmas, rotational motion is not only a feature of the electrons and ions, but also of the neutral gas and the confined dust clusters. A global neutral gas motion gives a natural explanation for the sense of rotation of dust structures in certain experimental configuration [A.1],[111] and the magnitude of the observed rotation frequencies [145, 146, 148] compared to the classical ion drag model, which assumes a neutral gas at rest.

Controlled dust cluster rotation can be used for diagnostic purposes:

For 2d clusters confined in the plasma sheath, the horizontal dust-dust interaction force can be well described by a Yukawa potential [69, 70], whereas it is difficult to deduce the effective dust charge Q_{eff} and the screening length λ_s from the plasma parameters (see Sec. 4.2). Therefore, experimental techniques to measure these quantities are of key interest. The dust centrifuge allows to probe the dust-dust interaction by exerting centrifugal forces on the dust particles and to measure Q_{eff} and λ_s . In contrast to the (phase-resolved) resonance method [14, 93], [A.4] this technique does not require any knowledge about the local plasma parameters, which are difficult to determine. In principle, this technique is also applicable at higher gas pressures, where other common techniques like the analysis of normal modes [128, 129, 130] or dust waves [125, 126, 127] suffer from the strong damping of the dust motion due to the neutral drag force. The dust centrifuge is a new tool to systematically study dust ensembles under the influence of centrifugal [A.3], Coriolis [A.10] or shear forces [122].

Dust cluster rotation mimics the effects of giant magnetic fields:

Physical systems governed by the simultaneous effects of strong coupling and magnetization are currently of high interest. Magnetic fields are believed to have a strong effect on, e.g., diffusion properties [45], wave spectra [139, 142, 143] and extreme states of matter [137]. For strongly-coupled clusters of micrometer-sized dust particles confined in the plasma sheath, the small value of the charge-to-mass ratio of the dust particles inhibits a magnetization, even for strong magnetic fields of the order of a few Tesla. One way to overcome this limitation is to mimic the magnetization of the dust particles and to replace the Lorentz force by the Coriolis force, since both forces are mathematically equivalent (Larmor theorem [51]). In this work, a proof-of-principle of this approach was given. Here, the oscillation spectra of a rotating dust cluster clearly shows features of magnetization [136]. Thus, rotating dusty plasmas are a new approach to study the simultaneous effects of strong coupling and (pseudo)

magnetization under laboratory conditions.

The phase-resolved resonance method (PRRM) is highly sensitive for changes of the charge-to-mass ratio of single dust particles:

In this work a modification of the classical resonance method [14, 93, 94] has been proposed, which allows to determine the confinement frequency of single dust particles with better than 1‰ precision by measuring phase and amplitude of a forced oscillation. This high accuracy makes PRRM sensitive for small changes of the charge-to-mass ratio of single dust particles. Therefore, secondary order effects become visible, which we have not been aware of so far. Even in pure argon plasmas, the longtime stability of MF- and PMMA-particles suffers from outgassing, coating and sputtering processes and over a few hours of measurement time a substantial change of the particle mass was observed. Moreover, PRRM allows to monitor the effective sputtering of PMMA-particles in the plasma sheath and to extend the idea of using microparticles as plasma probes (see [106], [A.7] and references therein) to measure the structure of the plasma sheath with high spatial resolution in comparison to measurements that make use of particles with different sizes [102, 104], hyper gravity [8], or thermophoretic forces [106].

PRRM allows to quantify the decharging effect of particles in the wake of another and the strength of the interaction force:

In the plasma sheath, the negatively charged dust particles polarize the flow of ions and extended wake structures are formed downstream to the dust particles. In particular, these wake fields have a strong influence on the dust-dust interaction force parallel to the ion flow. For a generic model system of two particles, PRRM allows to quantify two important features of the ion-wake-mediated interaction force: a strong nonreciprocity and a partial decharging of the downstream particle in the wake of the other. Both effects turned out not to be independent of each other, since the decharging effect in combination with the external confinement enhances the nonreciprocity of the interaction force. This results might help to improve models [186, 187, 188, 190], which are describing the transition from a vertical to a horizontal aligned particle pair, when altering the discharge parameters. There, the decharging effect is not taken into account and at least in the vertical configuration, a lowering of the confinement frequency (particle charge) should reduce the levitation height of the downstream particle, which might affect the stability of this configuration.

Strong magnetic fields modify the structure of ion wake fields:

A magnetic field parallel to the flow of ions can alter the structure of ion wakes, because the deflection of ions in the Coulomb field of a charged dust particle can give the ions a significant lateral velocity component, which leads to a helical ion motion. Here, we have found that a modification of the ion wake results in a lowering of the ion-wake-mediated interparticle forces, when the ion cyclotron frequency becomes comparable to the ion plasma frequency ($\omega_{ci}/\omega_{pi} \approx 1$), i.e., the ions become magnetized. This result is in qualitative agreement with

linear response calculations [41, 42, 43], which predict a reduction of the wake charge for increasing magnetic inductions and which in turn lowers the electrostatic interaction force between the ion wake and a nearby dust particle. For many dusty plasmas experiments, and especially for those performed in the plasma sheath, ion wakes are known to considerably influence the structure and dynamics of dust clusters, e.g., see Refs. [23, 28, 185, 190]. Thus, the behavior of dust clusters in the presence of strong magnetic fields can significantly differ from unmagnetized plasmas.

Extended clouds of nanodust can be confined in strongly magnetized plasmas:

Nanoparticles are one promising candidate for the experimental realization of a fully magnetized plasma [39], where the dust dynamics is governed by the simultaneous effects of collective motion and magnetization. In unmagnetized plasmas, the production and growth of nanoparticles in argon-acetylene discharges is a well known process. These nanoparticles form extended clouds, which fill the entire discharge volume. However, a small magnetic field of just a few mT was found to destroy the dust confinement in a conventional parallel-plate discharge. Here, a modified electrode geometry of two hollow-cylindrical electrodes operated in a push-pull mode was proposed to solve the problem of dust confinement in a magnetized plasma. So far, this new configuration was tested for magnetic inductions up to $B = 0.5$ T. An increase of the magnetic induction by one order of magnitude, which might allow to (partially) magnetize the dust, is envisaged for the near future.

I-Mie allows to measure size and density of nanodust particles with high spatiotemporal resolution:

In contrast to micrometer-sized dust particles, standard video microscopy does not allow to resolve individual particles in nanodust clouds. Therefore, new diagnostics for the dust density and size are required. Furthermore, a high temporal and spatial resolution is desirable, since the time scales of the motion of nanoparticles is much shorter and an inhomogeneous plasma may lead to a spatial distribution of the dust size. To meet those requirements we have build up an Imaging-Mie-Ellipsometer (I-Mie) based on two high-speed video cameras to measure the polarization ratio of the scattered light with spatial resolution. This technique has proven to resolve different types of instabilities of nanodust clouds, e.g., dust-density waves, in space and time and allows a reliable measurement of the particle size for dust particles larger than 15% of the wavelength of the scattered light. Thus, I-Mie provides key parameters for the studying of the dynamics of nanodust clouds.

References

- [1] V.E. FORTOV, A.V. IVLEV, S.A. KHRAPAK, A.G. KHRAPAK, AND G.E. MORFILL. *Complex (dusty) plasmas: Current status, open issues, perspectives*. Phys. Rep., **421**,1, (2005). 1, 5, 8, 26
- [2] G. E. MORFILL AND A. V. IVLEV. *Complex plasmas: An interdisciplinary research field*. Rev. Mod. Phys., **81**,1353, (2009). 1, 2, 5
- [3] M. BONITZ, N.J.M. HORING, AND P. LUDWIG. *Introduction to complex plasmas*. Springer series on atomic, optical, and plasma physics. Springer Berlin Heidelberg, (2010). 1, 5
- [4] A. PIEL. *Plasma Physics: An Introduction to Laboratory, Space, and Fusion Plasmas*. Springer Berlin Heidelberg, (2010). 1, 2, 5, 6
- [5] C. K. GOERTZ. *Dusty plasmas in the solar system*. Rev. Geophys., **27**,271, (1989). 1
- [6] P. J. ARMITAGE. *Dynamics of Protoplanetary Disks*. Annu. Rev. Astron. Astrophys., **49**,195, (2011). 1
- [7] J WINTER. *Dust in fusion devices a multi-faceted problem connecting high- and low-temperature plasma physics*. Plasma Phys. Control. Fusion, **46**,B583, (2004). 1
- [8] J. BECKERS, T. OCKENGA, M. WOLTER, W. W. STOFFELS, J. VAN DIJK, H. KERSTEN, AND G. M. W. KROESEN. *Microparticles in a Collisional Rf Plasma Sheath under Hypergravity Conditions as Probes for the Electric Field Strength and the Particle Charge*. Phys. Rev. Lett., **106**,115002, (2011). 1, 5, 20, 21, 23, 69
- [9] H.R. MAURER, V. SCHNEIDER, M. WOLTER, R. BASNER, T. TROTTEBERG, AND H. KERSTEN. *Microparticles as Plasma Diagnostic Tools*. Contrib. Plasma Phys., **51**,218, (2011). 1
- [10] R. C. CHITTICK, J. H. ALEXANDER, AND H. F. STERLING. *The Preparation and Properties of Amorphous Silicon*. J. Electrochem. Soc., **116**,77, (1969). 1
- [11] P. R. CABARROCAS, Y. DJERIDANE, T. NGUYEN-TRAN, E. V. JOHNSON, A. ABRAMOV, AND Q. ZHANG. *Low temperature plasma synthesis of silicon nanocrystals: a strategy for high deposition rate and efficient polymorphous and microcrystalline solar cells*. Plasma Physics and Controlled Fusion, **50**,124037, (2008). 1
- [12] J. H. CHU AND I. LIN. *Direct observation of Coulomb crystals and liquids in strongly coupled rf dusty plasmas*. Phys. Rev. Lett., **72**,4009, (1994). 1, 11
- [13] Y. HAYASHI AND K. TACHIBANA. *Observation of Coulomb-Crystal Formation from Carbon Particles Grown in a Methane Plasma*. Jpn. J. Appl. Phys., **33**,L804, (1994). 1, 11

- [14] A. MELZER, T. TROTTENBERG, AND A. PIEL. *Experimental determination of the charge on dust particles forming Coulomb lattices*. Phys. Lett. A, **191**,301, (1994). 1, 11, 13, 14, 15, 16, 31, 68, 69
- [15] H. THOMAS, G. E. MORFILL, V. DEMMEL, J. GOREE, B. FEUERBACHER, AND D. MÖHLMANN. *Plasma Crystal: Coulomb Crystallization in a Dusty Plasma*. Phys. Rev. Lett., **73**,652, (1994). 1, 11
- [16] H. LÖWEN. *Twenty years of confined colloids: from confinement-induced freezing to giant breathing*. J. Phys.: Condens. Matter, **21**,474203, (2009). 1
- [17] C. C. GRIMES AND G. ADAMS. *Evidence for a Liquid-to-Crystal Phase Transition in a Classical, Two-Dimensional Sheet of Electrons*. Phys. Rev. Lett., **42**,795, (1979). 1
- [18] D. J. WINELAND, J. C. BERGQUIST, WAYNE M. ITANO, J. J. BOLLINGER, AND C. H. MANNEY. *Atomic-Ion Coulomb Clusters in an Ion Trap*. Phys. Rev. Lett., **59**,2935, (1987). 1
- [19] F. DIEDRICH, E. PEIK, J. M. CHEN, W. QUINT, AND H. WALTHER. *Observation of a Phase Transition of Stored Laser-Cooled Ions*. Phys. Rev. Lett., **59**,2931, (1987). 1
- [20] M. DREWSSEN, C. BRODERSEN, L. HORNEKÆR, J. S. HANGST, AND J. P. SCHIFFFER. *Large Ion Crystals in a Linear Paul Trap*. Phys. Rev. Lett., **81**,2878, (1998). 1
- [21] S. M. REIMANN AND M. MATTL. *Electronic structure of quantum dots*. Rev. Mod. Phys., **74**,1283, (2002). 1
- [22] V. E. FORTOV. *Extreme states of matter on Earth and in space*. Phys. Uspekhi, **52**,615, (2009). 1
- [23] V. A. SCHWEIGERT, I. V. SCHWEIGERT, A. MELZER, A. HOMANN, AND A. PIEL. *Alignment and instability of dust crystals in plasmas*. Phys. Rev. E, **54**,4155, (1996). 2, 44, 45, 46, 56, 70
- [24] K. TAKAHASHI, T. OISHI, K. SHIMOMAI, Y. HAYASHI, AND S. NISHINO. *Analyses of attractive forces between particles in Coulomb crystal of dusty plasmas by optical manipulations*. Phys. Rev. E, **58**,7805, (1998). 2, 44, 45, 56
- [25] A. MELZER, V. A. SCHWEIGERT, AND A. PIEL. *Transition from Attractive to Repulsive Forces between Dust Molecules in a Plasma Sheath*. Phys. Rev. Lett., **83**,3194, (1999). 2, 44, 45, 46, 47, 49, 51, 56
- [26] M. NAMBU, S. V. VLADIMIROV, AND P. K. SHUKLA. *Attractive forces between charged particulates in plasmas*. Phys. Lett. A, **203**,40, (1995). 2, 45
- [27] A. V. IVLEV, M. H. THOMA, C. RÄTH, G. JOYCE, AND G. E. MORFILL. *Complex Plasmas in External Fields: The Role of Non-Hamiltonian Interactions*. Phys. Rev. Lett., **106**,155001, (2011). 2, 46, 56
- [28] R. KOMPANEETS, S. V. VLADIMIROV, A. V. IVLEV, V. TSYTOVICH, AND G. MORFILL. *Dust clusters with non-Hamiltonian particle dynamics*. Phys. Plasmas, **13**,072104, (2006). 2, 46, 56, 70
- [29] L. COUËDEL, V. NOSENKO, A. V. IVLEV, S. K. ZHDANOV, H. M. THOMAS, AND G. E. MORFILL. *Direct Observation of Mode-Coupling Instability in Two-Dimensional Plasma Crystals*. Phys. Rev. Lett., **104**,195001, (2010). 2, 46, 56
- [30] L. GIOVANNI. *Nature of the force field in plasma wakes*. Phys. Rev. E, **66**,026409, (2002). 2, 45

- [31] A. PIEL. *Alignment of dust particles by ion drag forces in subsonic flows*. Phys. Plasmas, **18**,073704, (2011). 2, 45
- [32] F. MELANDSØ AND J. GOREE. *Polarized supersonic plasma flow simulation for charged bodies such as dust particles and spacecraft*. Phys. Rev. E, **52**,5312, (1995). 2, 45
- [33] S. V. VLADIMIROV AND O. ISHIHARA. *On plasma crystal formation*. Phys. Plasmas, **3**,444, (1996). 2, 45
- [34] M. LAMPE, G. JOYCE, AND G. GANGULI. *Structure and dynamics of dust in streaming plasma: dust molecules, strings, and Crystals*. IEEE Trans. Plasma Sci., **33**,57, (2005). 2, 45
- [35] I. H. HUTCHINSON. *Forces on a Small Grain in the Nonlinear Plasma Wake of Another*. Phys. Rev. Lett., **107**,095001, (2011). 2, 45
- [36] S. V. VLADIMIROV, S. A. MAIOROV, AND N. F. CRAMER. *Kinetics of plasma flowing around two stationary dust grains*. Phys. Rev. E, **67**,016407, (2003). 2
- [37] W. J. MILOCH. *Wake effects and Mach cones behind objects*. Plasma Phys. Control. Fusion, **52**,124004, (2010). 2
- [38] V. R. IKKURTHI, K. MATYASH, A. MELZER, AND R. SCHNEIDER. *Computation of charge and ion drag force on multiple static spherical dust grains immersed in rf discharges*. Phys. Plasmas, **17**,103712, (2010). 2
- [39] E. THOMAS, R. L. MERLINO, AND M. ROSENBERG. *Magnetized dusty plasmas: the next frontier for complex plasma research*. Plasma Phys. Control. Fusion, **54**,124034, (2012). 2, 34, 38, 52, 57, 70
- [40] V. N. TSYTOVICH, N. SATO, AND G. E. MORFILL. *Note on the charging and spinning of dust particles in complex plasmas in a strong magnetic field*. New J. Phys., **5**,43, (2003). 2
- [41] M. NAMBU, M. SALIMULLAH, AND R. BINGHAM. *Effect of a magnetic field on the wake potential in a dusty plasma with streaming ions*. Phys. Rev. E, **63**,056403, (2001). 2, 12, 38, 52, 56, 70
- [42] M. SALIMULLAH, P. K. SHUKLA, M. NAMBU, H. NITTA, O. ISHIHARA, AND A. M. RIZWAN. *Modification of the shielding and wake potentials in a streaming dusty magnetoplasma*. Phys. Plasmas, **10**,3047, (2003). 2, 12, 38, 52, 53, 56, 70
- [43] S. BHATTACHARJEE AND N. DAS. *Effect of wake potential on Coulomb crystallization in the presence of magnetic field*. Phys. Plasmas, **19**,103707, (2012). 2, 12, 38, 52, 56, 70
- [44] L. PATACCHINI AND I. H. HUTCHINSON. *Spherical conducting probes in finite Debye length plasmas and $E \times B$ fields*. Plasma Phys. Control. Fusion, **53**,025005, (2011). 2, 5, 38, 52, 55
- [45] T. OTT AND M. BONITZ. *Diffusion in a Strongly Coupled Magnetized Plasma*. Phys. Rev. Lett., **107**,135003, (2011). 2, 34, 68
- [46] N. D'ANGELO. *Low-frequency electrostatic waves in dusty plasmas*. Planet. Space Sci., **38**,1143, (1990). 2
- [47] M. ROSENBERG. *A note on the electrostatic dust cyclotron instability in a collisional plasma with warm dust*. Phys. Scripta, **82**,035505, (2010). 2, 34
- [48] N. SATO, G. UCHIDA, T. KANEKO, S. SHIMIZU, AND S. IIZUKA. *Dynamics of fine particles in magnetized plasmas*. Phys. Plasmas, **8**,1786, (2001). 2, 12, 38, 43, 52, 58, 64

- [49] M.M. VASILEV, L.G. DYACHKOV, S.N. ANTIPOV, O.F. PETROV, AND V.E. FORTOV. *Dusty plasma structures in magnetic fields in a dc discharge*. JETP Letters, **86**,358, (2007). 2, 38, 43
- [50] M. SCHWABE, U. KONOPKA, P. BANDYOPADHYAY, AND G. E. MORFILL. *Pattern Formation in a Complex Plasma in High Magnetic Fields*. Phys. Rev. Lett., **106**,215004, (2011). 2, 38, 52, 54
- [51] J. LARMOR. *LXIII. On the theory of the magnetic influence on spectra; and on the radiation from moving ions*. Phil. Mag. S. 5, **44**,503, (1897). 3, 25, 26, 32, 68
- [52] U. KONOPKA, D. SAMSONOV, A. V. IVLEV, J. GOREE, V. STEINBERG, AND G. E. MORFILL. *Rigid and differential plasma crystal rotation induced by magnetic fields*. Phys. Rev. E, **61**,1890, (2000). 3, 37, 38, 68
- [53] P. K. SHUKLA AND A. A. MAMUN. *Introduction to Dusty Plasma Physics*. Plasma Phys. Control. Fusion, **44**,395, (2002). 5
- [54] M.A. LIEBERMAN AND A.J. LICHTENBERG. *Principles of Plasma Discharges and Materials Processing*. Wiley, (2005). 5
- [55] H. M. MOTT-SMITH AND IRVING LANGMUIR. *The Theory of Collectors in Gaseous Discharges*. Phys. Rev., **28**,727, (1926). 5
- [56] M. S. BARNES, J. H. KELLER, J. C. FORSTER, A. ONEILL, J, AND D. K. COULTAS. *Transport of dust particles in glow-discharge plasmas*. Phys. Rev. Lett., **68**,313, (1992). 5, 9, 10
- [57] E. C. WHIPPLE. *Potentials of surfaces in space*. Rep. Prog. Phys., **44**,1197, (1981). 5, 7, 20, 30
- [58] E. B. TOMME, D. A. LAW, B. M. ANNARATONE, AND J. E. ALLEN. *Parabolic Plasma Sheath Potentials and their Implications for the Charge on Levitated Dust Particles*. Phys. Rev. Lett., **85**,2518, (2000). 5, 11, 13, 14, 21, 23, 30, 31
- [59] A. DOUGLASS, V. LAND, L. MATTHEWS, AND T. HYDE. *Dust particle charge in plasma with ion flow and electron depletion near plasma boundaries*. Phys. Plasmas, **18**,083706, (2011). 5, 15, 20, 21, 22, 23, 25, 30, 31
- [60] VICTOR LAND, LORIN S. MATTHEWS, TRUELL W. HYDE, AND DIANA BOLSER. *Fluid modeling of void closure in microgravity noble gas complex plasmas*. Phys. Rev. E, **81**,056402, (2010). 6, 21
- [61] J. PAVLŮ, I. RICHTEROV, J. SAFRNKOV, AND Z. NEMECEK. *Impact of surface properties on the dust grain charging*. Adv. Space Res., **38**,2558, (2006). Middle and Upper Atmospheres, Active Experiments, and Dusty Plasmas. 6
- [62] F. X. BRONOLD, H. FEHSKE, H. KERSTEN, AND H. DEUTSCH. *Surface States and the Charge of a Dust Particle in a Plasma*. Phys. Rev. Lett., **101**,175002, (2008). 6
- [63] P. S. EPSTEIN. *On the Resistance Experienced by Spheres in their Motion through Gases*. Phys. Rev., **23**,710, (1924). 7
- [64] BIN LIU, J. GOREE, V. NOSENKO, AND L. BOUFENDI. *Radiation pressure and gas drag forces on a melamine-formaldehyde microsphere in a dusty plasma*. Phys. Plasmas, **10**,9, (2003). 7, 18, 19
- [65] Y. NAKAMURA AND O. ISHIHARA. *A complex plasma device of large surface area*. Rev. Sci. Instrum., **79**,033504, (2008). 7, 18, 19

- [66] H. CHU, M. SI, AND S. LIN. *Drag coefficient of the weakly ionized plasma in the high Knudsen number regime*. Phys. Plasmas, **16**,063704, (2009). 7, 18, 19
- [67] W. E. AMATUCCI, D. N. WALKER, G. GATLING, AND E. E. SCIME. *Direct observation of microparticle gyromotion in a magnetized direct current glow discharge dusty plasma*. Phys. Plasmas, **11**,2097, (2004). 7, 18, 19
- [68] E. THOMAS AND J. WILLIAMS. *Experimental Measurements of Velocity Dissipation and Neutral-Drag Effects during the Formation of a Dusty Plasma*. Phys. Rev. Lett., **95**,055001, (2005). 7, 18, 19
- [69] M. LAMPE, G. JOYCE, G. GANGULI, AND V. GAVRISHCHAKA. *Interactions between dust grains in a dusty plasma*. Phys. Plasmas, **7**,3851, (2000). 8, 25, 30, 31, 68
- [70] U. KONOPKA, G. E. MORFILL, AND L. RATKE. *Measurement of the Interaction Potential of Microspheres in the Sheath of a rf Discharge*. Phys. Rev. Lett., **84**,891, (2000). 8, 25, 31, 43, 68
- [71] S. KHRAPAK, D. SAMSONOV, G. MORFILL, H. THOMAS, V. YAROSHENKO, H. ROTHERMEL, T. HAGL, V. FORTOV, A. NEFEDOV, V. MOLOTKOV, O. PETROV, A. LIPAEV, A. IVANOV, AND Y. BATURIN. *Compressional waves in complex (dusty) plasmas under microgravity conditions*. Phys. Plasmas, **10**,1, (2003). 8, 26
- [72] T. NITTER. *Levitation of dust in rf and dc glow discharges*. Plasma Sources Sci. Technol., **5**,93, (1996). 8, 26
- [73] J. E. DAUGHERTY, R. K. PORTEOUS, M. D. KILGORE, AND D. B. GRAVES. *Sheath structure around particles in low-pressure discharges*. J. Appl. Phys., **72**,3934, (1992). 8, 31
- [74] A. PIEL AND A. MELZER. *Dynamical processes in complex plasmas*. Plasma Phys. Control. Fusion, **44**,R1, (2002). 9, 26, 31
- [75] R. KOMPANEETS, U. KONOPKA, A. V. IVLEV, V. TSYTOVICH, AND G. MORFILL. *Potential around a charged dust particle in a collisional sheath*. Phys. Plasmas, **14**,052108, (2007). 9, 26, 31
- [76] T. E. SHERIDAN. *Effect of radio frequency discharge power on dusty plasma parameters*. J. Appl. Phys., **106**,033303, (2009). 9, 26, 31
- [77] I. H. HUTCHINSON. *Collisionless ion drag force on a spherical grain*. Plasma Phys. Control. Fusion, **48**,185, (2006). 9, 10, 45
- [78] M. D. KILGORE, J. E. DAUGHERTY, R. K. PORTEOUS, AND D. B. GRAVES. *Ion drag on an isolated particulate in a low-pressure discharge*. J. Appl. Phys., **73**,7195, (1993). 9
- [79] S. A. KHRAPAK, A. V. IVLEV, G. E. MORFILL, AND H. M. THOMAS. *Ion drag force in complex plasmas*. Phys. Rev. E, **66**,046414, (2002). 9, 10
- [80] I. H. HUTCHINSON. *Ion collection by a sphere in a flowing plasma: 3. Floating potential and drag force*. Plasma Phys. Control. Fusion, **47**,71, (2005). 9, 10
- [81] C. ZAFIU, A. MELZER, AND A. PIEL. *Ion drag and thermophoretic forces acting on free falling charged particles in an rf-driven complex plasma*. Phys. Plasmas, **9**,4794, (2002). 9
- [82] C. ZAFIU, A. MELZER, AND A. PIEL. *Measurement of the ion drag force on falling dust particles and its relation to the void formation in complex (dusty) plasmas*. Phys. Plasmas, **10**,1278, (2003). 9, 10

- [83] V. SCHNEIDER, T. TROTTEBERG, I. TELIBAN, AND H. KERSTEN. *An experiment for the investigation of forces on microparticles in ion beams*. Rev. Sci. Instrum., **81**,013503, (2010). 9
- [84] K. KÖHLER, J. W. COBURN, D. E. HORNE, E. KAY, AND J. H. KELLER. *Plasma potentials of 13.56-MHz rf argon glow discharges in a planar system*. J. Appl. Phys., **57**,59, (1985). 11
- [85] S. ICHIMARU. *Strongly coupled plasmas: high-density classical plasmas and degenerate electron liquids*. Rev. Mod. Phys., **54**,1017, (1982). 11
- [86] O. ARP, D. BLOCK, A. PIEL, AND A. MELZER. *Dust Coulomb Balls: Three-Dimensional Plasma Crystals*. Phys. Rev. Lett., **93**,165004, (2004). 11
- [87] A.I. BYKOV, M.I. DOLOTENKO, N.P. KOLOKOLCHIKOV, V.D. SELEMIR, AND O.M. TATSENKO. *VNIIEF achievements on ultra-high magnetic fields generation*. Phys. B: Condens. Matter, **294295**,574, (2001). 12
- [88] R. C. DUNCAN AND C. THOMPSON. *Formation of very strongly magnetized neutron-stars - implications for gamma ray bursts*. Astrophys. J., **392**,L9, (1992). 12
- [89] L. PATACCHINI AND I. H. HUTCHINSON. *Forces on a spherical conducting particle in E B fields*. Plasma Phys. Control. Fusion, **53**,065023, (2011). 12
- [90] R. A. MILLIKAN. *The Isolation of an Ion, a Precision Measurement of its Charge, and the Correction of Stokes's Law*. Phys. Rev. (Series I), **32**,349, (1911). 13
- [91] J. PAVLŮ, A. VELYHAN, I. RICHTEROVÁ, Z. NĚMEČEK, J. ŠAFRÁNKOVÁ, I. ČERMÁK, AND P. ŽILAVÝ. *Mass-loss rate for MF resin microspheres*. IEEE Trans. Plasma Sci., **32**,704, (2004). 13, 16, 17
- [92] C. CHUNSHI AND J. GOREE. *Fluctuations of the charge on a dust grain in a plasma*. IEEE Trans. Plasma Sci., **22**,151, (1994). 13
- [93] T. TROTTEBERG, A. MELZER, AND A. PIEL. *Measurement of the electric charge on particulates forming Coulomb crystals in the sheath of a radiofrequency plasma*. Plasma Sources Sci. Technol., **4**,450, (1995). 13, 14, 15, 16, 31, 68, 69
- [94] A. HOMANN, A. MELZER, AND A. PIEL. *Measuring the charge on single particles by laser-excited resonances in plasma crystals*. Phys. Rev. E, **59**,R3835, (1999). 13, 14, 16, 69
- [95] S. K. SHARMA, R. KALITA, Y. NAKAMURA, AND H. BAILUNG. *Dust charge measurement in a strongly coupled dusty plasma produced by an rf discharge*. Plasma Sources Sci. Technol., **21**,045002, (2012). 14
- [96] W. PRESS, S. TEUKOLSKY, W. VETTERLING, AND B. FLANNERY. *Numerical Recipes in C*. Cambridge University Press, Cambridge, UK, 2nd edition, (1992). 16, 47
- [97] WWW.MICROPARTICLES.DE. *microParticles GmbH*. 16, 22
- [98] H. R. MAURER, R. BASNER, AND H. KERSTEN. *Temperature of particulates in low-pressure rf-plasmas in Ar, Ar/H2 and Ar/N2 mixtures*. Contrib. Plasma Phys., **50**,954, (2010). 17, 20
- [99] H. GRUNER. *Messung der Druckabhängigkeit des Gasreibungskoeffizienten von Edelgasen in staubigen Plasmen*. Bachelor thesis, (2011). 19
- [100] N. CLAIRE, G. BACHET, U. STROTH, AND F. DOVEIL. *Laser-induced-fluorescence observation of ion velocity distribution functions in a plasma sheath*. Phys. Plasmas, **13**,062103, (2006). 20

- [101] G. H. P. M. SWINKELS, H. KERSTEN, H. DEUTSCH, AND G. M. W. KROESEN. *Microcalorimetry of dust particles in a radio-frequency plasma*. J. Appl. Phys., **88**,1747, (2000). 20
- [102] C. ZAFIU, A. MELZER, AND A. PIEL. *Nonlinear resonances of particles in a dusty plasma sheath*. Phys. Rev. E, **63**,066403, (2001). 20, 69
- [103] B. M. ANNARATONE, T. ANTONOVA, H. M. THOMAS, AND G. E. MORFILL. *Diagnostics of the Electronegative Plasma Sheath at Low Pressures Using Microparticles*. Phys. Rev. Lett., **93**,185001, (2004). 20, 23
- [104] A. A. SAMARIAN AND B. W. JAMES. *Dust as fine electrostatic probes for plasma diagnostic*. Plasma Phys. Control. Fusion, **47**,B629, (2005). 20, 23, 69
- [105] G. THIEME, R. BASNER, R. WIESE, AND H. KERSTEN. *Microparticles in plasmas as diagnostic tools and substrates*. Faraday Discuss., **137**,157, (2008). 20, 23
- [106] V. LAND, B. SMITH, L. MATTHEWS, AND T. HYDE. *Probing the Sheath Electric Field With a Crystal Lattice by Using Thermophoresis in Dusty Plasma*. IEEE Trans. Plasma Sci., **38**,768, (2010). 20, 23, 69
- [107] V. LAND, J. CARMONA-REYES, J. CREEL, J. SCHMOKE, M. COOK, L. MATTHEWS, AND T. HYDE. *The effect of electrode heating on the discharge parameters in complex plasma experiments*. Plasma Sources Sci. Technol., **20**,015026, (2011). 20, 23
- [108] M. ZEUNER, J. MEICHSNER, AND H. U. POLL. *Oxidative decomposition of polymethylmethacrylate (PMMA) in plasma etching*. Plasma Sources Sci. Technol., **4**,406, (1995). 22
- [109] R. BASNER, F. SIGENEGER, D. LOFFHAGEN, G. SCHUBERT, H. FEHSKE, AND H. KERSTEN. *Particles as probes for complex plasmas in front of biased surfaces*. New J. Phys., **11**,013041, (2009). 23
- [110] A. V. NEDOSPASOV. *Motion of plasma-dust structures and gas in a magnetic field*. Phys. Rev. E, **79**,036401, (2009). 25, 26, 43, 44, 67
- [111] M. M. VASILIEV, L. G. D'YACHKOV, S. N. ANTIPOV, R. HUIJINK, O. F. PETROV, AND V. E. FORTOV. *Dynamics of dust structures in a dc discharge under action of axial magnetic field*. EPL (Europhysics Letters), **93**,15001, (2011). 25, 26, 43, 44, 67, 68
- [112] A.F. PAL, A.N. RYABINKIN, A.O. SEROV, N.A. DYATKO, A.N. STAROSTIN, AND A.V. FILIPPOV. *Orbital motion of dust particles in an rf magnetron discharge. Ion drag force or neutral atom wind force*. J. Exp. Theo. Phys., **114**,535, (2012). 25, 26, 37, 44, 67
- [113] K. W. MADISON, F. CHEVY, W. WOHLLEBEN, AND J. DALIBARD. *Vortex Formation in a Stirred Bose-Einstein Condensate*. Phys. Rev. Lett., **84**,806, (2000). 26, 32
- [114] J. R. ABO-SHAER, C. RAMAN, J. M. VOGELS, AND W. KETTERLE. *Observation of Vortex Lattices in Bose-Einstein Condensates*. Science, **292**,476, (2001). 26, 32
- [115] P. ROSENBUSCH, D. S. PETROV, S. SINHA, F. CHEVY, V. BRETIN, Y. CASTIN, G. SHLYAPNIKOV, AND J. DALIBARD. *Critical Rotation of a Harmonically Trapped Bose Gas*. Phys. Rev. Lett., **88**,250403, (2002). 26, 32
- [116] A. L. FETTER. *Rotating trapped Bose-Einstein condensates*. Rev. Mod. Phys., **81**,647, (2009). 26, 32
- [117] B.A. YOUNGLOVE AND H.J.M. HANLEY. *The Viscosity and Thermal Conductivity Coefficients of Gaseous and Liquid Argon*. J. Phys. Chem. Ref. Data, **15**,1323, (1986). 26

- [118] S.A. SCHAAF AND P.L. CHAMBRÃO. *Flow of Rarefied Gases*. Princeton aeronautical paperbacks, no. 8. Princeton University Press, (1961). 27, 67
- [119] J.D. JACKSON AND K. MÜLLER. *Klassische Elektrodynamik*. Gruyter, Walter de GmbH, (2002). 28
- [120] J. CARSTENSEN. *Experimente in magnetisierten staubigen Plasmen*. Diploma thesis, (2008). 28, 38, 39
- [121] M. KROLL. *Strukturanalyse staubiger Plasmen mittels digitaler Holographie*. PhD thesis, (2010). 28
- [122] A. MELZER, A. SCHELLA, T. MIKSCH, J. SCHABLINSKI, D. BLOCK, A. PIEL, H. THOMSEN, H. KHLERT, AND M. BONITZ. *Phase Transitions of Finite Dust Clusters in Dusty Plasmas*. *Contrib. Plasma Phys.*, **52**,795, (2012). 28, 67, 68
- [123] L. S. FROST. *Effect of Variable Ionic Mobility on Ambipolar Diffusion*. *Phys. Rev.*, **105**,354, (1957). 30, 40
- [124] M. KLINDWORTH, O. ARP, AND A. PIEL. *Langmuir probe diagnostics in the IMPF device and comparison with simulations and tracer particle experiments*. *J. Appl. Phys. D*, **39**,1095, (2006). 30
- [125] A. HOMANN, A. MELZER, S. PETERS, AND A. PIEL. *Determination of the dust screening length by laser-excited lattice waves*. *Phys. Rev. E*, **56**,7138, (1997). 31, 68
- [126] S. NUNOMURA, D. SAMSONOV, AND J. GOREE. *Transverse Waves in a Two-Dimensional Screened-Coulomb Crystal (Dusty Plasma)*. *Phys. Rev. Lett.*, **84**,5141, (2000). 31, 68
- [127] S. NUNOMURA, J. GOREE, S. HU, X. WANG, AND A. BHATTACHARJEE. *Dispersion relations of longitudinal and transverse waves in two-dimensional screened Coulomb crystals*. *Phys. Rev. E*, **65**,066402, (2002). 31, 68
- [128] A. MELZER. *Mode spectra of thermally excited two-dimensional dust Coulomb clusters*. *Phys. Rev. E*, **67**,016411, (2003). 31, 68
- [129] T. E. SHERIDAN. *Center-of-mass and breathing oscillations in small complex plasma disks*. *Phys. Rev. E*, **72**,026405, (2005). 31, 68
- [130] T. E. SHERIDAN, M. R. KATSCHKE, AND K. D. WELLS. *Measurement of electric field and gradient in the plasma sheath using clusters of floating microspheres*. *Rev. Sci. Instrum.*, **78**,023502, (2007). 31, 68
- [131] U. KONOPKA, L. RATKE, AND H. M. THOMAS. *Central Collisions of Charged Dust Particles in a Plasma*. *Phys. Rev. Lett.*, **79**,1269, (1997). 31
- [132] G. A. HEBNER, M. E. RILEY, D. S. JOHNSON, PAULINE HO, AND R. J. BUSS. *Direct Determination of Particle-Particle Interactions in a 2D Plasma Dust Crystal*. *Phys. Rev. Lett.*, **87**,235001, (2001). 31
- [133] Y. NAKAMURA AND O. ISHIHARA. *Measurements of electric charge and screening length of microparticles in a plasma sheath*. *Phys. Plasmas*, **16**,043704, (2009). 31
- [134] H. KÄHLERT AND M. BONITZ. private communication, (2011). 32

- [135] M. BONITZ, H. KÄHLERT, T. OTT, AND H. LWEN. *Magnetized strongly coupled plasmas and how to realize them in a dusty plasma setup*. Plasma Sources Sci. Technol., **22**,015007, (2013). 32
- [136] M. KONG, W.P. FERREIRA, B. PARTOENS, AND F.M. PEETERS. *Magnetic field dependence of the normal mode spectrum of a planar complex plasma cluster*. IEEE Trans. Plasma Sci., **32**,569, (2004). 33, 34, 68
- [137] A. Y. POTEKHIN. *The physics of neutron stars*. Phys. Uspekhi, **53**,1235, (2010). 34, 68
- [138] F. ANDEREGG, D. H. E. DUBIN, T. M. O'NEIL, AND C. F. DRISCOLL. *Measurement of Correlation-Enhanced Collision Rates*. Phys. Rev. Lett., **102**,185001, (2009). 34
- [139] G. UCHIDA, U. KONOPKA, AND G. MORFILL. *Wave Dispersion Relation of Two-Dimensional Plasma Crystals in a Magnetic Field*. Phys. Rev. Lett., **93**,155002, (2004). 34, 68
- [140] K. JIANG, L. HOU, X. XU, AND Y. WANG. *Waves and wakes excited by a moving disturbance in a 2D magnetized dusty plasma*. New J. Phys., **9**,57, (2007). 34
- [141] M. BONITZ, Z. DONKÓ, T. OTT, H. KÄHLERT, AND P. HARTMANN. *Nonlinear Magnetoplasmons in Strongly Coupled Yukawa Plasmas*. Phys. Rev. Lett., **105**,055002, (2010). 34
- [142] T. OTT, M. BONITZ, P. HARTMANN, AND Z. DONKÓ. *Higher harmonics of the magnetoplasmon in strongly coupled Coulomb and Yukawa systems*. Phys. Rev. E, **83**,046403, (2011). 34, 68
- [143] H. KÄHLERT, T. OTT, A. REYNOLDS, G. J. KALMAN, AND M. BONITZ. *Obliquely propagating waves in the magnetized strongly coupled one-component plasma*. Phys. Plasmas, **20**,057301, (2013). 34, 68
- [144] W. T. JUAN, J. W. HSU, Z. H. HUANG, Y. J. LAI, AND L. I. *Structures and motions of strongly coupled quasi-2D dust coulomb clusters in plasmas: From small N to large N*. Chin. J. Phys., **37**,184, (1999). 37, 38, 39
- [145] F. CHEUNG, A. SAMARIAN, AND B. JAMES. *Rotation of Coulomb Clusters in Magnetised Dusty Plasma*. Phys. Scripta, **2002**,143, (2002). 37, 38, 68
- [146] K. MATYASH, M. FRÖHLICH, H. KERSTEN, G. THIEME, R. SCHNEIDER, M. HANNEMANN, AND R. HIPPLER. *Rotating dust ring in an RF discharge coupled with a dc-magnetron sputter source. Experiment and simulation*. J. Appl. Phys. D, **37**,2703, (2004). 37, 38, 68
- [147] E.S. DZLIEVA, V.YU. KARASEV, AND A.I. IKHVALD. *The effect of a longitudinal magnetic field on the plasma-dust structures in strata in a glow discharge*. Opt. Spectrosc., **98**,569, (2005). 37, 38
- [148] F. CHEUNG, A. SAMARIAN, AND B. JAMES. *The rotation of planar-2 to planar-12 dust clusters in an axial magnetic field*. New J. Phys., **5**,75, (2003). 37, 38, 68
- [149] L. PATACCINI AND I. H. HUTCHINSON. *Ion-collecting sphere in a stationary, weakly magnetized plasma with finite shielding length*. Plasma Phys. Control. Fusion, **49**,1719, (2007). 38, 52
- [150] S. NUNOMURA, N. OHNO, AND S. TAKAMURA. *Effects of Ion Flow by ExB Drift on Dust Particle Behavior in Magnetized Cylindrical Electron Cyclotron Resonance Plasmas*. Jap. J. App. Phys., **36**,877, (1997). 38
- [151] P. K. KAW, K. NISHIKAWA, AND N. SATO. *Rotation in collisional strongly coupled dusty plasmas in a magnetic field*. Phys. Plasmas, **9**,387, (2002). 38

- [152] L. HOU, Y. WANG, AND Z. L. MIŠKOVIĆ. *Formation and rotation of two-dimensional Coulomb crystals in magnetized complex plasma*. Phys. Plasmas, **12**,042104, (2005). 39
- [153] MATLAB. *version 8.0.0.783 (R2012b)*. The MathWorks Inc., Natick, Massachusetts, (2012b). 42
- [154] V. YU KARASEV, E. S. DZLIEVA, A. YU. IVANOV, AND A. I. EIKHVALD. *Rotational motion of dusty structures in glow discharge in longitudinal magnetic field*. Phys. Rev. E, **74**,066403, (2006). 43
- [155] E. S. DZLIEVA, A. YU. IVANOV, V. YU. KARASEV, AND A.I. ?KHVALD. *On the possibility of phase transitions in dusty plasma structures in a glow discharge under the action of a magnetic field*. Opt. Spectrosc., **101**,816, (2006). 43
- [156] T. UMEDA, T. KIMURA, K. TOGANO, K. FUKAZAWA, Y. MATSUMOTO, T. MIYOSHI, N. TERADA, T. K. M. NAKAMURA, AND T. OGINO. *Vlasov simulation of the interaction between the solar wind and a dielectric body*. Phys. Plasmas, **18**,012908, (2011). 44
- [157] V. V. YAROSHENKO, W. J. MILOCH, S. VLADIMIROV, H. M. THOMAS, AND G. E. MORFILL. *Modeling of Cassini's charging at Saturn orbit insertion flyby*. J. Geophys. Res., **116**,A12218, (2011). 44
- [158] J. WANG, P. LEUNG, H. GARRETT, AND G. MURPHY. *Multibody-Plasma Interactions - Charging in the Wake*. J. Spacecr. Rockets, **31**,889, (1994). 44, 56
- [159] L. PATACCHINI AND I. H. HUTCHINSON. *Kinetic solution to the Mach probe problem in transversely flowing strongly magnetized plasmas*. Phys. Rev. E, **80**, (2009). 45
- [160] T. TAJIMA AND J. M. DAWSON. *Laser Electron Accelerator*. Phys. Rev. Lett., **43**,267, (1979). 45
- [161] E. ESAREY, C. B. SCHROEDER, AND W. P. LEEMANS. *Physics of laser-driven plasma-based electron accelerators*. Rev. Mod. Phys., **81**,1229, (2009). 45
- [162] P. CHEN, J. M. DAWSON, R. W. HUFF, AND T. KATSOULEAS. *Acceleration of Electrons by the Interaction of a Bunched Electron Beam with a Plasma*. Phys. Rev. Lett., **54**,693, (1985). 45
- [163] I. BLUMENFELD, C. E. CLAYTON, F. DECKER, M. J. HOGAN, C. HUANG, R. ISCHEBECK, R. IVERSON, C. JOSHI, T. KATSOULEAS, N. KIRBY, W. LU, K. A. MARSH, W. B. MORI, P. MUGGLI, E. OZ, R. H. SIEMANN, D. WALZ, AND M. ZHOU. *Energy doubling of 42[thinsp]GeV electrons in a metre-scale plasma wakefield accelerator*. Nature, **445**,741, (2007). 45
- [164] O. ARP, J. GOREE, AND A. PIEL. *Particle chains in a dilute dusty plasma with subsonic ion flow*. Phys. Rev. E, **85**,046409, (2012). 45
- [165] I. H. HUTCHINSON. *Electron velocity distribution instability in magnetized plasma wakes and artificial electron mass*. J. Geophys. Res., **117**, (2012). 45, 56
- [166] I. H. HUTCHINSON. *Nonlinear collisionless plasma wakes of small particles*. Phys. Plasmas, **18**,032111, (2011). 45
- [167] V. R. IKKURTHI, K. MATYASH, A. MELZER, AND R. SCHNEIDER. *Computation of dust charge and potential on a static spherical dust grain immersed in rf discharges*. Phys. Plasmas, **15**,123704, (2008). 45

- [168] W. J. MILOCH, H. L. PÉCSELI, AND J. TRULSEN. *Numerical simulations of the charging of dust particles by contact with hot plasmas*. *Nonlin. Processes Geophys.*, **14**,575, (2007). 45
- [169] J. E. HAMMERBERG, D. S. LEMONS, M. S. MURILLO, AND D. WINSKE. *Molecular dynamics simulations of plasma crystal formation including wake effects*. *IEEE Trans. Plasma Sci.*, **29**,247, (2001). 45
- [170] P. LUDWIG, W. J. MILOCH, H. KAEHLERT, AND M. BONITZ. *On the wake structure in streaming complex plasmas*. *New J. Phys.*, **14**,053016, (2012). 45
- [171] I. V. SCHWEIGERT, V. A. SCHWEIGERT, AND F. M. PEETERS. *Perturbation of collisional plasma flow around a charged dust particle: Kinetic analysis*. *Phys. Plasmas*, **12**,113501, (2005). 46
- [172] W. J. MILOCH, M. KROLL, AND D. BLOCK. *Charging and dynamics of a dust grain in the wake of another grain in flowing plasmas*. *Phys. Plasmas*, **17**,103703, (2010). 46, 49, 50, 55
- [173] I. H. HUTCHINSON. *Intergrain forces in low-Mach-number plasma wakes*. *Phys. Rev. E*, **85**,066409, (2012). 46
- [174] L. HOU, Y. WANG, AND Z. L. MIŠKOVIĆ. *Induced potential of a dust particle in a collisional radio-frequency sheath*. *Phys. Rev. E*, **68**,016410, (2003). 46
- [175] A. MELZER, V. A. SCHWEIGERT, I. V. SCHWEIGERT, A. HOMANN, S. PETERS, AND A. PIEL. *Structure and stability of the plasma crystal*. *Phys. Rev. E*, **54**,R46, (1996). 46
- [176] A. V. IVLEV, U. KONOPKA, G. MORFILL, AND G. JOYCE. *Melting of monolayer plasma crystals*. *Phys. Rev. E*, **68**,026405, (2003). 46
- [177] A. MELZER, B. BUTTENSCHN, T. MIKSCH, M. PASSVOGEL, D. BLOCK, O. ARP, AND A. PIEL. *Finite dust clusters in dusty plasmas*. *Plasma Phys. Control. Fusion*, **52**,124028, (2010). 46
- [178] C. M. TICOS, P. W. SMITH, AND P. K. SHUKLA. *Experimental wake-induced oscillations of dust particles in a rf plasma*. *Phys. Lett. A*, **319**,504, (2003). 46
- [179] J. D. WILLIAMS AND E. THOMAS. *Measurement of the kinetic dust temperature of a weakly coupled dusty plasma*. *Phys. Plasmas*, **14**,063702, (2007). 46
- [180] R. KOMPANEETS, A. V. IVLEV, V. TSYTOVICH, AND G. MORFILL. *Dust-lattice waves: Role of charge variations and anisotropy of dust-dust interaction*. *Phys. Plasmas*, **12**,062107, (2005). 46
- [181] L. COUEDEL, V. NOSENKO, S. K. ZHDANOV, A. V. IVLEV, H. M. THOMAS, AND G. E. MORFILL. *First Direct Measurement of Optical Phonons in 2D Plasma Crystals*. *Phys. Rev. Lett.*, **103**,215001, (2009). 46
- [182] S. K. ZHDANOV, A. V. IVLEV, AND G. E. MORFILL. *Mode-coupling instability of two-dimensional plasma crystals*. *Phys. Plasmas*, **16**,083706, (2009). 46
- [183] B. LIU, J. GOREE, V. E. FORTOV, A. M. LIPAIEV, V. I. MOLOTKOV, O. F. PETROV, G. E. MORFILL, H. M. THOMAS, AND A. V. IVLEV. *Dusty plasma diagnostics methods for charge, electron temperature, and ion density*. *Phys. Plasmas*, **17**,053701, (2010). 46
- [184] L. COUEDEL, S. K. ZHDANOV, A. V. IVLEV, V. NOSENKO, H. M. THOMAS, AND G. E. MORFILL. *Wave mode coupling due to plasma wakes in two-dimensional plasma crystals: In-depth view*. *Phys. Plasmas*, **18**,083707, (2011). 46

- [185] T. B. RÖCKER, A. V. IVLEV, R. KOMPANEETS, AND G. E. MORFILL. *Mode coupling in two-dimensional plasma crystals: Role of the wake model*. Phys. Plasmas, **19**,033708, (2012). 46, 70
- [186] S. V. VLADIMIROV AND A. A. SAMARIAN. *Stability of particle arrangements in a complex plasma*. Phys. Rev. E, **65**,046416, (2002). 46, 51, 69
- [187] J. D. E. STOKES, S. V. VLADIMIROV, AND A. A. SAMARIAN. *Critical exponents for structural transitions in a complex plasma*. Phys. Lett. A, **371**,145, (2007). 46, 51, 69
- [188] J. D. E. STOKES, A. A. SAMARIAN, AND S. V. VLADIMIROV. *Dynamics of two particles in a plasma sheath*. Phys. Rev. E, **78**,036402, (2008). 46, 51, 69
- [189] A. A. SAMARIAN, S. V. VLADIMIROV, AND B. W. JAMES. *Dust particle alignments and confinement in a radio frequency sheath*. Phys. Plasmas, **12**,022103, (2005). 46
- [190] V. STEINBERG, R. SÜTTERLIN, A. V. IVLEV, AND G. MORFILL. *Vertical Pairing of Identical Particles Suspended in the Plasma Sheath*. Phys. Rev. Lett., **86**,4540, (2001). 46, 47, 51, 69, 70
- [191] M. KROLL, J. SCHABLINSKI, D. BLOCK, AND A. PIEL. *On the influence of wakefields on three-dimensional particle arrangements*. Phys. Plasmas, **17**,013702, (2010). 46
- [192] N. J. PRIOR, L. W. MITCHELL, AND A. A. SAMARIAN. *Determination of charge on vertically aligned particles in a complex plasma using laser excitations*. J. Appl. Phys. D, **36**,1249, (2003). 47, 51
- [193] G. A. HEBNER AND M. E. RILEY. *Structure of the ion wakefield in dusty plasmas*. Phys. Rev. E, **69**,026405, (2004). 47, 51
- [194] J. KONG, T.W. HYDE, B. HARRIS, K. QIAO, AND J. CARMONA-REYES. *Measurement of the Vertical Nonuniformity of the Plasma Sheath in a Complex Plasma*. IEEE Trans. Plasma Sci., **37**,1620, (2009). 47, 49
- [195] W. J. MILOCH AND D. BLOCK. *Dust grain charging in a wake of other grains*. Phys. Plasmas, **19**,123703, (2012). 50
- [196] G. A. HEBNER AND M. E. RILEY. *Measurement of attractive interactions produced by the ion wakefield in dusty plasmas using a constrained collision geometry*. Phys. Rev. E, **68**,046401, (2003). 51
- [197] J. HALEKAS, V. ANGELOPOULOS, D. SIBECK, K. KHURANA, C. RUSSELL, G. DELORY, W. FARRELL, J. MCFADDEN, J. BONNELL, D. LARSON, R. ERGUN, F. PLASCHKE, AND K. GLASSMEIER. *First Results from ARTEMIS, a New Two-Spacecraft Lunar Mission: Counter-Streaming Plasma Populations in the Lunar Wake*. Space Sci. Rev., **165**,93, (2011). 10.1007/s11214-010-9738-8. 56
- [198] Y. WATANABE. *Formation and behaviour of nano/micro-particles in low pressure plasmas*. J. Phys. D: Appl. Phys., **39**,R329, (2006). 59
- [199] J. BERNDT, E. KOVACEVIC, I. STEFANOVIC, O. STEPANOVIC, S. H. HONG, L. BOUFENDI, AND J. WINTER. *Some Aspects of Reactive Complex Plasmas*. Contrib. Plasma Phys., **49**,107, (2009). 59
- [200] G. MIE. *Beiträge zur Optik trüber Medien, speziell kolloidaler Metallösungen*. Ann. Phys., **330**,377, (1908). 59

- [201] H. KETELSEN. *Mie-Ellipsometrie an staubigen Plasmen*. Diploma thesis, (2009). 59, 60
- [202] H. TOMPKINS AND E. A. HABER. *Handbook of Ellipsometry (Materials Science and Process Technology)*. William Andrew, (2006). 59
- [203] M. SHIRATANI, H. KAWASAKI, T. FUKUZAWA, AND Y. WATANABE. *In situ polarization-sensitive laser-light-scattering method for simultaneous measurements of two-dimensional spatial size and density distributions of particles in plasmas*. Dusty plasmas—'95 workshop on generation, transport, and removal of particles in plasmas, **14**,603, (1996). 59
- [204] N. KÖHLER. *Bildgebende Mie-Ellipsometrie an staubigen Plasmen*. Diploma thesis, (2013). 60
- [205] C. F. BOHREN AND D. R. HUFFMAN. *Absorption and Scattering of Light by Small Particles*. Wiley-VCH, (1998). 60
- [206] C. HOLLENSTEIN, J. L. DORIER, J. DUTTA, L. SANSONNENS, AND A. A. HOWLING. *Diagnostics of particle genesis and growth in RF silane plasmas by ion mass spectrometry and light scattering*. Plasma Sources Sci. Technol., **3**,278, (1994). 60, 61
- [207] G. PRABURAM AND J. GOREE. *A scattering ratio method for sizing particulates in a plasma*. Plasma Sources Sci. Technol., **5**,84, (1996). 60
- [208] Y. HAYASHI AND K. TACHIBANA. *Coulomb crystal formation from growing particles in a plasma and the analysis*. Dusty plasmas—'95 workshop on generation, transport, and removal of particles in plasmas, **14**,506, (1996). 61, 62
- [209] G. GEBAUER AND J. WINTER. *In situ nanoparticle diagnostics by multi-wavelength Rayleigh-Mie scattering ellipsometry*. New J. Phys., **5**,38, (2003). 62
- [210] S. KNIST, F. GREINER, F. BISS, AND A. PIEL. *Influence of Negative Ions on Drift Waves in a Low-Density Ar/O₂-Plasma*. Contrib. Plasma Phys., **51**,769, (2011). 62
- [211] D. GRUNER. *Sondendiagnostik in magnetisierten Plasmen*. Diploma thesis, (2012). 62
- [212] F. GREINER, J. CARSTENSEN, N. KÖHLER, I. PILCH, AND A. PIEL. *Trapping of nanodust clouds in a magnetized plasma*. AIP Conference Proceedings, **1521**,265, (2013). 63
- [213] K. O. MENZEL, O. ARP, AND A. PIEL. *Frequency clusters and defect structures in nonlinear dust-density waves under microgravity conditions*. Phys. Rev. E, **83**,016402, (2011). 63
- [214] K. O. MENZEL, O. ARP, AND A. PIEL. *Spatial Frequency Clustering in Nonlinear Dust-Density Waves*. Phys. Rev. Lett., **104**,235002, (2010). 63
- [215] A. PIEL, M. KLINDWORTH, O. ARP, A. MELZER, AND M. WOLTER. *Obliquely Propagating Dust-Density Plasma Waves in the Presence of an Ion Beam*. Phys. Rev. Lett., **97**,205009, (2006). 63
- [216] O. HAVNES, C. K. GOERTZ, G. E. MORFILL, E. GRN, AND W. IP. *Dust charges, cloud potential, and instabilities in a dust cloud embedded in a plasma*. J. Geophys. Res., **92**,2281, (1987). 64
- [217] O. HAVNES, T. K. AANESEN, AND F. MELANDS. *On dust charges and plasma potentials in a dusty plasma with dust size distribution*. J. Geophys. Res., **95**,6581, (1990). 64
- [218] I. GOERTZ, F. GREINER, AND A. PIEL. *Effects of charge depletion in dusty plasmas*. Phys. Plasmas, **18**,013703, (2011). 64

Appendix A

Reprints of peer-reviewed articles

A.1

EFFECT OF NEUTRAL GAS MOTION ON THE ROTATION OF DUST CLUSTERS IN AN AXIAL MAGNETIC FIELD

Jan Carstensen, Franko Greiner, Lu-Jing Hou, Horst Maurer, and
Alexander Piel

Reprinted with permission from
Jan Carstensen, Franko Greiner, Lu-Jing Hou, Horst Maurer, and
Alexander Piel,
Physics of Plasmas, Vol. 16, 013702 (2009).
Copyright 2009, American Institute of Physics

Effect of neutral gas motion on the rotation of dust clusters in an axial magnetic field

Jan Carstensen,^{a)} Franko Greiner, Lu-Jing Hou, Horst Maurer, and Alexander Piel
IEAP, Christian-Albrechts-Universität, D-24098 Kiel, Germany

(Received 28 July 2008; accepted 10 December 2008; published online 20 January 2009)

Experiments are carried out to investigate the rotation of dust clusters in a radio-frequency plasma sheath with a vertical magnetic field. Our observations are in disagreement with the standard model, in which it was assumed that the neutral gas is at rest and that a steady rotation is attained when the ion-drag force is balanced by neutral friction. Here, we re-examine this basic assumption by carefully designed experiments. Our results suggest that the neutral gas is set into rotation by $E \times B$ induced ion flow through ion-neutral collisions and that the dust particles are advected by this flow. A hydrodynamic model is proposed to describe the rotation of the neutral gas and it can explain our observations. © 2009 American Institute of Physics. [DOI: 10.1063/1.3063059]

I. INTRODUCTION

In the presence of a vertical magnetic field, two-dimensional (2D) dust clusters suspended in the sheath of a radio frequency (rf) discharge were found to perform a slow rotation about the vertical axis.^{1–4} In most experiments, the sense of rotation was found to agree with the azimuthal component of the ion motion that results from a radial electric field that confines the cluster in combination with the perpendicular, axial magnetic field.^{1–4} In general, a similar behavior was found in multilayer systems,^{5,6} but the rotational velocity was characterized by a vertical shear with increasing angular velocity in the upper layers. Most authors assume that the ion motion exerts an ion drag force on the dust particles, which sets the cluster into rotation.^{2–6} The effect of an ion $E \times B$ drift on a dust cloud had been experimentally demonstrated in Ref. 7, where a dust stream along the magnetic field was deflected in the $E \times B$ direction. In the regime of weak magnetic fields ($B < 0.05$ T, typically) the monolayer clusters are found to rotate as rigid bodies and the angular frequency generally increases with the magnetic field.^{2,3,5,6} At high magnetic fields, a radial velocity shear is found in monolayer clusters.⁴

Simple models for cluster rotation were discussed in Refs. 3, 4, and 8. The common feature of these models is the balance of the azimuthal component of the ion drag force with the neutral drag force, which dust particles experience when they move with respect to a neutral gas at rest. The same basic concept was used in simulations of dust transport in magnetized radio-frequency (rf) discharges under microgravity.⁹ A detailed simulation of the electric field distribution in a weakly magnetized rf-discharge combined with the force balance from ion drag and friction in a neutral gas at rest was described in Refs. 10 and 11. It was found that 2D clusters performed a rigid rotation and that the angular frequency increased linearly with the strength of the magnetic field. Only in one paper¹ it was conjectured that the dust

cluster may be embedded in a rotating neutral gas which is set into motion by the azimuthal component of the ion motion. Other recent observations that may be related to cluster rotation are the spurious dust rotation in a magnetron device,¹² the formation of vortex patterns,¹³ and a kind of dust gyromotion.¹⁴

Apart from experiments with flat clusters in rf discharges, there are observations of dust cloud rotation in narrow magnetized gas discharge tubes (see Refs. 15–17, and references therein). Particles trapped in a striation were found to perform a rotational motion and the angular velocity was found to change sign when the electrons become magnetized. In Ref. 15 it was concluded that the reversal of the angular velocity is a hint that the driving force for the rotation of the dust clouds is the ion wind force rather than neutral gas rotation. The reversal of the angular velocity for increasing magnetic field was recently attributed to the reversal of the radial ion velocity, which is outward at low and inward at high magnetic field.¹⁶ A similar reversal of angular motion was found in recent independent experiments.¹⁷ Successful measurements by laser induced fluorescence of simultaneous vortex flows of neutral atoms along and against the $E \times B$ direction were very recently reported.¹⁸

Therefore the role of neutral gas motion in magnetized plasmas and its competition with direct ion-drag force on dust particles is still an open issue. It is the very purpose of the present paper to re-examine the assumption of a static neutral gas background and to obtain more hints from carefully designed experiments about the effect of the neutral gas flow on the rotation of the dust cluster, while self-consistent theories and simulations are lacking.

The paper is organized as follows: In Sec. II the experimental setup and experiments with different boundary conditions are described. In Sec. III, discharge simulations with different refinements are presented. Cluster rotation by gas flows is studied in Sec. IV experimentally and with a hydrodynamic model. The results are discussed in Sec. V.

^{a)}Electronic mail: carstensen@physik.uni-kiel.de.

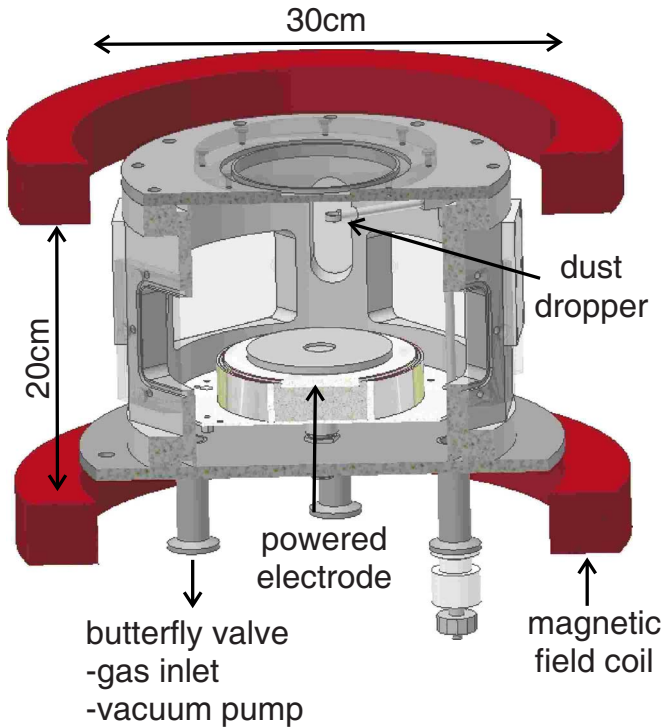


FIG. 1. (Color online) Sketch of the experimental arrangement. An argon plasma is established between the driven lower electrode and the chamber wall. The vacuum chamber has four large side windows and a large circular top window. Two magnetic field coils provide a homogenous magnetic field at the position of the dust cloud.

II. EXPERIMENT

A. Experimental setup

The experiments presented here are carried out in a 13.56 MHz capacitively coupled parallel plate rf discharge. Figure 1 shows the experimental setup. The lower powered electrode has a diameter of 10 cm and is radially terminated by a grounded Faraday shield, which is separated by a gap filled with PTFE dielectric. The chamber wall acts as grounded electrode. For dust confinement, a cylindrical cavity of 20 mm diameter and 2 mm depth is milled into the center of the lower electrode. The vacuum chamber has an inner diameter of 220 mm and a height of 170 mm. The vacuum pump and the gas inlet are connected to a common port at the bottom of the chamber. The pump and gas handling system are decoupled from the plasma chamber by a ring-shaped cover plate that encircles the powered electrode and has an equidistant pattern of holes. In this way the gas flow through the plasma volume is minimized. During the observation of cluster motion, the entire pump and gas handling can be completely separated by closing a butterfly valve.

To investigate dusty plasma under the influence of a weak magnetic field, a set of two coils of 30 cm diameter and a distance of 20 cm is mounted around the chamber, providing a homogeneous magnetic field of up to 15 mT at the electrode. The experiments are performed in argon and the discharge parameters are $p=15$ Pa, $U_{rf}=200$ V_{pp} and $n_i=5.8 \times 10^{14}$ m⁻³. The weak magnetic field has a negligible influence on the plasma parameters. The particles used in

these experiments are monodisperse melamine formaldehyde spheres with a diameter of 12.07 ± 0.21 μm. The charge $Q \approx 9000 e$ of the particles was obtained by the resonance method.¹⁹ The dust clusters are illuminated by a horizontally expanded laser fan with 16 mW@650 nm and are observed with two CCD cameras from the top and from the side. The dust clusters float at typical heights of $z=5-10$ mm above the lower electrode, depending on the discharge conditions.

B. Experimental results

1. The confining electric field

Langmuir-probe measurements yield an electron Debye length $\lambda_{De} \approx 0.3$ mm near the sheath edge, which is comparable to the typical interparticle distance d of a two-particle cluster. Because of the supersonic ion flow in the sheath, we neglect the ion contribution to shielding. Simulations (see Fig. 5 below) show that the confining potential $\phi_c(r)$ is approximately parabolic for small r . The interaction force between the two particles in the horizontal plane can be approximated by a shielded Coulomb potential²¹

$$\phi_{int}(r_{ij}) = \frac{Q}{4\pi\epsilon_0 r_{ij}} \exp\left(-\frac{r_{ij}}{\lambda_{De}}\right). \quad (1)$$

Hence we can estimate the radial confining electric field at the equilibrium position of the two particles $E_r(d/2)$ from the force balance with the repulsive force

$$E_r\left(\frac{d}{2}\right) = \frac{Q}{4\pi\epsilon_0 d} \left(\frac{1}{d} + \frac{1}{\lambda_{De}}\right) \exp\left(-\frac{d}{\lambda_{De}}\right). \quad (2)$$

Then, the confining electric field increases linearly with the radial position r and becomes

$$E_r(r) = E_r\left(\frac{d}{2}\right) \frac{2r}{d} \approx 5.3 \times 10^5 \text{ V m}^{-2} r. \quad (3)$$

The vertical component of the electric field at the levitation height of the cluster can be estimated from an equilibrium with the particle weight force, $E_z=(mg)/Q \approx 9000$ V m⁻¹ for a particle mass of $m=1.37 \times 10^{-12}$ kg.

2. Observation of cluster rotation

In the basic configuration of the experiment shown in Fig. 2(a), we investigate small 2D clusters comprised of three radial shells. Figure 2(b) shows a long-exposure photo (3 s) of a rotating cluster with 21 particles at 3 mT magnetic induction. The dependence of the rotation frequency on the magnetic induction is given in Fig. 2(c). A critical magnetic field of 1 mT is needed to set the cluster into rotation. The rotation frequency then increases with the magnetic induction but saturates at about 3 mT and tends to decrease for higher magnetic field. Earlier simulations of this situation had resulted in a linear dependence of the rotation frequency on the magnetic field.¹⁰

The observed sense of cluster rotation is against the expected local $E \times B$ direction. In the configuration (a), the magnetic field vector points downward and the confining electric field E_r points radially outwards, resulting in a counterclockwise rotation (when seen from above), whereas the

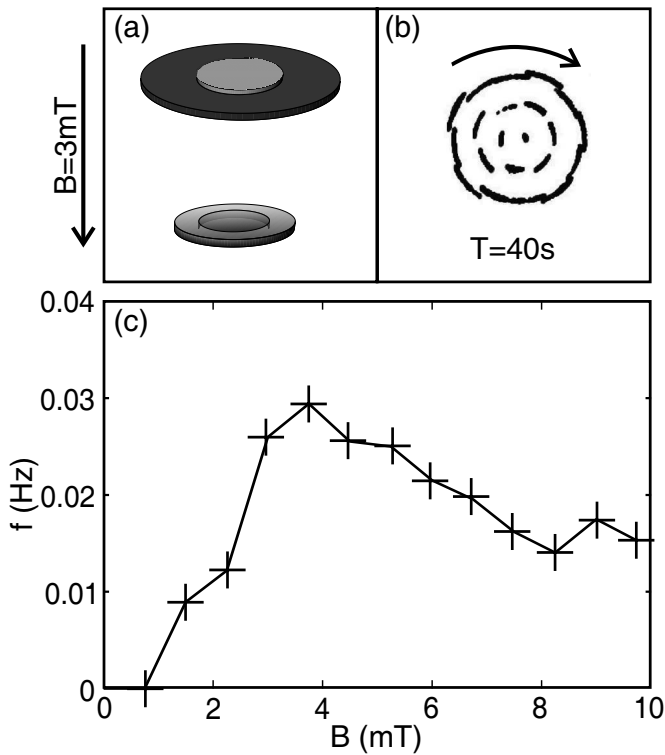


FIG. 2. (a) Setup with a top glass window 100 mm diameter. (b) Corresponding dust cluster rotation with a long exposure of 3 s ($B=3$ mT). The arrow gives the sense of rotation. (c) Dependence of the cluster rotation frequency on the magnetic induction.

observed motion is clockwise. This is in conflict with the assumption that the rotation is caused by the local ion-drag force that results from the azimuthal component of the ion flow. Both findings, the opposite sense of rotation and the nonmonotonic dependence of the rotation rate on the magnetic field strength, suggest that there is a competition of forces at work.

3. Influence of neutral gas flow

The observations described above give rise to the assumption, that an azimuthal component of the ion flow outside of the region that contains the dust cluster may lead to a global rotation of the neutral gas column, which in turn sets the cluster into rotation. A reversed radial electric field can be expected at the periphery of the driven electrode. To test this hypothesis we have, in a second step, modified our experimental setup by placing a cylindrical glass tube of 7.5 cm diameter and 5 cm height on the driven electrode [Fig. 3(a)]. Further, we have blocked the external gas rotation by a mesh grid on top of the glass tube. With the method described in Sec. IV A we have checked experimentally that the grid interrupts any neutral gas motion from penetrating into the glass tube. In this way, neutral gas rotation in the exterior region should be decoupled from the volume containing the cluster. A long-time exposure photo of a three-shell cluster is shown in Fig. 3(b).

Figure 3(b) shows that the cluster rotation is now counterclockwise and becomes very slow ($T=107$ s). The dependence of the rotation frequency on the magnetic induction is

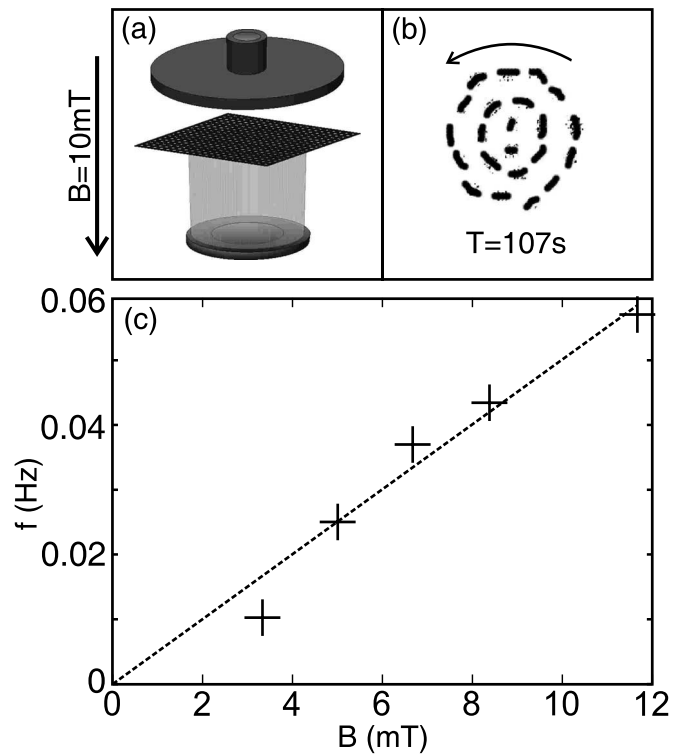


FIG. 3. Sketch of modified experimental setups. (a) A glass tube covered with a grid is placed on the driven electrode. (b) Long-time exposure photo of the rotating clusters at standard plasma density and $B=10$ mT. (c) Dependence of the rotation frequency of the cluster as a function of magnetic induction at an enhanced discharge voltage $U_{rf}=300$ V_{pp}.

shown in Fig. 3(c) and is linearly increasing as expected from simulations.¹⁰ These findings support our hypothesis that the observations in the original discharge geometry are a superposition of nonlocal ion forces, which set the entire neutral gas into rotation. This superposition of ion flows with opposite azimuthal components leads to a sense of cluster rotation against the locally expected $E \times B$ rotation at the position of the cluster.

III. COMPARISON WITH SIMULATION

A. Global discharge simulation with SIGLO

In order to give a general illustration of the distribution of plasma density and electric field in the geometry of our discharge and at typical discharge conditions, we have used the commercially available SIGLO-2D code.²⁰ This code, however, does not include a magnetic field and therefore may be only representative for the case of low magnetic field. The spatial resolution is restricted to 50×50 grid points in the $r-z$ section shown in Fig. 4. In these simulations, the powered electrode with its central depression is shown in dark grey. The electrode is radially terminated by a Faraday shield. The gap is filled with a dielectric medium. The remaining walls are grounded. The dense contour lines of the time-averaged electric potential in Fig. 4(a) show that strong electric fields only occur near the powered electrode. The radial electric field inside the central depression of the electrode is positive, whereas it becomes negative at the outer edge of the electrode and near the Faraday shield.

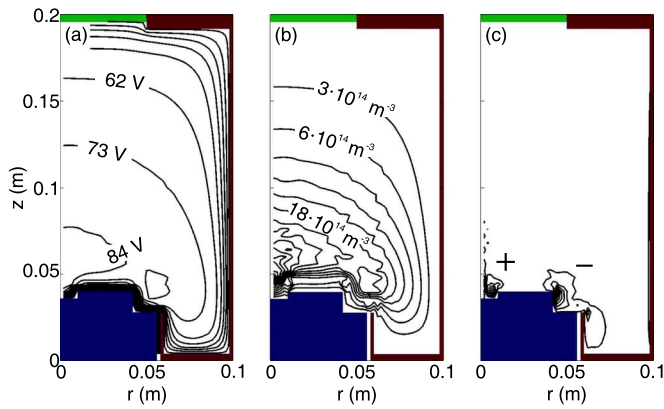


FIG. 4. (Color online) Simulation of (a) potential contours and (b) plasma density distribution with the SIGLO code. The profile of the powered electrode is shaded grey. High positive radial electric fields are found in the central depression, where the cluster is confined. High negative radial electric fields are found at the outer edge of the powered electrode and outside the Faraday shield. (c) Calculated product of radial electric field and ion density. The plus and minus signs indicate the opposite directions of the resulting ion fluxes.

In combination with a weak axial magnetic field, the ions generally follow a drift motion in the direction of the electric field, but with an additional small deflection into the $E \times B$ direction. Therefore, the local azimuthal motion of the ions will be counterclockwise in the central depression and clockwise at the outer rim. By means of ion-neutral collisions, the neutral gas can be set into slow rotation.

The ion density attains its highest values in front of the powered electrode, as shown in Fig. 4(b), and decreases in the z and r -direction. The azimuthal component of the ion flux is determined by the product of the radial electric field and the ion density, which is shown in Fig. 4(c). This product takes high positive values only at the inner edge of the central depression and high negative values at the outer edge of the powered electrode and at the outer side of the Faraday shield.

Comparing the volumes filled by these azimuthal ion streams, which are proportional to the radius of the respective edges, and noting that the ion density has only a weak radial variation, the outer region could have a stronger effect on neutral gas rotation than the inner region. Qualitatively, this finding supports our experimental observations that the superposition of the two sources could lead to the wrong sense of rotation and that confining the system to the central volume produces the expected local sense of rotation.

The finite resolution of the SIGLO code, unfortunately, is too poor to allow making quantitative predictions of the effect. This is why we have used a different simulation code to study the ion flow in the central region in more detail.

B. High-resolution simulation near the central depression

In order to understand dust rotation in the geometry of Fig. 3(b) in more detail, we have performed computer simulations with the simulation code described in Ref. 10. The formation and rotation of 2D dust clusters are studied in a self-consistent manner, based on a dynamical model for rf

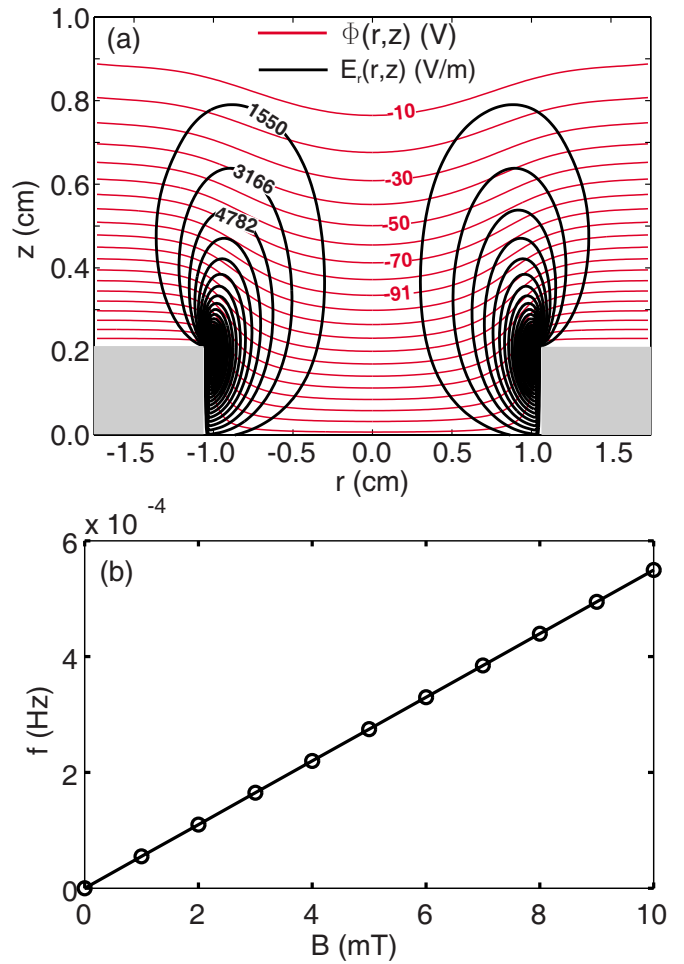


FIG. 5. (Color online) Simulation of the cluster rotation. (a) Potential structure in front of the confining circular cavity and contour lines for the strength of the radial electric field. (b) Dependence of the cluster rotation on the magnetic induction yielding a linear increase.

sheath over an electrode with a central depression in the presence of an axial magnetic field. However, this code cannot treat the entire discharge volume with its complex boundary conditions. Instead, the code provides high spatial resolution for the limited volume around the central depression.

The dynamics of the neutral gas was intentionally neglected in this model in order to obtain the pure effect from ion drag. These simulations use the actual plasma parameters, electron temperature T_e , plasma density n_i , and discharge pressure, as input. The resultant profiles of sheath potential $\Phi(r,z)$ and radial electrical field $E_r(r,z)$ are shown in Fig. 5(a).

Dust particles were then introduced into the sheath and their motion was tracked by the molecular dynamics method, with dust charge, sheath electrical field, and ion flow being provided by the sheath model. In the vertical direction, the dust particles are usually levitated at the upper edge of the sheath (6.8 mm above the electrode surface, for 15 Pa), which agrees well with the experimental observation with cylinder and mesh grid confinement. Horizontally, they are confined in the central region of the electrode and form stable 2D structures, which rotate in a plane perpendicular to

the magnetic field and in the $E \times B$ direction, as expected. The rotation frequency for a cluster of 19 particles is plotted in Fig. 5(b) against the magnetic field. The frequency rises linearly with magnetic field in a large range of magnetic field and reaches about 5.5×10^{-4} Hz at 10 mT. This value, however, is nearly two orders smaller than that observed in the present experiment, as shown in Fig. 3(c).

From this finding, we conclude that even in the central volume the $E \times B$ motion of the ions may affect the cluster particles by local gas rotation. This effect could be more important than the direct drive by the ion-drag force.

IV. CLUSTER ROTATION BY GAS FLOWS

A. Experiment with a spinning disk

In this section we are interested in studying details of gas flows close to the electrode. At typical experimental conditions, with pressures in the range of 10 Pa, and for slow streaming velocity, we can expect a laminar flow of the gas with no-slip boundary condition at the walls, because both the Reynolds and the Knudsen number $Kn = \lambda / \ell$ are small, where $\ell \approx 50$ mm is a representative length scale, i.e., half the height of the vacuum chamber.

To produce a laminar shear flow, which is independent of plasma conditions, a spinning disk of 7 cm diameter was mounted at $z_0 = 5$ cm above the lower electrode, as shown in Fig. 6(a). The dust cluster is simply advected by the gas flow and serves as a sensitive probe for the rotation speed near the lower electrode. The velocity field is explored by varying the levitation height with increasing rf voltage from 80 V_{pp} to 300 V_{pp}, whereas the pressure was kept constant at $p = 15$ Pa. The disk is driven by a stepper motor outside of the chamber. The spinning rate of the disk can be varied from 0.5 to 2 Hz, which is sufficiently low to avoid turbulence. No magnetic field was applied, in order to ensure that the observed rotation of the cluster is due to the neutral gas flow and not due to an ion drag.

The rotation frequency f of the cluster was measured for two different spinning rates of the disk. When a laminar flow of the gas is assumed with no-slip boundary condition at the spinning disk and at the lower electrode, a constant frequency gradient $df/dz = f_{\text{disk}}/z_0$ is expected. The influence of radial boundaries is neglected for simplicity, but the model should be valid near the center of the lower electrode.

The observed rotation frequencies near the lower electrode [see Fig. 6(b)] show a constant vertical gradient and can be extrapolated to zero at $z=0$ as expected from the no-slip condition. Doubling the speed of the spinning disk increases the gradient by a factor of 2. The measured gradient, however, is about 10% lower than expected from the spinning rate of the disk and its separation from the electrode. This small deviation may be attributed to the neglect of radial boundaries, which tend to slow down the rotation speed. Hence, under our experimental conditions, a slow, laminar neutral gas flow with constant vertical shear can be established. The change of plasma density that accompanies the variation of the rf voltage cannot explain the observed shear flow because a reduction in plasma density is used to

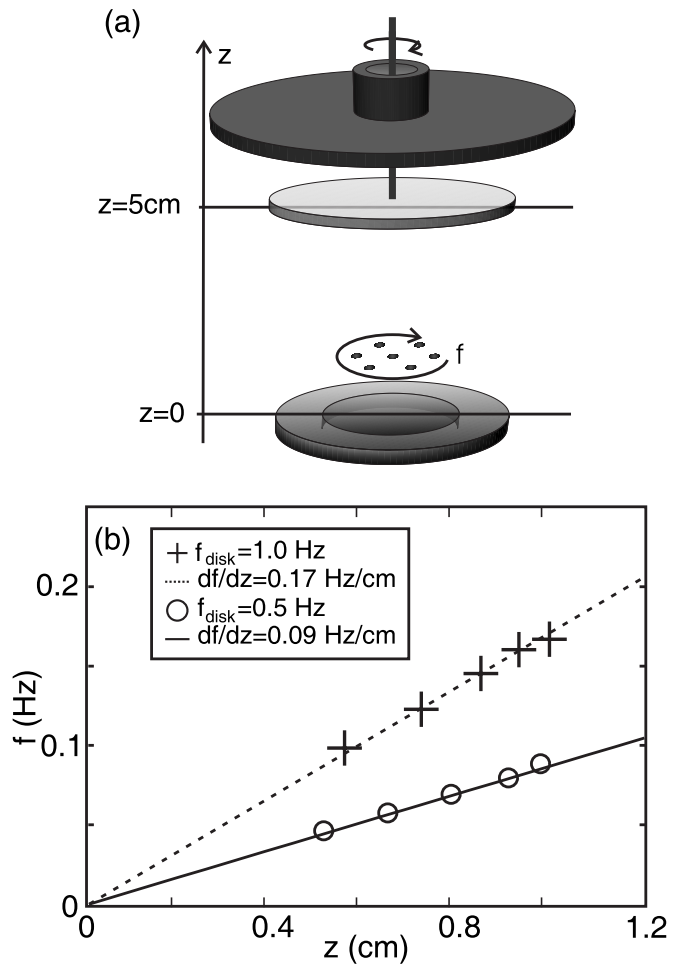


FIG. 6. (a) A spinning disk is mounted 5 cm above the lower electrode. (b) Rotation frequency of the cluster vs. levitation height z above the lower electrode for two different rotation frequencies of the spinning disk. The validity of the no-slip boundary condition is confirmed by the straight lines from the origin that match the observed data points.

increase the levitation height. Further, the spinning rate of the disk was chosen much higher than the plasma-induced rotation rates to clearly separate these effects.

B. Hydrodynamic model

For a qualitative understanding of the observed difference between simulation and experiment, we suggest a simple model taking the neutral gas motion into account. The basic idea is that ion motion in crossed electric and magnetic fields has a small velocity component in the azimuthal direction, which, by ion-neutral collisions sets the neutral gas into rotation. The neutral gas flow is damped by viscosity and obeys a sticking condition at the walls. Typical experimental parameters at $p = 10$ Pa and $B = 10$ mT are ion gyroradius $r_{ci} = 14$ mm, ion-neutral mean free path (mfp) $\lambda_{in} = 0.1$ mm, and argon neutral-neutral mfp $\lambda_{mfp} = 0.7$ mm.

For an analytic model a few assumptions have to be made. The only driving force stems from the confining radial electric field E_c in combination with the axial magnetic field B_z . The driving force is localized in a plasma layer of thick-

ness h . The boundary condition for the gas flow is, that the streaming velocities vanishes at the electrode and at the lid. No radial boundary condition is imposed.

The total ion drift velocity vector \vec{u}_i is given by

$$\vec{u}_i = \mu(\vec{E}_c + \vec{u}_i \times \vec{B}) \quad (4)$$

with $\vec{E}_c = E_r \vec{e}_r + E_z \vec{e}_z$ having components in the r and z -direction and $\vec{B} = B_z \vec{e}_z$. μ is the mobility of Ar^+ from Ref. 22. For calculating the ion flow velocity, any motion of the neutral gas can be neglected as small. The resulting azimuthal drift velocity in the weak magnetic field limit then becomes

$$u_{i,\phi} = \mu^2 B_z E_r. \quad (5)$$

For small r the confining potential can be considered as harmonic, which results in a linear dependence $u_\phi = \omega_i r$. This is equivalent to rigid rotation at a constant angular velocity ω_i . Due to the small Knudsen number Kn , and for a Mach number $M \ll 1$, the argon gas can be treated as an incompressible viscous fluid and obeys the Navier-Stokes equation. Likewise, the Reynolds number is much smaller than unity. For this reason inertial forces can be neglected. Thus, the viscous damping force in a volume dV at viscosity η becomes

$$d\vec{F}_{\text{visc}} = -\eta \Delta \vec{u}_n dV. \quad (6)$$

The driving force due to ion neutral collisions in the azimuthal-direction is

$$d\vec{F}_{i,\phi} = n_i m_i \omega_i r \nu_{in} dV, \quad (7)$$

with m_i being the ion mass, n_i the ion density and $\nu_{in} = f(|v_i|)$ the velocity-dependent ion-neutral collision frequency. The equilibrium of these forces yields

$$\Delta \vec{u}_n = -\frac{n_i m_i \omega_i \nu_{in}}{\eta} r \vec{e}_\phi = -\alpha r \vec{e}_\phi. \quad (8)$$

With a thickness h of the sheath, a gap width H between electrode and the lid, and a rotation frequency $\vec{\omega}_n$ of the neutral gas, the differential equation for the gas flow becomes

$$\Delta \vec{u}_n = \Delta(\vec{\omega}_n \times \vec{r}) = \begin{cases} -\alpha r \vec{e}_\phi & \text{for } z < h \\ 0 & \text{for } h < z < H. \end{cases} \quad (9)$$

If we assume a rigid body rotation of the neutral gas about the z -axis and a shear flow only in the z -direction $\vec{\omega}_n$ can be written as $\vec{\omega}_n = \omega_n(z) \vec{e}_z$. In this case Eq. (9) simplifies to

$$\frac{d^2 \omega_n(z)}{dz^2} = \begin{cases} -\alpha & \text{for } z < h \\ 0 & \text{for } h < z < H. \end{cases} \quad (10)$$

By integration we obtain

$$\omega_n(z) = \begin{cases} -\frac{1}{2} \alpha z^2 + c_1 z + c_2 & \text{for } z < h \\ -c_3 z + c_4 & \text{for } h < z < H. \end{cases} \quad (11)$$

The four parameters $c_1 - c_4$ can be specified by the boundary conditions $\omega_n(0) = \omega_n(H) = 0$ and the continuity of ω_n and its derivative at h . Then, the rotation frequency of the neutral gas column is given by

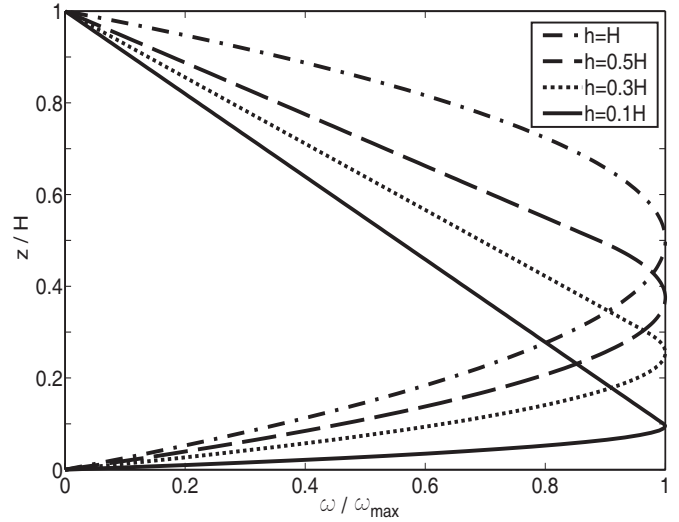


FIG. 7. Rotation frequency of the neutral gas column for an ion drag drive located in the sheath of height h above the lower electrode [Eq. (12)] for four different ratios of h/H . ω_{max} is the maximum value of each curve. The curve changes from a parabolic dependency in the driven region to a constant slope in the region with no driving force.

$$\omega_n(z) = \begin{cases} \alpha \left[-\frac{1}{2} z^2 + h \left(1 - \frac{1}{2} h/H \right) z \right] & \text{for } z < h \\ \alpha (h^2/2H)(H - z) & \text{for } h < z < H. \end{cases} \quad (12)$$

Figure 7 shows the variation of the rotation frequency of the neutral gas column between the lower electrode and the top of the chamber. In the bottom layer, where the neutral gas is driven by the azimuthal ion flow, a parabolic profile is found, whereas in the region with no driving force the shape is linear. The maximum rotation frequency

$$\omega_{\text{max}} = \frac{n_i m_i \omega_i \nu_{in}}{2\eta} \left(h - \frac{h^2}{2H} \right) \quad (13)$$

is attained at $z = h - h^2/2H$. Because $\omega_i \propto B_z$, the maximum rotation frequency increases with B .

For the experimental condition of the experimental setup, Fig. 3(b), the quantities are as follows: $\eta = 22 \times 10^{-6}$ Pa s is the viscosity of argon gas for low pressures at room temperature.²³ The ion density $n_i = 5.8 \times 10^{14} \text{ m}^{-3}$ was measured by a Langmuir probe. $h = 10$ mm is the assumed width of the plasma sheath above the driven electrode. We expect considerable electrical fields and an associated ion drift occurs only in the plasma sheath. $z_L = 7$ mm is the levitation height of the cluster. $H = 100$ mm is the distance between electrode and lid. $m_i = 6.64 \times 10^{-26}$ kg is the mass of an argon ion, $\nu_{in} = 4.5$ MHz is the ion neutral collision frequency at a pressure of $p = 15$ Pa. From Eqs. (3) and (5), $\omega_i = 400 \text{ s}^{-1}$ can be estimated. For these quantities and a magnetic induction of 10 mT, Eq. (12) gives a rotation period of 25 s, which represents a four times higher rotation rate than the experimental value in Fig. 3(b). However, as expected,

the hydrodynamical model gives an upper bound of the rotation frequency, because it does not include radial friction and assumes a constant radial electric field, which is independent of z .

V. DISCUSSION AND CONCLUSION

The experiments in the typical discharge geometry had shown that the observed clockwise sense of cluster rotation is opposite to the expected local azimuthal component of the ion drag force, which should lead to a counterclockwise rotation. By comparing the cluster rotation with a situation in which the pump and gas handling system was shut off, any unwanted neutral winds could be ruled out as explanation for the observed sense of rotation. This finding is the first hint that the cluster rotation is not based on a local force balance of ion wind force and friction with a neutral gas at rest as was suggested in Refs. 3, 4, and 8.

Restricting the plasma volume to a cylinder with a grid on top eliminates any coupling of gas flow in the exterior region from the interior of the cylinder. In this situation, the cluster rotation indeed exhibited the expected counterclockwise sense of rotation. Therefore, the reversal of the sign of rotation in the unrestricted original situation could be identified as the superposition of competing effects. This competition involves azimuthal ion flows, which have opposite sign in the exterior and interior region, as shown by global discharge simulations. A reversed radial electric field is found at the outer edge of the powered electrode [Figs. 4(a) and 4(c)]. In the absence of the flow barriers, the net torque communicated to the gas is apparently governed by the clockwise ion flows. Presently, the global discharge simulation does not include a magnetic field. Therefore, it can only be conjectured that the decrease of the rotation speed above a certain magnetic induction in Fig. 2 is due to a change in plasma density and potential distribution, which may shift the balance between clockwise and counterclockwise ion flows in different parts of the discharge.

Comparing the observed rotation frequency in the restricted volume with simulations shows that the observed frequency is more than an order of magnitude larger than expected from the local force balance between the ion drag force and neutral friction. This is a further hint that also in the restricted volume a global neutral gas flow develops. Such a discrepancy between observed rotation frequency and expectation from a simple model was reported before in Refs. 3 and 8. Therefore, we conclude that, in our situation, the ion drag force on the dust cluster is small compared to the neutral drag force.

Experiments with a rotating disk show that a steady rotational gas flow can be established at a low gas pressure of 10 Pa. The flow velocity was measured by levitating dust particles at different heights above the lower electrode. This gas flow was found to have a constant vertical velocity shear and extrapolation suggests that the no-slip boundary conditions is valid at the electrode.

A simple hydrodynamic model for the gas flow was presented for the regime of small Knudsen numbers. No-slip conditions were imposed at the top and bottom of the system.

However, radial boundary conditions were neglected for simplicity. The model has simple solutions for surface forces and homogeneous volume forces and is able to give a sufficient description of the vertically sheared velocity field of the neutral gas rotation. Even the magnitude of the observed speed of cluster rotation can be estimated from the total torque originating from ion-neutral collisions and viscous damping and reasonable agreement is found.

To conclude, the experiments have shown that neutral gas motion plays an important role in experiments with dust clusters in a magnetic field, when the neutral gas pressure is typically 10 Pa. The superposition of opposing ion flow directions in different parts of the discharge can lead to an unexpected magnitude and sense of rotation. The local ion wind force on flat two-dimensional clusters is negligibly small in our experiments. A clear evidence of dominant ion wind forces can only be expected at much lower neutral gas pressures and higher degrees of ionization. Such low gas pressures were only used in the experiments of Nunomura.⁷ Most previous experiments^{1,3-5,13} were operated at gas pressures higher than those in our experiment and at a comparable degree of ionization. Therefore, our conclusion on the importance of neutral gas motion pertains to the majority of observations. In the regime of small Knudsen numbers, the no-slip boundary condition leads to sheared neutral flows, which has not been taken into account yet for explaining sheared cluster motion.

ACKNOWLEDGMENTS

This work was supported by DFG in the frame of SFB-TR24 Greifswald-Kiel, Project No. A2. L.J.H. gratefully acknowledges support by the Alexander von Humboldt Foundation.

- ¹W.-T. Juan, J.-W. Hsu, Z.-H. Huang, Y.-J. Lai, and L. I. Chin, *J. Physiol.* **37**, 184 (1999).
- ²F. Cheung, A. Samarian, and B. James, *Phys. Scr.* **T98**, 143 (2002).
- ³F. Cheung, A. Samarian, and B. James, *New J. Phys.* **5**, 75 (2003).
- ⁴U. Konopka, D. Samsonov, A. V. Ivlev, J. Goree, V. Steinberg, and G. E. Morfill, *Phys. Rev. E* **61**, 1890 (2000).
- ⁵G. Uchida, R. Ozaki, S. Iizuka, and N. Sato, in *International Congress on Plasma Physics*, edited by P. Pavlo (European Physical Society, Prague, 1998), pp. 2557–2561.
- ⁶N. Sato, G. Uchida, T. Kaneko, S. Shimizu, and S. Iizuka, *Phys. Plasmas* **8**, 1786 (2001).
- ⁷S. Nunomura, N. Ohno, and S. Takamura, *Jpn. J. Appl. Phys., Part 1* **36**, 877 (1997).
- ⁸P. K. Kaw, K. Nishikawa, and N. Sato, *Phys. Plasmas* **9**, 387 (2002).
- ⁹V. Land, W. J. Goedheer, and M. R. Akdim, *Phys. Rev. E* **72**, 046403 (2005).
- ¹⁰L. J. Hou, Y. N. Wang, and Z. L. Mišković, *Phys. Plasmas* **12**, 042104 (2005).
- ¹¹Y. N. Wang and L. J. Hou, *Thin Solid Films* **506**, 647 (2006).
- ¹²K. Matyash, M. Fröhlich, H. Kersten, G. Thieme, R. Schneider, M. Hannemann, and R. Hippler, *J. Phys. D* **37**, 2703 (2004).
- ¹³F. Huang, M. Ye, L. Wang, and Y. Liu, *Plasma Sources Sci. Technol.* **9**, 11 (2007).
- ¹⁴W. E. Amatucci, D. N. Walker, G. Gatling, and E. Scime, *Phys. Plasmas* **11**, 2097 (2004).
- ¹⁵E. S. Dzljeva, A. Y. Ivanov, V. Y. Karasev, and A. I. Éikhval'd, *Opt. Spectrosc.* **101**, 816 (2006).
- ¹⁶V. Y. Karasev, E. S. Dzljeva, A. Y. Ivanov, and A. I. Eikhval'd, *Phys. Rev. E* **74**, 066403 (2006).
- ¹⁷M. M. Vasil'ev, L. G. D'yachkov, S. N. Antipov, O. F. Petrov, and V. E. Fortov, *JETP Lett.* **86**, 358 (2007).

¹⁸K. Ogiwara, S. Etoh, M. Aramaki, S. Yoshimura, T. Sugihara, and M. Y. Tanaka, International Congress on Plasma Physics, Fukuoka, Japan (2008), pp. P2-150.

¹⁹A. Melzer, T. Trottenberg, and A. Piel, *Phys. Lett. A* **191**, 301 (1994).

²⁰<http://www.siglo-kinema.com>.

²¹U. Konopka, G. E. Morfill, and L. Ratke, *Phys. Rev. Lett.* **84**, 891 (2000).

²²L. S. Frost, *Phys. Rev.* **105**, 354 (1957).

²³B. Younglove and H. Hanley, *J. Phys. Chem. Ref. Data* **15**, 1323 (1986).

A.2

EFFECT OF CENTRIFUGAL FORCES ON THE INTERPARTICLE DISTANCE OF TWO DUST PARTICLES CONFINED IN A PLASMA

Jan Carstensen, Franko Greiner, Lujing Hou, and Alexander Piel

**Reprinted with permission from
Jan Carstensen, Franko Greiner, Lujing Hou, and Alexander Piel,
IEEE Transactions on Plasma Science, Vol. 38, 788 (2010).
Copyright 2009, IEEE**

Effect of Centrifugal Forces on the Interparticle Distance of Two Dust Particles Confined in a Plasma

Jan Carstensen, Franko Greiner, Lujing Hou, and Alexander Piel

Abstract—Dusty-plasma experiments with flat dust clusters are often performed in radio frequency discharges at typical gas pressures of 1 to 100 Pa. For the understanding of the structure and the dynamical behavior of dust clusters, the grain charge and the effective Debye length are of key interest. Direct measurements of these quantities are a challenging task because the dust grains are confined in the plasma-boundary layer, where plasma diagnostics is difficult. Here, we present a new approach to determine the grain charge and the horizontal screening length, which does not require prior knowledge of the plasma parameters. The method is based on a slow and controlled rotation of the neutral-gas column due to a rotating electrode. This leads to centrifugal forces to the dust grains without changing the plasma conditions and allows studying the interparticle distance of a dust cluster as a function of its rotation frequency, which directly depends on the particle charge, the screening length, and the strength of the confining potential.

Index Terms—Diagnostic techniques, dusty plasma, neutral-gas flow, particle charge, screening length.

I. INTRODUCTION

DUST grains immersed in a plasma attain a negative charge. The electrostatic force between two grains embedded in a plasma is often assumed to be a Debye-shielded Coulomb interaction. However, this model is of limited validity. An analysis by Lampe *et al.* [1] shows that the potential distribution in front of a single dust grain in a nonflowing collisionless plasma can be approximated by a Debye potential only at intermediate distances

$$\phi(r) = \frac{Q_{\text{eff}}}{4\pi\epsilon_0 r} \exp\left(-\frac{r}{\lambda_D}\right) \quad (1)$$

where Q_{eff} is an effective charge, which is somewhat larger than the actual grain charge Q because of weak ion shielding close to the grain. The shielding length is

$$\lambda_D = \left(\frac{1}{\lambda_{De}^2} + \frac{1}{\lambda_{Di}^2} \right)^{-\frac{1}{2}} = \left(\frac{ne^2}{\epsilon_0 k_B T_e} + \frac{ne^2}{\epsilon_0 k_B T_i} \right)^{-\frac{1}{2}} \quad (2)$$

where $\lambda_{De,i}$ is the classical ion and electron Debye length. For particles confined in the plasma sheath, the situation is

Manuscript received June 30, 2009. First published October 23, 2009; current version published April 9, 2010. This work was supported by DFG in the frame of SFB-TR24 Greifswald-Kiel, Project A2.

J. Carstensen, F. Greiner, and A. Piel are with the Institut für Experimentelle und Angewandte Physik, Christian-Albrechts-Universität, 24098 Kiel, Germany (e-mail: Carstensen@physik.uni-kiel.de; Greiner@physik.uni-kiel.de; piel@physik.uni-kiel.de; http://www.ieap.uni-kiel.de).

L. Hou is with the Max-Planck Institute for Extraterrestrial Physics, 85748 Garching, Germany (e-mail: hou@mpe.mpg.de).

Digital Object Identifier 10.1109/TPS.2009.2032761

more complicated. Due to the ion flow, the potential distribution becomes anisotropic and can even be attractive (wake fields [2]). Nevertheless, upstream and to the side, the potential distribution is approximately of the Debye form, i.e., the screening length is an angular-dependent effective Debye length [1], which increases as θ goes from 0 (upstream) to $\pi/2$ (sideways).

For the experimental determination of particle charge and screening length, different methods exist. The probably most common charge-measurement techniques are based on the vertical oscillation of a single dust grain due to a low-frequency modulation of the electrode voltage [3] or due to the radiation pressure of a pulsed laser beam [4]. Here, the particle charge can be determined from the resonance curve of the particle, if the ion density in the sheath or the vertical electric-field gradient [5] is known.

As a technique for the diagnostic of the screening length, Kong *et al.* analyzed the levitation height of a dust cluster as a function of an externally applied dc bias [6]. The variation of the levitation height was taken as a measure of the sheath thickness. In combination with a collisional plasma-sheath model [7], this allows an evaluation of the screening length.

Another class of experiments allowing the determination of particle charge and Debye length simultaneously rests upon the observation of dust lattice waves in flat-dust crystals [8]–[10], the analysis of particle trajectories during collisions [11], [12], or the observation of normal-mode spectra in flat dust clusters [13]–[15].

All three techniques—the observations of dust waves, the observation of two-particle collisions, and the observation of normal modes—have the advantage that no prior knowledge about the plasma parameters is required. However, they are restricted to low-gas pressures, where the particle motion is not strongly damped by neutral-gas friction. In this paper, we present a new experimental method to determine the particle charge and the Debye length, which is also applicable at higher gas pressures. It bases on the introduction of centrifugal forces to a two-particle dust cluster. This is achieved by a slow rotation of the neutral-gas column due to a rotating electrode, which has no influence on the plasma parameters because the flow velocities of the neutral gas do not exceed a few meters per second. This is sufficiently slow, in order to avoid any drawback to the plasma.

II. THEORETICAL BACKGROUND

Here, we consider two identical particles with mass m confined in the boundary layer of a plasma sheath. Due to

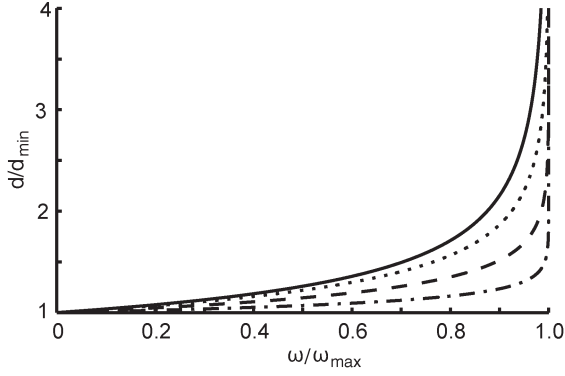


Fig. 1. Interparticle distance d versus rotation frequency ω according to (7) for different screening length (dotted line) $\lambda_D = 1.1d_{\min}$, (dashed line) $\lambda_D = 0.4d_{\min}$ and (dashed dotted line) $\lambda_D = 0.1d_{\min}$. The solid line indicates the case of pure Coloumb interaction.

the plasma, the particles attain a real charge Q . The resulting repulsion force F_E can be derived from a screened Coulomb potential

$$F_E = \frac{Q_{\text{eff}}^2}{4\pi\epsilon_0 d} \left(\frac{1}{\lambda_D} + \frac{1}{d} \right) \exp\left(-\frac{d}{\lambda_D}\right) \quad (3)$$

where d is the interparticle distance, λ_D the screening (Debye) length and $Q_{\text{eff}} > Q$ is the effective charge [1] of the dust grains. A rotation of the particles about their center of mass with an angular frequency ω leads to an additional centrifugal force

$$F_c = m\omega^2 \frac{d}{2}. \quad (4)$$

In a steady state, these two forces are balanced by confining electric fields. Here, the confining potential is considered as harmonic, therefore, the sum of the forces is

$$m\omega^2 \frac{d}{2} + \frac{Q_{\text{eff}}^2}{4\pi\epsilon_0 d} \left(\frac{1}{\lambda_D} + \frac{1}{d} \right) \exp\left(-\frac{d}{\lambda_D}\right) - \alpha \frac{d}{2} = 0 \quad (5)$$

where α is the strength of the confining potential.

The quantities Q_{eff} and α can be substituted by $\alpha = m\omega_{\text{max}}^2$ and

$$Q_{\text{eff}}^2 = 2\pi\epsilon_0 m\omega_{\text{max}}^2 d_{\min}^3 \frac{\lambda_D}{\lambda_D + d_{\min}} \exp\left(\frac{d_{\min}}{\lambda_D}\right) \quad (6)$$

where ω_{max} is the maximum frequency at which the rotating system is stable and d_{\min} the minimal interparticle distance, which is attained at $\omega = 0$ (no rotation of the cluster). In these terms (5) becomes

$$\omega = \omega_{\text{max}} \left[1 - \left(\frac{d_{\min}}{d} \right)^3 \frac{\lambda_D + d}{\lambda_D + d_{\min}} \exp\left(\frac{d_{\min} - d}{\lambda_D}\right) \right]^{\frac{1}{2}}. \quad (7)$$

Fig. 1 shows the interparticle distance d as a function of ω for different λ_D . The full line indicates the case of a pure Coloumb

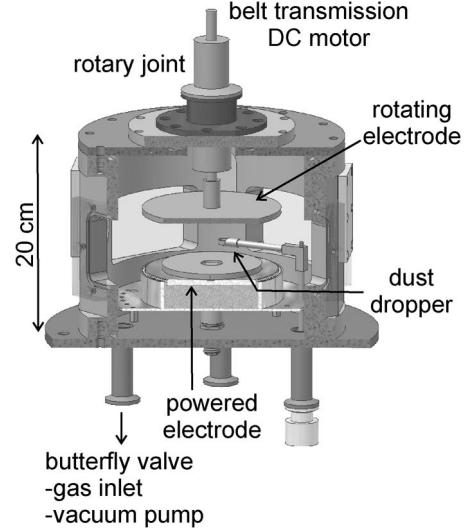


Fig. 2. Sketch of the experimental arrangement. An Argon plasma is established between the driven lower electrode and the grounded upper electrode, which is attached to a rotary joint 5 cm above the driven electrode.

interaction ($\lambda_D \rightarrow \infty$). The effect of screening can be seen as soon as λ_D is on the order of d_{\min} . Here, the pole at ω_{max} becomes sharper with decreasing screening length.

III. EXPERIMENTAL SETUP

The experiments presented here are performed in a 13.56-MHz capacitively coupled parallel-plate radio-frequency (RF) discharge. Fig. 2 shows the experimental setup. The powered lower electrode has a diameter of 10 cm and is radially terminated by a grounded Faraday shield, which is separated from the driven electrode by a gap filled with PTFE dielectric. The upper grounded electrode is placed 5 cm above the driven electrode. For dust confinement, a cylindrical cavity of 20-mm diameter and 2-mm depth is milled into the center of the lower electrode. The vacuum vessel has an inner diameter of 220 mm and a height of 170 mm. The vacuum pump and the gas inlet are connected to a common port at the bottom of the chamber. The pump and gas-handling system are decoupled from the plasma chamber by a ring-shaped cover plate that encircles the powered electrode and has an equidistant pattern of holes, in order to minimize neutral-gas flows. The particles used in these experiments are monodisperse melamine formaldehyde spheres with a diameter of $(20 \pm 0.2) \mu\text{m}$. They are illuminated by an expanded laser (45 mW at 630 nm) and can be observed side on by a high-speed camera. The dust grains are confined in a layer typically 5–10 mm above the electrode.

In order to expose the dust particles to centrifugal forces, the upper electrode is connected via a rotary joint to a dc motor outside the vacuum vessel, which allows rotation frequencies of the electrode of up to approximately 30 Hz. This causes a laminar rotational motion of the neutral gas, showing a decreasing flow velocity toward the lower electrode, due to viscose damping forces [16]. Close to the rotation axis, the rotation frequency of the neutral-gas column is constant in the horizontal direction and has a gradient in the vertical direction. Therefore, at the

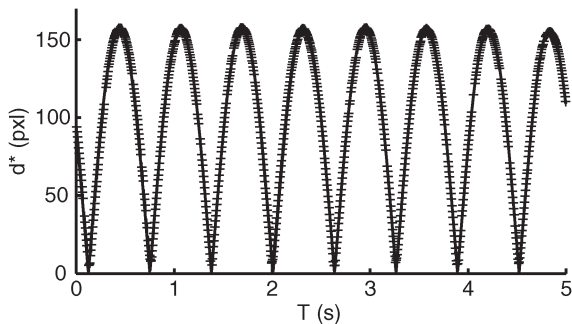


Fig. 3. Projection of the interparticle distance d^* into the camera plain versus time T for a fixed rotation frequency of the electrode. A Fourier transform of this time series yields a cluster rotation frequency of $f = 0.80$ Hz.

position of the dust clusters, rotation frequencies of up to 3 Hz can be obtained.

IV. MEASUREMENTS

The measurements were performed in an Argon RF plasma at 20 Pa gas pressure and an RF voltage of 300 V_{pp}. Two particles were confined in the boundary layer 6 mm above the driven electrode. The particles were illuminated by an expanded laser and observed by a high-speed camera through one of the side windows.

For a fixed frequency of the rotating electrode (and of the cluster), the particle motion is captured with a frame rate of 200 Hz over 16 s. Because the camera observation is made from the side of the cluster, only the projection of the interparticle distance d^* into the camera plane can be extracted from the video frames. As an example, Fig. 3 shows the projected interparticle distance as a function of time for a constant rotation frequency of the cluster. The rotation frequency f of the cluster and the interparticle distance d can be extracted from this time series by means of a Fourier transform or by fitting a function of the form $d^* = d \cdot |\sin(\omega t - \varphi_0)|$ to the data points.

The measured interparticle distance for different rotation frequencies is shown in Fig. 4. A least square fit of (7) to the data points leads to a particle charge of $Q_{\text{eff}} = -(65\,000 \pm 9000) e$ and a screening length of $\lambda_D = (0.8 \pm 0.3) \text{ mm}$. The given errors are estimated from Monte Carlo simulations [17] based on the assumption that the frequency resolution is given by $\Delta f = (16s)^{-1}$ and that the interparticle distance can be measured within an accuracy of ± 1.5 pixel ($\Delta d = 7 \mu\text{m}$).

V. DISCUSSION

The good correspondence of the fit and the measured values supports the assumption of a Debye-screened Coulomb interaction force, although the dust grains are located in the sheath, and the sheath is collisional (Ar⁺ mean-free path is $\lambda_{\text{mfp}} \approx 0.2 \text{ mm} < \lambda_D$). The screening length of $\lambda_D = 0.8 \text{ mm}$ found by the presented method is comparable with the interparticle distance $d = 0.7 \text{ mm}$. This is in good agreement with results from other experiments with flat dust clusters in RF discharges where typically $\kappa = d/\lambda_D$ values between 0.5 and 2 are found [18], [19].

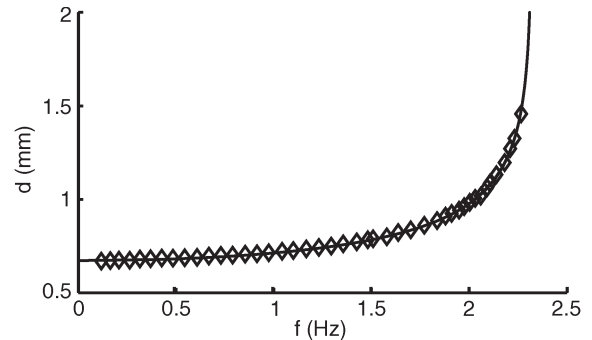


Fig. 4. Dependence of the interparticle distance d as a function of rotation frequency f . The solid line is a fit of (7).

The quantitative determination of the horizontal screening length from the plasma parameters is an open issue, e.g., in [20], the screening is attributed to the electrons, whereas in [21], it is argued that at least, at higher pressures, the screening is dominated by the ions. Recent experiments by Sheridan [22] have indicated that the horizontal screening length in the plasma sheath is determined by the local ion density in combination with the electron temperature.

Under our typical bulk-plasma conditions $n_{i,e} = 10^{15} \text{ m}^{-3}$, $T_e = 3 \text{ eV}$, and $T_i = 0.03 \text{ eV}$, the Debye lengths are $\lambda_{D,e} = 0.4 \text{ mm}$ and $\lambda_{D,i} = 0.04 \text{ mm}$, i.e., the shielding is dominated by the ions. We have performed computer simulations of the sheath with the simulation code described in [23]. The simulation shows that the local ion density at the positions of the 20 μm dust particles is roughly half the plasma bulk density. This density combined with the electron temperature gives an effective Debye length of $\lambda_{D,\text{eff}} = 0.6 \text{ mm}$, which is in good agreement with the measured value.

To conclude, the presented rotating-electrode method can be used as a diagnostic for screening length and particle charge. The method is applicable at higher gas pressures and does not affect the plasma properties. The obtained screening length is in good accordance with the aforementioned references.

REFERENCES

- [1] M. Lampe, G. Joyce, G. Ganguli, and V. Gavrishchaka, "Interactions between dust grains in a dusty plasma," *Phys. Plasmas*, vol. 7, no. 10, pp. 3851–3861, Oct. 2000.
- [2] S. V. Vladimirov and M. Nambu, "Attraction of charged particles in plasmas with finite flows," *Phys. Rev. E, Stat. Phys. Plasmas Fluids Relat. Interdiscip. Top.*, vol. 52, no. 3, pp. R2172–R2174, Sep. 1995.
- [3] A. Melzer, T. Trottenberg, and A. Piel, "Experimental determination of the charge on dust particles forming Coulomb lattices," *Phys. Lett. A*, vol. 191, no. 3/4, pp. 301–308, 1994.
- [4] N. J. Prior, L. W. Mitchell, and A. A. Samarian, "Determination of charge on vertically aligned particles in a complex plasma using laser excitations," *Jpn. J. Appl. Phys.*, vol. 36, no. 11, pp. 1249–1253, Jun. 2003.
- [5] A. A. Samarian and B. W. James, "Dust as fine electrostatic probes for plasma diagnostic," *Plasma Phys. Control. Fusion*, vol. 47, no. 12B, pp. B629–B639, Dec. 2005.
- [6] J. Kong, J. Carmona-Reyes, J. Creel, and T. W. Hyde, "Relationship between the dc bias and the Debye length in a complex plasma," *IEEE Trans. Plasma Sci.*, vol. 35, no. 2, pp. 323–327, Apr. 2007.
- [7] T. E. Sheridan and J. Goree, "Collisional plasma sheath model," *Phys. Fluids B, Plasma Phys.*, vol. 3, no. 10, pp. 2796–2804, Oct. 1991.
- [8] A. Homann, A. Melzer, S. Peters, R. Madani, and A. Piel, "Determination of the dust screening length by laser-excited lattice waves," *Phys. Rev. E, Stat. Phys. Plasmas Fluids Relat. Interdiscip. Top.*, vol. 56, no. 6, pp. 7138–7141, Dec. 1997.

- [9] S. Nunomura, D. Samsonov, and J. Goree, "Transverse waves in a two-dimensional screened-Coulomb crystal (dusty plasma)," *Phys. Rev. Lett.*, vol. 84, no. 22, pp. 5141–5144, May 2000.
- [10] S. Nunomura, J. Goree, S. Hu, X. Wang, and A. Bhattacharjee, "Dispersion relations of longitudinal and transverse waves in two-dimensional screened Coulomb crystals," *Phys. Rev. E, Stat. Phys. Plasmas Fluids Relat. Interdiscip. Top.*, vol. 65, no. 6, pp. 066402-1–066402-11, Jun. 2002.
- [11] U. Konopka, L. Ratke, and H. M. Thomas, "Central collisions of charged dust particles in a plasma," *Phys. Rev. Lett.*, vol. 79, no. 7, pp. 1269–1272, Aug. 1997.
- [12] U. Konopka, G. E. Morfill, and L. Ratke, "Measurement of the interaction potential of microspheres in the sheath of an RF discharge," *Phys. Rev. Lett.*, vol. 84, no. 5, pp. 891–894, Jan. 2000.
- [13] A. Melzer, "Mode spectra of thermally excited two-dimensional dust Coulomb clusters," *Phys. Rev. E, Stat. Phys. Plasmas Fluids Relat. Interdiscip. Top.*, vol. 67, no. 1, p. 016411, Jan. 2003.
- [14] T. E. Sheridan, "Center-of-mass and breathing oscillations in small complex plasma disks," *Phys. Rev. E, Stat. Phys. Plasmas Fluids Relat. Interdiscip. Top.*, vol. 72, no. 2, p. 026405, Aug. 2005.
- [15] T. E. Sheridan, M. R. Katschke, and K. D. Wells, "Measurement of electric field and gradient in the plasma sheath using clusters of floating microspheres," *Rev. Sci. Instrum.*, vol. 78, no. 2, p. 023502, Feb. 2007.
- [16] J. Carstensen, F. Greiner, L.-J. Hou, H. Maurer, and A. Piel, "Effect of neutral gas motion on the rotation of dust clusters in an axial magnetic field," *Phys. Plasmas*, vol. 16, no. 1, p. 013702, Jan. 2009.
- [17] W. Press, S. Teukolsky, W. Vetterling, and B. Flannery, *Numerical Recipes in C*, 2nd ed. Cambridge, U.K.: Cambridge Univ. Press, 1992.
- [18] V. Nosenko, J. Goree, Z. W. Ma, D. H. E. Dubin, and A. Piel, "Compressional and shear wakes in a two-dimensional dusty plasma crystal," *Phys. Rev. E, Stat. Phys. Plasmas Fluids Relat. Interdiscip. Top.*, vol. 68, no. 5, p. 056409, Nov. 2003.
- [19] A. Piel, V. Nosenko, and J. Goree, "Laser-excited shear waves in solid and liquid two-dimensional dusty plasmas," *Phys. Plasmas*, vol. 13, no. 4, p. 042104, Apr. 2006.
- [20] T. Nitter, "Levitation of dust in RF and dc glow discharges," *Plasma Sources Sci. Technol.*, vol. 5, no. 1, pp. 93–111, Feb. 1996.
- [21] R. Kompaneets, U. Konopka, A. V. Ivlev, V. Tsyтович, and G. Morfill, "Potential around a charged dust particle in a collisional sheath," *Phys. Plasmas*, vol. 14, no. 5, p. 052108, May 2007.
- [22] T. E. Sheridan, "Effect of radio frequency discharge power on dusty plasma parameters," *J. Appl. Phys.*, vol. 106, no. 3, p. 033303, Aug. 2009.
- [23] L. J. Hou and Y. N. Wang, "Formation and rotation of two dimensional Coulomb crystals in magnetized complex plasma," *Phys. Plasmas*, vol. 12, no. 4, p. 042104, Apr. 2005.

Jan Carstensen, photograph and biography not available at the time of publication.

Franko Greiner, photograph and biography not available at the time of publication.

Lujing Hou, photograph and biography not available at the time of publication.

Alexander Piel, photograph and biography not available at the time of publication.

A.3

DETERMINATION OF DUST GRAIN CHARGE AND SCREENING LENGTHS IN THE PLASMA SHEATH BY MEANS OF A CONTROLLED CLUSTER ROTATION

Jan Carstensen, Franko Greiner, and Alexander Piel

**Reprinted with permission from
Jan Carstensen, Franko Greiner, and Alexander Piel,
Physics of Plasmas, Vol. 17, 083703 (2010).
Copyright 2010, American Institute of Physics**

Determination of dust grain charge and screening lengths in the plasma sheath by means of a controlled cluster rotation

Jan Carstensen, Franko Greiner, and Alexander Piel
IEAP, Christian-Albrechts-Universität, D-24098 Kiel, Germany

(Received 14 June 2010; accepted 23 July 2010; published online 26 August 2010)

Dusty plasma experiments with flat dust clusters are often performed in the boundary sheath of radio frequency discharges at typical gas pressures of 1–100 Pa. The interaction of the dust grains is usually assumed to be of the Yukawa type, which is determined by the particle charge and the screening length. For the experimental determination of these quantities we present a method that does not require prior knowledge of the plasma parameters. The method is based on the application of centrifugal forces by means of a rotating electrode method (REM). The results are critically compared with an analysis of thermally excited normal modes, which can be studied at pressures below 10 Pa. The REM has a wider range of applicability that can be extended to 100 Pa. © 2010 American Institute of Physics. [doi:10.1063/1.3478994]

I. INTRODUCTION

The precise determination of dust charging in a plasma continues to be a challenge. Dust grains immersed in a plasma attain a negative floating potential, due to the higher mobility of the electrons. The standard model of orbital ion motion¹ (OML, orbital motion limit) yields a surface potential of $\Phi_f = -4k_B T_e / e$ for argon and $\Phi_f = -2.5k_B T_e / e$ for hydrogen with $T_e = T_i$, independent of the particle radius r_d . T_e and T_i denote the electron and ion temperature. The basic assumptions of this model are a Maxwellian energy distribution of electrons and ions and an isotropic, quasineutral, collisionless plasma.

In most gas discharges, the condition of a collisionless plasma does not hold. Ion neutral collisions enhance the ion current, which leads to a reduction of the negative potential.^{2,3} Contrariwise, trapping of ions on Keplerian orbits around the dust causes a reduction of the ion current.⁴

The charge Q of the dust particles is determined by the floating potential. For small particle radii with $r_d \ll \lambda_D$, the capacitance model⁵ gives

$$Q = 4\pi\epsilon_0 r_d. \quad (1)$$

Here λ_D is the screening (Debye) length of the plasma.

In the sheath of radio frequency (rf) discharges the charging mechanism is further influenced by the non-neutrality of the rf sheath and by a non-Maxwellian energy distribution of the electrons. Furthermore, the ion current to the dust grains is modified due to the directed flow of the ions.

For low gas pressures, plasma production is mainly due to electrons accelerated by the sheath expansion.⁶ This causes an additional electron population at high energies localized around the sheath edge resulting in a non-Maxwellian energy distribution of the electrons. It is found that the surface potential of the dust grains depends on the particle size and the position within the sheath, resulting in a nonlinear dependence of particle charge on particle radius.^{7–12}

Due to the ion flow, the potential distribution around the dust grains becomes anisotropic and can even be attractive (wake fields¹³). Results by Lampe *et al.*² indicated that, at least in the horizontal direction and at intermediate distances from the particle, the potential distribution is of the Debye form,

$$\phi(r) = \frac{eZ_{\text{eff}}}{4\pi\epsilon_0 r} \exp\left(-\frac{r}{\lambda_D}\right), \quad (2)$$

which was supported experimentally by Konopka *et al.*¹⁴ Here Z_{eff} is the effective charge number, which is somewhat larger than the actual grain charge number Z because of weak ion shielding close to the grain.¹⁵

In the bulk plasma, the screening is dominated by the ions because the ion temperature T_i is much smaller than the electron temperature T_e . However, the origin of screening within a rf sheath is not fully understood. Because the horizontal screening length in the sheath is often of the order of the bulk electron Debye length, screening is sometimes attributed to the electrons^{13,16–20} rather than to ions. On the other hand it is argued that in the sheath the ion density n_i exceeds the electron density n_e and the ion kinetic energy is of the order of $k_B T_e$, so shielding is still due to the ions.^{21,22} In a simplified picture, one can say that shielding is determined by the local ion density in combination with the electron energy.^{22,23}

In order to compare experimental with theoretical results, diagnostics for particle charge and screening length are needed. To do this, different methods exist. One established charge measurement technique is based on the vertical oscillation of a single dust grain due to a low frequency modulation of the electrode voltage²⁴ or due to the radiation pressure of a pulsed laser beam.^{25–27}

In Refs. 28 and 29 the levitation height of a dust cluster was analyzed as a function of an externally applied dc bias. In combination with a collisional plasma sheath model³⁰ this allows the determination of the screening length.

Other experiments for the simultaneous determination of particle charge and Debye length are based on the observa-

tion of dust lattice waves in flat dust crystals,^{31–33} the analysis of particle trajectories during collisions,^{14,34} or the observation of normal mode spectra in flat dust clusters.^{35–37}

All three techniques—the observations of dust waves, the observation of two particle collisions, and the observation of normal modes—have the advantage that no prior knowledge of the plasma parameters is required. However, they are restricted to low gas pressures, where the particle motion is not strongly damped by neutral gas friction. For the regime of higher gas pressures, we have recently proposed a new method,³⁸ which is based on the introduction of centrifugal forces to a two-particle dust cluster, due to a rotating electrode method (REM).

The intention of this contribution is the comparison of REM and normal mode analysis as two independent diagnostics for particle charge and screening length in flat dust clusters. It is the aim to prove the validity of the results obtained by both methods and to discuss its applications and limits. Furthermore the question of screening within the rf sheath is addressed.

This work is organized as follows: Sec. II gives a brief introduction to the theory of REM and normal mode analysis. In Sec. III the experimental setup is described and in Sec. IV the experimental results are shown. In Sec. V the findings are discussed. Section VI gives a short conclusion.

II. THEORY

Here we consider a two-dimensional system of N charged particles having equal mass m and equal charge number Z . The interaction potential is of the Yukawa form (2) and the particles are confined within a harmonic potential well of the form

$$V = \frac{1}{2}m\omega_0^2(x^2 + y^2), \quad (3)$$

with ω_0^2 being a measure of the strength of the harmonic confinement.

A. Normal modes analysis

This system can exhibit normal mode oscillations about its equilibrium position. The mode frequencies and the corresponding particle motion are determined by the dynamical matrix^{39–41}

$$E_{\alpha\beta,ij} = \frac{\partial^2 E}{\partial r_{\alpha,i} \partial r_{\beta,j}} \quad (4)$$

if damping is negligible. α and $\beta=x,y$ and $r_{\alpha,i}$ denote the x or y coordinate of the i th particle. E is the potential energy of the dust particles due to the confining potential and the interaction energy between the dust particles. The mode frequencies are obtained from the eigenvalues of the dynamical matrix, whereas the corresponding eigenvectors contain the amplitude and direction of motion for each particle.

In this contribution the focus lies on two particle clusters. For this case, E is given by

$$E = \frac{1}{2}m\omega_0^2(r_1^2 + r_2^2) + \frac{e^2 Z_{\text{eff}}^2}{4\pi\epsilon_0 d} \exp\left(-\frac{d}{\lambda_D}\right). \quad (5)$$

r_1 and r_2 are the radial positions of the first and second particle in the potential well and d is the interparticle distance. In this two particle system one finds a twofold degenerated sloshing mode, which occurs at the eigenfrequency of the confining potential well, $\omega_{\text{sl}}=\omega_0$, one rotating mode at a frequency of $\omega_r=0$ and one breathing mode. The screening length λ_D and the grain charge Z_{eff} can be determined from the angular frequency of the sloshing mode ω_{sl} , of the breathing mode ω_{br} and the equilibrium interparticle distance d .

B. REM

If we force a system of two particles to perform a rotation about their center of mass at an angular frequency ω , an additional centrifugal force is exerted on the dust grains. In a steady state, the centrifugal forces and the Yukawa repulsion must be balanced by the confining electric field. The confining potential is considered to be harmonic, $V(r)=\frac{1}{2}m\omega_0^2 r^2$ and the force balance reads

$$m\omega^2 \frac{d}{2} + \frac{e^2 Z_{\text{eff}}^2}{4\pi\epsilon_0 d} \left(\frac{1}{\lambda_D} + \frac{1}{d}\right) \exp\left(-\frac{d}{\lambda_D}\right) - m\omega_0^2 \frac{d}{2} = 0. \quad (6)$$

The equilibrium distance d of the dust particles now depends on the rotation frequency. Equation (6) can be written in the form³⁸

$$\omega = \omega_{\text{crit}} \left[1 - \left(\frac{d_0}{d}\right)^3 \frac{\lambda_D + d}{\lambda_D + d_0} \exp\left(\frac{d_0 - d}{\lambda_D}\right) \right]^{1/2}. \quad (7)$$

Here, d_0 is the interparticle distance at $\omega=0$ (no rotation of the cluster). $\omega_{\text{crit}}=\omega_0$ is given by the eigenfrequency of the confining potential well. If the rotation frequency exceeds the critical frequency ($\omega > \omega_{\text{crit}}$), the centrifugal force overcomes the confining force and the particles fly radially outward. (The particles are not longer confined.)

Figure 1 shows the interparticle distance d as a function of ω for different values of λ_D . The full line indicates the case of a pure Coulomb interaction ($\lambda_D \rightarrow \infty$). The effect of screening can be seen, as soon as λ_D is of the order of d_0 . Here the pole at ω_{crit} becomes sharper with decreasing screening length.

III. EXPERIMENTAL SETUP

The experiments presented were performed in a 13.56 MHz capacitively coupled parallel plate rf discharge. Figure 2 shows the experimental setup. The powered lower electrode has a diameter of 10 cm and is radially terminated by a grounded Faraday shield, which is separated from the driven electrode by a gap filled with a polytetrafluorethylene dielectric. The upper grounded electrode is placed 5 cm above the driven electrode. For dust confinement, a cylindrical cavity of 20 mm diameter and 2 mm depth was milled into the center of the lower electrode. The vacuum vessel has an inner diameter of 220 mm and a height of 170 mm. The vacuum pump and the gas inlet are connected to a common

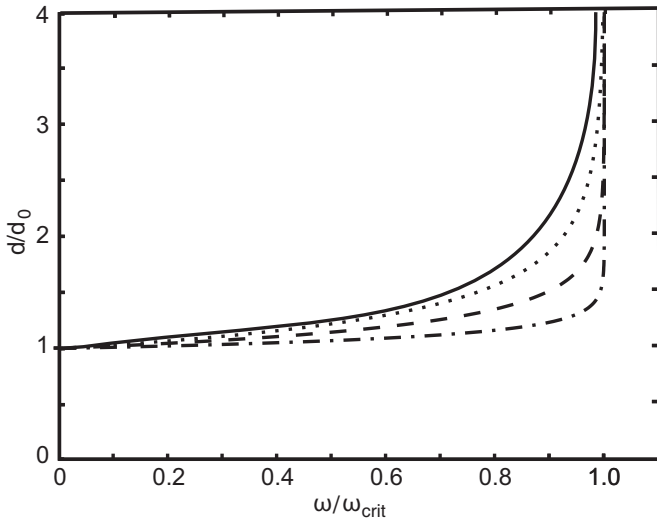


FIG. 1. Interparticle distance d vs rotation frequency ω [Eq. (7)] for different screening length $\lambda_D=1.1 d_{\min}$ (dotted line), $\lambda_D=0.4 d_{\min}$ (dashed line), and $\lambda_D=0.1 d_{\min}$ (dot-dashed line). The solid line indicates the case of pure Coulomb interaction.

port at the bottom of the chamber. The pump and gas handling system are decoupled from the plasma chamber by a ring-shaped cover plate that encircles the powered electrode and has an equidistant pattern of holes, in order to minimize directed neutral gas flows. The particles used in the experiments are monodisperse melamine formaldehyde spheres with a radius of 10 ± 0.1 and $6 \pm 0.1 \mu\text{m}$. They are illuminated by a laser fan (200 mW at 532 nm) and can be ob-

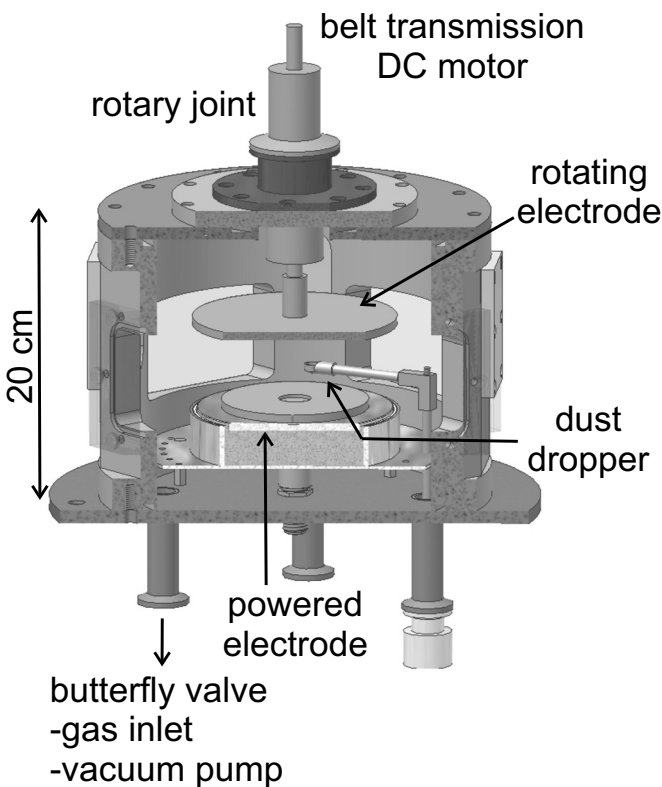


FIG. 2. Sketch of the experimental arrangement. An argon plasma is established between the driven lower electrode and the grounded upper electrode.

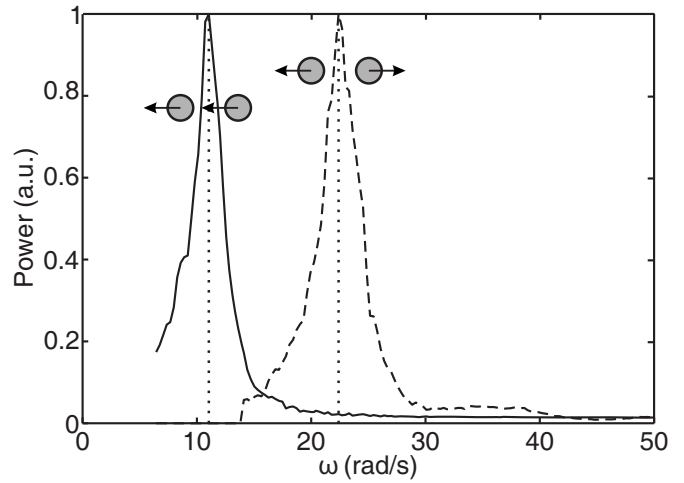


FIG. 3. Power spectrum of the center of mass motion (sloshing mode, full line) and of the interparticle distance (breathing mode, dashed line) for a two particle cluster ($r_d=6 \mu\text{m}$).

served side-on by two charge-coupled device (CCD) cameras under an angle of 90° . The dust grains are confined in a layer typically 5–10 mm above the electrode.

In order to expose dust particles to centrifugal forces, the upper electrode is connected via a rotary joint to a dc-motor outside the vacuum vessel, which allows rotation frequencies of the electrode up to approximately 30 s^{-1} . This causes a laminar rotational motion of the neutral gas, showing a decreasing flow velocity toward the lower electrode, due to viscous damping forces.⁴² Close to the rotation axis, the rotation frequency of the neutral gas column has a gradient in the vertical direction and does not depend on the radial position. So, at the position of the dust cluster, rotation frequencies up to 3 s^{-1} can be obtained.

IV. EXPERIMENTAL RESULTS

A. Normal modes

The experiments were performed at 4 Pa gas pressure and at a rf peak-to-peak voltage of $200 V_{pp}$. The thermal motion of a two-particle cluster was tracked with two CCD cameras from the side with 100 frames per second for a total observation time of 3000 s. This allows to reconstruct the time evolution of the interparticle distance and of the center of mass of the cluster. The sloshing and breathing mode frequencies were obtained from the power spectrum of this time series. In Fig. 3 the power spectrum for both modes for $6 \mu\text{m}$ particles are shown. The line widths of the peaks are a result of the neutral gas friction. The experimentally determined frequencies and the resulting effective charge number and screening lengths for 6 and $10 \mu\text{m}$ particles are summarized in Table I.

The normal mode analysis is particularly suitable for the regime of low gas pressures, where the particle motion can be treated as an underdamped harmonic oscillation. Hence,

$$\beta < \omega_0. \tag{8}$$

Here, ω_0 is the confinement frequency and

TABLE I. Experimentally determined values of the sloshing modes ω_{sl} and breathing modes ω_{br} , angular frequencies in rad/s for different particles radii r_d . Resultant effective charge number and screening length in millimeter.

r_d (μm)	ω_{sl}	ω_{br}	Z_{eff}	λ_D
6	11.0(± 0.3)	22.4(± 0.3)	20 600(± 3100)	0.49(± 0.11)
10	12.7(± 0.6)	24.8(± 0.6)	57 500($\pm 13 700$)	0.86(± 0.42)

$$\beta = \delta \frac{8}{\pi} \frac{p}{r_d \rho_d v_{\text{th},n}} \quad (9)$$

is the Epstein friction coefficient. p is the neutral gas pressure, ρ_d is the mass density of the oscillating particles, $v_{\text{th},n}$ is the thermal velocity of the gas atoms, and δ a coefficient of the order of unity, which takes into account how the gas atoms are deflected from the particle surface.⁴³ For $r_d = 6 \mu\text{m}$, $\rho_d = 1514 \text{ kg/m}^3$ (melamine formaldehyde), $\omega_0 = 10 \text{ rad/s}$, and argon at room temperature, Eq. (8) leads to the condition $p < 10 \text{ Pa}$. This is fulfilled for the presented experiments. However, in this parameter regime the normal mode analysis is ill conditioned. An uncertainty in the measurement of the mode frequencies is enhanced by one order of magnitude for the determination of the charge number and screening length. Therefore an accurate measurement of the mode frequencies is needed, which requires a long observation time. Furthermore, the power spectrum was averaged with a Hanning window of 20 s length resulting in a frequency resolution of $\Delta f = 0.05 \text{ Hz}$. This allows to determine the mode frequencies with an error smaller than 3%. Thus, the error of the obtained charge number and screening length is of the order of 30%.

B. REM

After the observation for the normal mode analysis was completed, the upper electrode, i.e., the two particle cluster was set into rotation. For a fixed rotation frequency of the cluster, the particle motion was tracked by the two CCD cameras for 60 s. This was done stepwise for increasing frequencies up to the critical value, where the centrifugal force overcomes the confining force and the dust grains flew radially outwards. In Fig. 4 the obtained interparticle distance d is plotted versus the rotation frequency f . The effective particle charge number, the screening length and the critical frequency can be obtained from the fit of Eq. (7) to the data points. The results are summarized in Table II.

The given errors are estimated from Monte Carlo simulations⁴⁴ based on the assumption that the frequency resolution is given by $\Delta f = (60 \text{ s})^{-1}$ and that the interparticle distance can be measured within an accuracy of ± 1.5 pixel ($\Delta d = 12 \mu\text{m}$).

The obtained values for effective charge number and screening length are in good agreement with the results from the normal mode analysis (previous section). The Debye length found is of the order of the interparticle distance, which is a typical result for experiments with flat dust clus-

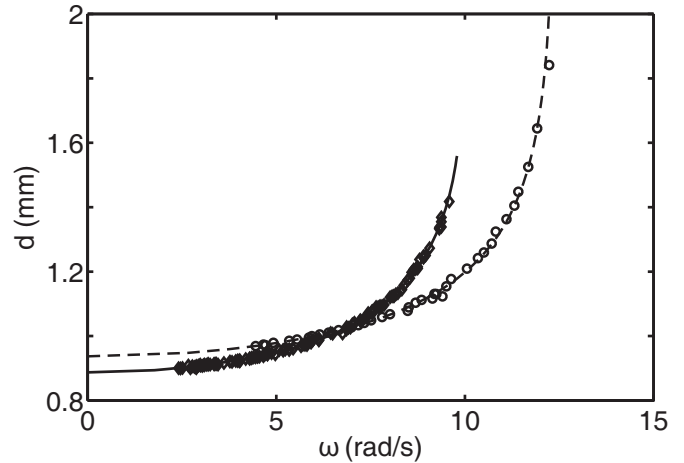


FIG. 4. Dependence of the interparticle distance d as a function of rotation frequency f for particles with $6 \mu\text{m}$ (diamonds) and $12 \mu\text{m}$ radius (circles). The solid and dashed lines are a fit of Eq. (7).

ters. Furthermore, both methods show a nonlinear dependency of particle charge and radius, which is contrary to the standard OML theory.

C. Verification of parabolic confinement

It is essential for the applicability of both techniques as a diagnostic of particle charge and screening length that the confining potential is harmonic. The measurement of the sloshing mode frequency of clusters with different particle numbers can be used to determine the curvature of the confining potential at the position of the dust grains. In fact, the one-particle sloshing mode is a measure of the curvature at the center of the potential well and the two-particle sloshing mode is a measure of the curvature at the equilibrium position of the particles. For this reason, the sloshing frequency of a one-particle $\omega_{sl,1}$ and a two-particle system $\omega_{sl,2}$ and the critical frequency ω_{crit} obtained by the REM method can be compared. In the case of a harmonic confinement it is

$$\omega_{sl,1} = \omega_{sl,2} = \omega_{\text{crit}} = \omega_0, \quad (10)$$

respectively, the curvature of the confining potential does not depend on the radial position.

The experimentally determined values for the 6 and 12 μm particle are shown in Table III. The measurements indicate that the confinement can be treated as harmonic, at least within the range, where the experiments are performed.

Furthermore, in Ref. 42 simulations of the plasma sheath for our electrode geometry and comparable plasma parameters are shown. A detailed description of the code is given in

TABLE II. Experimentally determined values of the critical angular frequency ω_{crit} in rad/s, effective charge number Z_{eff} , and screening length λ_D in millimeter.

r_d (μm)	ω_{crit}	Z_{eff}	λ_D
6	10.4(± 0.2)	19 500(± 1800)	0.68(± 0.18)
10	12.4(± 0.3)	60 300(± 8300)	0.6(± 0.16)

TABLE III. Experimentally determined values of the critical angular frequency ω_{crit} , the frequency of the sloshing mode for one $\omega_{\text{sl},1}$, and two $\omega_{\text{sl},2}$ particles in rad/s.

r_d (μm)	$\omega_{\text{sl},1}$	$\omega_{\text{sl},2}$	ω_{crit}
6	10.4(± 0.2)	11.0(± 0.3)	10.4(± 0.2)
10	12.6(± 0.3)	12.7(± 0.3)	12.4(± 0.3)

Ref. 45. As one result it was found that in a wide range of levitation heights, the potential is harmonic in the horizontal direction up to radial distances from the axis of 5 mm. The experiments mentioned above lie clearly within this harmonic range.

D. Vertical oscillation

Apart from normal modes oscillations in the horizontal plane, the dust grains perform a thermally excited oscillation in the vertical direction, too. The vertical oscillation frequency ω_z can be taken as a measure of the local ion n_i and electron density n_e , if the grain charge is known,²⁴

$$\omega_z^2 = \frac{Ze^2}{m_d \epsilon_0} n_i [1 - \alpha(z)]. \quad (11)$$

Here $\alpha(z) = \langle n_e/n_i \rangle_t$ is the time averaged ratio of electron and ion density depending on the vertical position z within the rf-sheath.

For $\omega_z = 125$ rad/s (6 μm particle) and $\omega_z = 86$ rad/s (10 μm particle) the resulting densities are shown in Table IV. Here, different $\alpha = 0.1, 0.2, 0.3$ are assumed and $Z = Z_{\text{eff}}$ is taken from the previous section.

The electron energy distribution in the rf sheath can be roughly considered as a two temperature Maxwellian with a small population at high energies.⁷ Hence, the electron contribution to the shielding length is dominated by the cold electrons with temperature T_e ,

$$\lambda_{De} = \left(\frac{e^2 n_e}{\epsilon_0 k_B T_e} \right)^{-1/2}. \quad (12)$$

In a plasma sheath with intermediate collisionality the streaming velocity of the ions u_i is of the order of the Bohm velocity v_B ,

$$u_i = v_B = \sqrt{\frac{k_B T_e}{m_i}}. \quad (13)$$

Therefore, the kinetic energy of the ions E_i is much larger than their thermal energy. For an isotropic, monoenergetic ion energy distribution Daugherty *et al.*⁴⁶ gave an ion screening length of

$$\lambda_{Di} = \left(\frac{e^2 n_i}{\epsilon_0 2 E_i} \right)^{-1/2}. \quad (14)$$

In Table IV estimations of λ_{Di} , λ_{De} , and the total screening length

$$\lambda_D = \left(\frac{1}{\lambda_{De}^2} + \frac{1}{\lambda_{Di}^2} \right)^{-1/2} \quad (15)$$

are given for an electron temperature of $T_e = 3$ eV.

The screening lengths λ_D derived from the electron and ion densities are comparable to the screening length measured in the previous sections. A comparison of electron and ion Debye length indicates that screening is dominated by the ions. Furthermore, the local ion density in combination with the plasma bulk electron temperature gives a good approximation of λ_D , as discussed in Refs. 22 and 23,

$$\lambda_D \approx \left(\frac{e^2 n_i}{\epsilon_0 k_B T_e} \right)^{-1/2}. \quad (16)$$

V. DISCUSSION

A. Diagnostics

The analysis of thermally excited normal modes is applicable at low gas pressures. For the presented experiments Eq. (8) leads to $p < 10$ Pa. This is fulfilled for the aforementioned experiments ($p \approx 4$ Pa), nevertheless it is a strong restriction because dusty plasma experiments are usually performed at pressures between 1 and 100 Pa.

In contrast to the normal mode analysis REM takes advantage of higher gas pressures. The Brownian motion of the particles is damped by the gas, which superimposes the cluster rotation and causes noise. Therefore this method, as described above, becomes difficult for gas pressures much lower than 4 Pa.

Both methods have the advantage that the determination of particle charge and screening length is independent of the knowledge of the plasma parameters. This is particularly valuable for dust particles in the sheath of rf plasmas, where Langmuir probes are not applicable. Furthermore, both methods are noninvasive. The normal mode analysis is based on the observation of the thermal motion of the particles and therefore is eminently noninvasive. REM requires a mechanically driven neutral gas flow. The flow velocities of the neutral gas do not exceed a few meters per second. This is sufficiently slow, so that no influence on the plasma is expected. However, the obtained values are only reliable, if the basic assumptions of a harmonic confinement and a Yukawa interaction are fulfilled.

The normal mode analysis requires a confinement, which can be treated as harmonic, for radial displacements from the

TABLE IV. Electron and ion density n_e , n_i in 10^{14} m^{-3} for different values of α and particle radii r_d . Screening lengths λ_{De} , λ_{Di} , and λ_D in millimeter.

r_d (μm)	α	n_i	n_e	λ_{De}	λ_{Di}	λ_D
6	0.1	4.1	0.41	2	0.63	0.60
	0.2	4.7	0.93	1.3	0.60	0.54
	0.3	5.3	1.6	1.0	0.56	0.49
12	0.1	3.0	0.30	2.3	0.74	0.71
	0.2	3.4	0.68	1.6	0.70	0.64
	0.3	3.9	1.2	1.2	0.66	0.57

center of the potential well up to the cluster radius. For REM, as described in Sec. IV B, the harmonic range must be considerably larger (twice the cluster radius), since the rotation frequency of the cluster had been increased until the cluster diameter was doubled. According to Sec. IV C a harmonic confinement is a good approximation for the presented experiments.

The potential distribution around a dust grain in the sheath of a rf discharges is a difficult issue and not fully understood yet. It is known that a Yukawa potential overestimates the ion density close to the grain and therefore the shielding effect of the ions. Hence, a Yukawa potential can only be valid for intermediate distances from the particle, typically between one and a few Debye lengths.² Here, the grain charge must be replaced with an effective charge, which is somewhat larger than the actual grain charge. Therefore REM and normal mode analysis can only be sensitive to the effective charge. The interparticle distance found in the experiments is of the order of the Debye length and in a range, where a Yukawa potential is a reasonable approximation. This is a characteristic result for experiments with flat dust clusters in rf discharges, where usually $\kappa=d/\lambda_D$ values between 0.5 and 2 are found.^{47,48}

The effective charge numbers obtained by both methods differ by approximately 5%, which is within the given error margin. The difference in the screening length λ_D is of the order of 30%, which can be explained by the larger uncertainty in λ_D . So, the REM is in fair agreement with the normal mode analysis.

B. Dust charge and screening length

The combination of normal mode analysis or REM with the vertical oscillation method (Sec. IV D) can be used as a measure of the local plasma densities n_e and n_i , which allows an estimation of the ion and electron Debye lengths λ_{Di} and λ_{De} . The electron Debye length found is considerably larger than the one obtained by the experiments, even for an electron duty cycle as high as $\alpha=0.3$. This indicates that shielding is not due to the electrons, but rather due to the ions. This is further supported by a simple approximation of the ion Debye length by assuming monoenergetic ions having Bohm energy. The local ion Debye length λ_{Di} is in good agreement with the observed λ_D .

Furthermore, a strong nonlinearity between particle radius and particle charge is found. The negative floating potential of the dust particles, $\Phi_f = -Ze/(4\pi\epsilon_0 r_d)$, rises from $\Phi_f = -4.8$ V to $\Phi_f = -8.6$ V as the particle radius r_d increases from 6 to 10 μm . This is in contrast to dust grains in the plasma bulk, where OML theory predicts a floating potential independent of the particle radius. Although a comparable behavior is found in other experiments in rf discharges,⁷⁻¹² the reason for this strongly enhanced floating potential is not fully understood.

However, for low gas pressures, where the ion flow is not mobility-limited, one possible explanation could be the acceleration of the ions within the plasma sheath. The larger the particles, the deeper the particle enter the sheath and the faster the ions. According to the OML theory, this leads to a

smaller collection radius for the ions and thus to a smaller ion current to the dust grain resulting in a more negative floating potential.

According to Ref. 49, the mean free path of the argon ions λ_{mfp} is approximately 1 mm for 4 Pa gas pressure. So, it is $\lambda_{\text{mfp}} > \lambda_D \gg r_d$ for the presented experiments. In this parameter regime the OML theory is a reasonable approximation.

VI. CONCLUSION

REM can be used as a reliable diagnostic for particle charge and screening length. The achievable accuracy can be better than 10% for the determination of the (effective) charge. Furthermore, it is noninvasive and does not require prior knowledge of the plasma parameters.

In contrast to methods that are based on the observation of wave phenomena or particle oscillations, the REM is also applicable at higher gas pressures. Results for higher pressures were shown in Ref. 38. In that regime the normal mode oscillations are overdamped.

A disadvantage of the REM is the long time for a single measurement, which requires stability of the experimental parameters. Furthermore, a smooth rotation of the cluster, due to rotating neutral gas column, requires a high cylindrical symmetry.

REM can be easily combined with a measurement of the vertical resonance frequency allowing a good estimation of the local plasma densities in the plasma sheath. Here, dust particles can be used as probes were Langmuir probes are not applicable.

For the discussed parameter regime the measurements give a strong indication that the horizontal screening is dominated by the ions. The combination of local ion density and electron bulk temperature give a good quantitative approximation of the horizontal screening length. This is in agreement with results described in Refs. 21 and 22.

ACKNOWLEDGMENTS

This work was supported by the Deutsche Forschungsgemeinschaft (DFG) in the framework of the SFB-TR24 Greifswald-Kiel, Project A2.

¹J. E. Allen, *Phys. Scr.* **45**, 497 (1992).

²M. Lampe, G. Joyce, G. Ganguli, and V. Gavrilchaka, *Phys. Plasmas* **7**, 3851 (2000).

³I. H. Hutchinson and L. Patacchini, *Phys. Plasmas* **14**, 013505 (2007).

⁴J. Goree, *Phys. Rev. Lett.* **69**, 277 (1992).

⁵E. C. Whipple, T. G. Northrop, and D. A. Mendis, *J. Geophys. Res.* **90**, 7405, doi:10.1029/JA090iA08p07405 (1985).

⁶J. Schulze, B. G. Heil, D. Luggenhölscher, R. P. Brinkmann, and U. Czarnetzki, *J. Phys. D: Appl. Phys.* **41**, 195212 (2008).

⁷X. Chen, *IEEE Trans. Plasma Sci.* **25**, 1117 (1997).

⁸U. Kortshagen and G. Mümken, *Phys. Lett. A* **217**, 126 (1996).

⁹E. B. Tomme, D. A. Law, B. M. Annaratone, and J. E. Allen, *Phys. Rev. Lett.* **85**, 2518 (2000).

¹⁰A. A. Samarian and S. V. Vladimirov, *Phys. Rev. E* **67**, 066404 (2003).

¹¹M. Bacharis, M. Coppins, and J. E. Allen, *Plasma Sources Sci. Technol.* **19**, 025002 (2010).

¹²J. Blažek, R. Bartoš, P. Basner, H. Kersten, and P. Špatenka, *Eur. Phys. J. D* **54**, 219 (2009).

¹³S. V. Vladimirov and M. Nambu, *Phys. Rev. E* **52**, R2172 (1995).

¹⁴U. Konopka, G. E. Morfill, and L. Ratke, *Phys. Rev. Lett.* **84**, 891 (2000).

- ¹⁵M. Chaudhuri, S. Khrapak, R. Kompaneets, and G. Morfill, *IEEE Trans. Plasma Sci.* **38**, 818 (2010).
- ¹⁶F. Melandsø and J. Goree, *Phys. Rev. E* **52**, 5312 (1995).
- ¹⁷V. E. Fortov, A. G. Khrapak, V. I. Molotkov, and O. F. Petrov, *Physics-Uspokhi* **47**, 447 (2004).
- ¹⁸V. E. Fortov, A. V. Ivlev, S. A. Khrapak, A. G. Khrapak, and G. E. Morfill, *Phys. Rep.* **421**, 1 (2005).
- ¹⁹S. Khrapak, D. Samsonov, G. Morfill, H. Thomas, V. Yaroshenko, H. Rothermel, V. Fortov, A. Nefedov, V. Molotkov, O. Petrov, A. Lipaev, A. Ivanov, and Y. Baturin, *Phys. Plasmas* **10**, 1 (2003).
- ²⁰T. Nitter, *Plasma Sources Sci. Technol.* **5**, 93 (1996).
- ²¹R. Kompaneets, U. Konopka, A. V. Ivlev, V. Tsytovich, and G. Morfill, *Phys. Plasmas* **14**, 052108 (2007).
- ²²T. E. Sheridan, *J. Appl. Phys.* **106**, 033303 (2009).
- ²³A. Piel and A. Melzer, *Plasma Phys. Controlled Fusion* **44**, R1 (2002).
- ²⁴A. Melzer, T. Trottenberg, and A. Piel, *Phys. Lett. A* **191**, 301 (1994).
- ²⁵A. Homann, A. Melzer, and A. Piel, *Phys. Rev. E* **59**, R3835 (1999).
- ²⁶N. J. Prior, L. W. Mitchell, and A. A. Samarian, *Jpn. J. Appl. Phys., Part 1* **36**, 1249 (2003).
- ²⁷A. A. Samarian and B. W. James, *Plasma Phys. Controlled Fusion* **47**, B629 (2005).
- ²⁸A. A. Samarian and B. W. James, *Phys. Lett. A* **287**, 125 (2001).
- ²⁹J. Kong, J. Carmona-Reyes, J. Creel, and T. Hyde, *IEEE Trans. Plasma Sci.* **35**, 323 (2007).
- ³⁰T. E. Sheridan and J. Goree, *Phys. Fluids B* **3**, 2796 (1991).
- ³¹A. Homann, A. Melzer, S. Peters, R. Madani, and A. Piel, *Phys. Rev. E* **56**, 7138 (1997).
- ³²S. Nunomura, D. Samsonov, and J. Goree, *Phys. Rev. Lett.* **84**, 5141 (2000).
- ³³S. Nunomura, J. Goree, S. Hu, X. Wang, and A. Bhattacharjee, *Phys. Rev. E* **65**, 066402 (2002).
- ³⁴U. Konopka, L. Ratke, and H. M. Thomas, *Phys. Rev. Lett.* **79**, 1269 (1997).
- ³⁵A. Melzer, *Phys. Rev. E* **67**, 016411 (2003).
- ³⁶T. E. Sheridan, *Phys. Rev. E* **72**, 026405 (2005).
- ³⁷T. E. Sheridan, M. R. Katschke, and K. D. Wells, *Rev. Sci. Instrum.* **78**, 023502 (2007).
- ³⁸J. Carstensen, F. Greiner, L. Hou, and A. Piel, *IEEE Trans. Plasma Sci.* **38**, 788 (2010).
- ³⁹A. Melzer, M. Klindworth, and A. Piel, *Phys. Rev. Lett.* **87**, 115002 (2001).
- ⁴⁰V. A. Schweigert and F. M. Peeters, *Phys. Rev. B* **51**, 7700 (1995).
- ⁴¹S. G. Amiranashvili, N. G. Gusein-zade, and V. N. Tsytovich, *Phys. Rev. E* **64**, 016407 (2001).
- ⁴²J. Carstensen, F. Greiner, L.-J. Hou, H. Maurer, and A. Piel, *Phys. Plasmas* **16**, 013702 (2009).
- ⁴³P. S. Epstein, *Phys. Rev.* **23**, 710 (1924).
- ⁴⁴W. Press, S. Teukolsky, W. Vetterling, and B. Flannery, *Numerical Recipes in C*, 2nd ed. (Cambridge University Press, Cambridge, 1992).
- ⁴⁵L. J. Hou and Y. N. Wang, *Phys. Plasmas* **12**, 042104 (2005).
- ⁴⁶J. E. Daugherty, R. K. Porteous, M. D. Kilgore, and D. B. Graves, *J. Appl. Phys.* **72**, 3934 (1992).
- ⁴⁷V. Nosenko, J. Goree, Z. W. Ma, D. H. E. Dubin, and A. Piel, *Phys. Rev. E* **68**, 056409 (2003).
- ⁴⁸A. Piel, V. Nosenko, and J. Goree, *Phys. Plasmas* **13**, 042104 (2006).
- ⁴⁹L. S. Frost, *Phys. Rev.* **105**, 354 (1957).

A.4

MASS CHANGES OF MICROPARTICLES IN A PLASMA OBSERVED BY A PHASE-RESOLVED RESONANCE METHOD

Jan Carstensen, Hendrik Jung, Franko Greiner, and Alexander Piel

Reprinted with permission from
Jan Carstensen, Hendrik Jung, Franko Greiner, and Alexander Piel,
Physics of Plasmas, Vol. 18, 033701 (2011).
Copyright 2011, American Institute of Physics

Mass changes of microparticles in a plasma observed by a phase-resolved resonance method

Jan Carstensen, Hendrik Jung, Franko Greiner, and Alexander Piel
IEAP, Christian-Albrechts-Universität, D-24098 Kiel, Germany

(Received 2 December 2010; accepted 30 January 2011; published online 3 March 2011)

The influence of a plasma environment on melamine formaldehyde particles is studied. High-precision measurements of the vertical confinement frequency with a phase-resolved resonance method indicate that the particle mass is affected in two ways: the deposition of sputtered material at the particle leads to a mass gain, whereas the outgassing of water causes a mass loss.

© 2011 American Institute of Physics. [doi:10.1063/1.3556677]

I. INTRODUCTION

Dust particles in a laboratory plasma attain a net negative charge q_d and a negative surface potential ϕ_f according to the floating condition, which is defined by the equality of electron and ion flux to the particle. In the capacitance model, charge and surface potential are related by $q_d = 4\pi\epsilon_0 r_d \phi_f$ for a small spherical particle of radius r_d .¹ Models for the dust charge were discussed in the orbital motion limit (OML),^{2,3} including ion-neutral collisions,^{4,5} and in terms of computer simulations.⁶

These charged particles can be confined in the plasma sheath, where the electric field compensates gravity. There, the dust grains can form flat crystal-like structures. This offers the possibility to study effects such as oscillations, waves, and instabilities in a two-dimensional geometry (see, e.g., Ref. 7).

The comparison between simulations, theory, and experiments of these dust systems requires a basic understanding of the electrostatic particle interaction and the confining forces. Therefore, the experimental determination of the particle charge q_d is of key interest. One established charge measurement technique is the resonance method,^{8–10} in which the particle is treated as a damped harmonic oscillator driven by a sinusoidal modulation of the electrode voltage. The eigenfrequency ω_0 of the vertical confinement well is related to the charge-to-mass ratio of the particle. This method requires a parabolic confinement. In Refs. 11–13, it was shown that the sheath potential is very close to parabolic over a large part of the plasma boundary. Hence, the vertical oscillation of a particle can be treated as harmonic for small oscillation amplitudes (typically less than 1/10 of the sheath width^{9,11}).

Melamine formaldehyde (MF) particles are a common dust simulant used in many dusty plasma experiments because they are available with a very narrow size distribution (almost monodisperse), a well-defined mass density and a spherical shape. Pavlů *et al.*¹⁴ have studied the properties of such MF particles confined in a Paul trap under ultrahigh vacuum conditions. High-precision measurements of the particle charge and mass showed a continuous mass loss of the MF particles during long-time exposure in vacuum, which is accelerated when the particle temperature is increased. This

effect was attributed to the outgassing of water bound in the bulk material.

So far, the resonance method or other *in situ* diagnostics for the charge-to-mass ratio of dust grains in a plasma have not achieved a precision comparable to the measurements in a Paul trap.¹⁴ In most dusty plasma experiments, relative mass changes of a few percent cannot be resolved; the mass of the particles is usually assumed constant. It is the intention of this contribution to show that MF particles in a plasma environment that is typical for dusty plasma experiments are subject to at least two effects, which can lead to an increase or decrease of the particle mass. Furthermore, it is demonstrated that a modified resonance method, accounting for the phase shift between particle oscillation and excitation, allows a high-precision measurement of ω_0 .

II. PHASE RESOLVED RESONANCE METHOD

A. Method

A dust particle confined in the plasma sheath, which is set into vertical oscillation of small amplitude by an external sinusoidal force $F_{\text{ext}} = K \cdot \sin(\omega t)$, can be treated as a damped harmonic oscillator. The trajectory $Y(t)$ depends on the eigenfrequency ω_0 and the damping rate γ

$$Y(t) = a(\omega)\sin(\omega t) + b(\omega)\cos(\omega t), \quad (1)$$

with

$$a(\omega) = \frac{K(\omega_0^2 - \omega^2)}{(\omega_0^2 - \omega^2)^2 + (2\gamma\omega)^2}, \quad (2)$$

$$b(\omega) = -\frac{2K\gamma\omega}{(\omega_0^2 - \omega^2)^2 + (2\gamma\omega)^2}. \quad (3)$$

The amplitude of the oscillation is given by

$$A(\omega) = \sqrt{a^2 + b^2} = \frac{K}{\sqrt{(\omega_0^2 - \omega^2)^2 + (2\gamma\omega)^2}}. \quad (4)$$

In Fig. 1(a), A , a , and b are plotted versus the excitation frequency ω for a quality factor $Q = \omega_0 / \gamma = 2.5$. The resonance frequency $\omega_r = \sqrt{\omega_0^2 - 2\gamma^2}$ is given by the maximum of $A(\omega)$. The root of $a(\omega)$ is at $\omega = \omega_0$.

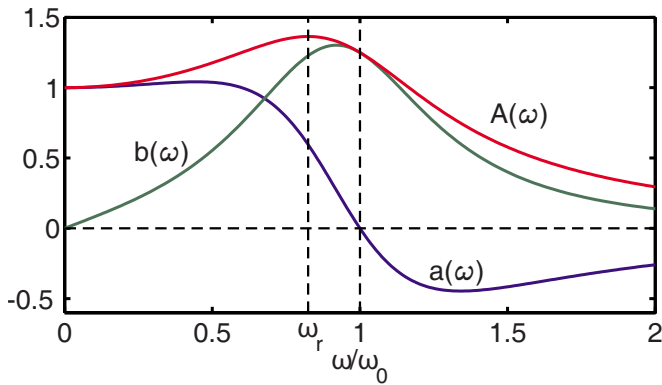


FIG. 1. (Color online) A , a , and b vs ω for $Q = \gamma/\omega_0 = 2.5$ normalized by ω_0^2/K [Eqs. (2)–(4)].

In the standard resonance method, the oscillation amplitude A is measured for different excitation frequencies. Figure 2 shows four typical resonance curves for gas pressures between 2 and 50 Pa and the corresponding fit by Eq. (4). Lower gas pressures (circles and crosses) result in a higher quality factor Q and a sharper peak around the resonance frequency than higher pressures (squares and triangles). The charge of the particle can be calculated from

$$\omega_0^2 = \frac{q_d \rho}{m \epsilon_0} \quad (5)$$

if the particle mass m and charge density ρ at the position of the dust particle is known.⁸ ρ can be determined by assuming a parabolic sheath potential and a measurement of the potential drop about the plasma sheath (e.g., by Langmuir probes), as it is discussed in Ref. 11. The relative uncertainty of ρ is typically of the order of 20%. Because of the large error in ρ , an estimate of q_d does not need a precise determination of ω_0 .

The focus of this contribution is on relative changes of the charge-to-mass ratio of the particles for constant plasma parameters ($\rho = \text{const.}$) and not on absolute measurements. Therefore, an accurate determination of ω_0 is desirable. This is achieved in two ways. On the one hand, a reduction of the gas pressure results in a higher quality factor and a sharper peak around the resonance frequency. For the following measurements, we have $Q \approx 30$. On the other hand, it is advantageous to measure $a(\omega)$ instead of $A(\omega)$. The reading of the zero crossing at ω_0 is more precise than the determination of the maximum of $A(\omega)$, which is somewhat smaller than ω_0 due to neutral gas friction. The quantities $a(\omega)$ and $b(\omega)$ can be derived from the phase difference between the excitation signal and the particle oscillation.

A stroboscopic observation of the particle trajectory, which is synchronized with the excitation signal, allows to measure the vertical position Y at a specific time t_φ within an oscillation period. The phase shift between the stroboscopic observation and the excitation signal is $\varphi = \omega t_\varphi$. The particle position as a function of φ is given by

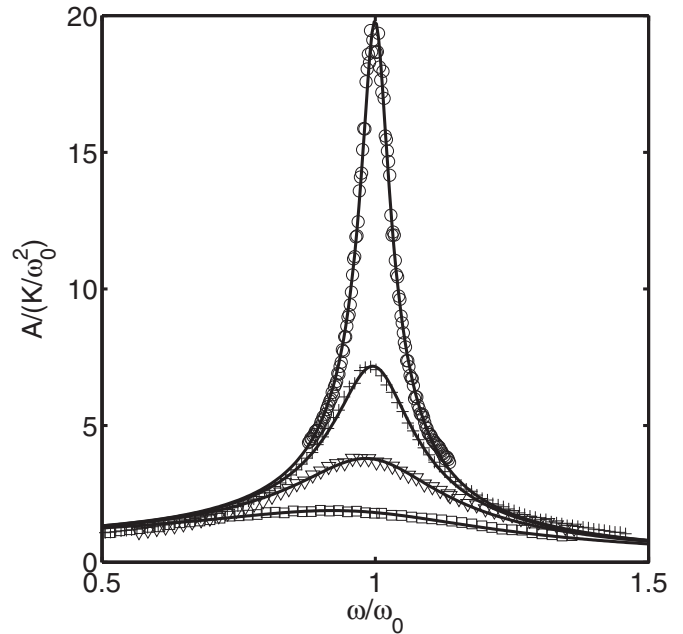


FIG. 2. Standard resonance curves (A vs ω) for different gas pressures $p = 2.5, 9, 20,$ and 50 Pa (circles, crosses, triangles, and squares). The full lines are fits of Eq. (4). The corresponding quality factors are $Q = 40, 14, 8, 4$.

$$Y_\varphi = a(\omega)\sin(\varphi) + b(\omega)\cos(\varphi). \quad (6)$$

Hence, a phase difference of $\varphi = 90^\circ$ between excitation signal and strobe allows a direct measurement of $a(\omega)$.

B. Setup and measurement

The experiments were performed in a capacitively coupled parallel-plate radio frequency (rf) discharge (13.56 MHz) at gas pressures $p \approx 10$ Pa (argon). The powered lower electrode had a diameter of 6 cm. The electrode consisted of an indium tin oxide (ITO) coated glass disk with a diameter of 2 cm that is surrounded by a stainless steel ring. Between the ITO glass and the steel ring was a 2 mm recession for the radial confinement of the dust particles. The electrode was radially terminated by a grounded Faraday shield, which was separated from the driven electrode by a gap filled with a polytetrafluorethylene (PTFE) dielectric (Fig. 3). The upper grounded electrode was placed 15 cm above the driven electrode. The vacuum pump and the gas inlet were connected to a common port at the bottom of the chamber to minimize unwanted gas flows. We used monodisperse melamine formaldehyde spheres with a radius of $(6 \pm 0.1) \mu\text{m}$ that were confined in a layer typically 5–10 mm above the center of the driven electrode. An expanded laser beam illuminated the particles from below (through the ITO glass) and the motion of the particles could be observed with a video camera from the side.

A sketch of the setup for the stroboscopic observation of the particle oscillation is shown in Fig. 3(a). The rf signal was modulated by a sinusoidal voltage from the function generator. The synchronization pulse of the function generator triggered the start of the camera exposure. The delay t_φ between the start of the exposure and the synchronization

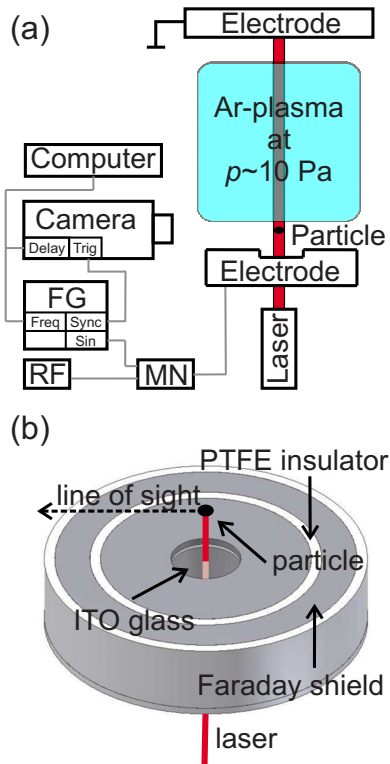


FIG. 3. (Color online) (a) Sketch of the experimental setup: The trigger delay of the camera and the frequency of the function generator (FG) are controlled by the computer. The exposure time of the camera is triggered by the FG. The signal of the rf generator (RF) is modulated by a sine wave from the FG and connected via a matching network (MN) to the driven electrode. (b) Detailed sketch of the driven electrode. A dust particle is confined in the plasma boundary. The particle is illuminated by a laser through the ITO coated glass plate. The particle position is tracked with the camera.

pulse was adjustable. This allowed to measure the Y_φ positions of the particles at a given phase $\varphi = \omega t_\varphi$ within an oscillation period. A resonance curve was obtained by measuring Y_φ for different excitation frequencies but constant phase shift.

Figure 4 shows the resonance curve for one particle at a gas pressure of 9 Pa and a rf voltage of 200 V_{pp}. The exposure time of the camera was ≈ 1 ms, which is much less than the period of the excitation signal. In order to reduce the error of Y_φ , the particle position was averaged over ten consecutive frames for each excitation frequency. Further, the rest position of the particle defines the zero point of the vertical length scale Y . Measuring two resonance curves using $Y_\varphi = \frac{1}{2}(Y_\varphi - Y_{\varphi+180^\circ})$ [according to Eq. (6)] allows an accurate determination of the zero point. In Fig. 4(a), Y_{90° and Y_{270° are plotted versus the excitation frequency ω ($Y_{90^\circ} - Y_{270^\circ}$) and a fit of Eq. (6) are shown in Fig. 4(b). From the fit parameter $\omega_0 = (162.92 \pm 0.04) \text{ s}^{-1}$ and $\gamma = (5.07 \pm 0.04) \text{ s}^{-1}$ are obtained.

The given errors are estimated from synthetic data as described in Ref. 15. It is assumed that the particle position can be measured within 1 pixel accuracy and that the error of the excitation frequency is negligible. The relative uncertainty of ω_0 is less than 10^{-3} and the uncertainty of γ is of the order of 10^{-2} .

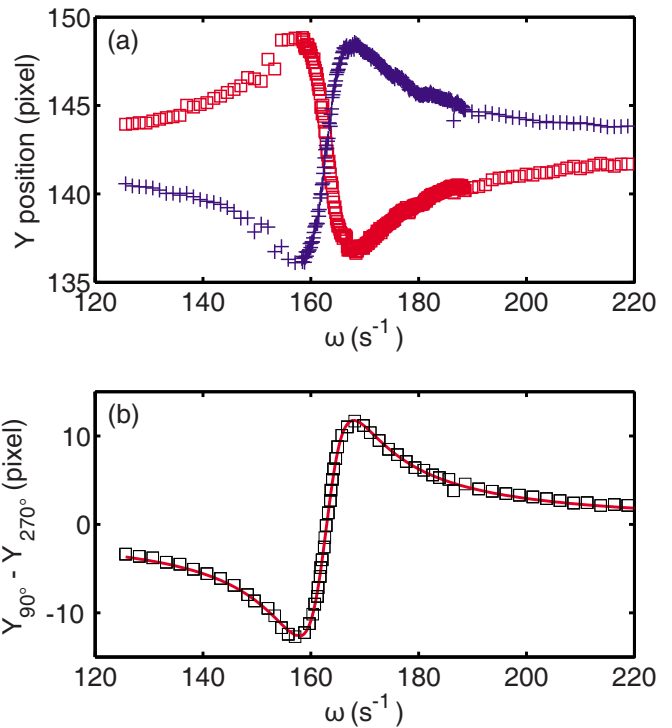


FIG. 4. (Color online) (a) $Y_{90^\circ}(Y_{270^\circ})$ position vs excitation frequency ω for a 90° (270°) phase-shifted strobe signal [squares (crosses)]. (b) ($Y_{90^\circ} - Y_{270^\circ}$) vs excitation frequency ω (squares). (The number of data points shown was reduced for clarity.) The full line is a fit of Eq. (6).

III. CONTINUOUS MEASUREMENT OF THE EIGENFREQUENCY

Repetitive measurements of the resonance curves over a few hours for constant plasma parameters were performed. We have found that the eigenfrequency ω_0 tends to increase or decrease depending on the preparation of the particles. This is shown in detail in the following subsections.

The eigenfrequency depends on the particle charge-to-mass ratio and the local charge density of the plasma sheath, which corresponds to the gradient of the sheath electric field. Parallel to the resonance method, the ion saturation current of a Langmuir probe was recorded, which remained constant over the full measurement time. So, the observed trend of the eigenfrequency cannot be attributed to a change of the plasma parameters.

A. Increasing eigenfrequency

For a gas pressure of 9 Pa and a rf voltage of 240 V_{pp}, the resonance frequency increases and reaches a saturation level after approximately 10 h [Fig. 5(a)]. The small frequency jump at T=8 h is possibly due to an adjustment of the pressure control unit or a change of the room temperature. If a constant particle charge is assumed, this frequency change corresponds to a relative mass loss of $\approx 10\%$. A comparable mass loss was observed by Pavlů *et al.*¹⁴ after the particles were baked out. This was attributed to the outgassing of water originally bound in the bulk material.

Assuming that the total mass of the dust particle m_d is given by the mass of the MF particle m_m and of the bound water m_w and that m_w is reduced exponentially by outgassing

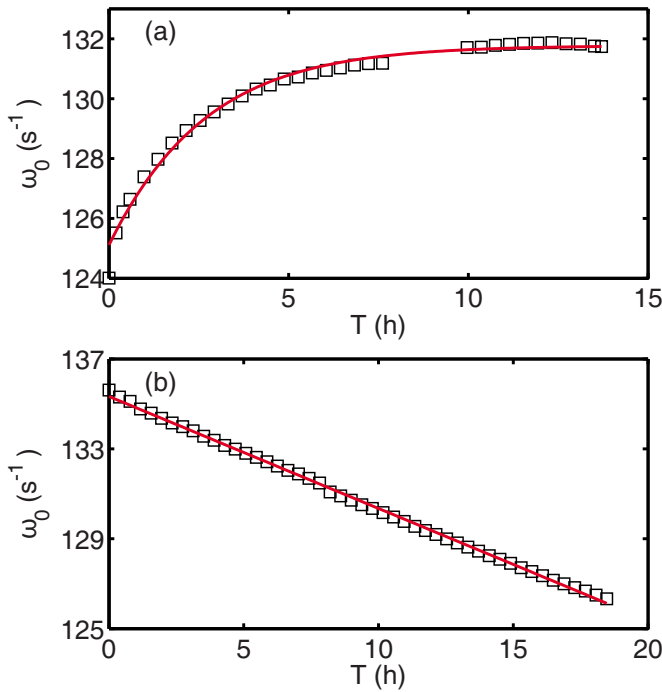


FIG. 5. (Color online) (a) Eigenfrequency ω_0 vs time T for a gas pressure of $p=9$ Pa and rf voltage of $U_{rf}=240 V_{pp}$ (squares). The full line is a fit of Eq. (8). (b) ω_0 vs T for $p=9$ Pa and $U_{rf}=340 V_{pp}$ (squares). The full line is a fit of Eq. (10). (For clarity, only every second data point is shown.)

$$m_w(t) = m_w(0) \exp\left(-\frac{t}{\tau}\right), \quad (7)$$

while m_m and the particle charge remain constant, the eigenfrequency of the particle evolves as

$$\omega_0(t) = \omega_0(0) \left[\frac{1 + m_w(0)/m_m}{1 + (m_w(0)/m_m) \exp(-t/\tau)} \right]^{1/2}. \quad (8)$$

The comparison of the measured eigenfrequency ω_0 with the model (8) is shown in Fig. 5(a) and shows good agreement. From the fit parameters, the ratio $m_w(0)/m_m=0.11$ is obtained. The timescale of the outgassing process is of the order of hours ($\tau=2.5$ h). The mass fraction of the bound water is in good agreement with the results by Pavlů *et al.*¹⁴ Furthermore, we performed a thermogravimetry analysis (TGA) of a MF particles sample. A 12% mass reduction was found at a sample temperature of 100 °C. This supports the assumption that the mass loss is due the outgassing of water. Alternative models for the eigenfrequency increase are discussed in Sec. IV.

B. Decreasing eigenfrequency

When the rf voltage is increased to 340 V_{pp} and the measurement is started several hours after the dust particle was dropped into the plasma, a linear decay of the eigenfrequency is observed, as shown in Fig. 5(b). In this case, most of the potentially bound water should have been outgassed, as expected from the time scale found in Sec. III A.

One explanation for this increase could be the deposition of material at the particle surface from sputtering of electrode material. If the radius of the dust grain is slightly in-

creased by the sputtered material and the accumulation rate is proportional to the particle surface, the dust radius changes as $r(t)=r_0(1+\alpha t)$. If the surface potential remains constant, the grain charge is given by $q_d(t)=q_d(0)(1+\alpha t)$. If ρ (ρ_m) is the mass density of the sputtered material (MF), the time dependence of the eigenfrequency is

$$\omega_0(t) = \omega_0(0) \left\{ \frac{1 + \alpha t}{1 + \rho/\rho_m[(1 + \alpha t)^3 - 1]} \right\}^{1/2}. \quad (9)$$

For $|\alpha t| \ll 1$, a Taylor expansion of Eq. (9) yields

$$\omega_0(t) = \omega_0(1 + ct), \quad (10)$$

with $c=(1-3\rho/\rho_m)\alpha/2$. Assuming $\rho/\rho_m \approx 1$, $|\alpha t|$ does not exceed 0.1 for the presented measurements. Hence, linearization is justified.

In order to verify that material was sputtered within the plasma chamber, a silicon wafer was placed on the electrode. After 7 h of plasma operation, the surface of the silicon wafer was analyzed by x-ray photoelectron spectroscopy (XPS). The wafer was coated with iron and fluorine compounds, which was expected because the electrode is made of stainless steel and the insulator is PTFE.

The almost linear decay of ω_0 allows an error estimation for the phase-resolved resonance method based on experimental data. As in the previous measurement, a small frequency jump occurs at $T=8$ h [Fig. 5(b)]. Therefore, only measurements for $T>8$ h are taken into account. The root-mean-square deviation between a linear regression and the data points is $\sigma=0.03$ s^{-1} , which is equivalent to a relative error of less than 3×10^{-4} . This is in good agreement with the error estimate from Sec. II.

IV. DISCUSSION

The phase-resolved resonance method (Sec. II) is a modification of the standard resonance method;⁸ it is highly sensitive to the vertical confinement frequency ω_0 . The sensitivity is achieved in two ways. First, an offset-free determination of $a(\omega)$ can be realized by a difference measurement of two resonance curves with a phase shift of 180°. Second, the stroboscopic observation allows a measurement of $a(\omega)$ having a zero crossing at $\omega=\omega_0$ instead of the amplitude $A(\omega)$ having a maximum at $\omega=\omega_r$. Furthermore, the measurements were performed at low gas pressures resulting in a high quality factor. Thus, $a(\omega)$ crosses zero with a steep slope.

The observed changes of the eigenfrequency can be attributed to a change of the particle properties. Langmuir probe measurements showed that the plasma parameters remained constant over the observation time (Sec. III). The deposition process could be separated from the outgassing process by starting the measurement a few hours after the particle had been dropped into the plasma. For low rf powers, the outgassing was the dominant effect.

The mass gain of the MF particles can explain the observed decrease of the eigenfrequency. Under the same plasma conditions, XPS measurements of the surface of a

small silicon wafer showed that electrode material is sputtered. Likewise, the model of a constant coating rate (Sec. III B) can explain the almost linear decay.

The outgassing of water is a reasonable explanation for the observed eigenfrequency increase and its saturation (Sec. III A). The mass loss of about 10% is in good agreement with the TGA measurement (Sec. III A) and the findings of Pavlů *et al.*¹⁴ for MF particles under ultrahigh vacuum conditions after baking out at 240 °C. However, for nonheated particles, only a very slow mass loss over a few weeks was observed.¹⁴ From experiments by Maurer *et al.*¹⁷ under comparable plasma conditions, we expect a particle temperature of ≈ 40 °C, which is somewhat higher than the electrode temperature (30 °C). Thus, a temperature increase of ≈ 20 °C above room temperature accelerates the mass reduction drastically.

Other explanations for the eigenfrequency increase could be a mass reduction due to sputtering of the MF particles or a modification of the surface properties, which affects the particle charging. These two possibilities are discussed in the following.

A mass loss due to sputtering of bulk material (melamine) by the impinging argon ions would cause an eigenfrequency increase. This cannot be the dominant effect in the presented measurement because of the high mass loss rate. According to Eq. (7), the mass loss rate at the start of the measurement ($T=0$) is $\partial m/\partial t = -1.6 \times 10^{-17}$ kg/s. The number of impinging argon ions per time can be approximated by the OML theory for streaming ions $\partial N_{Ar}/\partial t = \pi r_d^2 n_i v_i$. The ion velocity $v_i = \sqrt{k_b T_e/m_i}$ is of the order of the Bohm speed. Further, Langmuir probe measurements yield a plasma density of $n_i \approx 10^{15}$ m⁻³ and an electron temperature of $T_e = 3$ eV. The sputtering yield $Y_s = N_m/N_{Ar}$ is defined as the number of atoms sputtered per impinging argon ion. If the mass loss would be due to sputtering, it requires a sputtering yield of

$$Y_s = \frac{\partial m/\partial t}{\bar{m}_m \partial N_{Ar}/\partial t} \approx 4. \quad (11)$$

$\bar{m}_m \approx 7$ amu is the average atom mass of the melamine. (The chemical composition of the melamine $[C_6H_9N_6]_n$ is neglected.) The energy of the argon ions is of the order of 10 eV. For these low energies, the sputtering yields are generally very small ($Y_s \ll 1$). This is supported by findings by Stoffels *et al.*¹⁸ They continuously measured the radius of a MF particle in an oxygen-argon plasma. For a pure argon plasma, where no chemical sputtering can occur, no significant change of the particle radius was detected after several hours of plasma operation.

Another explanation for the eigenfrequency increase could be an increased particle charge due to a modification of the surface properties. A desorption of a monolayer of water or an adsorption of material sputtered from the electrode can modify the physical properties of the particle surface, while the particle mass remains nearly constant. In dusty plasma, it is usually assumed that the particle charge does not depend on the particle material. Nevertheless, for high floating potentials ($\phi_f \approx -1$ keV), Pavlů *et al.*¹⁹ found that the particle

charge is limited by field emission of electrons, which strongly depends on the surface properties (material). Furthermore, Bronold *et al.*²⁰ proposed a charging model that uses a quantum mechanical *ansatz* to describe the physisorption process of electrons at the particle surface. Here, the particle charge depends on the surface states of the material. The floating potential of the particles in the presented measurements is of the order of 10 V. Thus, field emission of electrons does not contribute to the particle charging. However, we cannot exclude that the observed eigenfrequency increase is in part a result of an increased particle charge due to a modification of the particle surface by the plasma environment.

V. CONCLUSION

It has been shown that the mass of MF particles, often used in dusty plasma experiments, is influenced by the plasma environment. Mass changes of the order of 10% have been found. This could be important for experiments, where the particle mass is a critical parameter.

The phase-resolved resonance method described in Sec. II allows to measure the vertical confinement frequency with high accuracy. We like to point out that the relative uncertainty of ω_0 for the presented measurements is less than 10^{-3} . So, small changes of the charge-to-mass ratio can be resolved. This could be useful for experiments, where relative measurements of the charge-to-mass ratio are of interest, rather than absolute measurements.

ACKNOWLEDGMENTS

This work was supported by the Deutsche Forschungsgemeinschaft (DFG Grant No. SFB TR24-A2) in the framework of the SFB-TR24 Greifswald Kiel, Project A2.

We like to thank T. Peter and F. Faupel (SFB-TR24, project B13) for the XPS analysis of the sputtered material and K. Raetzke for the TGA measurement. Furthermore, we thank H. Maurer, H. Kersten (SFB-TR24, project B4), and F. X. Bronold (SFB-TR24, project B10) for useful discussions and comments on the manuscript.

¹E. C. Whipple, T. G. Northrop, and D. A. Mendis, *J. Geophys. Res.* **90**, 7405, doi:10.1029/JA090iA08p07405 (1985).

²L. Spitzer, *Diffuse Matter in Space* (Wiley, New York, 1978).

³T. G. Northrop, *Phys. Scr.* **45**, 475 (1992).

⁴M. Lampe, R. Goswami, Z. Sternovsky, S. Robertson, V. Gavrichchaka, G. Ganguli, and G. Joyce, *Phys. Plasmas* **10**, 1500 (2003).

⁵S. A. Khrapak, S. V. Ratynskaia, A. V. Zobnin, A. D. Usachev, V. V. Yaroshenko, M. H. Thoma, M. Kretschmer, H. Höfner, G. E. Morfill, O. F. Petrov, and V. E. Fortov, *Phys. Rev. E* **72**, 016406 (2005).

⁶I. H. Hutchinson, *Plasma Phys. Controlled Fusion* **47**, 71 (2005).

⁷A. Piel and A. Melzer, *Adv. Space Res.* **29**, 1255 (2002).

⁸A. Melzer, T. Trottenberg, and A. Piel, *Phys. Lett. A* **191**, 301 (1994).

⁹T. Trottenberg, A. Melzer, and A. Piel, *Plasma Sources Sci. Technol.* **4**, 450 (1995).

¹⁰A. Homann, A. Melzer, and A. Piel, *Phys. Rev. E* **59**, R3835 (1999).

¹¹E. B. Tomme, D. A. Law, B. M. Annaratone, and J. E. Allen, *Phys. Rev. Lett.* **85**, 2518 (2000).

¹²H. Kersten, Escarpig Conference Proceedings, Novi Sad, Serbia, 2010.

¹³A. A. Samarian and B. W. James, *Phys. Lett. A* **287**, 125 (2001).

¹⁴J. Pavlů, A. Velyhan, I. Richterová, Z. Němeček, J. Šafránková, I. Čermák, and P. Žilavý, *IEEE Trans. Plasma Sci.* **32**, 704 (2004).

- ¹⁵W. Press, S. Teukolsky, W. Vetterling, and B. Flannery, *Numerical Recipes in C*, 2nd ed. (Cambridge University Press, Cambridge, U.K., 1992).
- ¹⁶T. A. Osswald and G. Menges, *Material Science of Polymers for Engineers*, 2nd ed. (Hanser, Munich, 2003).
- ¹⁷H. R. Maurer, R. Basner, and H. Kersten, *Contrib. Plasma Phys.* **50**, 954 (2010).
- ¹⁸W. W. Stoffels, E. Stoffels, G. H. P. M. Swinkels, M. Boufnichel, and G. M. W. Kroesen, *Phys. Rev. E* **59**, 2302 (1999).
- ¹⁹J. Pavlů, I. Richterová, J. Šafránková, and Z. Němeček, *Adv. Space Res.* **38**, 2558 (2006).
- ²⁰F. X. Bronold, H. Deutsch, and H. Fehske, *Eur. Phys. J. D* **54**, 519 (2009).

A.5

CHARGING AND COUPLING OF A VERTICALLY ALIGNED PARTICLE PAIR IN THE PLASMA SHEATH

Jan Carstensen, Franko Greiner, Dietmar Block, Jan Schablinski,
Wojciech J. Miloch, and Alexander Piel

Reprinted with permission from
Jan Carstensen, Franko Greiner, Dietmar Block, Jan Schablinski,
Wojciech J. Miloch, and Alexander Piel,
Physics of Plasmas, Vol. 19, 033702 (2012).
Copyright 2012, American Institute of Physics

Charging and coupling of a vertically aligned particle pair in the plasma sheath

Jan Carstensen,¹ Franko Greiner,¹ Dietmar Block,¹ Jan Schablinski,¹ Wojciech J. Miloch,² and Alexander Piel¹

¹JEAP, Christian-Albrechts-Universität, D-24098 Kiel, Germany

²Department of Physics, University of Oslo, P.O. Box 1048 Blindern, N-0316 Oslo, Norway

(Received 25 November 2011; accepted 30 January 2012; published online 5 March 2012)

The phenomenon of particle chain formation is studied in a two-particle system. A wake of positive ions leads to an alignment of the negatively charged particles parallel to the ion flow. The dynamic response of this dust system to a small external perturbation is evaluated. It is shown that the eigenfrequency of the downstream particle is reduced compared to an isolated particle. This effect can be identified as a decharging of the particle by the focused ion flow in the wake of the upstream particle. Furthermore, a strong asymmetry of the particle interaction parallel to the ion flow is found. This asymmetry may not be attributed entirely to the interaction forces mediated by the ion wake. © 2012 American Institute of Physics. [<http://dx.doi.org/10.1063/1.3689854>]

I. INTRODUCTION

Complex (or dusty) plasmas containing micrometer size solid particles allow studying the multi-faceted physics of strongly coupled many-particle systems at the level of single particle motion.¹ A fascinating phenomenon in the sheath region of complex plasmas is the spontaneous formation of chains of like-charged particles.^{2–4} An attractive force between the negatively charged dust particles can arise from the polarization of the flow of ions in the sheath, which forms a positively charged wake behind the particles.² Nambu *et al.*⁵ pointed out the similarity of the mechanism to the formation of Cooper pairs in superconductors. Besides wake charging,^{2,5–9} ion drag forces were discussed for particle alignment.^{10,11}

Another interesting aspect of ion wakes is an asymmetric (non-reciprocal) particle interaction. Typically, the upstream particle exerts a larger force on the downstream particle as compared to the other direction. This asymmetry is a source for different types of instabilities. For example, the melting of 2D crystals² or oscillatory instabilities in dust clusters.¹²

Particle pairs are often used as generic model system to study in detail the interparticle forces mediated by the ion wake.^{4,12–16} In laboratory experiments, the dust particles are usually confined in the sheath of a plasma, where the electric field compensates the force of gravity.^{4,13,16} Here, the alignment of the particles is determined by two competing mechanisms. On the one hand, the forces due to the ion wake lead to a vertical particle alignment (parallel to the ion flow) and, on the other hand, the vertical confinement favors a horizontal alignment of the particles (perpendicular to the ion flow). The transition from the vertical to the horizontal alignment can be induced by changes of the plasma parameters, e.g., by varying the gas pressure,⁴ the discharge voltage,¹³ the self bias,¹⁷ or by an external driver,¹⁶ and a distinct hysteresis effect was observed.

For a comparison of theory and experiment, the charge Q of the particles is of key interest. In the plasma sheath, Q cannot be treated as constant, since it depends on the levitation height of the particles.^{18–20} For vertically aligned particles, simulations further predict a decharging of the downstream particle by the ion wake.^{21–23} The latter effect was observed experimentally by Prior *et al.*²⁴ evaluating laser excited resonances and assuming a symmetric Yukawa interaction.

In this paper, the dynamic response of a vertically aligned particle pair to an external sinusoidal perturbation is studied experimentally. We applied a phase-resolved resonance method²⁵ to measure the dynamic properties of the particles with high precision. Different from earlier investigations,^{24,26} we are interested in a simultaneous determination of the non-reciprocity of forces and the charge reduction effect of the lower particle. For this purpose, we analyzed the coupled resonances of the two-particle system and compared the resonance frequencies with the single-particle resonance of the particle that acted as lower particle in the two-particle system.

II. EXPERIMENTAL PROCEDURE

The experiments were performed in an asymmetric capacitively coupled radio frequency (rf) discharge (13.56 MHz). A system of two vertically aligned melamine particles with a diameter of $\approx 12 \mu\text{m}$ is prepared in the plasma sheath above the driven electrode. A brief description of the applied phase-resolved resonance method is given in the following. A sketch of the setup is shown in Fig. 1.

A function generator provides a sinusoidal low frequency excitation voltage with amplitude U_{ext} and a radial frequency ω . This signal is coupled to the driven electrode by a low-pass filter. The transfer function of the coupling network can be approximated by

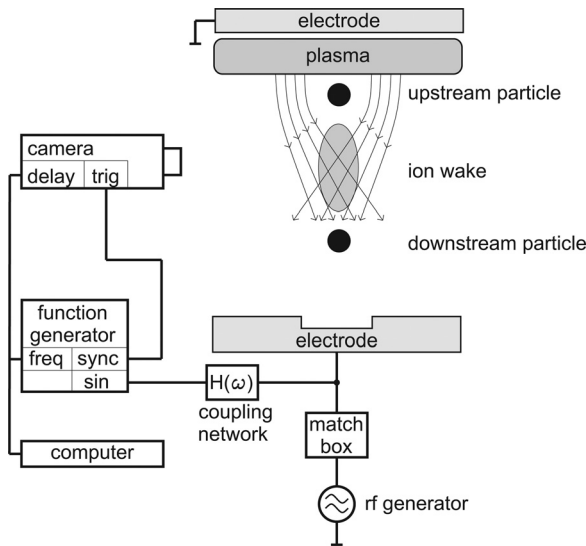


FIG. 1. Sketch of the experimental setup (not true to scale): two vertical aligned particles are confined in the plasma sheath above the driven electrode. A vertical oscillation is triggered by a sinusoidal modulation of the self bias. The position of the particles is recorded by a video camera which is synchronized with the excitation signal.

$$\frac{U_B}{U_{\text{ext}}} = H(\omega) = \left(1 + \frac{\omega_c}{i\omega}\right)^{-1}, \quad (1)$$

U_B is the amplitude of the self bias modulation and ω_c the cut-off frequency of the low pass. This bias modulation exerts a force on the particles and sets them into oscillations. The vertical position z_j of the particles is observed by a video camera. The camera is operated in triggered shutter mode and is synchronized with the excitation signal. An additional trigger delay t_φ allows to measure the position $z_{j,\varphi}$ of the particles at a given phase φ with respect to the excitation signal. Because the trajectory of the particles is sinusoidal, the excursion of the particles from their equilibrium position $\xi_{j,\varphi}$ at a certain phase φ can be measured offset-free by using $2\xi_{j,\varphi} = (z_{j,\varphi} - z_{j,\varphi+180^\circ})$. Resonance curves are obtained by measuring $\xi_{j,\varphi}$ versus ω for a constant phase shift φ and a constant excitation amplitude U_{ext} . The experiments were performed at low gas pressures $p = 3.4$ Pa (argon) and an rf voltage of 120 V_{pp}. At these parameters, the vertical particle configuration is stable and the resonance curves become sharp due to low friction forces. We further used particle pairs with slightly different masses. This ensures that the difference of the resonance frequencies of the particles can be resolved.

III. NON-RECIPROCAL COUPLED OSCILLATORS

We will treat the two vertically aligned particles as coupled harmonic oscillators, which are driven by an external force $m_j K_j H(\omega) \exp(i\omega t)$. In the following, $j=1$ will refer to the upstream particle and $j=2$ to the downstream particle, respectively. K_j is the amplitude of the excitation force normalized to the particle mass m_j . A parabolic confinement due to the (time averaged) sheath electric field is assumed. The restoring force then is $-m_j \omega_j^2 \xi_j$ with ω_j being the eigenfrequency. The gas background induces a damping force

$-2m_j \gamma_j \dot{\xi}_j$, with the friction coefficient γ_j . For small oscillation amplitudes compared to the equilibrium interparticle distance d_0 , we linearize the interaction force $F_{jk}(d) = F_{jk}(d_0) + m_j D_{jk}(d - d_0) = F_{jk}(d_0) + m_j D_{jk}(\xi_j - \xi_k)$ between the two particles and allow the force to be non-reciprocal ($D_{jk} \neq D_{kj}$).² d is the interparticle distance. The equation of motion then reads

$$\ddot{\xi}_1 + 2\gamma_1 \dot{\xi}_1 + \omega_1^2 \xi_1 + D_{12}(\xi_1 - \xi_2) = H(\omega) K_1 \exp(i\omega t),$$

$$\ddot{\xi}_2 + 2\gamma_2 \dot{\xi}_2 + \omega_2^2 \xi_2 + D_{21}(\xi_2 - \xi_1) = H(\omega) K_2 \exp(i\omega t).$$

The constants $F_{jk}(d_0)$ and the force of gravity do not appear in the equation of motion, because these constant forces only affect the position of the particles z_j and not the excursion from the equilibrium position ξ_j , since the confinement is parabolic.

We are looking for oscillatory solutions of the form $\xi_j(t) = A_j \exp(i\omega t)$. The complex amplitudes A_j are

$$A_1 = H(\omega) \frac{K_1(\Gamma_2 + D_{21}) + K_2 D_{12}}{\Gamma_1 \Gamma_2 + \Gamma_2 D_{12} + \Gamma_1 D_{21}}, \quad (2)$$

$$A_2 = H(\omega) \frac{K_2(\Gamma_1 + D_{12}) + K_1 D_{21}}{\Gamma_1 \Gamma_2 + \Gamma_2 D_{12} + \Gamma_1 D_{21}}, \quad (3)$$

with $\Gamma_j = \omega_j^2 - \omega^2 + i2\gamma_j \omega$. The real part $\Re(A_j)$ can be identified with the position of the particles at a phase $\varphi = 0^\circ$ and the imaginary part $\Im(A_j)$ is equivalent to the position at $\varphi = 90^\circ$. In Figs. 2(a) and 2(b), the resonance curves of the upstream particle and the downstream particle are shown for a phase shift of $\varphi = 0^\circ$ (crosses) and $\varphi = 90^\circ$ (circles). The excitation voltage $U_{\text{ext}} = 0.4$ V was chosen such that the oscillation amplitude of the particles is much less than the interparticle distance. The full lines are fits of $\Re(A_j)$, $\Im(A_j)$. The resulting fit parameters are compiled in Table I. By using synthetic data, we have estimated the errors of the fit parameters (as described in Ref. 27). When the error in ω is neglected and the error of the particle position is within one camera pixel, the relative (1σ) error for all fit parameters is less than 1%. The excellent agreement between the model and the measurements shows that for this parameter regime the assumptions of a harmonic confinement and a linearized interparticle force are well satisfied.

An important property of ion wakes is an asymmetric (non-reciprocal) particle interaction parallel to the ion flow.^{2,4,28} For the present experiment, the asymmetry of the particle interaction is reflected by the different coupling parameters D_{12}, D_{21} . We can quantify the degree of asymmetry in this situation $D_{21}/D_{12} \approx 5.5$.

IV. CHARGE REDUCTION OF THE DOWNSTREAM PARTICLE

The confinement frequencies ω_j of the particles depend on the charge-to-mass ratio of the particles and the charge density of the undisturbed plasma sheath ρ ,²⁹

$$\omega_j^2 = \frac{\rho Q_j}{\epsilon_0 m_j}. \quad (4)$$

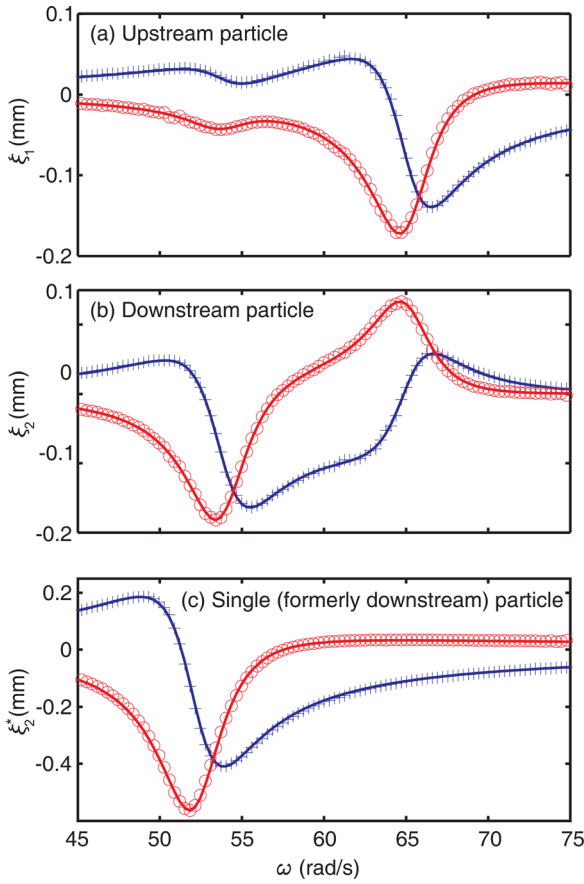


FIG. 2. (Color online) (a) Vertical excursion from the equilibrium position ξ of the upstream particle for a phase shift of $\varphi = 0^\circ$ (crosses) and $\varphi = 90^\circ$ (circles) vs. the excitation frequency ω . The full lines are $\Re(A_1(\omega))$, $\Im(A_1(\omega))$ for the parameters compiled in Table I. (b) Resonance curves of the downstream particle. (c) Resonance curves of the undisturbed, formerly downstream, particle.

Thus, for a parabolic sheath potential ($\rho = \text{const.}$), ω_j can be taken as a measure of the charge-to-mass ratio of the particles. The confinement frequency of the downstream particle is significantly smaller than that of the upstream particle (Table I). This can be due to either a reduced charge of the downstream particle or a higher particle mass. To distinguish between these two quantities, the upstream particle was removed from the discharge. Then we have measured again the resonance curve of the remaining (formerly downstream) particle under identical conditions [Fig. 2(c)]. It is found that the eigenfrequency of the downstream particle in the particle pair is significantly smaller than that of the same particle in

TABLE I. Fit parameters.

Two-particle system				
ω_1	γ_1	K_1	D_{12}	U_{ext}
63.1 rad/s	2.25 s^{-1}	0.133 ms^{-2}	156 s^{-2}	0.4 V
ω_2	γ_2	K_2	D_{21}	ω_c
46.3 rad/s	2.34 s^{-1}	0.045 ms^{-2}	868 s^{-2}	125 rad/s
Single-particle system				
ω_2^*	γ_2^*	K_2^*	U_{ext}	
52.3 rad/s	2.37 s^{-1}	0.371 ms^{-2}	2.0 V	

the absence of the upper particle ($\omega_2 < \omega_2^*$). This effect can be attributed to a reduced particle charge

$$\frac{Q_2}{Q_2^*} = \left(\frac{\omega_2}{\omega_2^*}\right)^2 = 0.78. \quad (5)$$

We repeated the experiment for another particle pair, but this time the downstream particle was removed. In this case, the eigenfrequency of the upstream particle is not affected. Thus, the charge of the downstream particle is modified by the presence of the upstream particle but not vice versa.

The partial discharging of the downstream particle can be reproduced by particle-in-cell simulations. The simulation code described in Ref. 30 was adopted to the plasma parameters of the present experiment, electron temperature $T_e = 3 \text{ eV}$, ion temperature $T_i = 0.03 \text{ eV}$, Debye length $\lambda_D \approx 0.7 \text{ mm}$, and a Mach number $M = 1$. For the self-consistent equilibrium position, the charge reduction was found to be $\approx 50\%$. The trend and the order of magnitude are comparable to the experimental finding. Deviations between the experimental and simulated value are reasonable, because the simulation does not account for the DC electric field in the sheath and the simulated particles were larger ($100 \mu\text{m}$) than the particles used in the present experiment ($12 \mu\text{m}$).

V. POSITION DEPENDENT PARTICLE CHARGE

When the upstream particle is removed, the particle charge of the downstream particle increases. Furthermore, an increase of the levitation height by 0.4 mm is observed. Thus, the charge difference found in Sec. IV can either be an effect of the ion wake or due to different positions within the plasma sheath.^{19,20,31} A position-depending particle charge or a non-harmonic electric field can be a source of non-linearity.¹⁸ In order to give an estimate of the charge variation within the plasma sheath, we evaluate the harmonicity of the particle oscillation.

For an excitation frequency of 8 Hz, the motion of the particle was tracked with 200 fps over 5 s. The amplitude was chosen such that the particle passes its former equilibrium position in the two particle configuration (dashed line). The amplitude of the oscillation is larger than in the two particle configuration to ensure that non-linear effects appear. A part of the trajectory is shown in Fig. 3(a). The spectrum of this time series is shown in Fig. 3(b). The trajectory is to a good approximation sinusoidal, the total harmonic distortion (THD) is -43 dB .

In order to find an upper limit for the charge variation in the sheath, it is assumed that the THD is entirely due to a position dependence of the particle charge and that the charge variation is given by a constant charge gradient. It is further assumed that the strength of the confinement and the excitation force are proportional to the particle charge. Then the modified equation of motion reads

$$\ddot{\xi}_2 + 2\gamma_2 \dot{\xi}_2 + \omega_2^2(1 + q'\xi_2)\xi_2 = H(\omega)(1 + q'\xi_2)K_2 \exp(i\omega t),$$

q' is the charge gradient normalized to the equilibrium charge. We solved this modified equation of motion numerically for different values of q' , while the other parameters

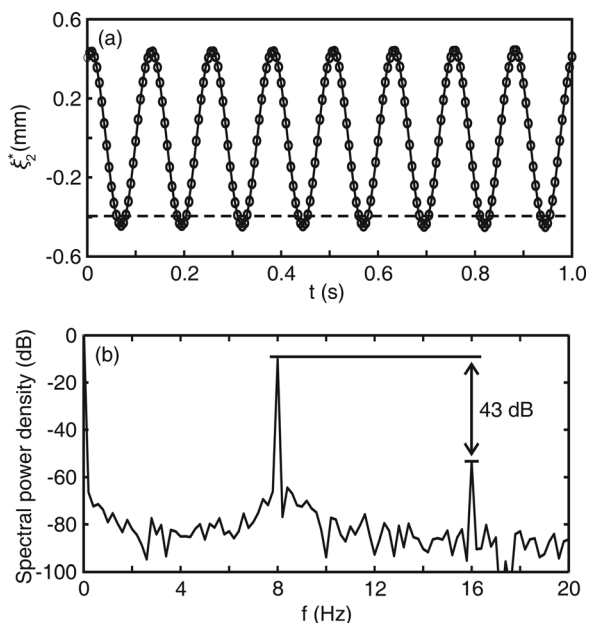


FIG. 3. (a) Trajectory of the undisturbed particle. Vertical excursion from the equilibrium position ξ_z^* versus time t . The full line is a fit of a sine wave. The dashed line marks the equilibrium position of the particle in the two particle configuration. (b) Power spectrum of the trajectory.

remained the same, as they were measured for the single particle case. For $q' = 90 \text{ m}^{-1}$, the total harmonic distortion of the trajectory matches the value of the experiment. This corresponds to a charge difference between the equilibrium positions of the downstream particle and the single particle of 3.4%. So, the charge reduction of 20% found in Sec. IV is mainly an effect of the ion wake and not due to a change of the equilibrium position.

VI. DISCUSSION AND CONCLUSION

The externally excited oscillation of a vertically aligned particle pair is in excellent agreement with the model Eq. (2). The deviations between model and fit are within the error of the particle positions. This shows that to a good approximation the particle ensemble can be described by asymmetric coupled harmonic oscillators. The dynamical properties $(\omega_j, \gamma_j, D_{ij})$ were determined with high precision by the means of the phase-resolved resonance method.²⁵ In this way, two major effects of ion wakes can be quantified: the partial decharging of a particle within a wake and the non-reciprocal interparticle coupling.

The partial decharging of the downstream particle by $\approx 20\%$ compared to the single particle configuration can be qualitatively reproduced by simulations, though the magnitude of the decharging is overestimated (see Sec. IV). Prior *et al.* measured this effect experimentally using laser excited resonances.²⁴ There, a charge ratio between downstream and upstream particles of $Q_2/Q_1 \approx 0.7$ was found. This value is in fair agreement with the presented measurement, deviations may result from different plasma parameters and different experimental approaches. In contrast to Ref. 24, we restricted the particle oscillations to small amplitudes. This allows to linearize the effective interparticle forces and accounts for the non-reciprocity by two

coupling constants. We further compared the eigenfrequency of the downstream particle inside and outside of the wake of the upstream particle to ensure identical particle masses instead of comparing upstream and downstream particle.

The non-reciprocity of the particle interaction is often discussed for the horizontal component of the interparticle force, which is responsible for the alignment of the particles. Takahashi *et al.*³ and Melzer *et al.*⁴ demonstrated this by pushing the upstream particle sideways by a laser beam. In that case, the downstream particle followed the motion of the upstream particle. On the other hand, when the downstream particle is pushed to the side, the upstream particle remains at its position. Thus, for horizontal disturbances, there is no (or only a weak) horizontal force from the downstream particle on the upstream particle. In the present experiment, we examined the forces in the vertical direction. For this component of the force, as expected from the direction of the ion flow, the same trend is observed, i.e., small (vertical) disturbances of the downstream particle have a weak impact on the upstream particle, $D_{21}/D_{12} = 5.5$. However, this result is in contrast to the findings by Kong *et al.*²⁶ There, comparable to our approach, the particle pairs were treated as asymmetric coupled harmonic oscillators. The coupling constants were derived from the pulse response of the particle ensemble. The ratio of the measured coupling constants was $D_{21}/D_{12} < 0.66$. A reason for the discrepancy to our results may be the occurrence of transients. In Ref. 26, the damped oscillations after an excitation pulse were evaluated. In the present experiments, the measurements were started when the particle oscillation had reached a stationary state, i.e., all transients were damped out.

The strong asymmetry of the coupling constants $D_{21}/D_{12} = 5.5$ is not reproduced by the simulations described in Sec. IV. For the self consistent equilibrium, distance of the particles $D_{21}/D_{12} \approx 1.5$ is found. The coupling constants were derived from the interparticle forces, which strongly depend on the interparticle distance. This discrepancy can be resolved if the particle charge is treated as a variable. The simulation predicts a strong dependence of the charge of the downstream particle on the interparticle distance. This gives rise to an additional effective interparticle force due to the confinement within the plasma sheath. For example, when the two particles approach each other, the charge of the downstream particle is reduced. Then the force of gravity is not fully compensated by the sheath electric field and the downstream particle feels a net force which is directed downwards. This additional effective force enhances the asymmetry of the particle interaction, because it only affects the downstream particle (according to the simulation, the charge of the upstream particle is to a good approximation independent of the particle distance). This mechanism may be an explanation for the observed strong asymmetry of the coupling constants.

To conclude, the decharging of a particle within an ion wake of another and the non-reciprocal coupling between two particle parallel to an ion flow were measured experimentally with high precision in the limit of small amplitude oscillations. A partial decharging of the downstream particle

by $\approx 20\%$ compared to an undisturbed particle was found. Furthermore, a strong asymmetry of the coupling constants $D_{21}/D_{12} = 5.5$, which cannot be explained by a pure ion wake potential, may be interpreted as an effective force from the confinement due to a variable charge.

ACKNOWLEDGMENTS

This work was supported by the Deutsche Forschungsgemeinschaft DFG in the framework of the SFB-TR24 Greifswald Kiel, Project A2 and A3.

- ¹G. E. Morfill and A. V. Ivlev, *Rev. Mod. Phys.* **81**, 1353 (2009).
- ²V. A. Schweigert, I. V. Schweigert, A. Melzer, A. Homann, and A. Piel, *Phys. Rev. E* **54**, 4155 (1996).
- ³K. Takahashi, T. Oishi, K. Shimomai, Y. Hayashi, and S. Nishino, *Phys. Rev. E* **58**, 7805 (1998).
- ⁴A. Melzer, V. A. Schweigert, and A. Piel, *Phys. Rev. Lett.* **83**, 3194 (1999).
- ⁵M. Nambu, S. V. Vladimirov, and P. K. Shukla, *Phys. Lett. A* **203**, 40 (1995).
- ⁶F. Melandsø and J. Goree, *Phys. Rev. E* **52**, 5312 (1995).
- ⁷S. V. Vladimirov and O. Ishihara, *Phys. Plasmas* **3**, 444 (1996).
- ⁸M. Lampe, G. Joyce, and G. Ganguli, *IEEE Trans. Plasma Sci.* **33**, 57 (2005).
- ⁹I. H. Hutchinson, *Phys. Rev. Lett.* **107**, 095001 (2011).
- ¹⁰G. Lapenta, *Phys. Rev. E* **66**, 026409 (2002).
- ¹¹A. Piel, *Phys. Plasmas* **18**, 073704 (2011).
- ¹²R. Kompaneets, S. V. Vladimirov, A. V. Ivlev, V. Tsytovich, and G. Morfill, *Phys. Plasmas* **13**, 072104 (2006).
- ¹³V. Steinberg, R. Sütterlin, A. V. Ivlev, and G. Morfill, *Phys. Rev. Lett.* **86**, 4540 (2001).
- ¹⁴A. A. Samarian and S. V. Vladimirov, *Contrib. Plasma Phys.* **49**, 260 (2009).
- ¹⁵K. Qiao, L. Matthews, and T. Hyde, *IEEE Trans. Plasma Sci.* **38**, 826 (2010).
- ¹⁶M. Kroll, J. Schablinski, D. Block, and A. Piel, *Phys. Plasmas* **17**, 013702 (2010).
- ¹⁷A. A. Samarian, S. V. Vladimirov, and B. W. James, *Phys. Plasmas* **12**, 022103 (2005).
- ¹⁸C. Zafiu, A. Melzer, and A. Piel, *Phys. Rev. E* **63**, 066403 (2001).
- ¹⁹J. Beckers, T. Ockenga, M. Wolter, W. W. Stoffels, J. van Dijk, H. Kersten, and G. M. W. Kroesen, *Phys. Rev. Lett.* **106**, 115002 (2011).
- ²⁰A. Douglass, V. Land, L. Matthews, and T. Hyde, *Phys. Plasmas* **18**, 083706 (2011).
- ²¹S. V. Vladimirov, S. A. Maiorov, and N. F. Cramer, *Phys. Rev. E* **67**, 016407 (2003).
- ²²W. J. Miloch, *Plasma Phys. Controlled Fusion* **52**, 124004 (2010).
- ²³V. R. Ikkurthi, K. Matyash, A. Melzer, and R. Schneider, *Phys. Plasmas* **17**, 103712 (2010).
- ²⁴N. J. Prior, L. W. Mitchell, and A. A. Samarian, *J. Phys. D: Appl. Phys.* **36**, 1249 (2003).
- ²⁵J. Carstensen, H. Jung, F. Greiner, and A. Piel, *Phys. Plasmas* **18**, 033701 (2011).
- ²⁶J. Kong, T. Hyde, B. Harris, K. Qiao, and J. Carmona-Reyes, *IEEE Trans. Plasma Sci.* **37**, 1620 (2009).
- ²⁷W. Press, S. Teukolsky, W. Vetterling, and B. Flannery, *Numerical Recipes in C*, 2nd ed. (Cambridge University Press, Cambridge, 1992).
- ²⁸A. V. Ivlev, M. H. Thoma, C. R ath, G. Joyce, and G. E. Morfill, *Phys. Rev. Lett.* **106**, 155001 (2011).
- ²⁹T. Trottenberg, A. Melzer, and A. Piel, *Plasma Sources Sci. Technol.* **4**, 450 (1995).
- ³⁰W. J. Miloch, M. Kroll, and D. Block, *Phys. Plasmas* **17**, 103703 (2010).
- ³¹A. A. Samarian and S. V. Vladimirov, *Phys. Rev. E* **67**, 066404 (2003).

A.6

ION-WAKE-MEDIATED PARTICLE INTERACTION IN A MAGNETIZED PLASMA FLOW

Jan Carstensen, Franko Greiner, and Alexander Piel

Reprinted with permission from
Jan Carstensen, Franko Greiner, and Alexander Piel,
Physical Review Letters, Vol. 109, 135001 (2012).
Copyright 2012, American Physical Society

Ion-Wake-Mediated Particle Interaction in a Magnetized-Plasma Flow

Jan Carstensen, Franko Greiner, and Alexander Piel

IEAP, Christian-Albrechts-Universität, D-24098 Kiel, Germany

(Received 11 July 2012; published 27 September 2012)

The interaction forces between dust grains in a flowing plasma are strongly modified by the formation of ion wakes. Here, we study the interparticle forces mediated by ion wakes in the presence of a strong magnetic field parallel to the ion flow. For increasing magnetic flux densities a continuous decay of the interaction force is observed. This transition occurs at parameters, where the ion cyclotron frequency starts to exceed the ion plasma frequency, which is in agreement with theoretical predictions. The modification of the interparticle forces is important for the understanding of the structure and dynamics of magnetized dusty plasmas.

DOI: [10.1103/PhysRevLett.109.135001](https://doi.org/10.1103/PhysRevLett.109.135001)

PACS numbers: 52.30.-q, 52.25.Xz, 52.27.Lw, 52.40.Kh

Wake fields occur in numerous plasma environments, when macroscopic objects interact with flowing plasmas. In space, the solar wind creates extended wake structures behind moons [1,2] and planets affecting the charging of asteroids and satellites passing through it [3]. Further, wake charging can be a real concern for space-craft docking operations, since large potential differences may lead to arc discharges [4]. In the context of dusty plasmas [5], where particles are typically small (and light), forces mediated by the positively charged ion wakes become important and are of fundamental interest for the understanding of the structure and dynamics of strongly coupled particle ensembles. Attractive forces between like-charged particles can trigger the spontaneous formation of particle chains [6–8]. The upstream propagation of any disturbance is inhibited by the supersonic ion flow, which results in a strongly asymmetric (nonreciprocal) particle interaction parallel to the flow. This provides an effective mechanism to transfer energy from the flowing ions to the particles [9] resulting in different types of instabilities [6,10,11].

In dusty plasmas, these ion-wake-related phenomena have been studied extensively for unmagnetized plasma flows. For magnetized plasma flows, as they appear, e.g., in fusion devices or space plasmas, there is a lack of experimental observations and only a few theoretical predictions [12,13] and computer simulations [14,15] exist. In this parameter regime, the trajectories of ions scattered in the Coulomb field of highly charged dust particles can be strongly modified by a magnetic field parallel to the ion flow (see Fig. 1). Even in this simplified model (neglecting collisions and collective phenomena), it becomes apparent that a magnetic field severely modifies the ion distribution downstream to the dust particle. Without a magnetic field [Fig. 1(a)], the focusing effect and therefore an enhanced ion density on the axis is clearly visible. In the magnetized case [Fig. 1(b)], the scattering process transfers energy from the parallel to the perpendicular motion, which triggers a helical ion motion and creates an extended ion-depleted shadow.

In the limit of linear response theory, Nambu *et al.* [12] have predicted a damping of the wake oscillations by the presence of the magnetic field. Particle-in-cell simulations by Patacchini *et al.* [14] showed an additional ion cyclotron wake further away from the dust particle (probe) at parameters, where the cyclotron damping is not too strong. Thus, for particle ensembles, where the interaction forces are mediated by ion wakes, we expect a strong influence of the magnetic field on the particle interaction. It is the intention of this Letter to analyze this situation experimentally. The focus hereby lies on a quantitative determination of the nonreciprocal interaction forces and the charging of the particles.

In a magnetized plasma the ions are subject to the Lorentz force. Based on Refs. [12,13], we use the dimensionless parameter $\beta_i = \omega_{ci}/\omega_{pi}$ to describe the magnetization of the ions. ω_{ci} is the ion cyclotron frequency and ω_{pi} the ion plasma frequency. For our particular situation of dust grains in the plasma sheath, this definition can be interpreted in the following way: For ions flowing at Bohm speed $v_B = \sqrt{k_B T_e/m_i}$ the screening length provided by

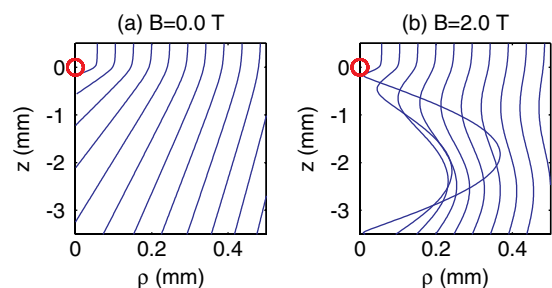


FIG. 1 (color online). Trajectories of Argon ions scattered in the pure Coulomb field of a single charged dust grain with $Q_d = -20\,000e$ (a) without magnetic field ($B = 0$ T) and (b) with magnetic field ($B = 2$ T) in cylindrical coordinates. The magnetic field is aligned parallel to the ion flow in the z direction. ρ is the distance from the z axis. Cold Argon ions with an initial velocity equal to the Bohm speed are assumed.

the ions can be approximated by $\lambda_D = \sqrt{\epsilon_0 k_B T_e / (n_i e^2)}$ [16,17], T_e is the electron temperature and m_i the ion mass. The deflection of the ions passing by a charged dust particle happens mainly within the Debye sphere of the particle. The Lorentz force must be taken into account, when the transit time of the ions $\tau_i = \lambda_D / v_B$ is comparable to the time scale of the cyclotron motion $\tau_{ci} = 1 / \omega_{ci}$, e.g., $\beta_i = \tau_i / \tau_{ci} = \omega_{ci} / \omega_{pi}$. However, ion-neutral collisions can suppress the magnetization of the ions, when the ion-neutral collision frequency ν_{in} exceeds ω_{ci} . For the present measurements the Hall parameter $H_i = \omega_{ci} / \nu_{in}$ is comparable to the magnetization β_i . Although collisions affect the wake fields, $\beta_i \geq 1$ is a reasonable criterion to separate unmagnetized and magnetized wakes, because $H_i \geq 1$ holds in this parameter regime.

The sheath of a plasma is ideally suited to study wake effects. The sheath electric field sustains a strong ion flow and, in addition, it can be used to levitate the negatively charged particles against the force of gravity. A sketch of the experimental situation is shown in Fig. 2. Two melamine particles with 11.66 μm in diameter are confined in the sheath of a capacitively coupled radio frequency (rf) discharge. A small recession of 2 mm in depth ensures the horizontal confinement of the particles. At sufficient low gas pressures, $p = 8$ Pa (Argon), and moderate rf voltages ($U_{rf} = 100 V_{pp}$) the particles align vertically due to the formation of ion wakes [8,18]. Under these conditions the ion flow velocity is of the order of the Bohm speed with a Mach number $M \approx 1$, the ion density is $n_i \approx 10^{14} \text{ m}^{-3}$, and the electron temperature is typically $T_e = 3$ eV [19]. The whole plasma chamber is mounted in a superconducting solenoid, which provides a homogeneous magnetic field of up to 4 T at its center. The direction of the magnetic field is parallel to the ion flow.

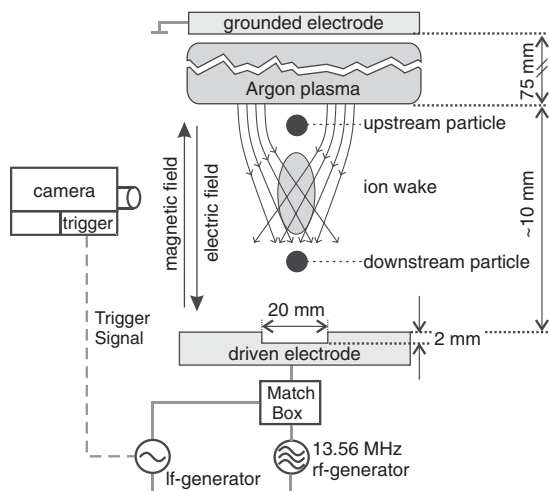


FIG. 2. Sketch of the experimental setup (not true to scale): Two particles are confined in the plasma sheath above the driven electrode. A magnetic field parallel to the ion flow up to $B = 4$ T can be applied. The vertical resonances of the particle ensemble are measured by the phase resolved resonance method [21].

To probe the ion-wake-mediated interaction forces between the particles, we evaluated the vertical resonances of the particle pair [20]. For this purpose, the particles are set into vertical oscillation by a sinusoidal modulation of the electrode bias. For small oscillation amplitudes the particles can be treated as asymmetrically coupled driven harmonic oscillators [21]. The corresponding equation of motion reads

$$\ddot{\xi}_1 + 2\gamma_1 \dot{\xi}_1 + \omega_1^2 \xi_1 + D_{12}(\xi_1 - \xi_2) = K_1 \exp(i\omega t), \quad (1)$$

$$\ddot{\xi}_2 + 2\gamma_2 \dot{\xi}_2 + \omega_2^2 \xi_2 + D_{21}(\xi_2 - \xi_1) = K_2 \exp(i\omega t). \quad (2)$$

ξ_j is the excursion from the equilibrium positions of the upstream ($j = 1$) and downstream ($j = 2$) particle, γ_j is the friction coefficient accounting for friction induced by the ambient neutral gas, ω_j is the confinement frequency of the particles, and K_j the amplitude of the excitation force normalized by the particle mass m_j . The D_{ij} can be considered as effective spring constants describing the strength of the interaction force. Here, we allow $D_{12} \neq D_{21}$ to account for the nonreciprocity of the particle interaction [6]. In order to determine the dynamical properties (ω_j , D_{ij} , γ_j) of this system, the phase resolved resonance method [20] is applied. Resonance curves are obtained by varying the excitation frequency ω and measuring the particle positions ξ_j at a certain phase φ with respect to the excitation. For comparison, the resonance curves for $B = 0.2$ T and $B = 1.2$ T magnetic induction are shown in Fig. 3. The fits of model Eq. (1) (full lines) are in good

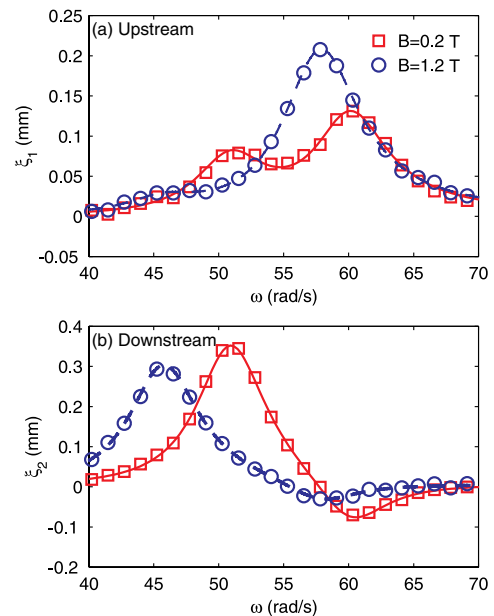


FIG. 3 (color online). Resonance curves of the (a) upstream and (b) downstream particle for magnetic inductions of $B = 0.2$ T (squares) and $B = 1.2$ T (circles). ξ_j is the excursion from the equilibrium position at a phase of $\varphi = 0^\circ$ with respect to the excitation signal. The full and dashed lines are fits of the model Eq. (1).

agreement with the measurement allowing an accurate determination of ω_j , D_{ij} , γ_j .

We analyzed the resonances of the particles for a range of magnetic inductions from $B = 0.2$ T to $B = 2.5$ T. At $B = 0.2$ T the electrons are strongly magnetized, e.g., the Hall parameter of the electrons is $H_e \gg 1$ and a further increase of the magnetic induction does not alter the electron dynamics. For $B > 2.5$ T the particle ensemble becomes unstable due to the filamentation of the plasma [22]. In this parameter regime, we find only a weak dependence of the plasma parameters and the particle charges on the magnetic induction. This is shown in Figs. 4 and 5(a). Figure 4 shows the plasma glow intensity I_p above the lower electrode ($z = 0$) versus the magnetic induction B . The plasma glow is an indicator for the electron density and the electron temperature. Thus, for magnetic inductions of $0.2 \text{ T} < B < 2.0 \text{ T}$ the plasma glow (parameters) can be considered constant. In Fig. 5(a) the confinement frequencies of the upstream and downstream particle are plotted versus B . Since ω_j depends on the charge-to-mass ratio of the particles ($\omega_j^2 \propto Q_j/m_j$), Fig. 5(a) shows that the particle charges remain approximately constant over the entire range of magnetic induction. Further, we have verified that the levitation heights of the particles are nearly unaffected in this range of magnetic inductions, which supports the finding that the particle charges remain constant. The measurements were started at $B = 1.8$ T, then B was decreased to $B = 0.2$ T and increased again to $B = 2.5$ T (dashed line in Fig. 5). There is a small drift in ω_0 indicating a change of the plasma parameters or particle properties [21,23] over the measurement time of a few hours, which will be neglected in the following.

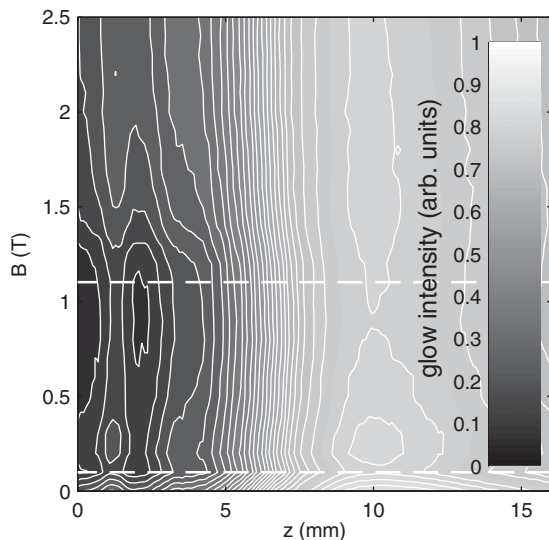


FIG. 4. Plasma glow intensity I_p versus magnetic induction B and vertical position z . I_p is averaged in the horizontal direction. The driven electrode is at $z = 0$. The dashed lines correspond to $B = 0.2$ T and $B = 1.2$ T, as chosen for the sample curves in Fig. 3.

In contrast to the plasma glow and the particle charges, the interparticle forces are strongly affected by the magnetic field [see Fig. 5(b)]. For $B = 0.2$ T, the ions are partially magnetized ($\beta_i < 1$) and the coupling constants are comparable to those found in an unmagnetized plasma [20] under similar conditions. However, for $B = 1.5$ T the ions are magnetized ($\beta_i > 1$) and D_{12} and D_{21} are reduced by a factor of three. For small and large values of B , the degree of asymmetry D_{21}/D_{12} is between 5 and 6 with a minimum at $B \approx 1$ T in the transition region. This gradual change of the particle interaction occurs at magnetic inductions of the order of 1 T. As stated above, this is the parameter regime where the ion cyclotron frequency ω_{ci} becomes comparable to the ion plasma frequency ω_{pi} , e.g., the magnetization is $\beta_i \approx 1$. Because the particle charges Q_j and the plasma parameters are to a good approximation independent of the magnetic induction B , this reduction of the coupling forces can be attributed to a modification of the ion wake structure around the particles.

For the presented parameter regime the particle charges show only a weak dependence on the magnetic induction. The charging of the upstream particle is only weakly influenced by the downstream particle, e.g., the charging is comparable to that of an isolated dust grain. This is in agreement with particle-in-cell simulations by Patacchini *et al.* [24] addressing the problem of a (single) spherical

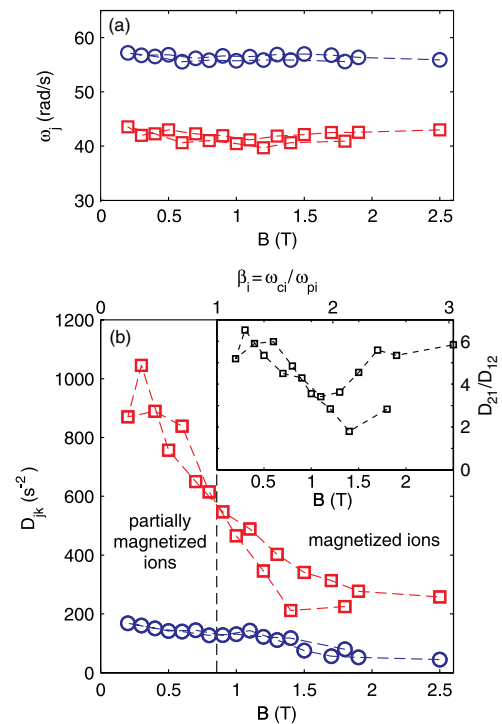


FIG. 5 (color online). (a) Eigenfrequency ω_j of the upstream (circles) and downstream (squares) particle versus magnetic induction B . The dashed line indicates the measurement sequence. (b) The coupling constants of the upstream particle D_{12} (circles) and of the downstream particle D_{21} (squares) versus magnetic induction B .

probe or dust particle in a collisionless streaming magneto plasma. There the particle charge does not depend on the magnetic induction for particles which are small compared to the Debye length and the averaged Larmor radius of the ions, which is the case for the present experiments. For the downstream particle the situation is more complex. As we had shown for unmagnetized plasmas in Ref. [20], the charging of particles in the wake of another can be quite different compared to isolated particles, which is in agreement with simulations [25]. Here, the charging of the downstream particle is not significantly altered when the ion wake becomes magnetized. To our knowledge there are no theories or simulations available addressing the question of particle charging in a magnetized ion wake. This issue should be addressed in the future and is beyond the scope of this Letter.

The interparticle forces D_{ij} decrease for increasing magnetic inductions B . This result is in agreement with linear response theory [13], which predicts a damping of the wake oscillations by the magnetic field. Further this damping occurs at parameters where the ion cyclotron frequency ω_{ci} starts to exceed the ion plasma frequency ω_{pi} , which is also in agreement with Ref. [13]. We like to mention that it is difficult to determine the local plasma density n_i . Since $\omega_{pi} \propto \sqrt{n_i}$, the systematic error of the magnetization scale β_i in Fig. 5(b) can be of the order of 30%, but this does not change the conclusions.

For small magnetic inductions ($B < 0.2$ T), the magnetization of the electrons changes the discharge properties, which is accompanied by a change in the plasma glow and a lowering of the confinement frequencies ω_j and a change of the levitation heights of the dust particles. For this reason we restricted the measurements to the high B regime ($B > 0.2$ T), where the plasma glow, the particle charges, and the levitation heights of the particles show only a weak dependence on the magnetic field. Thus, the sudden drop of the D_{ij} at $B \approx 0.8$ T must be a result of the magnetization of the ion wake and cannot be attributed to modified plasma parameters.

To conclude, at parameters typical for dusty plasmas we demonstrated for the first time that strong magnetic fields of the order of 1–2 Tesla substantially alter the interparticle forces parallel to the ion flow. This effect occurs at parameters, where the magnetization of the ions β_i is of the order of unity. Here, a reduction of the interparticle forces is observed. Since the nonreciprocal interaction forces are important for the structure and stability of particle ensembles, this result implies that the dynamics of strongly coupled particles in magnetized plasma flows is substantially different from unmagnetized plasmas. A detailed understanding into this mechanism can be expected from self-consistent simulations. Further, the experiments indicate that the magnetization of the ions does not alter the charge of the upstream and downstream particle. In the future, it might be promising to check whether this result persists for larger particles with diameters larger than the

Debye length, as is the situation for small objects (satellites, asteroids) in the solar wind.

This work was supported by the Deutsche Forschungsgemeinschaft DFG in the framework of the SFB-TR24 Greifswald Kiel, Project A2.

-
- [1] J. S. Halekas, V. Angelopoulos, D. G. Sibeck, K. K. Khurana, C. T. Russell, G. T. Delory, W. M. Farrell, J. P. McFadden, J. W. Bonnell, and D. Larson, *Space Sci. Rev.* **165**, 93 (2011).
 - [2] I. H. Hutchinson, *J. Geophys. Res.* **117** (2012).
 - [3] V. V. Yaroshenko, W. J. Miloch, S. Vladimirov, H. M. Thomas, and G. E. Morfill, *J. Geophys. Res.* **116**, A12218 (2011).
 - [4] J. Wang, P. Leung, H. Garrett, and G. Murphy, *J. Spacecr. Rockets* **31**, 889 (1994).
 - [5] G. E. Morfill and A. V. Ivlev, *Rev. Mod. Phys.* **81**, 1353 (2009).
 - [6] V. A. Schweigert, I. V. Schweigert, A. Melzer, A. Homann, and A. Piel, *Phys. Rev. E* **54**, 4155 (1996).
 - [7] K. Takahashi, T. Oishi, K.-i. Shimomai, Y. Hayashi, and S. Nishino, *Phys. Rev. E* **58**, 7805 (1998).
 - [8] A. Melzer, V. A. Schweigert, and A. Piel, *Phys. Rev. Lett.* **83**, 3194 (1999).
 - [9] A. V. Ivlev, M. H. Thoma, C. R ath, G. Joyce, and G. E. Morfill, *Phys. Rev. Lett.* **106**, 155001 (2011).
 - [10] R. Kompaneets, S. V. Vladimirov, A. V. Ivlev, V. Tsytovich, and G. Morfill, *Phys. Plasmas* **13**, 072104 (2006).
 - [11] L. Couedel, V. Nosenko, A. V. Ivlev, S. K. Zhdanov, H. M. Thomas, and G. E. Morfill, *Phys. Rev. Lett.* **104**, 195001 (2010).
 - [12] M. Nambu, M. Salimullah, and R. Bingham, *Phys. Rev. E* **63**, 056403 (2001).
 - [13] M. Salimullah, M. Torney, P. K. Shukla, and A. K. Banerjee, *Phys. Scr.* **67**, 534 (2003).
 - [14] L. Patacchini and I. H. Hutchinson, *Plasma Phys. Controlled Fusion* **49**, 1719 (2007).
 - [15] L. Patacchini and I. H. Hutchinson, *Plasma Phys. Controlled Fusion* **53**, 065023 (2011).
 - [16] A. Piel and A. Melzer, *Plasma Phys. Controlled Fusion* **44**, R1 (2002).
 - [17] T. E. Sheridan, *J. Appl. Phys.* **106**, 033303 (2009).
 - [18] V. Steinberg, R. S utterlin, A. V. Ivlev, and G. Morfill, *Phys. Rev. Lett.* **86**, 4540 (2001).
 - [19] M. Klindworth, O. Arp, and A. Piel, *J. Phys. D* **39**, 1095 (2006).
 - [20] J. Carstensen, F. Greiner, D. Block, J. Schablinski, W. J. Miloch, and A. Piel, *Phys. Plasmas* **19**, 033702 (2012).
 - [21] J. Carstensen, H. Jung, F. Greiner, and A. Piel, *Phys. Plasmas* **18**, 033701 (2011).
 - [22] M. Schwabe, U. Konopka, P. Bandyopadhyay, and G. E. Morfill, *Phys. Rev. Lett.* **106**, 215004 (2011).
 - [23] J. Pavl , A. Velyhan, I. Richterov , Z. N eme ek, J. Safr nkov , I. ˇCerm k, and P. Žilav , *IEEE Trans. Plasma Sci.* **32**, 704 (2004).
 - [24] L. Patacchini and I. H. Hutchinson, *Plasma Phys. Controlled Fusion* **53**, 025005 (2011).
 - [25] W. J. Miloch, M. Kroll, and D. Block, *Phys. Plasmas* **17**, 103703 (2010).

A.7

PROBING THE PLASMA SHEATH BY THE CONTINUOUS MASS-LOSS OF MICRO-PARTICLES

Jan Carstensen, Fabian Haase, Hendrik Jung, Benjamin Tadsen, Sebastian Groth, Franko Greiner, and Alexander Piel

Reprinted with permission from
Jan Carstensen, Fabian Haase, Hendrik Jung, Benjamin Tadsen, Sebastian Groth, Franko Greiner, and Alexander Piel,
IEEE Transactions on Plasma Science, Vol. 41, 764 (2013).
Copyright 2012, IEEE

Probing the Plasma Sheath by the Continuous Mass Loss of Microparticles

Jan Carstensen, Fabian Haase, Hendrik Jung, Benjamin Tadsen, Sebastian Groth, Franko Greiner, and Alexander Piel

Abstract—A novel approach of using microparticles as probes for the sheath structure of radio-frequency discharges is presented. Starting with a heavy (large) particle confined deep in the plasma sheath, the ambient plasma causes a continuous mass loss, which increases the levitation height of the particle. It is shown that this process can be precisely monitored with the phase-resolved resonance method, which allows probing the force balance of the particle with high spatial resolution. The resulting force profile is in reasonable agreement with recent sheath models.

Index Terms—Complex plasma, diagnostic, dusty plasma, Epstein friction, plasma sheath.

I. INTRODUCTION

THE DIAGNOSTIC of the plasma sheath is an experimental challenge and of key interest for many plasma applications. In addition to spectroscopic techniques [1], [2], standard plasma diagnostics as electrostatic probes [3] can be a major disturbance to the plasma sheath or be limited to the quasi-neutral conditions of the plasma bulk. One solution for this is to use microparticles as probes [4]–[13], which are only a minor disturbance to the plasma.

Zafiu *et al.* [5] and Samarian and James [7] used microparticles of different sizes to determine the sheath electric field with spatial resolution. Basner *et al.* [9] adapted this method to particles confined in the sheath of floating and biased surfaces. To increase the spatial resolution of this technique, which is so far limited by the number of available particle sizes, Land *et al.* [11] heated the electrode, introducing a thermophoretic force [14], to control the levitation height of a flat dust cluster. An alternative approach was presented by Beckers *et al.* [12]. There, the entire plasma chamber was mounted on a centrifuge, which allows pushing a single particle continuously through the plasma sheath by effectively increasing the acceleration of gravity. Furthermore, photophoretic forces [15], [16] can be used to manipulate particles without disturbing the plasma.

One way to obtain information about the plasma sheath is to determine the strength of the vertical confinement of a dust particle. A common technique to do this is the resonance method [17], as applied in [5], [7]–[9], and [12]. Evaluating the resonances of the dust particles allows measuring the confine-

ment frequency ω_0 , which can be related to the sheath electric field $E(z)$ and the particle charge $Q(z)$, i.e.,

$$\omega_0^2 = \frac{1}{m} \frac{\partial}{\partial z} [E(z)Q(z)] \quad (1)$$

where m is the particle mass, and z is the vertical coordinate. The integration of (1) allows determining the electric field force $F_E(z) = E(z)Q(z)$, when ω_0 and m are known with some spatial resolution in z , e.g., by using particles of different sizes (levitation heights) [7], [9] or one particle under hypergravity conditions [12]. The major disadvantage of this method is that it does not allow to separate the quantities $E(z)$ and $Q(z)$ without further assumptions. Hence, if one is interested in the particle charge Q , one needs further information about the sheath electric field, e.g., a sheath model.

The intention of this contribution is twofold. First, we demonstrate that polymethylmethacrylate (PMMA) particles confined in the plasma sheath can be subject to a continuous mass loss affecting the charge-to-mass ratio and the levitation height. This rises the possibility to probe the force balance of the particles with high spatial resolution. Second, a quantitative comparison to the sheath model of Douglass *et al.* [18] is made. The advantage of this model is that it includes the particle charging, which allows avoiding the problem of separating E and Q .

II. METHOD VERIFICATION

To determine the temporal evolution of the particle size and the confinement frequency ω_0 , the phase-resolved resonance method (PRRM) [19] is applied, which is particularly sensitive for ω_0 and the gas friction coefficient γ . Since the precise determination of these two quantities is critical for the succeeding measurements, the aim here is to demonstrate the reliability of the results obtained with the PRRM.

A. Method Description

The vertical confinement of a dust particle in the plasma sheath is to a good approximation harmonic, as long as the excursion from the equilibrium position ξ is small compared with the sheath width d_{sh} (e.g., $\xi/d_{sh} < 0.2$) [20]. If we apply a sinusoidal force to the dust particle, the trajectory can be described by that of a driven damped harmonic oscillator. The corresponding equation of motion is

$$\ddot{\xi} + 2\gamma\dot{\xi} + \omega_0^2\xi = Ke^{i\omega t} \quad (2)$$

where K is the amplitude of the excitation force normalized to the particle mass, γ is the neutral gas friction coefficient,

Manuscript received June 29, 2012; revised September 4, 2012; accepted October 2, 2012. Date of publication October 22, 2012; date of current version April 6, 2013. This work was supported by DFG in the frame of SFB-TR24 Greifswald-Kiel, Project A2.

The authors are with the Institut für Experimentelle und Angewandte Physik, Christian-Albrechts-Universität zu Kiel, 24098 Kiel, Germany.

Color versions of one or more of the figures in this paper are available online at <http://ieeexplore.ieee.org>.

Digital Object Identifier 10.1109/TPS.2012.2224330

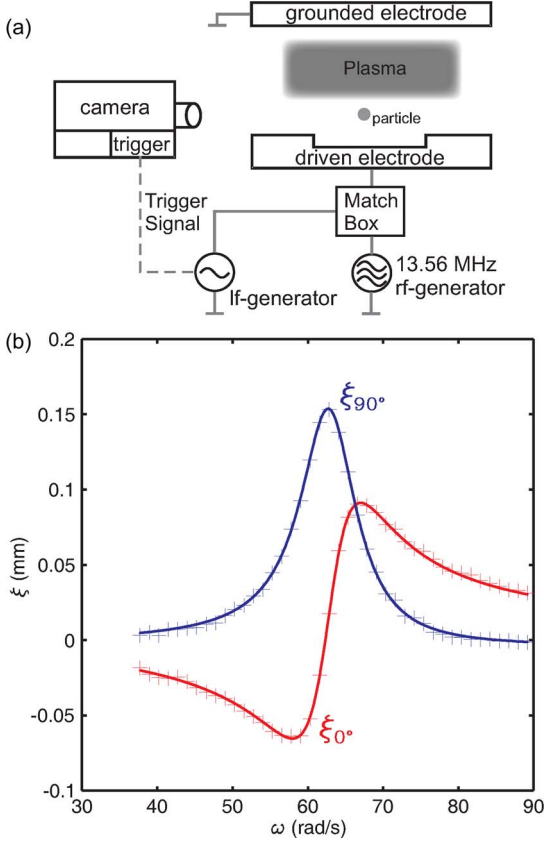


Fig. 1. (a) Sketch of the experimental setup. (b) Typical resonance curves: ξ_{0° and ξ_{90° versus (crosses) excitation frequency ω . The full lines are fits of $a(\omega)$ and $b(\omega)$.

ω_0 is the eigenfrequency of the oscillator, and ω is the driving frequency. Here, we are only interested in the oscillatory solutions $\xi(t) = A(\omega) \exp(i\omega t)$. The complex amplitude $A(\omega)$ can be written as $A(\omega) = a(\omega) + i b(\omega)$, with

$$a(\omega) = \frac{K(\omega_0^2 - \omega^2)}{(\omega_0^2 - \omega^2)^2 + (2\gamma\omega)^2} \quad (3)$$

$$b(\omega) = -\frac{2K\gamma\omega}{(\omega_0^2 - \omega^2)^2 + (2\gamma\omega)^2}. \quad (4)$$

A sketch of the experimental setup is shown in Fig. 1(a). A dust particle is confined in the sheath of an RF parallel-plate discharge above the driven electrode. The function generator modulates the self-bias of the driven electrode sinusoidally and triggers the camera. This sets the particle into vertical oscillation and allows measuring the particle position ξ_φ at a given phase φ within one oscillation period. This phase-resolved technique yields the complex amplitude. It is $a(\omega) = \xi_{0^\circ}(\omega)$ and $b(\omega) = \xi_{90^\circ}(\omega)$.

Resonance curves are obtained by measuring ξ_{0° and ξ_{90° versus the excitation frequency ω for a constant driving amplitude. An exemplary pair of resonance curves are shown in Fig. 1(b). The full lines are fits of (3) and (4), which yield the parameters ω_0 , γ , and K . The excellent agreement between the measurement and the fit results in small errors $\Delta\omega_0$, $\Delta\gamma$, and ΔK . Typically, it is $\Delta\omega_0/\omega_0 < 10^{-3}$, $\Delta\gamma/\gamma < 10^{-2}$, and $\Delta K/K < 10^{-2}$ [19].

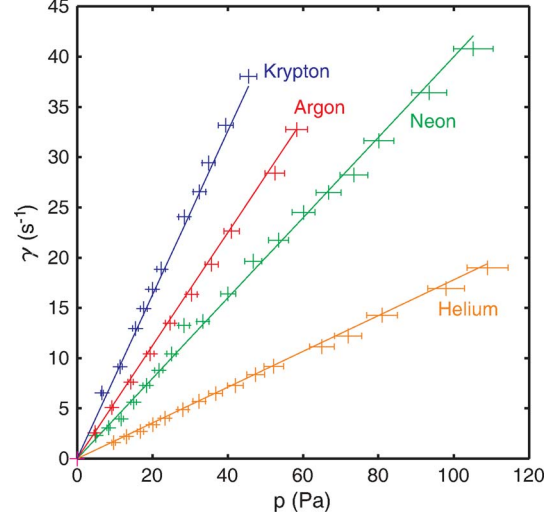


Fig. 2. Gas friction coefficient γ versus gas pressure p for MF particles with $r_d = 6.0 \pm 0.1 \mu\text{m}$ and different noble gases. The full lines represent the Epstein relation in (5).

B. Epstein Friction

We want to demonstrate that the PRRM gives reliable values of the friction coefficient γ in a pressure range between 1 and 100 Pa, which is in agreement with the friction coefficient given by Epstein [21], i.e.,

$$\gamma = \delta \frac{4}{\pi} \frac{p}{r_d \rho_d v_{\text{th},n}} \quad (5)$$

where δ is a parameter between 1 and 1.44, accounting for the type of reflection of the neutral gas atoms at the particle surface, e.g., specular reflection $\delta = 1$ or diffuse reflection $\delta = 1.44$. p is the neutral gas pressure, r_d is the radius of the dust particle, ρ_d is the mass density of the particle, and $v_{\text{th},n}$ is the thermal velocity of the gas atoms.

For Helium, Neon, Argon, and Krypton, we determined the friction coefficient γ versus the neutral gas pressure p (see Fig. 2). For each measurement sequence (noble gas), all measurements were performed with the same particle. We used melamine formaldehyde (MF) particles with a radius of $r_d = 6.0(\pm 0.1) \mu\text{m}$. The particles were baked out before filled into the dust dispenser to avoid an outgassing of water, e.g., a mass loss of the particles over the measurement time. As we have shown in [19], the mass density $\rho = 1360 \text{ kg/m}^3$ is $\approx 10\%$ smaller than the value given by the manufacturer. The RF voltage was $U_{\text{rf}} \approx 200 \text{ V}_{\text{pp}}$, but for technical reasons, it had to be adjusted for different gases and pressure ranges. Nonetheless, this should have no influence on the gas friction experienced by the particles.

The linear dependence between the friction coefficient γ and the neutral gas pressure p , as predicted by Epstein [see (5)], is well reproduced for the entire pressure range between 1 and 100 Pa for all gases. For a quantitative comparison, we assumed a neutral gas temperature of $T_n = 300 \text{ K}$ and a reflection coefficient $\delta = 1.44$ (see full lines in Fig. 2). For all gases, the measurements are in good agreement with the Epstein relation. The dominant error source is the pressure measurement. Although we used a Baratron manometer and a gas viscometer vacuum gauge to calibrate the pressure measurement, there can be a

systematic error of p on the order of $\pm 5\%$. Further error sources are the size distribution of the particles (see Section II-C) and the outbaking of the particles since we do not know if it affects the size (distribution) of the particles. Here, we assume a mass reduction of 10% and an unaffected particle radius; this may result in an additional systematic error, which we cannot quantify. The error of the temperature estimation is negligible compared with the other error sources, because γ is proportional to $\sqrt{1/T_n}$.

C. Size Distribution of MF Particles

The PRRM is particularly sensitive to the confinement frequency ω_0 because $a(\omega)$ [see (3)] has a sharp zero crossing directly at ω_0 , as shown in Fig. 1(b). This allows resolving even the very narrow size distribution of MF particles, which is shown in the succeeding discussion.

For small oscillation amplitudes, we assume the particle charge to be independent of the position z . Then, it is $\omega_0^2 \propto Q/m$. In the orbital motion limit [22], the floating potential of the particles is independent of the particle radius r_d , and the charge Q is proportional to the particle radius r_d . Since the mass scales as $m \propto r_d^3$, it is $\omega_0 \propto 1/r_d$. If we assume a normal distribution of the particle sizes with a standard deviation Δr_d , this should result in a distribution of the confinement frequencies with

$$\frac{\Delta\omega_0}{\omega_0} = \frac{\Delta r_d}{r_d}. \quad (6)$$

To check this relation, we have measured the eigenfrequency of 29 MF particles with $r_d = 5.83(\pm 0.085) \mu\text{m}$, e.g., $\Delta r_d/r_d = 1.5\%$. In contrast to Section II-B, the particles were not baked out so that the size values given by the manufacturer are reliable. Since the measurement of the resonance curves for each particle takes only a few minutes, the mass of the particles can be considered constant over this time. To ensure constant plasma parameters over the entire measurement series, the measurements were started a few hours after the ignition of the discharge. The resulting distribution of ω_0 is shown in Fig. 3. For comparison, we plotted the corresponding normal distribution for the obtain values of $\bar{\omega}_0 = 78.6 \text{ rad/s}$ and $\Delta\omega = 1.2 \text{ rad/s}$. Thus, it is $\Delta\omega_0/\omega_0 = 1.5\%$, which is in good agreement with (6) and the size distribution of the particles given by the manufacturer.

III. CONTINUOUS MASS LOSS OF A PMMA PARTICLE

We exposed a PMMA particle to an Argon plasma for a long time. In the succeeding discussion, it is shown that the plasma environment causes a continuous mass loss over time. As described in Section II, the PRRM gives reliable values of the friction coefficient γ satisfying the Epstein formula in (5). Here, we will make use of this relation to determine the temporal evolution of the particle size (mass).

Since this measurement requires constant plasma parameters for more than 20 h, we let the plasma burn for more than one day to reach stable conditions. The experiments were performed at a gas pressure of $p = 11.5 \text{ Pa}$ (Argon) and a discharge voltage of $U_{\text{rf}} = 200 \text{ V}_{\text{pp}}$. A single PMMA particle (radius

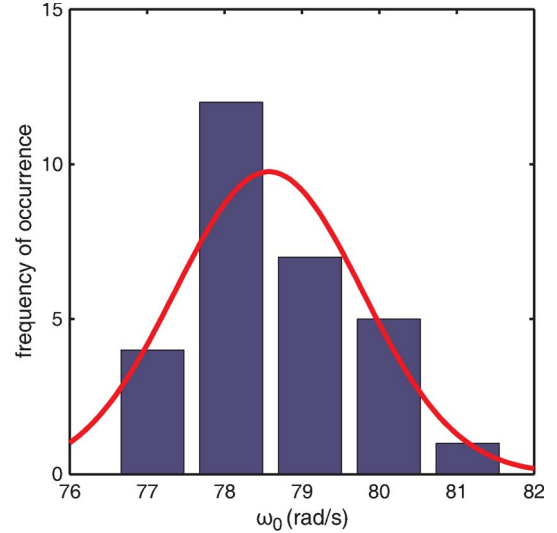


Fig. 3. Histogram of the confinement frequencies ω_0 for 29 MF particles. The full line indicates a normal distribution with $\bar{\omega}_0 = 78.6 \text{ rad/s}$ and $\Delta\omega = 1.2 \text{ rad/s}$.

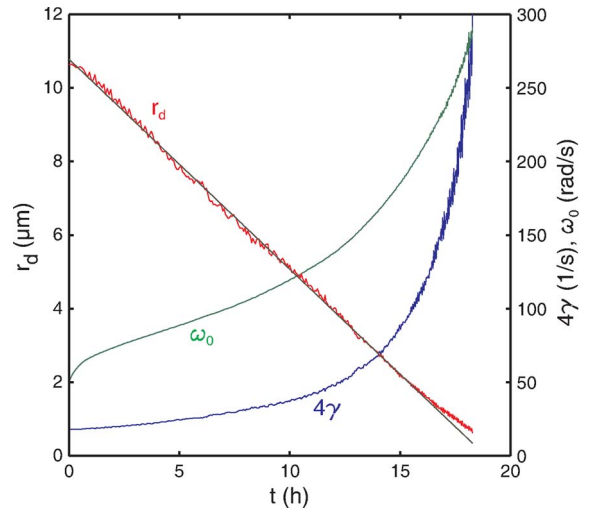


Fig. 4. Time evolution of the confinement frequency ω_0 (green line), the gas friction coefficient γ (blue line), and the particle radius r_d (red line) for a single PMMA particle confined in the plasma sheath. The straight gray line is a linear regression yielding an initial particle radius of $r_0 = 10.8 \mu\text{m}$ and a radius decrease rate of $\alpha = 0.57 \mu\text{m/h}$.

$r_d = 10.9(\pm 0.18) \mu\text{m}$) was injected into the plasma, and we continuously measured resonance curves for more than 20 h. In Fig. 4, the gas friction coefficient γ and the eigenfrequency ω_0 are plotted versus time t . Obviously, the particle properties change over time due to the ambient plasma.

The radius r_d of the PMMA particle can be calculated from the gas friction coefficient γ . To reduce the number of free parameters (e.g., gas temperature T_n and reflection coefficient δ), we used the MF particles from Section II-C as a reference. After the measurement sequence of the PMMA particle was completed, we measured resonance curves of 15 MF particles under the same conditions. This gives an average gas friction coefficient $\bar{\gamma}_{\text{MF}} = 6.45 \text{ s}^{-1}$. Thus, the radius of the PMMA particle follows from (5), i.e.,

$$r_d = \frac{\bar{\gamma}_{\text{MF}}}{\gamma} \frac{\rho_{\text{MF}}}{\rho} \bar{r}_{\text{MF}} \quad (7)$$

where $\rho_{\text{MF}} = 1514 \text{ kg/m}^3$ and $\bar{r}_{\text{MF}} = 5.83 \mu\text{m}$ are the mass density and the average particle radius of the MF particles, respectively; and $\rho = 1190 \text{ kg/m}^3$ is the mass density of the PMMA particle.

In Fig. 4, the radius of the PMMA particle is plotted versus time t . The particle radius decreases almost linearly with a rate of $\alpha = 0.57 \mu\text{m/h}$. Furthermore, the initial size of the PMMA particle ($t = 0 \text{ h}$), as deduced from (7), is $r_0 = 10.8 \mu\text{m}$. This value agrees well with the manufacturer specifications of $r_d = 10.9 \pm 0.18 \mu\text{m}$.

IV. PROBING THE PLASMA SHEATH

We have monitored the mass loss of a PMMA particle for more than 17 h (see Section III). At this time, the radius of the particle changes from 10.8 to 0.8 μm , e.g., the particle lost more than 99% of its initial mass. This affects the levitation height of the particle above the lower electrode h . Large (heavy) particles are located deep within the plasma sheath, whereas smaller (lighter) particles are located close to the sheath edge. Since the levitation height z , the eigenfrequency ω_0 , the particle radius r_d , and the particle mass m are known at any time, it is possible to reconstruct the force balance of the particles at any levitation height.

We compare our measurements with the sheath model of Douglass *et al.* [18], which gives a spatial-resolved profile of the sheath electric field $E(z)$ and the floating potential of the dust $\phi_d(z)$. The particle charge Q can be related to the floating potential ϕ_d by the spherical capacitor model [23]; it is $Q_d = 4\pi\epsilon_0 r_d \phi_d$. Inserting this in (1) yields

$$\omega_0^2 = \frac{4\pi\epsilon_0 r_d}{m} \left(\phi_d \frac{\partial E}{\partial z} + E \frac{\partial \phi_d}{\partial z} \right). \quad (8)$$

Thus, from the measurements in Section III, we can determine the quantity

$$D = \left(\phi_d \frac{\partial E}{\partial z} + E \frac{\partial \phi_d}{\partial z} \right) = \frac{m\omega_0^2}{4\pi\epsilon_0 r_d} \quad (9)$$

which can be considered as an effective spring constant describing the strength of the (harmonic) confinement. In Fig. 5, D is plotted versus the levitation height z of the particle (red line). D , as deduced from the model [18], is plotted in blue.

Since the results of the model for the sheath width tend to be more extended in the z -direction [18] and the pressure assumed ($p = 20 \text{ Pa}$) was not the same as in the experiment ($p = 11.5 \text{ Pa}$), it is reasonable that both D profiles do not exactly match. Nonetheless, some features are well reproduced. In both cases, there is a distinct maximum with a steep decrease toward the sheath edge. The height of the maximum is of the same order of magnitude, whereas the maximum for the measurement is larger than for the model. This is reasonable because the voltage drop about the sheath is the same, and if the sheath is thinner, the electric field $E(z)$ and therefore D must be larger.

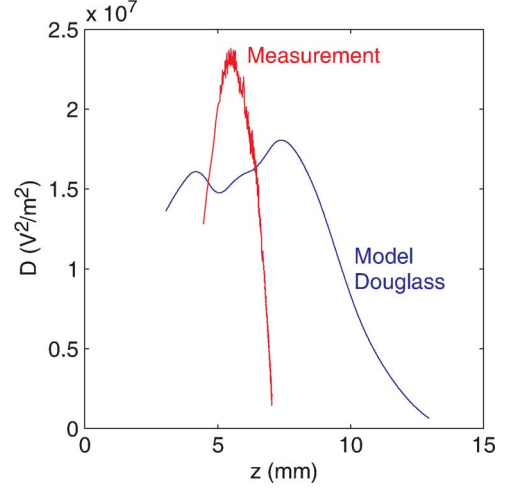


Fig. 5. Parameter D versus the levitation height z of the particles, as obtained from the measurement (red) and the sheath model (blue).

V. DISCUSSION AND CONCLUSION

Here, we have proposed an alternative method to use particles as probes for the plasma sheath. The continuous mass loss of the PMMA particle causes a steady increase in the equilibrium position. This allows probing the force balance with high spatial resolution, as compared with experiments [5], [7], [9] where particles of different sizes are used. This approach is complementary to the hypergravity experiments [12]. In both experiments, the force of gravity $F = mg$ is varied. Here, we reduced the particle mass m , whereas in [12], the acceleration of gravity g was effectively increased. While our setup is less complicated to realize, it is limited to situations where the plasma substantially reduces the particle mass over time. Among others, this depends on the type/composition of the gas, the discharge pressure, the RF voltage, and the material that the microparticles are made of.

A possible mechanism for the continuous mass loss of the particles could be reactive sputtering due to impurities (e.g., Oxygen), as it was found by Zeuner *et al.* [24] for the etching of PMMA in an Argon discharge. Furthermore, the sputtering of PMMA by the impinging Argon ions might contribute to this process. However, a detailed discussion of the origin of the observed mass loss is beyond the scope of this paper and will be addressed in the future.

The proposed technique of making use of the continuous mass loss of a dust grain in combination with a PRRM allows probing the electric field force $F_E(z) = E(z)Q(z)$ with high spatial resolution, which can be used to benchmark sheath models. Here, we have not obtained a quantitative agreement between the measurement and the sheath model [18], and we leave a detailed discussion of the discrepancies for future work. Nevertheless, some qualitative features are reproduced, e.g., the distinct maximum of D found in the measurements strengthens the finding of Douglass *et al.* [18] that the floating potential of the dust particles ϕ_d is maximal at an intermediate levitation height. This might explain the disproportionate increase of the particle charge Q to the particle radius r_d for small- (light) to medium-sized particles [20], [25] since smaller particles are confined at levitation heights, where ϕ_d decreases toward the sheath edge.

Further assumptions on the sheath structure [12] or additional measurement [11] would allow to separate the sheath electric field E from the particle charge Q . We like to mention that, for smaller particles ($r_d < 3 \mu\text{m}$) located close to the sheath edge, the ion drag must be taken into account [26], which we have neglected so far and is beyond the scope of this paper. This might explain the more rapid decrease in D toward the sheath edge, as compared with the sheath model [18] (see Fig. 5).

The applicability of the Epstein model [21] and, in particular, the exact value of the reflection coefficient δ for parameters typical to dusty plasmas are still an open question. So far, most work on this issue was done in pure Argon plasmas (e.g., see [9], [27], [28], and [29]). We studied the friction coefficient of MF particles systematically for a wide pressure range in common noble gases (He, Ne, Ar, and Kr). Within the error margin, the results agree with the findings described in [27] and [28], which suggest to choose the reflection coefficient δ close to the upper limit of 1.44.

ACKNOWLEDGMENT

The authors would like to thank A. Douglass and T. Hyde for providing the data of the sheath model.

REFERENCES

- [1] U. Czarnetzki, D. Luggenhölscher, and H. F. Döbele, "Space and time resolved electric field measurements in helium and hydrogen RF-discharges," *Plasma Sources Sci. Technol.*, vol. 8, no. 2, p. 230, May 1999.
- [2] E. Wagenaars, M. D. Bowden, and G. M. W. Kroesen, "Measurements of electric-field strengths in ionization fronts during breakdown," *Phys. Rev. Lett.*, vol. 98, no. 7, p. 075002, Feb. 2007.
- [3] H. Yamada and D. L. Murphree, "Electrostatic probe measurements in a collisionless plasma sheath," *Phys. Fluids*, vol. 14, no. 6, pp. 1120–1126, Jun. 1971.
- [4] G. H. P. M. Swinkels, H. Kersten, H. Deutsch, and G. M. W. Kroesen, "Microcalorimetry of dust particles in a radio-frequency plasma," *J. Appl. Phys.*, vol. 88, no. 4, pp. 1747–1755, 2000.
- [5] C. Zafiu, A. Melzer, and A. Piel, "Nonlinear resonances of particles in a dusty plasma sheath," *Phys. Rev. E*, vol. 63, no. 6, p. 066403, Jun. 2001.
- [6] B. M. Annaratone, T. Antonova, H. M. Thomas, and G. E. Morfill, "Diagnostics of the electronegative plasma sheath at low pressures using microparticles," *Phys. Rev. Lett.*, vol. 93, p. 185001, Oct. 2004.
- [7] A. A. Samarian and B. W. James, "Dust as fine electrostatic probes for plasma diagnostic," *Plasma Phys. Control. Fusion*, vol. 47, no. 12B, p. B629, Dec. 2005.
- [8] G. Thieme, R. Basner, R. Wiese, and H. Kersten, "Microparticles in plasmas as diagnostic tools and substrates," *Faraday Discuss.*, vol. 137, pp. 157–171, 2008.
- [9] R. Basner, F. Sigeneger, D. Loffhagen, G. Schubert, H. Fehske, and H. Kersten, "Particles as probes for complex plasmas in front of biased surfaces," *New J. Phys.*, vol. 11, no. 1, p. 013041, 2009.
- [10] H. R. Maurer, R. Basner, and H. Kersten, "Temperature of particulates in low-pressure RF-plasmas in Ar, Ar/H₂ and Ar/N₂ mixtures," *Contrib. Plasma Phys.*, vol. 50, no. 10, pp. 954–961, Nov. 2010.
- [11] V. Land, B. Smith, L. Matthews, and T. Hyde, "Probing the sheath electric field with a crystal lattice by using thermophoresis in dusty plasma," *IEEE Trans. Plasma Sci.*, vol. 38, no. 4, pp. 768–773, Apr. 2010.
- [12] J. Beckers, T. Ockenga, M. Wolter, W. W. Stoffels, J. van Dijk, H. Kersten, and G. M. W. Kroesen, "Microparticles in a collisional RF plasma sheath under hypergravity conditions as probes for the electric field strength and the particle charge," *Phys. Rev. Lett.*, vol. 106, no. 11, p. 115002, Mar. 2011.
- [13] V. Land, J. Carmona-Reyes, J. Creel, J. Schmoke, M. Cook, L. Matthews, and T. Hyde, "The effect of electrode heating on the discharge parameters in complex plasma experiments," *Plasma Sources Sci. Technol.*, vol. 20, no. 1, p. 015026, Feb. 2011.
- [14] H. Rothermel, T. Hagl, G. E. Morfill, M. H. Thoma, and H. M. Thomas, "Gravity compensation in complex plasmas by application of a temperature gradient," *Phys. Rev. Lett.*, vol. 89, no. 17, pp. 175001–1–175001–4, Oct. 2002.
- [15] A. Ashkin, "Acceleration and trapping of particles by radiation pressure," *Phys. Rev. Lett.*, vol. 24, no. 4, pp. 156–159, Jan. 1970.
- [16] A. Melzer, "Laser-experiments on particle interactions in strongly coupled dusty plasma crystals," *Phys. Scr.*, vol. 2001, no. T89, p. 33, 2001.
- [17] T. Trottenberg, A. Melzer, and A. Piel, "Measurement of the electric charge on particulates forming Coulomb crystals in the sheath of a radiofrequency plasma," *Plasma Sources Sci. Technol.*, vol. 4, no. 3, p. 450, Aug. 1995.
- [18] A. Douglass, V. Land, L. Matthews, and T. Hyde, "Dust particle charge in plasma with ion flow and electron depletion near plasma boundaries," *Phys. Plasmas*, vol. 18, no. 8, p. 083706, Aug. 2011.
- [19] J. Carstensen, H. Jung, F. Greiner, and A. Piel, "Mass changes of microparticles in a plasma observed by a phase-resolved resonance method," *Phys. Plasmas*, vol. 18, no. 3, p. 033701, Mar. 2011.
- [20] E. B. Tomme, D. A. Law, B. M. Annaratone, and J. E. Allen, "Parabolic plasma sheath potentials and their implications for the charge on levitated dust particles," *Phys. Rev. Lett.*, vol. 85, no. 12, pp. 2518–2521, Sep. 2000.
- [21] P. S. Epstein, "On the resistance experienced by spheres in their motion through gases," *Phys. Rev.*, vol. 23, no. 6, pp. 710–733, Jun. 1924.
- [22] H. M. Mott-Smith and I. Langmuir, "The theory of collectors in gaseous discharges," *Phys. Rev.*, vol. 28, no. 4, pp. 727–763, Oct. 1926.
- [23] E. C. Whipple, "Potentials of surfaces in space," *Rep. Progr. Phys.*, vol. 44, no. 11, p. 1197, Nov. 1981.
- [24] M. Zeuner, J. Meichsner, and H. U. Poll, "Oxidative decomposition of polymethylmethacrylate (PMMA) in plasma etching," *Plasma Sources Sci. Technol.*, vol. 4, no. 3, p. 406, Aug. 1995.
- [25] J. Carstensen, F. Greiner, and A. Piel, "Determination of dust grain charge and screening lengths in the plasma sheath by means of a controlled cluster rotation," *Phys. Plasmas*, vol. 17, no. 8, p. 083703, Aug. 2010.
- [26] G. A. Hebner, M. E. Riley, and K. E. Greenberg, "Analysis of the particle interactions in a two-dimensional-plasma dust crystal and the use of dust as a probe of the time-averaged presheath electric field," *Phys. Rev. E, Stat. Nonlin. Soft Matter Phys.*, vol. 66, no. 4, p. 046407, Oct. 2002.
- [27] B. Liu, J. Goree, V. Nosenko, and L. Boufendi, "Radiation pressure and gas drag forces on a melamine-formaldehyde microsphere in a dusty plasma," *Phys. Plasmas*, vol. 10, no. 1, pp. 9–20, Jan. 2003.
- [28] Y. Nakamura and O. Ishihara, "A complex plasma device of large surface area," *Rev. Sci. Instrum.*, vol. 79, no. 3, p. 033504, Mar. 2008.
- [29] G. Schubert, R. Basner, H. Kersten, and H. Fehske, "Determination of sheath parameters by test particles upon local electrode bias and plasma switching," *Eur. Phys. J. D*, vol. 63, no. 3, pp. 431–440, Aug. 2011.

Authors' photographs and biographies not available at the time of publication.

A.8

IMAGING MIE ELLIPSOMETRY: DYNAMICS OF NANODUST CLOUDS IN AN ARGON-ACETYLENE PLASMA

Franko Greiner, Jan Carstensen, Nils Köhler, Iris Pilch, Helge Ketelsen,
Sascha Knist and Alexander Piel

Reprinted with permission from
Franko Greiner, Jan Carstensen, Nils Köhler, Iris Pilch, Helge Ketelsen,
Sascha Knist and Alexander Piel,
Plasma Sources Science and Technology, Vol. 21, 065005 (2012).
Copyright 2012, IOP Publishing Ltd

Imaging Mie ellipsometry: dynamics of nanodust clouds in an argon–acetylene plasma

Franko Greiner, Jan Carstensen, Nils Köhler, Iris Pilch¹, Helge Ketelsen², Sascha Knist³ and Alexander Piel

Institut für Experimentelle und Angewandte Physik, Christian-Albrechts-Universität zu Kiel, 24098 Kiel, Germany

¹ Plasma and Coatings Physics Division, IFM-Materials Physics, Linköping University, SE-581 83 Linköping, Sweden

² SENTECH Instruments GmbH, Schwarzschildstraße 2, 12489 Berlin, Germany

³ Graforce Hydro GmbH, Carl-Scheele-Str. 16, 12489 Berlin, Germany

E-mail: greiner@physik.uni-kiel.de

Received 13 July 2012, in final form 14 September 2012

Published 7 November 2012

Online at stacks.iop.org/PSST/21/065005

Abstract

For the *in situ* analysis of nano-sized particles in a laboratory plasma, Mie ellipsometry is a well established technique. We present a simple setup with two CCD cameras to gain online spatiotemporal resolved information of the growth dynamics of particles which are produced by plasma chemical processes in an argon–acetylene plasma. Imaging Mie ellipsometry proves to be a powerful technique to study the growth processes of nanodust in all its details.

 Online supplementary data available from stacks.iop.org/PSST/21/065005/mmedia

(Some figures may appear in colour only in the online journal)

1. Introduction

It has been long known that plasma chemical reactions can lead to the growth of particles (dust) in the plasma volume. These dust particles are observed as unwanted by-products during plasma etching of silicon wafers. Unfortunately, the dust grains fall down to the wafer, if they become too heavy or when the plasma is switched off, and spoil the etched structures on the wafer. On the other hand, it has been found that particles produced in plasmas have great technological potential. One example is amorphous hydrogenated silicon (a-Si:H) nanoparticles produced by plasma-enhanced chemical vapor deposition (PECVD) [1, 2] and embedded in thin films, which can be used to produce low-cost solar cells. It should be mentioned that nano-sized dust particles are also an important component of the interstellar medium [3] and the comparison with laboratory experiments is very fruitful [4].

In situ measurements of size and density of plasma-grown particles were first realized by looking at the amount of unpolarized scattered light [5] or *ex situ* using transmission

electron microscopy [6]. Later, improved techniques were developed which used Mie ellipsometry to get information about size and density of the dust [7, 8]. Mie ellipsometry with CCD cameras was first presented by Shiratani [9]. The combination of *in situ* and *ex situ* measurements led to a detailed picture of the genesis and growth process of nanodust particles in a noble gas plasma with silane (SiH₄) or acetylene (C₂H₂) admixtures (see [10, 11] for an overview).

In addition to the plasma technological relevance, basic plasma research with nanodust has the advantage that gravitation is not a dominant force, i.e. nanodust clouds can be produced and investigated in the laboratory without gravity compensation. Compared to dusty plasmas with micrometer-sized particles, the observation of single particles with sizes smaller than the illumination wavelength by video microscopy of single particles is not feasible. Nevertheless, the dynamics of large ensembles of nanodust (clouds) can be studied using fast CCD cameras.

Amorphous hydrogenated carbon (a-C:H) particles grow inside an argon–acetylene plasma. Following Berndt *et al* [11], the growth process can be divided into three distinct phases:

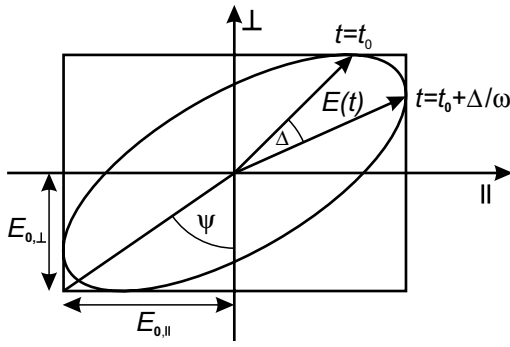


Figure 1. The elliptically polarized EM wave is described by two orthogonal waves $E_{\parallel}(t) = E_{0,\parallel} \exp(i(\omega t + \delta_{\parallel}))$ and $E_{\perp}(t) = E_{0,\perp} \exp(i(\omega t + \delta_{\perp}))$. The ellipsometric angles are defined as amplitude ratio Ψ and relative phase Δ . The wave propagates along the z -axis, which points toward the reader [12].

(i) nucleation of small ($r < 1$ nm) clusters by plasma chemical reactions, (ii) coagulation of the clusters by collisions up to radii of around 10 nm, (iii) accretion of the particles by sticking of molecules (mostly radicals) and ions from the gas phase to the negatively-charged dust grains. The nucleation phase depends on many different discharge parameters and chemical properties. During the fast coagulation phase the dust density rapidly decreases, whereas it remains nearly constant during the slow accretion phase. Often a nearly linear increase in the particle radius with time is observed during the accretion phase leading to spherical grains with a quasi-monodisperse size distribution [11].

This paper focuses on the diagnostic of nanodust with radii larger than 100 nm, i.e. dust in the accretion phase. To understand the behavior of nanodust clouds, spatiotemporal information on the particle growth and transport is needed. We present a method, named imaging Mie ellipsometry (I-Mie), which is based on the direct measurement of the polarization state of the scattered light using a polarizing beam splitter and two CCD cameras to obtain two-dimensional information about the dust particle size. The proposed method enables us to study the size-resolved dynamics of nanodust clouds in great detail. The method is calibrated with a commercial polarimeter to get information about the complex refractive index of the dust particles.

2. Basics of Mie ellipsometry

In this section a short description of Mie scattering is given, which will be needed for the understanding of the proposed technique. Mie theory describes the change in the polarization of an electromagnetic (EM) wave interacting with a dielectric object. In general, an EM wave is elliptically polarized, and its electric field components in a Cartesian coordinate system (\parallel , \perp) can be described by the relative phase $\Delta = \delta_{\parallel} - \delta_{\perp}$ and the ratio $\Psi = \text{atan}(E_{0,\parallel}/E_{0,\perp})$ of the amplitudes, see figure 1. For partially polarized wave fields the ellipsometric angles, Ψ and Δ , and a set of measurable intensities, the Stokes vector,

can be used to describe the polarization state of the light

$$\begin{bmatrix} I \\ Q \\ U \\ V \end{bmatrix} = \begin{pmatrix} I_0 \\ I_{\parallel} - I_{\perp} \\ I_{\pi/4} - I_{-\pi/4} \\ I_R - I_L \end{pmatrix} = \begin{pmatrix} I_p \\ -I_p \cos(2\Psi) \\ I_p \sin(2\Psi) \cos(\Delta) \\ -I_p \sin(2\Psi) \sin(\Delta) \end{pmatrix} + \begin{pmatrix} I_u \\ 0 \\ 0 \\ 0 \end{pmatrix} = I_p \begin{pmatrix} (I_p + I_u)/I_p \\ -\cos(2\Psi) \\ \sin(2\Psi) \cos(\Delta) \\ -\sin(2\Psi) \sin(\Delta) \end{pmatrix}. \quad (1)$$

$I_0 = I_p + I_u$ is the total intensity (polarized part I_p and unpolarized part I_u). The unpolarized part I_u accounts for light that reaches the detector and is not coherent with the incident EM wave. For Mie ellipsometry in a plasma I_u is likely to result from the ambient plasma glow. The intensities in equation (1) I_{\parallel} , I_{\perp} , $I_{\pi/4}$ and $I_{-\pi/4}$ denote the intensities passing through an ideal linear polarizer aligned at angles of 0 , $\pi/2$, $\pi/4$ and $-\pi/4$, respectively. I_R and I_L are the intensities transmitted by ideal right- and left-circular polarizers [12]. The right-hand side of equation (1) shows how the Stokes vector is related to the ellipsometric angles Ψ and Δ . It is noted that only for a fully polarized wave the relation $I_0^2 = Q^2 + U^2 + V^2$ is valid. If the wave is partially polarized the degree of polarization (DoP) is defined as the ratio of the intensity of the polarized part of the beam to the total intensity

$$\text{DoP} = \frac{I_p}{I_p + I_u} = \frac{\sqrt{Q^2 + U^2 + V^2}}{I_0}. \quad (2)$$

It is straightforward to describe an ellipsometer system that is built from, e.g., polarizers, retarders and analyzers mathematically by using Stokes vectors. If S_{in} is the Stokes vector of the incoming wave and S_{out} that of the wave after propagating through an optical component, the Stokes vector of the outgoing wave is given by $S_{\text{out}} = \vec{M} S_{\text{in}}$, where \vec{M} is the Mueller matrix [12] of that optical component.

The Mueller matrices for linear polarizers along the \parallel or \perp axis $\vec{M}_{\text{LP},\parallel}$ and $\vec{M}_{\text{LP},\perp}$ are defined as

$$\vec{M}_{\text{LP},\parallel} = \frac{1}{2} \begin{pmatrix} 1 & 1 & 0 & 0 \\ 1 & 1 & 0 & 0 \\ 0 & 0 & 0 & 0 \\ 0 & 0 & 0 & 0 \end{pmatrix}, \quad \vec{M}_{\text{LP},\perp} = \frac{1}{2} \begin{pmatrix} 1 & -1 & 0 & 0 \\ -1 & 1 & 0 & 0 \\ 0 & 0 & 0 & 0 \\ 0 & 0 & 0 & 0 \end{pmatrix}. \quad (3)$$

Since the Stokes vectors are defined in a Cartesian coordinate system of the propagating wave, it has to be taken into account that a rotation of the coordinate system of the wave leads to an additional rotation matrix [12]

$$\vec{R}(\alpha) = \begin{pmatrix} 1 & 0 & 0 & 0 \\ 0 & \cos(2\alpha) & \sin(2\alpha) & 0 \\ 0 & -\sin(2\alpha) & \cos(2\alpha) & 0 \\ 0 & 0 & 0 & 1 \end{pmatrix}. \quad (4)$$

Note that I , $Q^2 + U^2$ and V are invariant under rotation of the reference directions.

To account for the scattering of light of nano-sized particles, the particle is input to the analysis by its own Mueller matrix, called the scattering matrix \vec{S} [13]. The elements $S_{i,j}$

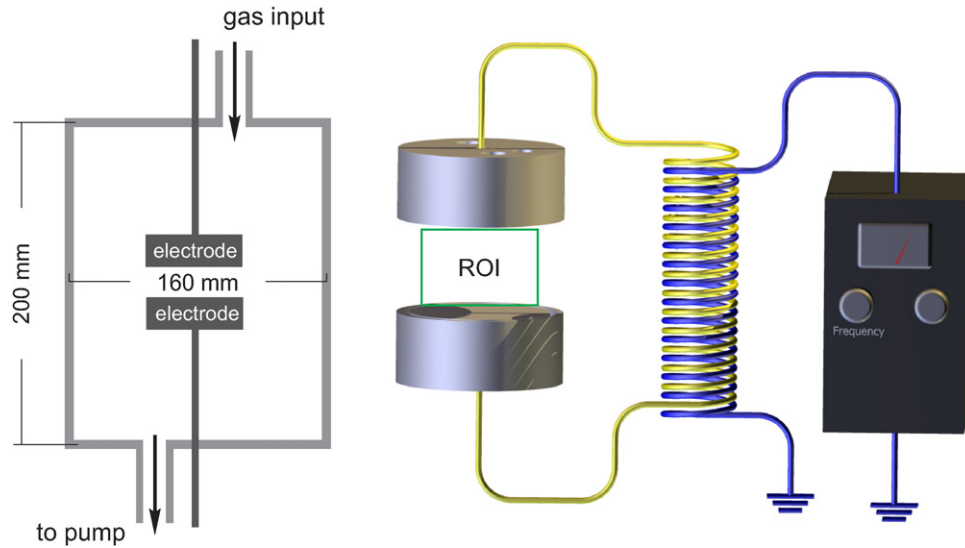


Figure 2. Sketch of the experimental system. The electrodes have a diameter of 60 mm and a gap width of 40 mm. The argon–acetylene gas mixture is injected from the top, and the vacuum pump is connected to the bottom of the chamber. The balun isolates the electrodes galvanically from the grounded vacuum chamber.

of \vec{S} can be derived from the vector wave equations of the scattering of an EM wave on a particle. The $S_{i,j}$ are functions of the scattering angle (90° for our setup), the relative refractive index N and the size parameter x . The relative refractive index N is a complex number

$$N = \frac{m}{m_0} = m_r + im_i, \quad (5)$$

where m and m_0 are the refractive indices of the particle and the surrounding medium ($m_0 = 1$ for a plasma). The real part of the refractive index m_r is related to the change in the speed of light, the imaginary part m_i to the absorption of the light. The size parameter is the relative size of the particles

$$x = kr = \frac{2\pi m_0 r}{\lambda}, \quad (6)$$

i.e. the circumference of the particle normalized to the wavelength of light in the surrounding medium, λ is the vacuum wavelength of the light. The job of an ellipsometer is to measure quantities that can be used to determine x and N from the scattering matrix of the particles. More details can be found in the textbook of Bohren and Huffman [13].

3. Setup of I-Mie

The experiments were performed in a conventional capacitively coupled rf discharge (8 W@13.56 MHz) in a parallel-plate reactor with circular electrodes of 60 mm diameter and a gap width of 40 mm, as sketched in figure 2. Both electrodes are driven over a balun in push–pull drive and the discharge vessel is grounded. The balun has a very small parasitic capacity and isolates the electrodes galvanically from ground, creating an almost symmetric drive of the discharge. At a discharge pressure of 30 Pa the argon flow is 20 sccm and the acetylene flow is 3 sccm. The two gases are mixed together before the gas enters the vacuum chamber. The

pumping power of the vacuum pump is very low to ensure a homogeneous, laminar flow. To prevent large dust particles from re-entering the electrode gap after being repelled from the plasma, a large chamber volume below and above the electrode system is necessary. If the chamber walls are too close to the electrode gap, the dust particles ejected from the electrode region accumulate around the electrodes and the dynamics of the growth instability would be modified.

For I-Mie the plasma volume was illuminated from one side with a laser (200 mW, 532 nm), widened to a laser stripe of 1.5 mm thickness and 40 mm width in the direction perpendicular to the electrode surfaces. The scattered light from the nanodust was detected at a scattering angle of 90° . The scattered light passes a wavelength filter (at 532 nm), a camera lens, and a polarizing beam splitter. The two orthogonal directions of polarization were recorded by two CCD cameras with a resolution of 640×480 pixel. The region of interest (ROI), which shows the center region between the electrodes, is 440×330 pixel at a resolution of $100 \mu\text{m}/\text{pixel}$, i.e. $44 \text{ mm} \times 33 \text{ mm}$. The cameras were externally triggered for time-synchronous recordings.

The details of the ellipsometric assembly are shown in figure 3. The polarization of the laser stripe is 45° with respect to the plane of incidence. This ensures that the incident intensities $I_{\perp,i}$ and $I_{\parallel,i}$ have the same absolute value before scattering. The symbol ‘ \perp ’ indicates scattered light with a polarization perpendicular to the plane of incidence and the symbol ‘ \parallel ’ indicates light with a parallel polarization. Following Hollenstein *et al* [7] it is assumed that the cameras detect the spatially resolved power $W_{\perp,s}(x, y)$ and $W_{\parallel,s}(x, y)$, where x and y refer to the positions on the CCD sensors. In the case of single-particle scattering $W_{\perp,s}(x, y)$ and $W_{\parallel,s}(x, y)$ are proportional to the intensities $I_{\perp,s}$ and $I_{\parallel,s}$ of the scattered light, i.e.

$$\begin{aligned} W_{\perp,s}(x, y) &\propto N_P(x, y) \Delta V \Delta \Omega I_{\perp,s}(x, y), \\ W_{\parallel,s}(x, y) &\propto N_P(x, y) \Delta V \Delta \Omega I_{\parallel,s}(x, y). \end{aligned} \quad (7)$$

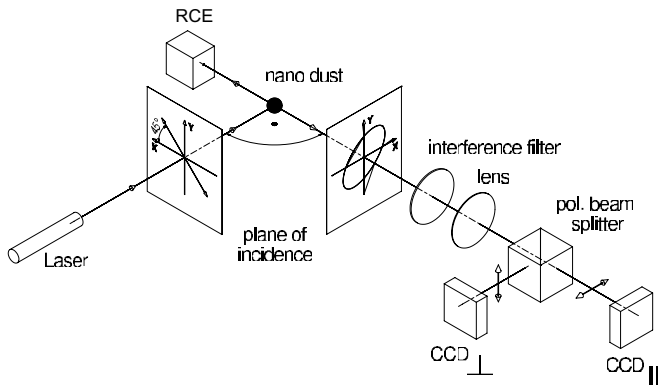


Figure 3. Setup of imaging Mie ellipsometry. The incident laser light is linearly polarized with an angle of 45° with respect to the plane of incidence. The scattered light is observed under a scattering angle of 90° , split into its orthogonal parts by a polarizing beam splitter and detected by two CCD cameras. In addition, the scattered light is monitored by a rotating compensator ellipsometer (RCE).

$N_p(x, y)$ is the number density of nanodust in the observation volume ΔV from which the light is scattered into the solid angle $\Delta\Omega$. This angle should be small enough to ensure a small error of the scattering angle, which was chosen to be 90° . It is assumed that the observation volume ΔV and the solid angle $\Delta\Omega$ have the same value for all camera pixels. For the sake of clarity the light intensities I will be used instead of the powers W . The measured camera power signals deviate from the intensities of the EM waves only by a factor that does not affect the polarization of the scattered light.

For deducing information from the scattered light detected by the cameras, the Stokes vector can be used. For this, the Stokes vector of the scattered light $S_s = (I_p + I_u, Q, U, V)^T$ needs to be multiplied by the Mueller matrices of the polarizing beam splitter $\vec{M}_{LP,\parallel}$ and $\vec{M}_{LP,\perp}$ as given in equation (3). The Stokes vector of the light behind the analyser, which is parallel to the scattering plane, is then given by

$$S_{\parallel,s} = \frac{1}{2} \begin{pmatrix} 1 & 1 & 0 & 0 \\ 1 & 1 & 0 & 0 \\ 0 & 0 & 0 & 0 \\ 0 & 0 & 0 & 0 \end{pmatrix} \cdot \begin{pmatrix} I_p + I_u \\ Q \\ U \\ V \end{pmatrix} = \frac{1}{2} \begin{pmatrix} I_p + I_u + Q \\ I_p + I_u + Q \\ 0 \\ 0 \end{pmatrix}. \quad (8)$$

As a result, the intensity detected from camera CCD_{\parallel} (see figure 3) is

$$I_{\parallel,s} = \frac{1}{2}(I_p + I_u + Q). \quad (9)$$

In the same way, the signal reaching camera CCD_{\perp} can be derived

$$I_{\perp,s} = \frac{1}{2}(I_p + I_u - Q). \quad (10)$$

The sum and the difference of equations (10) and (9) are

$$I_0 = I_{\parallel,s} + I_{\perp,s}, \quad (11)$$

$$Q = I_{\parallel,s} - I_{\perp,s}. \quad (12)$$

These equations show that the Stokes parameter Q of the polarized part of the light reaching the camera can directly be measured by the two CCD cameras. However, the Stokes parameter Q is an absolute intensity, i.e. during the growth of

the particles it changes drastically over several decades. To get a suitable quantity the relative $q = Q/I_p$ can be used. With $I_p = I_0 - I_u$ it follows that

$$q(x, y) = \frac{Q(x, y)}{I_p(x, y)} = \frac{I_{\parallel,s}(x, y) - I_{\perp,s}(x, y)}{I_{\parallel,s}(x, y) + I_{\perp,s}(x, y) - I_u(x, y)} \\ = \frac{Q(x, y)}{I_0(x, y)} \cdot \frac{1}{\text{DoP}(x, y)}. \quad (13)$$

The last step follows from equation (2).

Unfortunately, the two camera signals do not carry information about the DoP, i.e. additional, spatially resolved information of DoP is required to compute $q(x, y, t)$. However, a simple scheme of I-Mie can be built, when measuring the DoP at a fixed position and assuming a spatially constant value $\text{DoP}(x, y) = \text{DoP}$. In the next section it will be shown that this assumption is fulfilled for our experimental conditions.

The relative value q can be used to generate a colormap that contains size information computed from the signals of the CCD cameras. In this way, the spatiotemporal growth of nanodust can be studied in detail. The q -colormap gives relative size information. To transform the q -scale into a size scale, the whole scattering matrix of the nanodust has to be known. For this purpose a rotating compensator ellipsometer (RCE) [12] was used which measures the ellipsometric angles Ψ and Δ at a single spatial position. This measurement was made continuously during growth and ejection of the nanodust, leading to a so-called *kinetic* Mie ellipsometry scheme that is capable of estimating the refractive index for the full period of the growth oscillation. The RCE measures the ellipsometric angles Ψ and Δ simultaneously with the CCD cameras for the same scattering angle of 90° . By doing so, the measured parameter q from the camera system can be compared with the information obtained from the RCE. The RCE also measures the time-resolved DoP parameter needed to compute q .

In the next sections it will be shown that the described simple I-Mie scheme is capable of analyzing the spatiotemporal evolution of growing nanodust in an argon-acetylene plasma.

4. Experimental results

When the rf is switched on, the growth process starts, leading to the above-mentioned growth cycle of dust particles. The periodic behavior can be seen in figure 4 where the scattered light $I_0 = I_{\parallel,s} + I_{\perp,s}$ averaged over the whole CCD data is shown for several cycles. The development of the dust cloud over one cycle of the growth instability is shown in figure 5 for the averaged intensities and a set of images. When the particles' size increases, a void develops in the center of the plasma, which becomes larger over time. At a specific point the void fills the whole electrode gap and all dust is depleted from the plasma. After a short time the next growth cycle starts.

For determining the relative value $q(x, y, t)$ from equation (13) the $\text{DoP}(x, y, t)$ is needed. In the present setup, the DoP was measured with the RCE at a fixed position near the lower electrode. In figure 6 the $q(x, y, t)$ values measured with the RCE are compared with the values measured with the

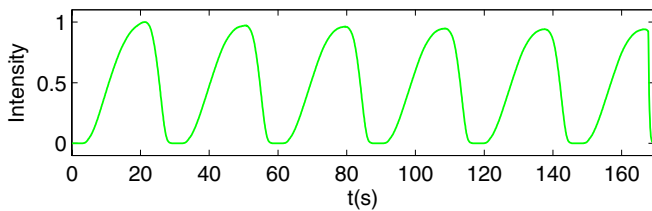


Figure 4. The total intensity of the scattered light averaged over the whole dust cloud is shown vs.time. After switching on the discharge, the growth oscillation establishes.

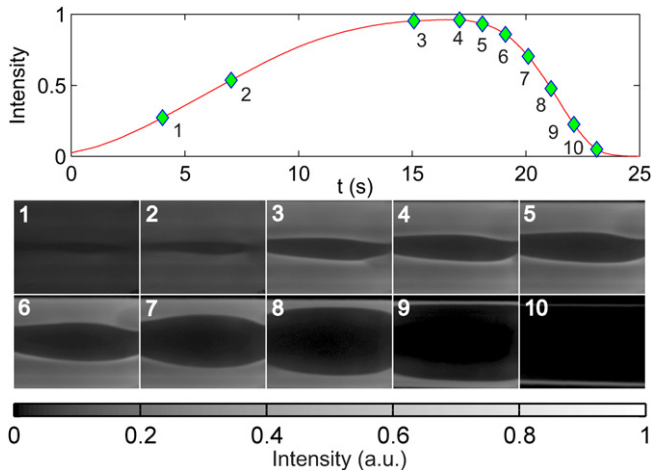


Figure 5. Total intensity of the scattered light averaged over the whole dust cloud for one growth cycle and the corresponding CCD images. When the particles become larger, a dust-free region (void) develops in the plasma center. At a certain particle size the whole dust content has left the electrode gap and a new growth cycle starts. (See online supplementary movie at stacks.iop.org/PSST/21/065005/mmedia).

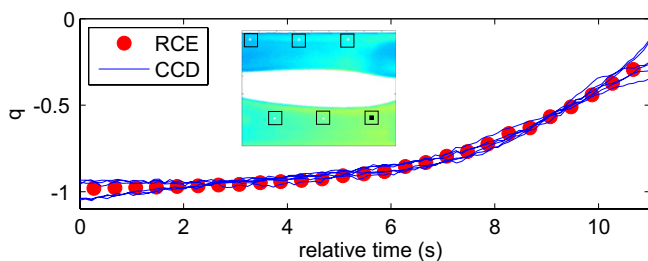


Figure 6. Comparison of the q -parameter measured with the rotating compensator ellipsometer (RCE) and calculated from the CCD data (average of 6×6 Pixel) at six positions spread over the ROI. All measurements are in good agreement. The inset shows the position where the measurements were taken. The small filled square gives the position where the RCE data were taken.

cameras, where the data has been taken at six positions over the ROI. It is found that the q values measured by the RCE and the CCD cameras are in good agreement.

However, the particle growth at the six positions is not synchronous. Therefore, the q curves were shifted along the time axis to compare their slopes. The finding that the detailed dynamic of growth process shows an identical but slightly asynchronous temporal behavior at different positions is in agreement with the well known fact that the particles grow nearly monodispersely over time [11] and have only a small spread in size.

The assumption of a constant DoP is justified. This result is reasonable considering the fact that the plasma glow is the main source for omnidirectional unpolarized light, which can reach all channels of the CCD cameras.

To get *in situ* information about the particle size, the (Δ, Ψ) signals of the RCE are plotted as function $\Delta(\Psi)$ and fitted with a model that assumes a linear change in the refractive index with the particle radius. A linear $N(r)$ model seems to be a reasonable approximation for the refractive index, when the nanoparticles are coated spheres. The refractive index of the core, which is built during the coagulation phase, is assumed to be different from the refractive index of the shell, which is built during the accretion phase. The coated sphere model is supported by the chemical *ex situ* analysis of the of (a-C:H) particles [14]. The result of the fitting procedure is shown in figures 7(a) and (b). With the known refractive index, the increase in the particle radius over time can be computed, see figure 7(c). This relation can be used to compute the growth $r(q)$, which is a function that delivers a distinct particle radius r for every value of q , shown in figure 7(d).

Finally we calculate the color-coded images from each pair of images acquired during the growth process. Figure 8 shows a sequence of events over one period of the growth oscillation. The color corresponds directly to the radius of the nanodust. The dynamics of the growth process are clearly visible by the varying color.

The growth process starts with a very homogeneous distribution of particles and a void develops when the particles grow larger in time. A further increase in nanodust size leads to a sedimentation of the dust, where the larger particles are found at the lower edge of the dust cloud. In addition, it can be seen that the growth is slightly inhomogeneous, i.e. ‘growth fronts’ are moving through the nanodust cloud. This may be attributed to an inhomogeneous transport of the (neutral) molecules and radicals, which are needed to grow dust particles during the accretion phase. The dynamics of the neutrals and radicals is a key parameter for the production of nanoparticles. A homogeneous flow of the acetylene leads to a nearly monodisperse production of nanoparticles. The interplay between production of neutrals, radicals and small clusters plays a critical role for the growth of particles. This was also shown in simulations [15, 16]. In our experiment, we arranged for a homogeneous, laminar flow of acetylene. The ‘growth fronts’, one of which is clearly visible in the upper right corner of frame 13–18 (region indicated in figure 8 frame 13), can arise due to two different processes: residual inhomogeneities in the flow of the acetylene or exhaustion of the building blocks of the nanodust.

5. Conclusion

A simple but powerful technique for imaging the growth dynamics of dust particles grown in an acetylene plasma has been implemented. The technique provides two-dimensional spatial information of the dust-particle size distribution that can be followed in time. The main components needed for imaging Mie ellipsometry (I-Mie) scheme are a polarizing beam splitter, which divides the scattered beam into two orthogonal polarized

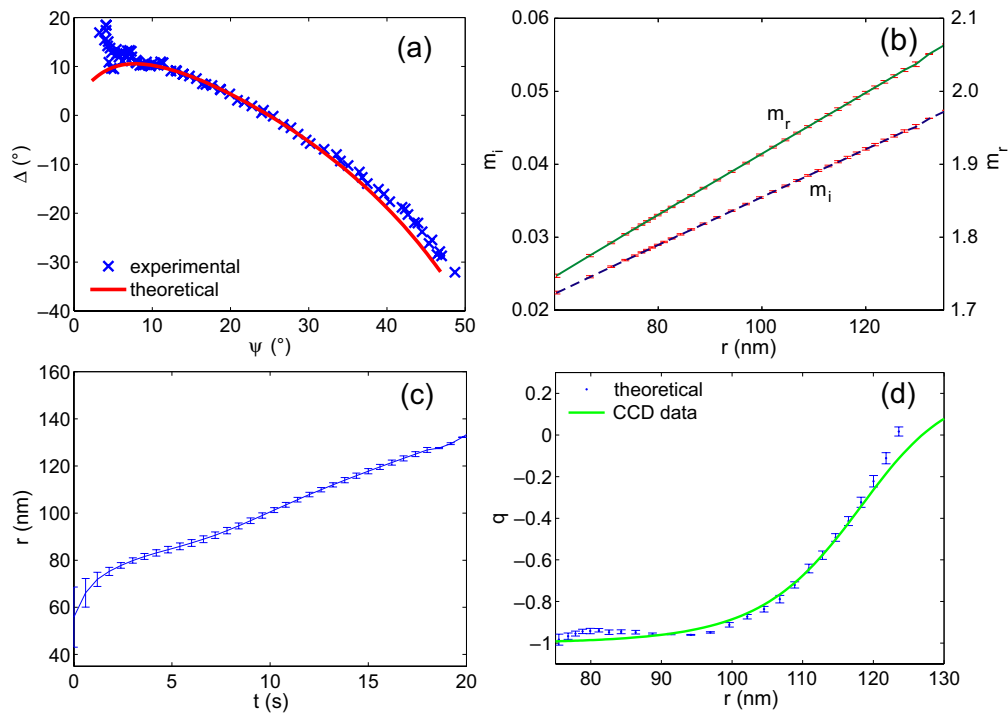


Figure 7. (a) The $\Delta(\Psi)$ data measured with the RCE. The data is fitted by a linear $N(r)$ model to determine the refractive index and the radii of the particles. (b) Values of the refractive index estimated from the linear model used to fit the $\Delta(\Psi)$ curve of figure (a). (c) Increase in the particle radius averaged over time for several growth cycles. (d) $r(q)$ curve giving a particle radius for every value of q . The line is the q estimated from the linear $N(r)$ model. All error bars are the standard deviation of the average over the six cycles of the growth oscillation shown in figure 4.

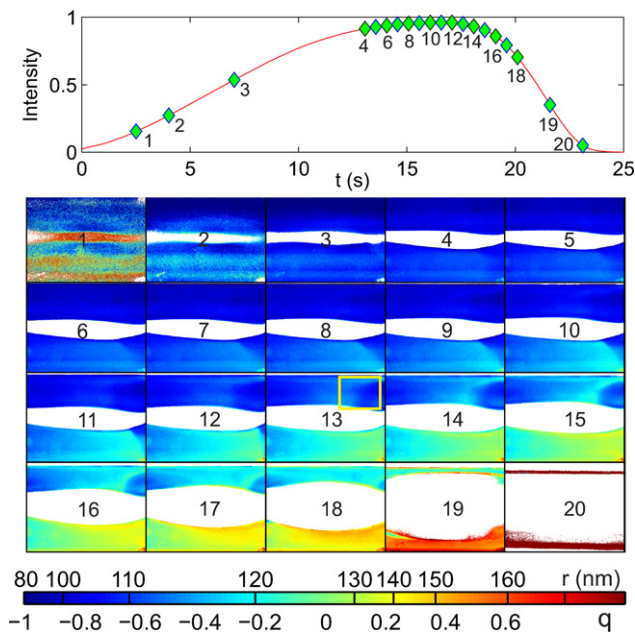


Figure 8. Spatiotemporal evolution of the q -parameter (equation (13)) during one period of the growth instability. The color of the data corresponds directly to the radius of the growing particles. The upper graph shows the times at which the images are taken. The signal detected by the CCD_{\parallel} camera in the first two frames was too small to determine a significant q . Sedimentation and several ‘growth fronts’ are observed during the growth of the particles. The square in frame 13 indicates one position where a ‘growth front’ is clearly seen. (Movie online, see online supplementary movie (stacks.iop.org/PSST/21/065005/mmedia)).

beams, and two conventional CCD cameras for recording the polarized beams. The spatial resolution of the setup depends on the used camera lens, the thickness of the laser stripe and the dust gradients inside the nanodust cloud.

The normalized Stokes parameter $q = Q/I_P$ can be determined from the recorded data allowing for spatiotemporal investigations of the growth dynamic. The proposed simple scheme is based on the fact that, under the conditions of the present experiment, the unpolarized part of the scattered light, which originates from the plasma background glow, is constant over the whole observation region. I-Mie would also work if the polarization degree $P = -q/\text{DoP}$ [13] is used for the diagnostic of the nanodust [7]. However, the $P(t)$ curve shows a local maximum in the size region of interest, impeding a one-to-one relation between time and size. Nevertheless, the I-Mie technique using P still gives qualitative information about the particle size.

The investigation of the well-known growth instability in an argon–acetylene plasma shows that the I-Mie technique provides new insight into the dynamics as it makes it possible to study spatial inhomogeneities during growth. Sedimentation, which occurs when the dust particles become so large that the force of gravity becomes noticeable, was clearly observed and it could be verified that the bigger dust particles were sedimenting while the smaller ones were still found above the void. These details have not previously been accessible with high spatial resolution, since the size of the dust particles is much too small for distinguishing the sizes by standard video microscopy. Other small-scale features during growth such as ‘growth fronts’ became visible.

The presented I-Mie scheme can be further improved when the unpolarized part of the light is measured independently. This can be done by taking two images for each time step, in which the laser stripe is alternating between on and off.

There is a strong demand for the I-Mie technique as it provides more detailed information, which is needed for the understanding of the dynamics of complex situations with nanoparticle growth involved. For example, situations where instabilities are observed inside the void [17] or the so-called 'carousel instability' [18] would benefit. It is believed that the size of the dust particles plays a decisive role for these dynamical phenomena but it has not been possible to prove this assumption.

Acknowledgments

This work was supported by the Deutsche Forschungsgemeinschaft DFG in the framework of the SFB-TR24 Greifswald Kiel, Project A2 and by the Swedish Research Council under grant 2008-6572, Linköping Linneaus Environment LiLi-NFM.

References

- [1] Chittick R C, Alexande J H and Sterling H F 1969 Preparation and properties of amorphous silicon *J. Electrochem. Soc.* **116** 77
- [2] Roca i Cabarrocas P, Djeridane Y, Nguyen-Tran Th, Johnson E V, Abramov A and Zhang Q 2008 Low temperature plasma synthesis of silicon nanocrystals: a strategy for high deposition rate and efficient polymorphous and microcrystalline solar cells *Plasma Phys. Control. Fusion* **50** 124037
- [3] Draine B T 2003 Interstellar dust grains *Annu. Rev. Astron. Astrophys.* **41** 241–89
- [4] Kovacevic E, Stefanovic I, Berndt J, Pendleton Y J and Winter J 2005 A candidate analog for carbonaceous interstellar dust: formation by reactive plasma polymerization *Astrophys. J.* **623** 242
- [5] Selwyn G S, Singh J and Bennett R S 1989 Insitu laser diagnostic studies of plasma-generated particulate contamination *J. Vac. Sci. Technol. A* **7** 2758–65
- [6] Boufendi L, Plain A, Blondeau J P, Bouchoule A, Laure C and Toogood M 1992 Measurements of particle-size kinetics from nanometer to micrometer scale in a low-pressure argon–silane radiofrequency discharge *Appl. Phys. Lett.* **60** 169–71
- [7] Hollenstein Ch, Dorier J-L, Dutta J, Sansonnens L and Howling A A 1994 Diagnostics of particle genesis and growth in RF silane plasmas by ion mass spectrometry and light scattering *Plasma Sources Sci. Technol.* **3** 278–85
- [8] Hayashi Y and Tachibana K 1996 Coulomb crystal formation from growing particles in a plasma and the analysis *J. Vac. Sci. Technol. A* **14** 506–10 *Dusty Plasmas-95 Workshop on Generation, Transport, and Removal of Particles in Plasmas (WICKENBURG, AZ, 01–07 October, 1995)*
- [9] Shiratani M, Kawasaki H, Fukuzawa T and Watanabe Y 1996 In situ polarization-sensitive laser-light-scattering method for simultaneous measurements of two-dimensional spatial size and density distributions of particles in plasmas *J. Vacuum Sci. Technol. A* **14** 603–7 *Dusty Plasmas-95 Workshop on Generation, Transport, and Removal of Particles in Plasmas (WICKENBURG, AZ, 01–07 October, 1995)*
- [10] Watanabe Y 2006 Formation and behaviour of nano/micro-particles in low pressure plasmas *J. Phys. D: Appl. Phys.* **39** R329–61
- [11] Berndt J, Kovacevic E, Stefanovic I, Stepanovic O, Hong S H, Boufendi L and Winter J 2009 Some aspects of reactive complex plasmas *Contrib. Plasma Phys.* **49** 107–33 (Special Issue SI)
- [12] Tompkins H G and Irene A I (ed) 2005 *Handbook of Ellipsometry* (Norwich: William Andrew Publishing)
- [13] Bohren C F and Huffman D R 1983 *Absorption and Scattering of Light by Small Particles* (New York: Wiley)
- [14] Kovacevic E, Berndt J, Strunskus T and Boufendi L 2012 Size dependent characteristics of plasma synthesized carbonaceous nanoparticles *J. Appl. Phys.* **112** 013303
- [15] Warthesen S and Girshick S 2007 Numerical simulation of the spatiotemporal evolution of a nanoparticle–plasma system *Plasma Chem. Plasma Process.* **27** 292–310
- [16] Ravi L and Girshick S L 2009 Coagulation of nanoparticles in a plasma *Phys. Rev. E* **79** 026408
- [17] Couedel L, Mikikian M, Samarian A A and Boufendi L 2010 Self-excited void instability during dust particle growth in a dusty plasma *Phys. Plasmas* **17** 083705
- [18] Mikikian M, Couedel L, Tessier Y and Boufendi L 2011 Carousel instability in a capacitively coupled RF dusty plasma *IEEE Trans. on Plasma Sci.* **39** (Issue 11, part 1) 2748–9 (Special Issue)

A.9

WAKE FORMATION AND WAKE FIELD EFFECTS IN COMPLEX PLASMAS

D. Block, J. Carstensen, P. Ludwig, W. J. Miloch, F. Greiner, A. Piel, M. Bonitz, and A. Melzer

Reprinted with permission from
D. Block, J. Carstensen, P. Ludwig, W. J. Miloch, F. Greiner, A. Piel, M.
Bonitz, and A. Melzer,
Contr. Plasma Phys., Vol. 52, 804 (2012).
Copyright 2012, WILEY-VCH Verlag GmbH & Co. KGaA, Weinheim

Wake Formation and Wake Field Effects in Complex Plasmas

D. Block^{1*}, J. Carstensen¹, P. Ludwig², W.J. Miloch³, F. Greiner¹, A. Piel¹, M. Bonitz², and A. Melzer⁴

¹ Institut für Experimentelle und Angewandte Physik, Christian-Albrechts-Universität zu Kiel, Leibnizstraße 19, 24098 Kiel, Germany

² Institut für Theoretische und Astrophysik, Christian-Albrechts-Universität zu Kiel, Leibnizstraße 15, 24098 Kiel, Germany

³ Department of Physics, University of Oslo, P.O. Box 1048 Blindern, N-0316 Oslo, Norway

⁴ Institut für Physik, Ernst-Moritz-Armdt Universität Greifswald, Felix-Hausdorff-Straße 6, 17489 Greifswald, Germany

Received 27 April 2012, accepted 21 May 2012

Published online 08 November 2012

Key words Wake field, grain charging, simulation, experiment, complex plasma

The formation of wake fields downstream of an objects in flowing plasmas has strong implications on structure, stability and dynamics of complex plasmas. This paper aims at putting recent experimental investigations and different theoretical approaches on charging of dust grains, stability of dust grain arrangements and the dynamical properties of complex plasmas into perspective. Further, the combination of wake fields and grain confinement is discussed, which is the generic situation in complex plasmas. It is shown that in spherical traps the resulting competition of trap geometry and vertical alignment leads to a sophisticated mixture of nested shell and string order.

1 Introduction

Symmetry plays a fundamental role in physics. The interaction of dust grains in a complex plasma is generally adequately described by an isotropic and spherically symmetric Yukawa potential. This symmetry is lost as soon as plasma and dust grains move relative to each other. Thus, studies of objects in streaming plasmas are interesting from a very fundamental point of view. The broken symmetry is known to have a large impact on structure, stability and dynamical properties of this strongly coupled system [1–3]. Non-equilibrium and streaming effects are omnipresent in nature and play an important role in many laboratory situations. Therefore, a profound understanding of objects in streaming plasmas is essential for a variety of problems in plasma physics, e.g. processes in the plasma sheath, probe theory, and measurements near spacecrafts. However, it is the field of complex plasmas that provides unique opportunities to investigate these basic processes in detail [4].

In laboratory plasmas strong ion flows are typically found in the plasma sheath. Due to a balance of gravitational and electric field forces dust grains are typically confined in this region. Thus, the plasma sheath region is ideally suited to study the interaction of dust grains in supersonic ion flows. Already with the first attempts to create three dimensional dust crystals it turned out, that grains tend to align in the direction of the ion flow. The reason for this alignment is that the upstream (highly negatively charged) grain acts as an electrostatic lens, which focuses the flowing ions downstream in a distance of about one electron Debye length λ_{De} . The resulting positive space charge region attracts downstream grains, which thus favor an aligned position. The existence and characteristics of the attractive wake field has been studied by a number of analytical and numerical studies [5–21] and experiments [22–29]. Based on systems consisting of two grains the wake field topology [27], the ion focus strength [23, 25, 26] and the influence of the confinement [24, 27, 30] have been studied.

While these investigations provide a basic understanding of wake fields in complex plasmas, fundamental questions remained unanswered. Recent progress in experiment [28–30] and simulation [31–33] now allows to

* Corresponding author. E-mail: block@physik.uni-kiel.de, Phone: +49 431 880 3862, Fax: +49 431 880 3809

address these open issues. First, advanced numerical studies of wake fields [21, 31, 33] allow for an one-to-one comparison of different simulation approaches. Second, the formation of ion wakes has been intensively studied for supersonic flows. In contrast, much less attention was paid to the subsonic regime, although the subsonic regime is of high interest for experiments where grains are confined in the pre-sheath region or the plasma bulk [28, 30, 34]. Recently, numerical approaches [31–33, 35] started to focus on wake field formation in this regime. Third, it has been assumed that the charging process for dust grains is not affected by the wake field. Experiments by Kong et al. [36], however, have indicated that the charging process of the dust grains should be affected by the ion flow and the arrangement of the grains. Recent experiments [28, 29] in combination with simulations [33] clearly show that in extended dust clouds identical dust charges are only a rough estimate.

This paper aims at putting the experimental and numerical progress on charging of dust grains, stability of dust grain arrangements and their dynamical properties into perspective and discusses the implications for research on complex plasmas.

2 Wake Fields in Theory, Simulation, and Experiment

A rigorous method to compute the wake field should be based on first principle calculations which solve the Vlasov equations for all plasma constituents and mimic collisions for instance with a Monte-Carlo approach. Powerful tools for this purpose are Molecular Dynamics (MD) simulations and Particle-In-Cell (PIC) methods. Multi-scale MD and PIC simulations are, however, computationally very demanding and limited to the static description of very few grains ($N < 10$). On the other hand, they include nonlinear effects, possible deviations from a shifted Maxwellian ion velocity distribution and allow for treating the charging process of the grains self-consistently. Compared to MD, the PIC method can handle significantly more plasma particles and thus reduces the numerical noise. Recent PIC codes, e.g. SCEPTIC [15], COPTIC [21], a hybrid P³M-code [37] and DiP3D [16] use three-dimensional grids to simulate the plasma dynamics around dust grains with realistic grain properties (i.e. dimensions, shape and conductance). SCEPTIC and COPTIC simulate ions with the PIC kinetic scheme assuming Boltzmann distributed electrons. The hybrid P³M-code and DiP3D are full PIC codes, where also the electrons are treated on first principles. Usually, 10^7 plasma particles are simulated around the grain. In addition, the hybrid P³M-code, DiP3D, and COPTIC allow to compute the charging of multiple grains. To correctly resolve the interaction of dust grains, which have an intergrain distance of the order of the electron Debye length, these codes (COPTIC, DiP3D, hybrid P³M) use the Particle-Particle-Particle Mesh scheme [38]. Since the relevant time scale for PIC simulations is given by the ion plasma frequency, which is several orders higher than that of the dust grains, the dust grains are generally treated as stationary objects.

Therefore, in order to access structure and dynamics of dust clouds it is necessary to capture the dust-plasma interaction in a time-averaged model (for electrons and ions). A common simplification for a complex plasma, consisting of electrons, ions, neutral atoms and dust grains, is the so called one component plasma (OCP) model, where the dust grains are treated individually and all plasma properties are represented by the longitudinal dielectric function $\epsilon(\mathbf{k}, \omega)$. In linear approximation this results in an effective grain potential

$$\Phi(\mathbf{r}) = \int d^3k \frac{Q_d}{2\pi^2 k^2 \epsilon(\mathbf{k}, \mathbf{k} \cdot \mathbf{u}_i)} e^{i\mathbf{k} \cdot \mathbf{r}}, \quad (1)$$

where Q_d is the dust charge and \mathbf{r} denotes the distance from the grain. For isotropic and stationary plasma conditions, this gives the well known Yukawa potential. However, for a streaming plasma the response of the plasma in direction of the flow is more complicated. Linear Response (LR) theory allows for a high precision numerical computation of the dynamically screened Coulomb potential from the dielectric function. A detailed description of the numerical treatment is given in [31] and references therein. LR allows to study the generic features of wake fields in great detail with low numerical noise over broad parameter ranges, i.e. for collisionless and collisional plasmas [31]. Furthermore, LR provides in combination with Molecular Dynamics (MD) simulations the unique opportunity to study the impact of streaming plasmas on the dynamical, correlated interplay of many dust grains with unrivalled precision (within the linear approximation) [32, 39, 40]. However, this approach assumes point-like (non-absorbing) grains and does not account for self-consistent grain charging processes yet.

Experimental approaches to study wake fields are difficult and only a few measurements have been made. The non-reciprocal nature of the grain interaction of aligned grains has been demonstrated by Takahashi et al. [22].

Melzer et al. [23] showed that the attractive character of the wakes potential critically relies on ion collisions and gave a first estimation of the attractive force. The strong influence of the confinement on the grain arrangement was studied by Steinberg et al. [24] and Samarian et al. [41]. The ion focus strength has been studied by Hebner and Riley using binary collisions [25,26]. Unfortunately, most investigations so far assumed that the downstream grain neither affects the wake of the upstream grain nor is affected itself by the upstream grain. Basically, ion drag forces and variations of grain charge were neglected. First experimental evidence that the grain charge changes for aligned grains was reported by Kong et al. [36]. Recently, Kroll et al. [28] studied the relaxation process in a system consisting of two grains and showed that the wake strongly alters the grain charge and Carstensen et al. developed a phase resolved resonance method [42] which allows to determine grain charges with high accuracy. Thus, the combination of advances in simulation and experiment now provides the possibility to compare results quantitatively. The following sections are devoted to this task.

3 Comparison of Theory and Simulation

In a first step, we compare the electrostatic potential around a single grain as obtained from LR-theory and from PIC simulations. Fig 1(a) shows the contours of the wake field potential of a dust grain which is placed in the origin of the plot (black dot). The collisionless plasma is streaming with supersonic ion velocity in positive z -direction, e.g. $v_d \geq C_s$ and $C_s = \sqrt{k_b T_e / m_i}$ (where m_i is the ion mass and T_e is the electron temperature). The plasma potential is computed using the DiP3D code. Clearly, a deep potential minimum is observed in direct vicinity of the grain. In x -direction, i.e. perpendicular to the flow, the potential is in good agreement with a Yukawa potential $\Phi_{z=0} \sim \exp(-x/\lambda_{De})$ [31] which is supported by experiments [43]. In z -direction the potential strongly deviates from a statically screened Coulomb (Yukawa) potential. Downstream of the grain a pronounced potential maximum is found near $z = 2\lambda_{De}$. The potential maximum has a triangular shape and a Mach-cone like structure is formed. Thus, our PIC simulations nicely confirm previous findings, e.g. [12]. Furthermore, Fig 1(b) shows that all topological features are well reproduced by the LR calculations. The potential maximum is found at $z = 2\lambda_{De}$ and the shape and the Mach cone angle agree as well. A more detailed comparison of DiP3d and LR results is given in a recent paper [31]. There, it is shown that the peak positions generally agree well for supersonic ion flows. Even in the subsonic regime, where PIC codes are more noisy, a reasonable agreement is found. A quantitative comparison of the potential profile for a collisional plasma is given in Fig. 1(c). Again, the peak shape and wavelength agreement is very good. However, as LR uses the grain charge as an input parameter while in PIC simulations the charge is computed self-consistently, the amplitude of the LR results are rescaled according to the grain charge (see normalized ordinate in Fig. 1(c)).

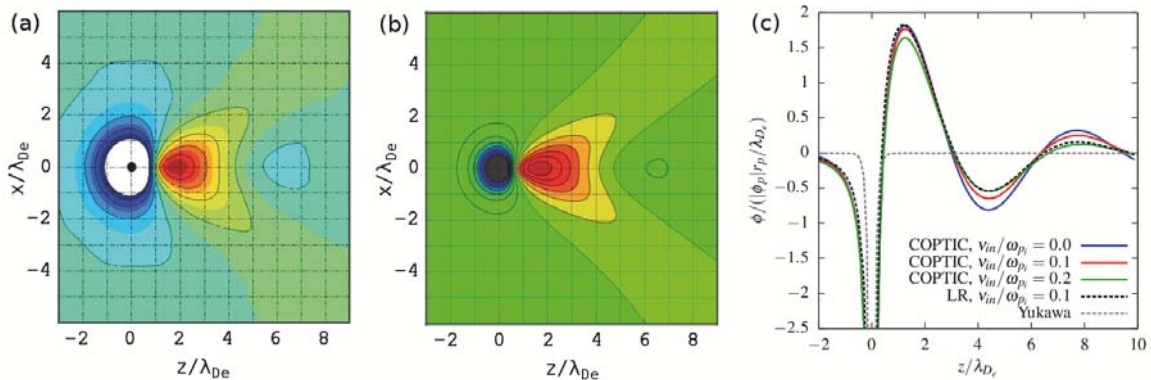


Fig. 1 Comparison of complementary numerical approaches: (a) full 3D PIC result from DiP3D for the wake field potential of a single dust grain (black dot, radius $a = 0.185\lambda_{De}$) at supersonic ion flow ($v_d = 1.5C_s$). The ion flow is from left to right and positive potential values are yellow or red while negative values are blue. The white area corresponds to very negative potential values. Despite the fact that the PIC simulations correspond to the nonlinear regime, the corresponding LR result in (b) reveals the same topological wake structure [31]. (c) wake field potential along z -direction for $x = 0$ computed with LR-theory and with PIC simulations using COPTIC for different collision frequencies ($v_d = C_s$).

Nonetheless, the results clearly show that for a single grain LR and PIC simulations can yield comparable results even for relatively large grains (radius $a = 0.185\lambda_{De}$) [31].

For a complex plasma the calculations of the wake of a single grain is of basic interest, but equally important is the question how a second grain will modify the results. Fig. 2 shows the ion density for a system consisting of two dust grains (radius $a = 0.1\lambda_{De}$). The results are all obtained for a collisionless situation using the DiP3D code. While Fig. 2(a) and (b) are self-consistent computations, the panels (c) and (d) are superpositions of wakes computed for isolated grains with adjusted charges to match the conditions of panel (a) and (b). Thus, a comparison of Fig. 2(a) and (b) and Fig. 2(c) and (d) can be regarded as an estimate for the importance of nonlinear effects. Generally, the results agree well, but there are some differences. First, the ion focus region of the upstream grain is significantly stronger in (a) and (b). Second, the ion focus regions are not separated in panel (a) and (b). The relative deviations of panel (a) and (c) as well as for (b) and (d) can locally reach 50 percent. A comparison of plasma potential leads to similar results [31]. This implies that nonlinear effects are relevant in a situation with multiple grains, but for small grains these deviations are reasonable [21]. Thus, combined MD/LR simulations with an advanced grain-charging model are certainly a very promising approach to describe many experimental conditions.

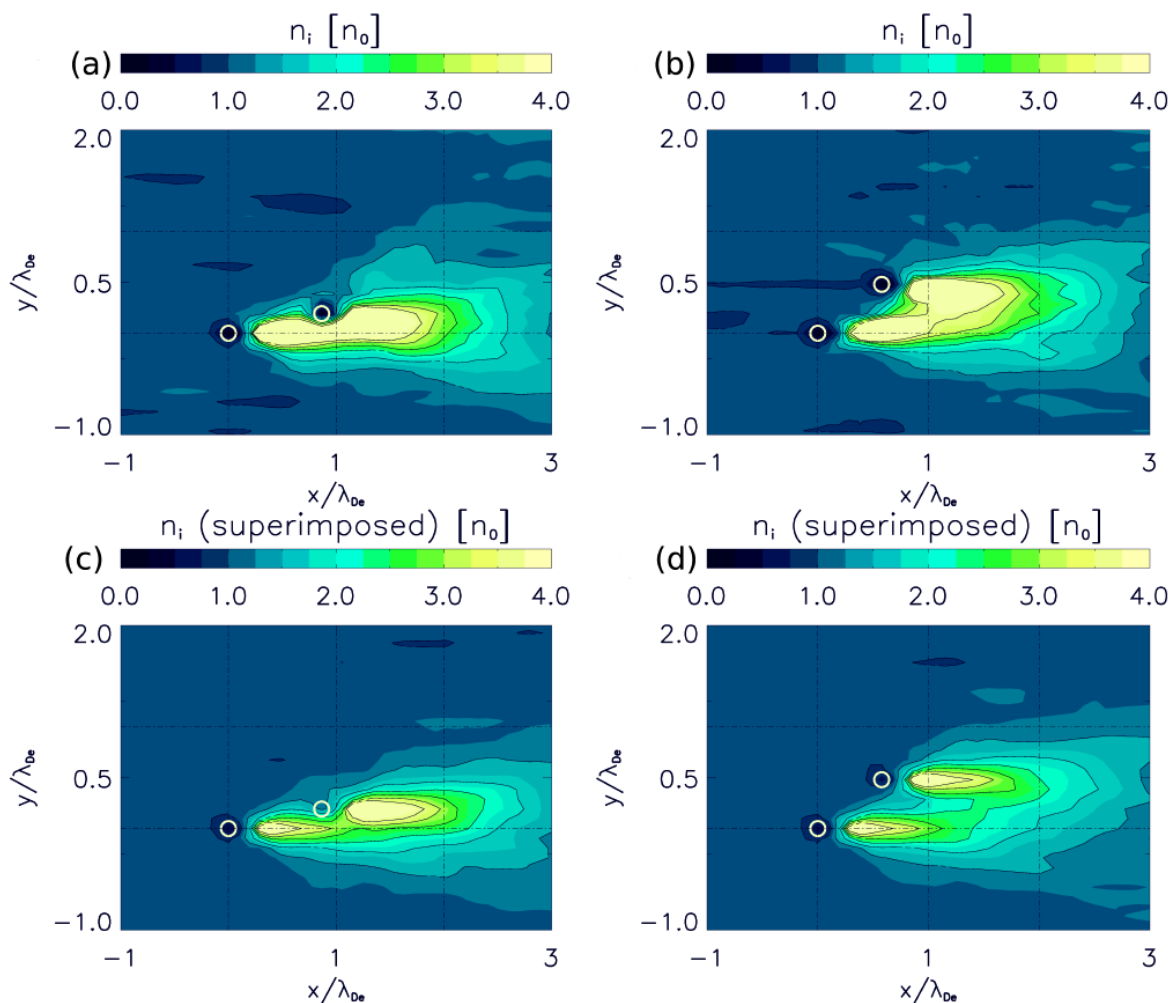


Fig. 2 Ion density (color coded) for two dust grains in a slightly supersonic ion flow ($v_d = 1.2C_s$). The grain positions are marked with white circles. (a) and (b) are self-consistent computations with the DiP3D code for (a) an almost aligned grain arrangement and (b) for a notable grain separation perpendicular to the ion flowing. In both cases the intergrain distance is λ_{De} . The panels (c) and (d) show the same situation but here the ion density is obtained from a superposition of wakes from isolated grains which were calculated with DiP3d and account for a charge adjustment on the downstream grain.

For experiments [23, 25, 26, 41], this finding has consequences as well. The fact that the downstream grain modifies the ion focus of the upstream grain implies that the downstream grain cannot be used straight forward as a probe for the ion focus region of upstream grains. Only for a sufficient distance between the grains the assumption of linear superposition is generally justified.

4 Charging of grains in streaming plasmas

The grain charge is determined by the plasma conditions. The floating potential of the grain establishes in such a way that electron and ion currents balance. The influence of a single dust grain on the overall quasi-neutrality $n_e = n_i$ can be neglected and for collisionless plasma conditions OML-theory is widely used to compute the grain potential and finally the grain charge. In a streaming plasma the grain charge additionally depends on the flow velocity v_d . As the cross-section for ion collection reduces with increasing v_d the electron and ion currents are only balanced at a more negative floating potential. The grain charge becomes more negatively with increasing v_d . In collisionless PIC simulations the charging process is computed self-consistently and agrees well with OML-theory [33, 44, 45].

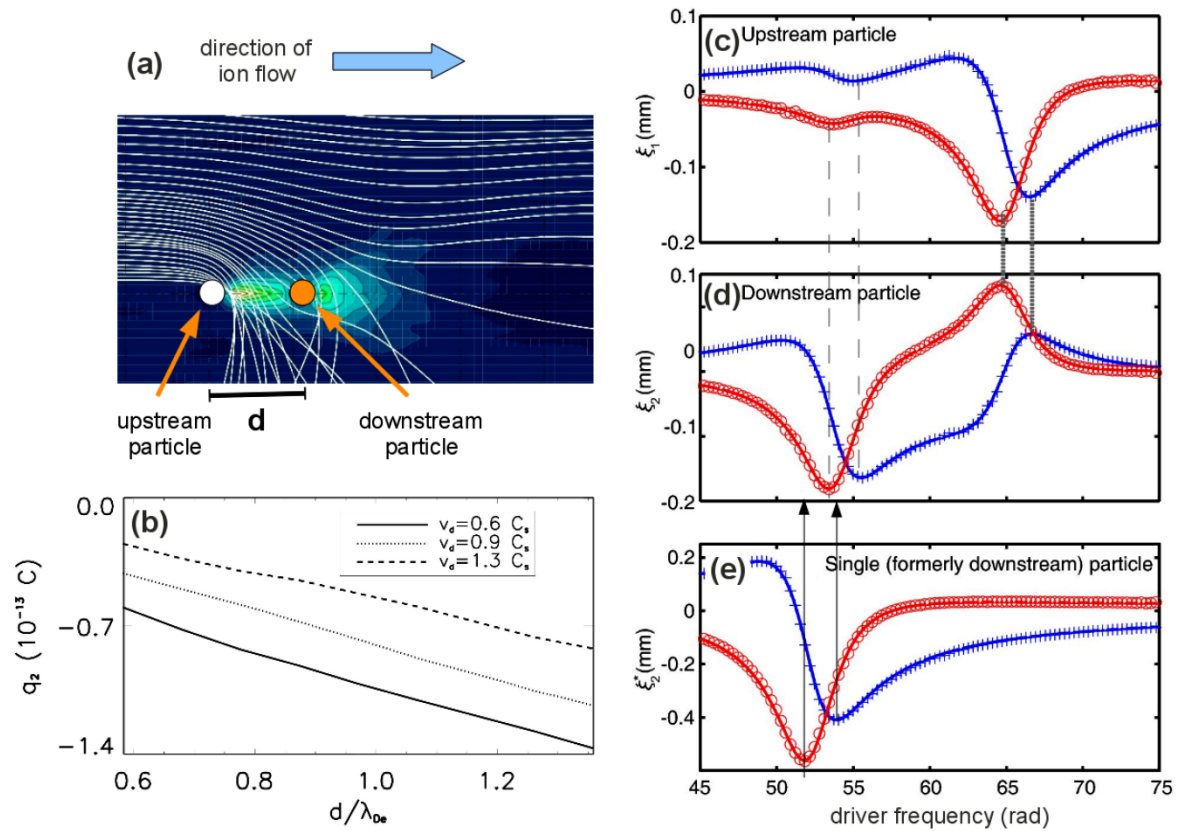


Fig. 3 Charge reduction of a grain in the wake of another grain: (a) ion density contour plot for two dust grains aligned in direction of the ion flow obtained with DiP3D PIC-code. The distance between grains is d . The ion density is clearly enhanced downstream of each grain. The solid lines visualize collisionless ion trajectories. (b) shows the charge of the downstream grain q_2 as a function of d . The downstream grain charges negatively and its charge increases with increasing distance d . Compared to the charge $q_1 \approx -1.6 \times 10^{-13}$ C of the upstream grain a significant charge reduction is observed. (c,d) Resonance curves obtained in experiment with PRRM for two aligned grains, which are confined in the plasma sheath. Corresponding resonances of up- and downstream grain are indicated by dashed/dotted lines. (e) shows the resonance curve of a single (formerly downstream) grain. The resonance frequency has shifted to lower frequencies. Taking the coupling of the grains into account, this corresponds to a charge reduction for the downstream grain.

For two (identical) grains in a flowing plasma the situation is more sophisticated. Fig. 3(a) shows the ion density for a pair of grains, which are aligned in direction of the ion flow. In addition, trajectories of individual ions are plotted in white. Obviously, the upstream grain shadows the downstream grain but at the same time its negative charge deflects ions into the focus region. Thus, the current balance for the downstream grain differs completely from those of the upstream grain. Fig. 3(b) depicts the charge of the downstream grain as a function of grain distance d . Compared to the charge $q_1 \approx -1.6 \times 10^{-13}$ C of the upstream grain, the charge q_2 of the downstream grain is significantly reduced. A significant charge reduction is observed for both sub- and supersonic flow velocities. A systematic investigation of grain charges q_1 and q_2 as a function of inter-grain distance and flow velocity can be found in Ref. [45].

In experiments the Phase Resolved Resonance Method (PRRM) [42] has been developed to measure grain charges with high precision. The results shown in Fig. 3(c)-(e) are measured for two grains which are confined in the plasma sheath above a powered rf-electrode. A small sinusoidal bias modulation of the electrode drives vertical oscillations of the grains. Now, the grain positions at two distinct phase angles (red and blue) with respect to the driver signal are measured. This allows to determine phase and amplitude of the oscillation. The plots (c) and (d) show the grain positions of upstream and downstream grain as a function of the driver frequency ω . Based on a simple model for coupled harmonic oscillators including a external drive $F_{ext}(\omega)$ and neutral gas friction, the equation of motion for this system then reads

$$\ddot{\xi}_1 + 2\gamma_1\dot{\xi}_1 + \omega_1^2\xi_1 + D_{12}(\xi_1 - \xi_2) = \frac{F_{ext}(\omega)}{m_1} \quad (2)$$

$$\ddot{\xi}_2 + 2\gamma_2\dot{\xi}_2 + \omega_2^2\xi_2 + D_{21}(\xi_2 - \xi_1) = \frac{F_{ext}(\omega)}{m_2} \quad (3)$$

where the positions of the grains $\xi_j(t)$ are oscillatory solutions, i.e. $\xi_j(t) = A_j \exp i\omega t$. From Fig. 3(c) and (d) it is seen, that the solutions (solid blue and red lines) fit the experimental data very well [29]. An essential feature of this oscillator model is that we allow for non-reciprocal forces between the grains. The reason for this is directly seen from plot (c) and (d). While the downstream grain shows two pronounced resonances at 53 rad/s and 64 rad/s the upstream grain shows only a pronounced resonance at 64 rad/s. The resonance at 53 rad/s is visible but weak. Therefore, the upstream grain clearly has a strong influence on the dynamics of the downstream grain, but not vice versa. This non-reciprocal character had been demonstrated earlier [22, 23] and is caused by the supersonic ion flow, which inhibits any upstream propagation of an ion density perturbation. In a second part of the experiment the upstream grain was removed and the downstream grain remained trapped. The discharge conditions were not changed and the resonance curves of the single grain was measured (see Fig. 3(e)). Obviously the resonances of the single downstream grain shifted to lower frequencies. Usually lower resonance frequencies are related to a lower charge to mass ratio, but here we have to compare the resonance of a single grain with the resonance of two coupled grains, where the coupling significantly influences the resonance frequencies. A detailed evaluation of the resonance frequencies found in Figs. 3(c-e) yields a reduction of charge for the aligned downstream grain of 22 percent. Repeating the same experiment but removing the downstream grain, the charge of the upstream grain does not change. Thus, the experiment proves a considerable charge reduction in the wake of other grains.

In addition, the analysis allows to determine the coupling constants for both oscillators. With $D_{12}/D_{21} = 5.5$ the ratio of the coupling constants is significantly larger than one, which means that the upstream grain strongly influences the downstream grain but not vice versa. This asymmetry has two reasons. The first is the supersonic ion flow. However, according to PIC simulations the ion flow alone only yields $D_{12}/D_{21} \approx 1.5$. Thus a second mechanism is required. In Fig. 3(b) the charge reduction was found to depend strongly on the intergrain distance d and that the charge gradient is to a good approximation linear. Taking into account that the equilibrium position of the grains is determined by a balance of gravity and electric field forces, the charge variation on the downstream grain caused by an oscillation of the upstream grain generates an imbalance of electric field forces and gravity and thus an effective enhancement of the coupling constant [29].

Therefore, the experiments show that the force balance, coupling and charging of only two aligned grains is a sophisticated problem. This problem is further complicated if the grains are not aligned or if multiple grains are studied [46]. The experiments of Kroll et al. [28] in combination with PIC simulations [33] showed that the charging of grains dramatically changes as soon as they enter the wake region. Finally, drag forces have not been considered so far. Extensive PIC-simulations by Patacchini et al. [47] have shown that drag forces along the flow are positive for all relevant conditions. Thus, an upstream motion of grains as observed in MD simulations

with LR-wake potentials (which neglect momentum transfer) [40] is not expected in experiments. Lapenta [9] and recently Piel [35] discussed the stability of chains of grains perpendicular to the ion flow. Both find that the drag forces have a stabilizing effect on chains of grains, but Piel's trajectory calculations show that the transverse momentum transfer originating from a loss of rotational symmetry for a displaced downstream grain gives the dominant contribution. The maximum of the transverse force is predicted for subsonic flows ($v_d \approx 0.6C_s$). A regime where the ion focus and thus its attractive force on a downstream grain is still weak. For sonic flows, drag forces are reported to be less important than the attractive wake field itself [48].

5 Dust clouds in streaming plasmas

Chains of grains are naturally the first step to understand the structural and dynamical properties of dust clouds. As today's simulations are just beginning to explore this regime [31, 40, 45, 46], the current understanding is based on experimental results. Experiments under microgravity conditions [1] and in the laboratory [49–51] allow to confine dust clouds outside the sheath region. Especially for Yukawa balls [52] the structural and dynamical properties are well explored [3, 53]. Yukawa balls exhibit a pronounced concentric shell structure without any chain formation, and neither structural nor dynamical processes show indications for an attractive grain interaction. From discharge simulations the ion drift velocities are known to be well below the sound speed. Fig. 4 shows measurements of a dust cloud that is confined in a trap in which Yukawa balls form. Here, two observations differ with respect to Yukawa balls. The neutral gas pressure is just $p = 4$ Pa, which is a factor of ten below the reference value of typical Yukawa balls, and with a diameter of $20 \mu\text{m}$ the grains are five times larger. The resulting structure of this dust cloud has similarities with Yukawa balls. The shape is roughly spherical and the grains arrange in shells (Fig. 4(b,c)).

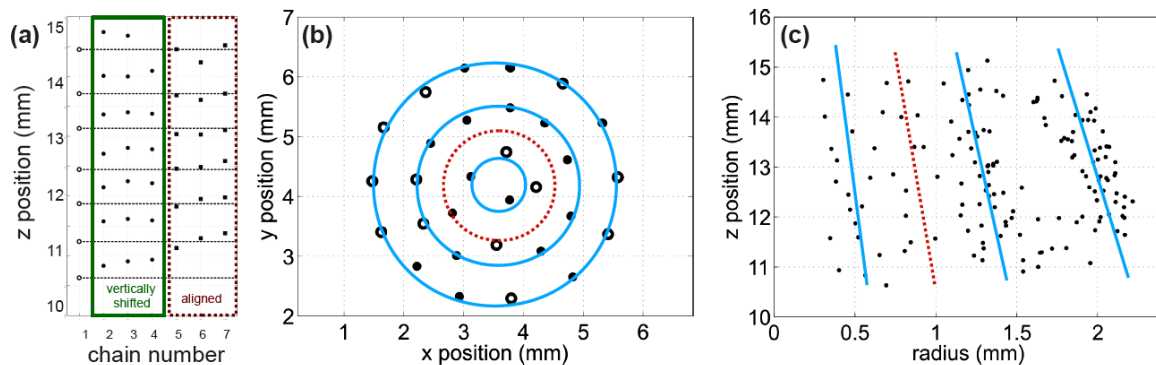


Fig. 4 Structural analysis of a 3D dust cloud consisting of 150 grains confined in a Yukawa ball trap. The grains arrange themselves in vertical chains. (a) The vertical positions of grains are shown for a reference chain (No. 1) and its six neighboring chains (No. 2-7). The neighboring chains are either horizontally aligned (No. 5-7) or vertically displaced by half an inter-grain distance (No. 2-4). (b) shows the midplane of the cluster. Vertically displaced chains are indicated with open symbols. The chains clearly arrange in shells with an additional subshell close to the center (dashed line). (c) Radial distribution of grains with respect to their z -position. The shells shown in (b) are seen at all vertical positions.

However, in vertical direction a pronounced chain formation is observed (Fig. 4(a)), where neighboring chains are either horizontally aligned or vertically shifted by half an inter-grain distance (Fig. 4(a)). Additional experiments with two grains [28] and with normal mode analysis [54] at similar discharge conditions have demonstrated that the chain formation is clearly caused by an attractive potential below each grain. The grain dynamics are similar to those observed for two grains in the plasma sheath [24, 27] where the supersonic ion flow produces a strong ion focus region. However, for the experimental conditions described here supersonic ion flows are not expected. Thus, the experiments suggest that an attractive ion focus region exists even at subsonic conditions. This interpretation is supported by LR and PIC simulations [31, 45] as well as the stability analysis of chains by Piel [35]. In all approaches large grains as well as a collisionless situation are beneficial for chain formation. The low neutral gas pressure results in a larger mean free path for ions and the larger grains result in a higher grain charge, which in turn deflects more ions into the wake region. However, this alone is not sufficient to finally

prove attractive forces for subsonic flows, but recent experiments by Arp et al. [34] report chain formation in the plasma bulk region where the ion flow is definitely subsonic and Killer et al. [30] have shown that a weak ion focus affects the structure of elongated Yukawa balls. Thus, there is strong evidence that ion focusing and wake fields are relevant even in the subsonic regime.

6 Conclusion and Outlook

Ion flows change the interaction between dust grains significantly and introduce anisotropic order along the flow. Both LR and PIC simulations show the formation of a highly anisotropic wake region downstream of grains. The quantitative comparison revealed that the resulting wake calculated from both methods are in good agreement for individual grains. Also, the strength of the resulting ion focus downstream of the grain agrees well for PIC and LR calculations. To achieve a very good quantitative agreement an accurate charging model for the dust grains is essential to provide the correct input parameter for LR. For two grains, we found that a simple superposition of wake fields of individual grains is not fully reproduced by PIC simulations. However, for small grains ($a \ll \lambda_{De}$) and adjusted grain charges (see sect. 4) the linear superposition of wake potentials is certainly a reasonable approximation.

Experiments with two aligned grains and especially charge measurements with high precision have shown that the charge of the downstream grain is significantly reduced if the grain is placed in the wake region of the other grain. This important result is found to agree well with results from PIC simulations. The computed charge reductions as a function of the relative grain position explain the static as well as the dynamic properties of a confined system consisting of two grains in detail. In addition, the results clearly indicate, that the assumption of a fixed charge for all grains in a dust cloud is questionable as soon as the cloud is exposed to a substantial ion flow. Therefore, for simulations as well as the interpretation of experiments refined charging models are required which are capable to predict the individual charges in systems with many grains.

Furthermore our LR and PIC results show in very good agreement, that even for subsonic flows, wake field effects may play a role such as in the pre-sheath or even in the plasma bulk. Experiments on confined systems show the competition of spherical order which is induced by the external confinement on the one hand and chain formation under subsonic flow conditions on the other hand.

To conclude, further research is required to study the formation of wake fields and their influence on the static and dynamic properties of larger dust clouds. Especially the subsonic regime, many-particle effects and the role of grain confinement need to be investigated. A promising approach to tackle this multi-scale problem is the dynamical screening approach [32], which allows to study the structural and dynamical consequences of the wake field in large dusty plasma systems. Since wake fields also represent a source of free energy that can drive instabilities [7], this aspect will have to be included in future explorations of phase transitions in continuation of the investigations described in the companion paper Ref. [53]. Furthermore, the influence of magnetic fields on the structure of wake fields is of fundamental importance. Thus, extending the study of dust dynamics in the companion paper Ref. [55] into the large magnetic field regime opens a promising new direction of research.

Acknowledgements We gratefully acknowledge financial support by Deutsche Forschungsgemeinschaft under SFB-TR24 project numbers A2, A3, A5, and A7. Further, we thank I. H. Hutchinson for providing the data for a comparison of COPTIC and LR.

References

- [1] G.E. Morfill and A.V. Ivlev, *Rev. Mod. Phys.* **81**, 1353 (2009).
- [2] P.K. Shukla and B. Eliasson, *Rev. Mod. Phys.* **81**, 25 (2009).
- [3] M. Bonitz, C. Henning, and D. Block, *Reports on Progress in Physics* **73**, 066501 (2010).
- [4] J. Meichsner et al., *Contrib. Plasma Phys.* **52**, 789 (2012).
- [5] M. Nambu, S.V. Vladimirov, and P.K. Shukla, *Phys. Lett. A* **203**, 40 (1995).
- [6] F. Melandsø and J. Goree, *Phys. Rev. E* **52**, 5312 (1995).
- [7] V.A. Schweigert, I.V. Schweigert, A. Melzer, A. Homann, and A. Piel, *Phys. Rev. E* **54**, 4155 (1996).
- [8] O. Ishihara and S.V. Vladimirov, *Phys. Plasmas* **4**, 69 (1997).
- [9] G. Lapenta, *Phys. Plasmas* **6**, 1442 (1999).
- [10] D.S. Lemons, M.S. Murillo, W. Daughton, and D. Winske, *Phys. Plasmas* **7**, 2306 (2000).

- [11] D. Winske, W. Daughton, D.S. Lemons, and M.S. Murillo, *Phys. Plasmas* **7**, 2320 (2000).
- [12] M. Lampe, G. Joyce, G. Ganguli, and V. Gavrishchaka, *Phys. Plasmas* **7**, 3851 (2000).
- [13] F. Jenko, G. Joyce, and H.M. Thomas, *Phys. Plasmas* **12**, 022309 (2005).
- [14] I. Schweigert, V.A. Schweigert, and F.M. Peeters, *Phys. Plasmas* **12**, 113501 (2005).
- [15] I.H. Hutchinson, *Plasma Phys. Control. Fusion* **48**, 185 (2006).
- [16] W.J. Miloch, H.L. Pécseli, and J. Trulsen, *Nonlin. Processes Geophys.* **14**, 575 (2007).
- [17] R. Kompaneets, S.V. Vladimirov, A.V. Ivlev, and G. Morfill, *New J. Physics* **10**, 063018 (2008).
- [18] B. Rovagnati, G. Lapenta, and F. Mashayek, *Phys. Lett. A* **372**, 5991 (2008).
- [19] P. Guio, W.J. Miloch, H.L. Pécseli, and J. Trulsen, *Phys. Rev. E* **78**, 016401 (2008).
- [20] W.J. Miloch, *Plasma Phys. Control. Fusion* **52**, 124004 (2010).
- [21] I.H. Hutchinson, *Phys. Plasmas* **18**, 032111 (2011).
- [22] K. Takahashi, T. Oishi, K. Shimomai, Y. Hayashi, and S. Nishino, *Phys. Rev. E* **58**, 7805 (1998).
- [23] A. Melzer, V. Schweigert, and A. Piel, *Phys. Rev. Lett* **83**, 3194 (1999).
- [24] V. Steinberg, R. Sütterlin, A.V. Ivlev, and G.E. Morfill, *Phys. Rev. Lett* **86**, 4540 (2001).
- [25] G.A. Hebner, M.E. Riley, and B.M. Marder, *Phys. Rev. E* **68**, 046401 (2003).
- [26] G.A. Hebner and M.E. Riley, *Phys. Rev. E* **69**, 026405 (2004).
- [27] A.A. Samarian and S.V. Vladimirov, *Contrib. Plasma Phys.* **49**, 260 (2009).
- [28] M. Kroll, J. Schablinski, D. Block, and A. Piel, *Phys. Plasmas* **17**, 013702 (2010).
- [29] J. Carstensen, F. Greiner, D. Block, J. Schablinski, W.J. Miloch, and A. Piel, *Phys. Plasmas* **19** (2012).
- [30] C. Killer, A. Schella, T. Miksch, and A. Melzer, *Phys. Rev. B* **84** (2011).
- [31] P. Ludwig, W.J. Miloch, H. Kählert, and M. Bonitz, *New J. Phys* **14**, 053016 (2012).
- [32] P. Ludwig, H. Kählert, and M. Bonitz, *PPCF* **54**, 045011 (2012).
- [33] W.J. Miloch, M. Kroll, and D. Block, *Phys. Plasma* **17**, 103703 (2010).
- [34] O. Arp, submitted to *Phys. Rev. E.* (2012).
- [35] A. Piel, *Phys. Plasmas* **18**, 073704 (2011).
- [36] J. Kong, T.W. Hyde, B. Harris, K. Qiao, and J. Carmona-Reyes, *IEEE Trans. Plasma Sci.* **37**, 1620 (2009).
- [37] V.R. Ikkurthi, K. Matyash, A. Melzer, and R. Schneider, *Phys. Plasmas* **15**, 123704 (2008).
- [38] R. Hockney and J.W. Eastwood, *Computer Simulations using Particles* (Taylor and Francis, 1988).
- [39] J.E. Hammerberg, D.S. Lemons, M.S. Murillo, and D. Winske, *IEEE Trans. Plasma Sci.* **29**, 247 (2001).
- [40] M. Lampe, G. Joyce, and G. Ganguli, *IEEE Trans. Plasma Sci.* **33**, 57 (2005).
- [41] A.A. Samarian, S.V. Vladimirov, and B.W. James, *Phys. Plasmas* **12**, 022103 (2005).
- [42] J. Carstensen, H. Jung, F. Greiner, and A. Piel, *Phys. Plasmas* **18**, 033701 (2011).
- [43] U. Konopka, L. Ratke, and H.M. Thomas, *Phys. Rev. Lett.* **79**, 1269 (1997).
- [44] I.H. Hutchinson, *Plasma Phys. Control. Fusion* **47**, 71 (2005).
- [45] W. Miloch, submitted to *Phys. Plasmas*.
- [46] V.R. Ikkurthi, K. Matyash, A. Melzer, and R. Schneider, *Phys. Plasmas* **17**, 103712 (2010).
- [47] L. Patacchini and I.H. Hutchinson, *AIP Conf. Proc* **1041**, 297 (2008).
- [48] I. Hutchinson, *Phys. Rev. Lett.* **107**, 095001 (2011).
- [49] B.M. Annaratone, T. Antonova, D. Goldbeck, H. Thomas, and G.E. Morfill, *Plasma Phys. Control. Fusion* **46**, B495 (2004).
- [50] O. Arp, D. Block, M. Klindworth, and A. Piel, *Phys. Plasmas* **12**, 122102 (2005).
- [51] H. Rothermel, T. Hagl, G.E. Morfill, M.H. Thoma, and H.M. Thomas, *Phys. Rev. Lett.* **89**, 175001 (2002).
- [52] O. Arp, D. Block, and A. Piel, *Phys. Rev. Lett.* **93**, 165004 (2004).
- [53] A. Melzer et al., *Contrib. Plasma Phys.* **52**, 795 (2012).
- [54] Y. Ivanov and A. Melzer, *Phys. Plasmas* **12**, 072110 (2005).
- [55] T. Reichstein et al., *Contrib. Plasma Phys.* **52**, 813 (2012).

A.10

MAGNETIZING A COMPLEX PLASMA WITHOUT A MAGNETIC FIELD

H. Kählert, J. Carstensen, M. Bonitz, H. Löwen, F. Greiner, and A. Piel

Reprinted with permission from
H. Kählert, J. Carstensen, M. Bonitz, H. Löwen, F. Greiner, and A. Piel,
Physical Review Letters, Vol. 109, 155003 (2012).
Copyright 2012, American Physical Society

Magnetizing a Complex Plasma without a Magnetic Field

H. Kählert,¹ J. Carstensen,² M. Bonitz,^{3,*} H. Löwen,¹ F. Greiner,² and A. Piel²

¹Heinrich-Heine-Universität Düsseldorf, Institut für Theoretische Physik II: Weiche Materie, Universitätsstraße 1, 40225 Düsseldorf, Germany

²Christian-Albrechts-Universität zu Kiel, Institut für Experimentelle und Angewandte Physik, Leibnizstraße 19, 24098 Kiel, Germany

³Christian-Albrechts-Universität zu Kiel, Institut für Theoretische Physik und Astrophysik, Leibnizstraße 15, 24098 Kiel, Germany

(Received 21 June 2012; published 10 October 2012)

We propose and demonstrate a concept that mimics the magnetization of the heavy dust particles in a complex plasma while leaving the properties of the light species practically unaffected. It makes use of the frictional coupling between a complex plasma and the neutral gas, which allows us to transfer angular momentum from a rotating gas column to a well-controlled rotation of the dust cloud. This induces a Coriolis force that acts exactly as the Lorentz force in a magnetic field. Experimental normal mode measurements for a small dust cluster with four particles show excellent agreement with theoretical predictions for a magnetized plasma.

DOI: 10.1103/PhysRevLett.109.155003

PACS numbers: 52.27.Lw, 52.25.Xz, 52.27.Gr, 45.50.Jf

Strongly coupled Coulomb systems have very unusual properties including spontaneous spatial ordering and the formation of liquids or even crystals. Coulomb crystals and liquids, originally predicted by Wigner [1], were eventually observed on the surface of helium droplets [2], in ion traps [3], and in complex plasmas [4,5]. They are also believed to occur in semiconductor quantum dots and quantum wells [6], as well as in white dwarf and neutron stars [7]. Of particular current interest is their behavior in a magnetic field, where strongly modified oscillation spectra [8–11] or anomalous diffusion properties [12] have been predicted, and even applications to verify enhanced nuclear reaction rates have been demonstrated [13]. Especially in neutron stars [14], giant magnetic fields are present that considerably modify the properties of the liquid and crystal states in the outer layers and alter the whole evolution of the star.

In a strongly coupled plasma (SCP), the Coulomb interaction energy of two particles, $Q^2/(4\pi\epsilon_0 a)$ [charge Q , typical interparticle distance a], is much larger than their thermal energy, $k_B T$. In a magnetized SCP the particles are, in addition to the electrostatic interactions, subject to the Lorentz force. The degree of magnetization can be measured by comparing the relevant time scales associated with these two forces [15]: while the Coulomb interactions lead to a characteristic vibration frequency [8] $\omega_0 = \sqrt{Q^2/(4\pi\epsilon_0 m a^3)}$, the cyclotron frequency $\omega_c = QB/m$ is the relevant parameter for the Lorentz force. For a given magnetic field B and mass density of the plasma $\rho_m = mn$ (particle mass m , number density n), the ratio of the two becomes $\omega_c/\omega_0 = B\sqrt{3\epsilon_0/\rho_m}$. Estimates for various strongly coupled astrophysical [7,14] and laboratory plasmas [13,16] are presented in Fig. 1.

Complex (dusty) plasmas [17] have, in recent years, become a prototypical system to study strong correlation effects in unmagnetized Coulomb systems. They contain

highly charged, micrometer-sized particles embedded in a partially ionized electron-ion plasma. Complex plasmas are found in numerous space environments including interstellar clouds, cometary tails, or planetary rings [18]. In laboratory experiments, the large particle size and mass make it possible to follow individual particle trajectories with unprecedented spatial and temporal resolution [19–21], providing valuable insight into strong coupling phenomena. However, until now, it has not been possible to extend this analysis to magnetized Coulomb systems. The large particle mass (via large ρ_m) limits ω_c/ω_0 to values below 0.1...0.5, even if superconducting magnets and particles with submicron diameters are used [8,10], see Fig. 1. Also, inevitably, such fields radically alter the plasma conditions and may lead to filamentation [22].

Here, we propose a completely different approach to achieve very strong magnetization effects that overcomes all these limitations. It can be used with standard

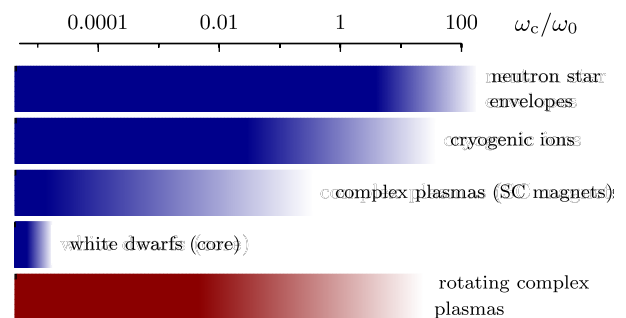


FIG. 1 (color online). Estimates of ω_c/ω_0 in various SCPs: White dwarf stars [7] ($\rho_m \gtrsim 10^9 \text{ kg m}^{-3}$, $B \lesssim 10^5 \text{ T}$), neutron stars [14] ($\rho_m \sim 10^7 \dots 10^{14} \text{ kg m}^{-3}$, $B \lesssim 10^{11} \text{ T}$), ions in Penning traps [13,16] ($n \sim 10^7 \dots 10^8 \text{ cm}^{-3}$, fields of several Tesla), and complex plasmas [8,10,11]. The method presented in this Letter (rotating complex plasmas) covers a wide range of magnetizations at room temperature.

(micron-sized) particles, does not significantly alter the plasma properties, and does not require expensive magnets at all. The basic idea to effectively *magnetize* the complex plasma is to impose the global motion of a rotating neutral gas column on the dust particles, which can be achieved, e.g., by a rotating electrode [23]. In the frame corotating with the neutral gas, the Coriolis force takes over the role of the Lorentz force and mimics the effect of a magnetic field, while the centrifugal force renormalizes the confinement. In all other aspects, the equations of motion are equivalent to those in a gas at rest. Related methods, where rotation is induced by different means, have been applied in the context of cold quantum gases [24–27].

In the following, we first present the theory underlying our concept and work out the scaling relations for the plasma parameters in a two-dimensional harmonic trap. We then perform a proof-of-principle experiment for the normal modes of a small cluster and find excellent agreement with the theoretical predictions.

In our model, the neutral gas is assumed to rotate as a rigid body with a velocity profile $\mathbf{u}(\mathbf{r}) = (\Omega \hat{e}_z) \times \mathbf{r}$. Here, \hat{e}_z denotes the unit vector in the z direction and Ω the rotation frequency. Particle confinement is provided by a harmonic trapping potential $V(\rho, z) = \frac{m}{2}(\omega_\perp^2 \rho^2 + \omega_z^2 z^2)$, where $\rho = \sqrt{x^2 + y^2}$. The equations of motion for the dust particles then have the form ($i = 1, \dots, N$)

$$m\ddot{\mathbf{r}}_i = -\nabla_i V(\rho_i, z_i) + \sum_{j \neq i}^N \mathbf{F}_{ij}^{\text{int}} - \nu m[\dot{\mathbf{r}}_i - \mathbf{u}(\mathbf{r}_i)] + \mathbf{f}_i.$$

Here, $\mathbf{F}_{ij}^{\text{int}} = -\nabla_i \phi(\rho_{ij}, z_{ij})$ denotes the interaction force [$z_{ij} = z_i - z_j$, $\rho_{ij} = \sqrt{x_{ij}^2 + y_{ij}^2}$], $\phi(\rho, z)$ the associated potential [28], ν the dust-neutral friction coefficient, and $\mathbf{f}_i(t)$ the stochastic force. The latter has zero mean and the correlation $\langle f_i^\alpha(t) f_j^\beta(t') \rangle = 2m\nu k_B T_n \delta_{ij} \delta^{\alpha\beta} \delta(t - t')$, where $i, j \in \{1, \dots, N\}$ and $\alpha, \beta \in \{x, y, z\}$. The neutral gas temperature is denoted by T_n .

In a frame rotating around the z axis at the angular velocity Ω of the neutral gas, the equations of motion take a form that illustrates the influence of the gas flow. Denoting the coordinates in the rotating frame with an overbar, the relation between the laboratory frame and the rotating frame reads $\mathbf{r}(t) = \mathbf{R}(t)\bar{\mathbf{r}}(t)$, where $\mathbf{R}(t)$ is the matrix for rotations around the z axis (see, e.g., Ref. [29]). Replacing the coordinates leads to

$$m\ddot{\bar{\mathbf{r}}}_i = -\bar{\nabla}_i \bar{V}(\bar{\rho}_i, \bar{z}_i) + \sum_{j \neq i}^N \bar{\mathbf{F}}_{ij}^{\text{int}} + \bar{\mathbf{F}}_{\text{Cor}}(\dot{\bar{\mathbf{r}}}_i) - \nu m\dot{\bar{\mathbf{r}}}_i + \bar{\mathbf{f}}_i,$$

where the effective confinement potential is now given by $\bar{V}(\bar{\rho}, \bar{z}) = \frac{m}{2}[(\omega_\perp^2 - \Omega^2)\bar{\rho}^2 + \omega_z^2 \bar{z}^2]$.

The first observation is that, in the rotating frame, the effective confinement frequency $\bar{\omega}_\perp = \sqrt{\omega_\perp^2 - \Omega^2}$ in the direction perpendicular to the rotation axis is being

reduced as a consequence of the centrifugal force. Second, the rotation induces the Coriolis force

$$\bar{\mathbf{F}}_{\text{Cor}}(\dot{\bar{\mathbf{r}}}) = m\dot{\bar{\mathbf{r}}} \times (2\Omega \hat{e}_z),$$

which has the same form as the Lorentz force for a homogeneous magnetic field $\mathbf{B}_{\text{eff}} = (2m\Omega/Q)\hat{e}_z$. The doubled rotation frequency can be identified with the cyclotron frequency, $\omega_c = 2\Omega$. The neutral gas flow velocity $\mathbf{u}(\mathbf{r})$ no longer appears explicitly because the coordinate frame rotates at the same angular velocity as the gas. While the form of the interparticle forces remains unaffected, $\bar{\mathbf{F}}_{ij}^{\text{int}} = -\bar{\nabla}_i \phi(\bar{\rho}_{ij}, \bar{z}_{ij})$, the components of the random force occur in a mixed form, $\bar{\mathbf{f}}_i(t) = \mathbf{R}^T(t)\mathbf{f}_i(t)$. However, its statistical properties are the same as in the laboratory frame; i.e., a Gaussian white noise is retained, $\langle \bar{\mathbf{f}}_i(t) \rangle = 0$, and $\langle \bar{f}_i^\alpha(t) \bar{f}_j^\beta(t') \rangle = 2m\nu k_B T_n \delta_{ij} \delta^{\alpha\beta} \delta(t - t')$.

Let us now estimate the effective magnetic fields $|\mathbf{B}_{\text{eff}}| = 2m\Omega/Q$ that can be reached. With rotation frequencies of $\Omega \approx 10$ Hz, a charge of $|Q| \approx 10^4 e$, and a mass of $m \approx 10^{-12}$ kg, one easily generates effective magnetic fields exceeding 10⁴ T, which is far beyond the capabilities of superconducting magnets. At very high rotation speeds, the centrifugal force weakens the horizontal confinement [30], which may give rise to a deformed plasma shape and a lower dust density. However, especially in two-dimensional systems [31], the shape of the dust monolayer will remain unaffected, and a lower density could even be beneficial as it decreases ω_0 , thus allowing one to reach even larger magnetizations $2\Omega/\omega_0$.

To illustrate these effects in more detail, we consider the limit $\omega_z \gg \omega_\perp$. This situation is typically encountered in dusty plasma experiments in radiofrequency discharges, where the particles are located in the sheath region above the lower electrode. Their interaction is well described by the Yukawa potential $\phi(r) = (Q^2/4\pi\epsilon_0 r) \exp(-r/\lambda)$ with the Debye screening length λ . As a typical interparticle distance we choose $a(\Omega) = [Q^2/(4\pi\epsilon_0 m \bar{\omega}_\perp^2)]^{1/3}$, which is equivalent to (up to a numerical factor) the ground state distance of two trapped particles with Coulomb interaction. The effective trap frequency $\bar{\omega}_\perp$ then coincides with the previous definition of $\omega_0 = \sqrt{Q^2/(4\pi\epsilon_0 m a^3)}$ and provides a natural frequency unit for particle vibrations. Both the distance and time scales, $a(\Omega)$ and $\bar{\omega}_\perp^{-1}(\Omega)$, increase upon faster rotation. Since the electron and ion time scales are orders of magnitude larger than the rotation frequencies, the charge Q and the Debye length λ (i.e., the plasma properties) remain constant to high accuracy.

The problem is then governed by the following dimensionless parameters: the coupling parameter $\Gamma(\Omega) = Q^2/(4\pi\epsilon_0 a(\Omega) k_B T_n)$, the screening parameter $\kappa(\Omega) = a(\Omega)/\lambda$, the damping rate $\gamma(\Omega) = \nu/\bar{\omega}_\perp(\Omega)$, and the effective magnetization

$$\frac{2\Omega}{\bar{\omega}_\perp(\Omega)} = \frac{2(\Omega/\omega_\perp)}{(1 - \Omega^2/\omega_\perp^2)^{1/2}}. \quad (1)$$

It is obvious that, already for a relatively slow rotation with $\Omega = \omega_\perp/2$, the plasma is strongly “magnetized” ($2\Omega/\bar{\omega}_\perp = 1.15$), see the left panel of Fig. 2. The associated changes (compared to the nonrotating system) of the coupling and screening parameter are small. These parameters scale as $\Gamma(\Omega)/\Gamma(0) = (1 - \Omega^2/\omega_\perp^2)^{1/3}$ and $\kappa(\Omega)/\kappa(0) = (1 - \Omega^2/\omega_\perp^2)^{-1/3}$, respectively, and start to change substantially when the centrifugal force noticeably increases the interparticle distance ($\Omega/\omega_\perp \gtrsim 0.7$), see the left panel of Fig. 2. In this regime, the decrease of $\bar{\omega}_\perp$ is largely responsible for the dramatic increase of the magnetization parameter. We also show the dimensionless damping rate, which scales as $\gamma(\Omega)/\gamma(0) = (1 - \Omega^2/\omega_\perp^2)^{-1/2}$. This means that, in experiments, the gas pressure should be sufficiently low allowing for a small neutral gas friction coefficient ν before start of the rotation. The right panel of Fig. 2 shows Γ and κ as a function of the effective magnetization in a parameter regime that should be easily accessible in dusty plasma experiments, see below [32].

In the following, we present a proof-of-principle experiment to verify the efficiency of the proposed concept. A sketch of the experimental setup is shown in Fig. 3. The experiments were performed in a 13.56 MHz capacitively coupled radiofrequency discharge at a gas pressure of $p = 0.4$ Pa (argon). Spherical PMMA particles with a diameter of $d = 21.8 \mu\text{m}$ and a mass of $m = 6.46 \times 10^{-12}$ kg are injected into the plasma, where they form two-dimensional clusters. The upper electrode can be set into rotation with frequencies up to 30 Hz, which causes a vertically sheared rotational motion of the neutral gas column [23].

We concentrate on the dynamics of a small ensemble of $N = 4$ particles and analyze their normal modes. The normal modes of small two-dimensional clusters have

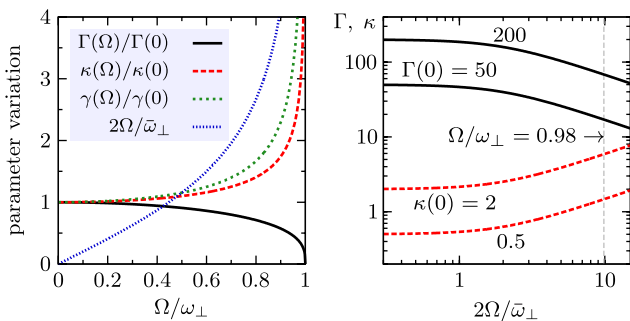


FIG. 2 (color online). Left: Variation of the effective magnetization, the coupling parameter, screening parameter, and damping constant with the rotation frequency in a finite two-dimensional system. Right: Scaling of Γ and κ as a function of the effective magnetization $2\Omega/\bar{\omega}_\perp$ for typical complex plasma conditions.

already been studied experimentally [33], but for magnetized dusty plasmas only theoretical predictions exist [34]. We first consider the center-of-mass (sloshing) mode. Since the effective confinement in the rotating frame is harmonic, the center-of-mass coordinate $\bar{\mathbf{r}}_{\text{cm}}(t)$ is independent of the interaction (Kohn theorem) and obeys the same equation of motion as a single particle [35]. In the absence of rotation, the two center-of-mass modes are degenerate with $\omega_{\text{cm}} = \omega_\perp$. For $\Omega > 0$, however, this degeneracy is lifted, and the frequencies read $\omega_{\text{cm}}^\pm = \sqrt{(\omega_c/2)^2 + \bar{\omega}_\perp^2} \pm \omega_c/2 = \omega_\perp \pm \Omega$. Here, $\bar{\omega}_\perp = \sqrt{\omega_\perp^2 - \Omega^2}$ is the effective trap frequency in the rotating frame. In Penning traps, these frequencies are known as the reduced cyclotron and magnetron frequency. The experimental results obtained from the spectrum of $\bar{\mathbf{r}}_{\text{cm}}(t)$ are depicted in Fig. 4 and show remarkable agreement with the theoretical prediction.

It is crucial for our scheme to further verify the accuracy of the remaining modes, which are sensitive to both the magnetic field and interparticle correlations. By linearizing the equations of motion in the rotating frame, we

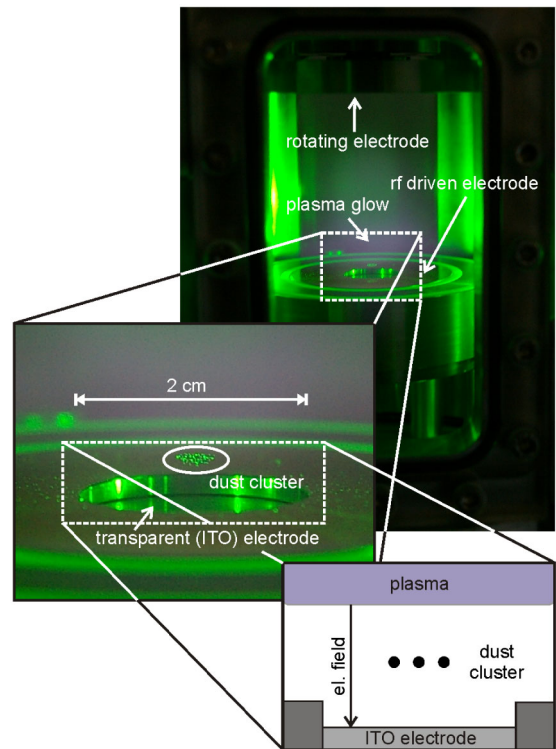


FIG. 3 (color online). Experimental setup: Dust particles are confined in a layer approximately 1 cm above the driven electrode. The electric field within the plasma sheath compensates gravity and provides vertical confinement, while horizontal confinement is realized by a cylindrical cavity of 20 mm in diameter and 2 mm in depth. The particles are illuminated from the side by a laser fan and can be observed from the bottom through a transparent electrode coated with indium tin oxide (ITO). The top electrode is rotatable.

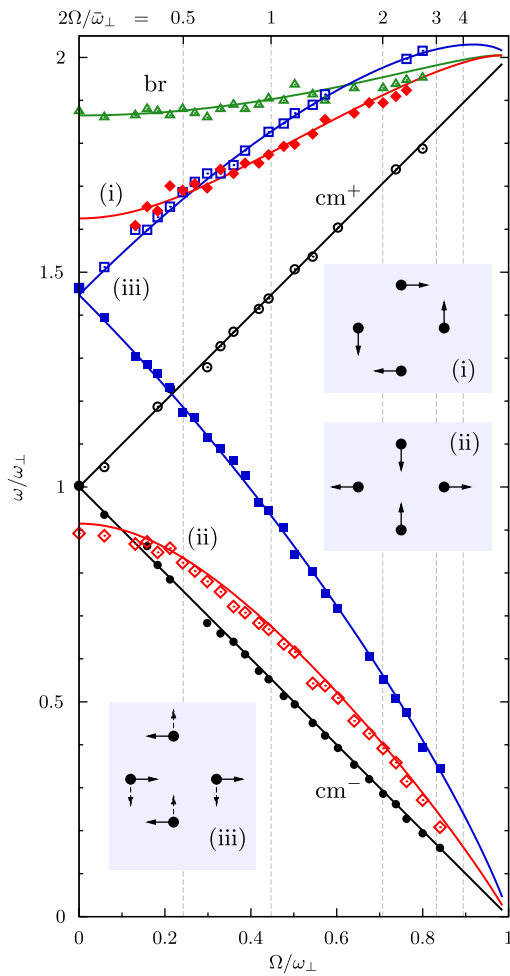


FIG. 4 (color online). Comparison of experiment and theory: Frequencies of the seven nontrivial normal modes of $N = 4$ dust particles as a function of the scaled rotation frequency. Symbols denote experimental results ($\omega_{\perp}/2\pi = 2.52 \text{ s}^{-1}$), lines are the theoretical eigenfrequencies with $\kappa(0) = 0.7$. The eigenvectors in the unmagnetized limit [36] ($\Omega = 0$) are sketched for four particular modes. Note that the two modes (iii) are degenerate in this case. The breathing mode and the two center-of-mass modes are indicated by “br” and “cm $^{\pm}$,” respectively. The effective magnetization $2\Omega/\bar{\omega}_{\perp}$ is shown on the upper axis [Eq. (1)].

determine the eigenfrequencies ω and eigenvectors \mathbf{v}_i from $(\omega^2 \delta_{ij} \delta^{\alpha\beta} - \bar{H}_{ij}^{\alpha\beta}/m - 2i\omega\Omega \delta_{ij} \epsilon^{\alpha\beta z}) v_j^{\beta} = 0$, where $\alpha, \beta \in \{x, y\}$ and $i, j \in \{1, \dots, N\}$, see Ref. [34]. Further, $\bar{H}_{ij}^{\alpha\beta}$ denotes the Hessian of the total potential energy in the rotating frame, δ_{ij} ($\delta^{\alpha\beta}$) the Kronecker delta, and $\epsilon^{\alpha\beta z}$ the Levi-Civita symbol. The cluster configuration for $N = 4$ is a square with particles located a distance R from the trap center, which is calculated from Eq. (6) in Ref. [36]. Even though a finite dust-neutral friction parameter is essential to put the plasma into rotation, it is sufficiently low to be negligible for the calculation of the eigenfrequencies ($\nu/\omega_{\perp} \approx 1/50$). To determine the mode frequencies experimentally, we calculated the projection $P(t) = \sum_{i=1}^N \bar{\mathbf{r}}_i(t) \cdot \mathbf{v}_i$ of the particle trajectories $\bar{\mathbf{r}}_i(t)$ on the

eigenvectors \mathbf{v}_i of the unmagnetized system, see Fig. 4. The breathing mode corresponds to a radial expansion and contraction of the cluster. The spectrum of $P(t)$ shows a peak at the associated mode frequency, which can be tracked as the rotation frequency is varied.

The measurements are compared with the theoretical results in Fig. 4. As for the case of the sloshing modes, we observe excellent agreement with the normal modes of a magnetized plasma. Effective magnetizations $2\Omega/\bar{\omega}_{\perp} \gtrsim 3$ allow us to clearly verify the predicted splitting of the normal modes into the upper and lower branch [34].

To summarize, we have presented a simple approach to *magnetize* a complex plasma. The idea is based on the correspondence between charged particles in a magnetic field and particles in a rotating gas column. The possibility to put the plasma into rotation takes advantage of the dissipative nature of complex plasmas in which the neutral gas acts as a highly effective transmission agent of angular momentum. We demonstrated that, with very modest rotation frequencies applied to only one electrode, strongly correlated particles in a rotating dusty plasma reproduce, to high accuracy, the normal modes of a magnetized system. Evidently, our concept can also be realized by other means and opens new unique possibilities for highly accurate studies of strongly correlated and strongly magnetized plasmas. The advantage compared to cryogenic ions is the broad range of accessible plasma parameters that can be varied independently (coupling strength, screening, dissipation) and the availability of single-particle resolution at room temperature conditions. It should be possible to create SCP states with extreme magnetizations potentially even comparable to those exotic ones in the outer layers of neutron stars. While our technique does not require any (superconducting) magnet at all, use of the latter in combination with plasma rotation allows one to create novel types of plasmas. In such plasmas, there would be effectively two *magnetic fields* that can be controlled independently—one of which (the rotation) affects only the heavy particles whereas the second (*real*) field influences the electrons and ions, allowing for an effective control of the interaction between the dust particles [37]. The combination of a rotating flow with a magnetic field also provides a promising avenue to access magnetorotational instabilities on the particle scale, which are relevant for the understanding of accretion disks [38].

This work was supported by the DFG via SFB TR6 and SFB TR24.

*bonitz@physik.uni-kiel.de

- [1] E. Wigner, *Phys. Rev.* **46**, 1002 (1934).
- [2] C.C. Grimes and G. Adams, *Phys. Rev. Lett.* **42**, 795 (1979).

- [3] D. J. Wineland, J. C. Bergquist, W. M. Itano, J. J. Bollinger, and C. H. Manney, *Phys. Rev. Lett.* **59**, 2935 (1987).
- [4] Y. Hayashi and K. Tachibana, *Jpn. J. Appl. Phys.* **33**, L804 (1994).
- [5] H. Thomas, G. E. Morfill, V. Demmel, J. Goree, B. Feuerbacher, and D. Möhlmann, *Phys. Rev. Lett.* **73**, 652 (1994).
- [6] S. M. Reimann and M. Manninen, *Rev. Mod. Phys.* **74**, 1283 (2002).
- [7] V. E. Fortov, *Phys. Usp.* **52**, 615 (2009).
- [8] G. Uchida, U. Konopka, and G. Morfill, *Phys. Rev. Lett.* **93**, 155002 (2004).
- [9] K. Jiang, Y.-H. Song, and Y.-N. Wang, *Phys. Plasmas* **14**, 103708 (2007).
- [10] M. Bonitz, Z. Donkó, T. Ott, H. Kählert, and P. Hartmann, *Phys. Rev. Lett.* **105**, 055002 (2010); T. Ott, M. Bonitz, P. Hartmann, and Z. Donko, *Phys. Rev. E* **83**, 046403 (2011).
- [11] T. Ott, H. Kählert, A. Reynolds, and M. Bonitz, *Phys. Rev. Lett.* **108**, 255002 (2012).
- [12] T. Ott and M. Bonitz, *Phys. Rev. Lett.* **107**, 135003 (2011).
- [13] F. Andereg, D. H. E. Dubin, T. M. O'Neil, and C. F. Driscoll, *Phys. Rev. Lett.* **102**, 185001 (2009).
- [14] A. Y. Potekhin, *Phys. Usp.* **53**, 1235 (2010).
- [15] Other parameters based on the comparison of length scales (e.g., the cyclotron radius and the Landau length [13]) are also being used.
- [16] M. J. Jensen, T. Hasegawa, J. J. Bollinger, and D. H. E. Dubin, *Phys. Rev. Lett.* **94**, 025001 (2005).
- [17] P. K. Shukla and B. Eliasson, *Rev. Mod. Phys.* **81**, 25 (2009).
- [18] C. K. Goertz, *Rev. Geophys.* **27**, 271 (1989).
- [19] G. E. Morfill and A. V. Ivlev, *Rev. Mod. Phys.* **81**, 1353 (2009).
- [20] M. Rubin-Zuzic, G. E. Morfill, A. V. Ivlev, R. Pompl, B. A. Klumov, W. Bunk, H. M. Thomas, H. Rothermel, O. Havnes, and A. Fouquet, *Nature Phys.* **2**, 181 (2006).
- [21] M. Bonitz, C. Henning, and D. Block, *Rep. Prog. Phys.* **73**, 066501 (2010).
- [22] M. Schwabe, U. Konopka, P. Bandyopadhyay, and G. E. Morfill, *Phys. Rev. Lett.* **106**, 215004 (2011).
- [23] J. Carstensen, F. Greiner, L.-J. Hou, H. Maurer, and A. Piel, *Phys. Plasmas* **16**, 013702 (2009).
- [24] K. W. Madison, F. Chevy, W. Wohlleben, and J. Dalibard, *Phys. Rev. Lett.* **84**, 806 (2000).
- [25] P. Rosenbusch, D. S. Petrov, S. Sinha, F. Chevy, V. Bretin, Y. Castin, G. Shlyapnikov, and J. Dalibard, *Phys. Rev. Lett.* **88**, 250403 (2002).
- [26] M. Zwierlein, J. Abo-Shaeer, A. Schirotzek, C. Schunck, and W. Ketterle, *Nature (London)* **435**, 1047 (2005).
- [27] A. L. Fetter, *Rev. Mod. Phys.* **81**, 647 (2009).
- [28] This form includes ion-wake potentials.
- [29] D. Hestenes, *New Foundations for Classical Mechanics (Fundamental Theories of Physics)* (Kluwer Academic Publishers, Dordrecht, 1999).
- [30] J. Carstensen, F. Greiner, and A. Piel, *Phys. Plasmas* **17**, 083703 (2010).
- [31] Y. Feng, J. Goree, and B. Liu, *Phys. Rev. Lett.* **100**, 205007 (2008).
- [32] Evidently, the analogy between the rotation and the cyclotron frequency reaches certain limits when plasma confinement is considered. While an increase of Ω decreases the effective confinement of the dust cloud, a stronger magnetic field gives rise to an improved plasma confinement.
- [33] A. Melzer, M. Klindworth, and A. Piel, *Phys. Rev. Lett.* **87**, 115002 (2001).
- [34] M. Kong, W. P. Ferreira, B. Partoens, and F. M. Peeters, *IEEE Trans. Plasma Sci.* **32**, 569 (2004).
- [35] J. I. Jiménez-Aquino, R. M. Velasco, and F. J. Uribe, *Phys. Rev. E* **77**, 051105 (2008).
- [36] S. G. Amiranashvili, N. G. Gousein-zade, and V. N. Tsytovich, *Phys. Rev. E* **64**, 016407 (2001).
- [37] J. Carstensen, F. Greiner, and A. Piel, *Phys. Rev. Lett.* **109**, 135001 (2012).
- [38] P. J. Armitage, *Annu. Rev. Astron. Astrophys.* **49**, 195 (2011).

List of Publications

Publications in peer-reviewed journals

- [A.1] Jan Carstensen, Franko Greiner, Lu-Jing Hou, Horst Maurer, and Alexander Piel, *Effect of neutral gas motion on the rotation of dust clusters in an axial magnetic field*, Physics of Plasmas, **16**, 013702 (2009)
- [A.2] Jan Carstensen, Franko Greiner, Lujing Hou, and Alexander Piel, *Effect of Centrifugal Forces on the Interparticle Distance of Two Dust Particles Confined in a Plasma*, IEEE Transactions on Plasma Science, **38**, 788(2010).
- [A.3] Jan Carstensen, Franko Greiner, and Alexander Piel, *Determination of dust grain charge and screening lengths in the plasma sheath by means of a controlled cluster rotation*, Physics of Plasmas, **17**, 083703(2010).
- [A.4] Jan Carstensen, Hendrik Jung, Franko Greiner, and Alexander Piel, *Mass changes of microparticles in a plasma observed by a phase-resolved resonance method*, Physics of Plasmas, **18**, 033701(2011).
- [A.5] Jan Carstensen, Franko Greiner, Dietmar Block, Jan Schablinski, Wojciech J. Miloch, and Alexander Piel, *Charging and coupling of a vertically aligned particle pair in the plasma sheath*, Physics of Plasmas, **19**, 033702(2012).
- [A.6] Jan Carstensen, Franko Greiner, and Alexander Piel, *Ion-Wake-Mediated Particle Interaction in a Magnetized-Plasma Flow*, Physical Review Letters, **109**, 135001(2012)
- [A.7] Jan Carstensen, Fabian Haase, Hendrik Jung, Benjamin Tadsen, Sebastian Groth, Franko Greiner, and Alexander Piel, *Probing the plasma sheath by the continuous mass-loss of micro-particles*, IEEE Transactions on Plasma Science, **113**, 064503(2013).
- [A.8] Franko Greiner, Jan Carstensen, Nils Köhler, Iris Pilch, Helge Ketelsen, Sascha Knist and Alexander Piel, *Imaging Mie ellipsometry: dynamics of nanodust clouds in an argon-acetylene plasma*, Plasma Sources Science and Technology, **21**, 065005(2012).
- [A.9] D. Block, J. Carstensen, P. Ludwig, W. J. Miloch, F. Greiner, A. Piel, M. Bonitz, and A. Melzer, *Wake Formation and Wake Field Effects in Complex Plasmas*, Contributions to Plasma Physics, **52**, 804(2012).
- [A.10] H. Kählert, J. Carstensen, M. Bonitz, H. Löwen, F. Greiner, and A. Piel, *Magnetizing a Complex Plasma without a Magnetic Field*, Physical Review Letters, **109**, 155003(2012).

Selected Contributions to International Conferences

[B.1] Franko Greiner, Jan Carstensen, Lu-Jing Hou, and Alexander Piel, *Dynamics of 2D Dust Clusters with a Perpendicular Magnetic Field*, AIP Conference Proceedings, **1041**, 217(2008).

[B.2] J. Carstensen , F. Greiner, A. Piel, *Comparison of non-invasive diagnostics for particle charge and screening length for flat dust clusters in rf discharges*, 37th EPS Conference on Plasma Physics, **P1.308**, 2010.

[B.3] Jan Carstensen, Franko Greiner, and Alexander Piel, *Dust trajectories as high precision diagnostic*, AIP Conference Proceedings, **1397**, 439(2011).

[B.4] F. Greiner, J. Carstensen, N. Kohler, I. Pilch, and A. Piel, *Trapping of nanodust clouds in a magnetized plasma*, AIP Conference Proceedings, **1521**, 265(2013).

Danksagung

An dieser Stelle möchte ich mich bei allen Personen bedanken, die mich während der letzten Jahre bei meiner Arbeit unterstützt haben. An erster Stelle möchte ich mich bei Herrn Prof. Dr. Alexander Piel für die Aufnahme in seine Arbeitsgruppe und die Betreuung dieser Arbeit bedanken. Er hat mich nicht zuletzt durch zahlreiche Diskussionen und mit konstruktiver Kritik ermutigt, meine wissenschaftliche Arbeit stets zu verbessern, von der Herangehensweise an neue Fragestellungen bis zur Darstellung der Ergebnisse in Wort und Schrift. Insbesondere möchte ich mich auch bei Herrn Dr. Franko Greiner bedanken, der mir seit meiner Diplomarbeit immer mit Rat und Tat zu Seite stand, und es nicht zuletzt mit seiner lebhaften und offenen Art schafft, den Arbeitsalltag nie langweilig werden zu lassen, aber es auch versteht, mit klaren Worten auf Fehler hinzuweisen.

Mein besonderer Dank gilt auch allen Mitgliedern der Arbeitsgruppe für ein angenehmes Arbeitsklima und die zahlreichen Kuchen(wetten), ob nun bei der Arbeit, während der Kaffeepausen, auf diversen Tagungen oder andere Veranstaltungen, was ein motiviertes und produktives Arbeiten über einen längeren Zeitraum erst möglich macht. Ich möchte mich auch bei Sebastian Groth, Fabian Haase, Hendrik Jung und Benjamin Tadsen bedanken, die sowohl als Hiwi, Bachelor- oder Masterstudent mit mir zusammen im Labor standen und mit viel Motivation versucht haben, unseren Experimentaufbauten sinnvolle Ereignisse zu entlocken, die dann auch teilweise Eingang in diese Arbeit gefunden haben. Mario Knüppel, Volker Rohwer und Michael Poser danke ich für die Bereitschaft, jederzeit bei technischen oder elektronischen Problemen aller Art zu helfen.

Eine große Hilfe bei den letzten Korrekturen an dieser Arbeit waren mir Torben Reichstein und Katja Wulf, die mich auf diverse Rechtschreib-/Grammatikfehler, Inkonsistenzen in der Nomenklatur oder ungeschickte Formatierungen aufmerksam gemacht haben. Und nicht zuletzt möchte ich mich bei meinen Eltern und meiner Familie bedanken, die mich bei meiner Entscheidung Physik zu studieren und dann auch zu promovieren, immer unterstützt haben.

Lebenslauf

Persönliche Daten

Name: Jan Carstensen
Geburtsdatum: 15.11.1982
Staatsangehörigkeit: deutsch
Familienstand: ledig

Schulbildung

1989 - 1993 Theodor-Heuss-Grundschule Kiel
1993 - 2002 Max-Planck-Schule Kiel
Juni 2002 Abitur mit den Leistungskursen
Mathematik und Physik

Studium

April 2003 Immatrikulation im Fach Physik
an der Christian-Albrechts-Universität zu Kiel
September 2005 Vordiplom mit Nebenfach Chemie
Dezember 2008 Beendigung des Studiums der Physik mit Abschluss
Diplom
Nebenfach: Mathematik
Thema der Diplomarbeit:
Experimente in magnetisierten staubigen Plasmen
seit November 2008 Promotion in der Arbeitsgruppe "Plasmadynamik"
am Institut für Experimentelle und Angewandte
Physik der Christian-Albrechts-Universität zu Kiel

Erklärung

Hiermit versichere ich, dass die vorliegende Dissertation - abgesehen von der Beratung durch meinen wissenschaftlichen Lehrer und der Verwendung der angegebenen Hilfsmittel - nach Inhalt und Form meine eigene ist. Sie hat weder ganz noch teilweise an einer anderen Stelle im Rahmen eines Prüfungsverfahrens vorgelegen. Die Arbeit ist unter Einhaltung der Regeln der guten wissenschaftlichen Praxis der Deutschen Forschungsgemeinschaft entstanden.

Kiel, den